Experimental Study on Heat Transfer Characteristics of Microchannel Systems Using Liquid Crystal Thermography

Roland Ssonko Muwanga

A thesis

in

The Department

of

Mechanical and Industrial Engineering

Presented in Partial Fulfillment of the Requirements

For the Degree of Doctor of Philosophy

Concordia University

Montréal, Québec, Canada

June 2007

Abstract

Experimental Study on Heat Transfer Characteristics of Microchannel Systems Using Liquid Crystal Thermography

Roland Ssonko Muwanga, Ph.D.

Concordia University, 2007

Microchannel heat transfer governs the performance of the microchannel heat sink, which is a recent technology aimed at managing the stringent thermal requirements of today's high-end electronics. The present thesis investigates the single-phase and flow boiling heat transfer characteristics in microchannel systems. A state-of-the-art test facility has been constructed for the experimental investigations. It is composed of a closed loop flow setup, a microscopic imaging system and an automated data acquisition system. A technique for using un-encapsulated thermochromic liquid crystals (TLC's) to measure the local heat transfer coefficient in microchannel geometries is developed. A unique localized calibration of the TLC material is employed to minimize the effects of lighting non-uniformity and variable coating thickness. Measurements are carried out in three different microtubes, and in two innovative parallel and radial microchannel heat sinks with 3.5 cm^2 footprint areas. The working fluids are distilled water, FC-72 and air.

Local single-phase heat transfer and frictional pressure drop measurements are presented for the laminar, transitional and turbulent flow regimes, in microtubes down

to 0.25 mm. Local flow boiling heat transfer coefficient data are presented for a quality up to 0.3, and for the conditions investigated, suggest a nucleation dominated region. Flow boiling oscillation characteristics in two parallel silicon microchannel heat sink configurations aimed at micro/nano- spacecraft thermal management are investigated. One is a standard heat sink with 45 parallel channels, whereas the second is similar, except with cross-linked paths at three locations. The oscillation amplitudes are relatively large and identical in frequency for the fluid pressure and temperature. Oscillation properties for the standard heat sink are correlated for different heat fluxes, while a first glimpse of the cross-linked heat sink performance under flow boiling instability conditions is presented. Optimization of a radial inflowing microchannel heat exchanger has been investigated numerically, after preliminary fabrication and experimentation trials. Unique to this optimization was consideration of channels with axially varying cross-sections. Three-dimensional conjugate analysis shows that when constrained by a fixed channel outlet area, increasing the channel inlet area will improve the thermal performance.

Overall, a method utilizing un-encapsulated TLC thermography for local heat transfer measurements in microgeometries has been developed, while investigating the flow and heat transfer characteristics in microchannel systems. The present work along with the advances in MEMS based manufacturing is expected to lead to the creation and development of a number of miniaturized technologies, from DNA analysis to power-plants-on-chips.

Acknowledgments

Achieving the work presented in this thesis would not have been possible without the help and support of a number of people. I would like to thank my supervisor and mentor Dr. Ibrahim Hassan. He continually challenged me to achieve above and beyond what I thought was possible, and believed in me at each step of the way. I would like to thank the research colleagues I have had the pleasure of working with. Many have graduated now including Korhan Pehlivan, Mohamed Abdelgawad, Ariane Immarigeon, Patricia Phutthavong and Min Min Le. As well, the present research group members, Dino Bowden, Tariq Ahmad, Minh Dang, Wael Saleh, Mohamed Ghorab, Ayman Megahed, Mohamed Rahman, Chad Zhang and Dr. Sung In Kim. The Washington Technology Center is gratefully acknowledged for their assistance and capabilities in fabricating the silicon heat sinks. I would like to extend my gratitude to Pratt and Whitney Canada for financial assistance and in particular to Sri Sreekanth and Terry Lucas.

The love of family and friends brings meaning to life, and my sincerest gratitude to all. In particular I would like to say thank you to my favorite siblings, Robin, Rita

and Laura. Thank you to my late good friend, Joseph Kriyan de Leon. A special thanks to the one who has been by my side through all the ups and downs, Mackenzie Baker. Finally, but not least of all, thank you to my parents.

To my parents, Mary Victoria and Roland Sr., for all your love.

Contents

List of Figures

List of Tables

Nomenclature

A   area, m^2

Bo   boiling number, $(Bo = \frac{q''}{Gh_{fg}})$

Cp   fluid specific heat capacity, kJ/(kg·°C)

D   diameter, m

D_h hydraulic diameter $(\frac{4A_{cs}}{2(W_{chn}+H_{chn})})$, m

d_{heated} heated area hydraulic diameter $(\frac{4A_{cs}}{2H_{chn}+W_{chn}})$, m

f   friction factor

f_ω frequency, Hz

f^* non-dimensional frequency, $(f^* = \frac{f_\omega L_{chn}}{u_{chn,in}})$

g   gravity, m/s^2

G   mass flux, kg/(m²·s)

H   height, m

h   heat transfer coefficient, W/(m²·°C)

h_{fg} latent heat of vaporization, kJ/(kg·K)

I current, A

k   thermal conductivity, W/(m·°C)

K_{loss} entrance and exit loss factors

L   length, m

$\dot{m}$ mass flow rate, kg/s

N_{sub} subcooling number, $\left(N_{sub} = \frac{Cp(T_{sat}-T_{in})}{h_{fg}} \frac{\rho_f - \rho_g}{\rho_g} \right)$

Nu   Nusselt number

$\tilde{P}$ power generated, W

P   pressure, Pa

P_r reduced pressure

Pr   Prandtl number

$\dot{q}$ heat generated per unit volume, W/(m^3)

q'' heat flux, W/m^2

Q_{vol} volumetric flowrate, m^3/s, unless otherwise specified

r   radial coordinate

Re   Reynolds number

r^+ normalized radial coordinate, $\left(r^+ = \frac{r_{out}-r}{r_{out}-r_{in}} \right)$

T   temperature, °C, unless otherwise specified

u   velocity, m/s

V voltage, V

$\vec{V}$ 3-component velocity vector, m/s

W   width, m

We_D Weber number, $\left(We_D = \frac{G^2 D_h}{\sigma \rho_f}\right)$

We_{Lchn} Weber number, $\left(We_{Lchn} = \frac{G^2 L_{chn}}{\sigma \rho_f}\right)$

x quality

z^+ normalized streamwise coordinate, $\left(z^+ = \frac{z}{L_{chn}}\right)$

z^* non-dimensional streamwise coordinate, $\left(z^* = z/RePrD_h\right)$

Abbreviations

BNC   bayonet Neill-Concelman

CCD   charged-coupled device

CFD   computational fluid dynamics

CHF   critical heat flux

CTF   continuous two-phase flow

DNA   deoxyribonucleic acid

DRIE   deep reactive ion etching

EBO   explosive boiling oscillations

FD   fully developed

IR   infrared

LALPO   large amplitude long period oscillations

LCD   liquid crystal display

LTAF   liquid to two-phase alternating flow

LTVAF   liquid to two-phase to vapor alternating flow

MEMS   micro-electro-mechanical systems

NTSC   National Television System(s) Committee

PCR   polymerase chain reaction

PIV   particle image velocimetry

RGB   red-green-blue

ROI   region of interest

SASPO   small amplitude small period oscillations

SEE   standard error estimate

SIMPLE   semi-implicit method for pressure-linked equations

TD   thermally developing

TIFF   tagged image file format

TLC   thermochromic liquid crystal

UV   ultraviolet

Greek Letters

α channel aspect ratio (width/height)

μ viscosity, N·s/m^2

ρ density, kg/m^3

σ surface tension, N/m

θ Non-dimensional temperature, $\left(\theta = \frac{T - T_{b,in}}{\frac{q'' H_{chn}}{k}}\right)$

Subscripts

amp	amplitude
avg	averaged parameter
b	fluid bulk property
chn	channel parameter
crit	critical heat flux
f	liquid property
fluid	fluid condition
heated	heated surface parameter
i	inner wall parameter
in	channel inlet condition
∞	free stream condition
o	outer wall parameter
out	channel outlet condition
sat	saturation property
sub	subcooled conditions with respect to entry
tp	two-phase conditions
tube	tube parameter
v	vapour property
w	condition at the wall

y spanwise coordinate

z streamwise coordinate

0 zero quality location

Chapter 1

Introduction

1.1 Motivation

Advances in Micro-Electro-Mechanical System (MEMS) based manufacturing has led

to the creation and development of a number of miniaturized technologies, from DNA

analysis (Li et al., 2006) to power generation (Epstein, 2003). For the electronics in-

dustry this has enabled the fabrication of electronic circuits with an ever decreasing

size. As a result, there has been an increase in the heat produced per unit area

of microelectronic chips, which in turn has generated the requirement for effective

miniature cooling technologies. One such device is the pumped cooling loop using

microchannel heat sinks and pioneered in the early 1980's by Tuckerman and Pease

(1981). The microchannel heat sink is characterized by a set of microchannels conven-

tionally machined or micromachined into a conducting block. It has been proposed as

a viable thermal management solution for high heat flux electronics that include land

based (Jiang et al., 2001), avionic (Mudawar, 2001) and extraterrestrial applications

1

(Paris et al., 2002).

Fundamental to the microchannel heat sink and a number of MEMS based systems under development, is the microchannel and its corresponding thermo-fluidic characteristics. The study of convective heat transfer in small diameter channels or microchannels, typically considered less than 0.5 mm for single phase flows and 3 mm for boiling flows, is still in its infancy and much fundamental work remains in this area.

1.2 Objectives and Organization

The objectives of this work are:

- To develop a test facility for local thermal measurements in microchannel systems.

- To investigate the local heat transfer characteristics in microchannel systems.

- To address flow boiling instabilities in two-phase microchannel systems.

- To develop novel microchannel heat sinks aimed at micro/nano- spacecraft thermal management applications.

- To numerically investigate heat transfer in microchannel systems with axially varying cross-sections.

Chapter 2 presents a review of the heat transfer in single and multi-channel microsystems with single phase and boiling flows. Additionally, the literature review

discusses the problem of flow boiling instabilities and oscillations, which is one of the constraints in applying two-phase microchannel heat sinks to demanding applications such as spacecraft systems. Finally, the literature review provides a summary of the current state of thermal measurement techniques for microscale applications. Chapter 3 provides a description of the test facility, which has been developed for convective heat transfer investigations in microgeometries. This includes design and procurement of the mechanical rig, the instrumentation and automated data acquisition system, and the optical measurement equipment. The methodology developed for utilizing un-encapsulated thermochromic liquid crystals (TLC's) for measurement in microgeometries is presented in Chapter 4. This includes validation through single phase heat transfer measurements in a 1 mm tube. An investigation of the transport phenomena in microtubes under single phase and flow boiling conditions is presented in Chapter 5. The work to this point provides a foundation on the methods that will be utilized in studying the heat transfer characteristics in various applications of microchannel systems. The development of a cross-linked silicon microchannel heat sink is presented in Chapter 6. Experimental measurements are presented under single phase and flow boiling conditions. Finally, Chapter 7 explores a radially flowing, varying cross-sectional area microchannel heat sink. Numerical investigations using a one-dimensional thermal resistance model and a three dimensional conjugate heat transfer model, are carried out to evaluate its performance. In the closing (Chapter 8), a summary of the contributions is presented and recommendations for future studies are provided.

Chapter 2

Literature Review

2.1 Single Phase Flow and Heat Transfer

2.1.1 Single Channel Studies

Some recent reviews on single phase flow heat transfer in mini and microchannels may be found in Hetsroni et al. (2005b), Morini (2004), Sobhan and Garimella (2000) and Bailey et al. (1995). Some of the prevalent characteristics and remarks related to single phase continuum flows include discrepancies reported between microchannel results and the accepted correlations and trends for their macro counterparts. For example, the critical Reynolds number for transition to turbulent flow in microchannels has been reported to be as low as 200 (Sobhan and Garimella, 2000), compared to the conventionally accepted range of 2100 to 2300 confirmed by other researchers in microchannels (Sharp and Adrian, 2004). In addition, significant variations between the results of different investigators have been reported for the heat transfer coefficients

and friction factor with no clear relationship for the differences in some instances (Mehendale et al., 2000). Hetsroni et al. (2005b) reviewed a number of single phase flow studies, with the aim of revealing the potential sources of disparity. In general they noted that discrepancies may be due to i) differences between the experimental conditions and assumptions in the model not considered, ii) error in the measurements, and iii) increasing influence of surface forces and conditions usually neglected for conventional size systems. The authors' proposed a range of applicability of conventional size channel theory for microchannels ranging in hydraulic diameter from 15 μm to 4010 μm.

The channel size at which deviations will occur from conventionally sized channels remains undetermined and in present work microchannels are considered channels with nominal diameter of 1 mm and less. Overall, a review of the literature indicates the need for additional and improved studies of heat transfer in mini and microchannels due to a lack of consensus in a number of areas on the flow and heat transfer characteristics (Morini, 2004; Sobhan and Garimella, 2000).

2.1.2 Multi-Channel Microsystems

Recently, there have been a number of investigations considering radical modifications to the standard straight microchannel heat sink for pumped cooling loops. Amongst these, single phase flow studies have considered pin fins (Kosar and Peles, 2006a; Peles et al., 2005), fractal networks (Chen and Cheng, 2005; Alharbi et al., 2004; Pence, 2002), constructal networks with loops (Wang et al., 2006) and cross-linked

channels (Xu et al., 2005; Cho et al., 2003; Jiang et al., 2002). Radially flowing configurations, as opposed to the standard parallel channel configurations, have been proposed through fractal network and constructal network schemes (Wang et al., 2006; Alharbi et al., 2004; Pence, 2002). The aims of the fractal and constructal schemes have been for improved surface temperature uniformity and decreased pressure drop compared to equivalently sized standard parallel channel schemes. Xu et al. (2005) utilized a concept of cross-links along 10 triangular channels of 155 μm hydraulic diameter. The objective here, was to increase the heat transfer by introduction of a constantly re-developing thermal boundary layer. They compared this configuration with a standard straight channel configuration. Temperature profiles for the straight channel had a constant rise, whereas for the cross-linked section would rise, then drop giving a lower mean temperature. Additionally, the cross-linked design showed a lower pressure drop than the straight channel. Cho et al. (2003) also studied a cross-linked configuration, however with rectangular channels. Heat transfer studies considered localized heating to better simulate real chip conditions. Under single phase flow, the cross-linked configuration showed better performance, but contrary to the previous study, showed an increase in pressure drop. Colgan et al. (2005) studied a configuration with fins rather than channels combined with multiple entries and exits along the flow path. The fins were arranged in an in-line or staggered configuration and had sharp or blunt ends. The sharp versus blunt end configurations did not show any significant benefit, however the staggered fins had better thermal performance, though a higher pressure drop.

Bau (1998) proposed the use of channels with slowly varying cross sections for improving the thermal performance of micro heat exchangers. The author showed that through optimizing the wall contour with streamwise distance, the maximum wall temperature or the maximum wall gradient could be reduced in comparison to straight parallel channels. There have been a number of investigations considering flow without heat transfer in channels of slowly varying cross-sections, with one of the first studies dating back over 35 years (Mantion, 1971). Studies considering flow with heat transfer in slowly varying ducts, however, are limited, partially due to their limited applicability to conventional heat exchangers. Brod (2001) considered flow in a circular tube and a two-dimensional plane channel of slowly varying cross-section, which was directed at the process industries using melts. Assuming a similarity solution whereby the velocity at each cross-section was fully developed, the author obtained expressions for the fluid bulk temperature and heat transfer distribution. The study showed the non-dimensional fluid bulk temperature and the local Nusselt number to be invariant on the tube's contour function. MEMS based fabrication can readily produce rectangular channels with variable widths. In the work of Li et al. (2006), a polymerase chain reaction (PCR) microchip with serpentine microchannels of varying width was designed and fabricated for control of the velocity at different areas of the chip. Control of the velocity allowed for optimization of the sample exposure times at the different temperature phases, while minimizing the transition time during temperature phase transition.

2.2 Boiling Heat Transfer

Recent reviews on boiling heat transfer in mini and microchannels have been presented by Thome (2004) and Kandlikar (2002). Kandlikar (2002) suggested a channel size criterion whereby 3 mm and greater are conventional (macro) channels, 0.2 mm to 3 mm are mini channels and 0.01 mm to 0.2 mm are microchannels. With the exception of the Confinement number (N_{conf}), however, no physics based classification of channel sizes has been presented (Thome, 2004). The Confinement number was introduced by Kew and Cornwell (1997) and was suggested as a parameter to differentiate between microscale and macroscale boiling phenomena. It is given by,

$$N_{conf} = \frac{[\sigma / (g (\rho_f - \rho_v))]^{1/2}}{D}.$$ (2.1)

It was found that for a Confinement number greater than 0.5, the macroscale correlations did not predict microchannel results well (Kew and Cornwell, 1997).

It has been generally accepted that both nucleate boiling and convective boiling mechanisms exist in mini and microchannels, although the dominant mechanism remains inconclusive. Some investigators have shown that there is a decreasing trend in the heat transfer coefficient with mass flux, and so have concluded that forced convection is the dominant mechanism (Lee and Lee, 2001; Qu and Mudawar, 2003). While for macro size channels, the dominant mechanism is convective boiling, the majority of the mini and microchannel studies suggest that nucleate boiling is the dominant mechanism (Thome, 2004). This has been determined by observing the

stronger dependence of the heat transfer coefficient with heat flux, and not with mass flux.

2.2.1 Small Diameter Tubes

There have been a number of recent investigations of flow boiling heat transfer in small diameter tubes. Lin et al. (2001) investigated the two-phase heat transfer characteristics of R141B in circular tubes of diameter 1.1 mm, 1.8 mm, 2.8 mm, and 3.6 mm. They deduced that there were three boiling regions. A nucleate boiling region whereby the heat transfer coefficient was dominated by the heat flux, a convective boiling region whereby the heat transfer coefficient was independent of heat flux but increased with quality, and a partial dryout region. In the partial dryout region, the heat transfer coefficient was reduced dramatically, and dryout was observed to occur earlier with increasing Confinement number. Additionally, the heat transfer coefficient was found to have a more marked decrease with quality, with decreasing tube diameter. The mean heat transfer coefficient was independent of mass flux and diameter and dependent only on heat flux in the region before dryout. Recently Saitoh et al. (2005) investigated flow boiling of R-134a in circular tubes of 0.51 mm, 1.12 mm and 3.1 mm diameter. The two-phase heat transfer coefficient was observed to be governed by convective and nucleation effects, though the convective effects decreased with decreasing diameter. Dryout was observed to occur at a lower quality with decreasing diameter. Through tracking the wall temperature, flow oscillations were observed in the 3.1 mm and 1.12 mm tube at low quality entry, but not in the

0.51 mm tube. The authors concluded that these were density wave type oscillations due to their period. Grohmann (2005) studied the two-phase and single-phase heat transfer characteristics of Argon in circular tubes, with nominal diameters of 0.50 mm and 0.25 mm. In the nucleate boiling regime, there was no influence of mass flux or quality on the heat transfer coefficient. Flow condition oscillations were sometimes observed with subcooled entry conditions, however these could be controlled with the entry quality greater than zero.

2.2.2 Flow Boiling of Dielectric Fluids in Mini and Microchannels

The fluid type is an important parameter in the heat transfer performance. Many studies on flow boiling heat transfer in mini and microchannels have used water or refrigerants, few studies however have utilized dielectric fluids. These fluids will typically have lower heat transfer performance than water, however are advantageous in situations whereby the fluid may be in contact with an electrically charged component. Warrier et al. (2002) investigated two-phase heat transfer in an array of five 0.75 mm hydraulic diameter rectangular channels using FC-84 as the working fluid. They compared their heat transfer results with correlations valid for channels ranging in size from 2.4 mm to 32 mm and found none to be in good agreement. The heat transfer coefficient was observed to have a decreasing trend with quality. They developed a correlation relating the saturated flow boiling heat transfer coefficient with quality and Boiling number. Yen et al. (2003) studied boiling heat transfer in microtubes

of 0.19 mm, 0.3 mm and 0.51 mm inner diameter, using FC-72 and HCFC123. The study was carried out at low mass flux ranging from 145 kg/(m²·s) to 295 kg/(m²·s). Local heat transfer coefficient results were only presented for HCFC123. The results showed a decreasing heat transfer coefficient with quality, but independent of mass flux, suggesting nucleate boiling as the dominant mechanism. Recently, Chen and Garimella (2005) investigated the effects of dissolved air on the subcooled flow boiling characteristics of FC-77 in an array of 10 parallel channels, 0.50 mm wide and 2.5 mm deep. The study showed boiling incipience to occur at lower wall temperatures for the un-degassed fluid compared to the degassed fluid. Flow instability fluctuations were larger for the un-degassed fluid and larger pressure drops were measured. Although the earlier boiling inception caused higher initial heat transfer coefficients for the un-degassed fluid, the authors recommended working with a degassed fluid for better predictability and control.

2.2.3   Flow Boiling Incipience

Important to the safe and reliable design of two-phase heat exchangers with subcooled entry is the prediction of the wall superheat required to initiate boiling, or inversely, for a given subcooling, prediction of the incipient heat flux. Classical approaches for boiling incipience consider a bubble to grow if the minimum temperature surrounding the bubble is equal to or greater than the saturation temperature given by the pressure inside the bubble (Collier and Thome, 1999). The superheat in this case is related explicitly to the heat flux and the pressure. This method tends to under

11

predict the incipient superheat, particularly for well wetting fluids such as refrigerants and perfluorocarbons, as it does not consider the fluid-solid contact angle, and it assumes all nucleation sites to be active. Recently, Basu et al. (2002) demonstrated a correlation based on adaptations of boiling incipience classical methods, which includes effects of the static contact angle of the fluid-solid system. The correlation showed good agreement with a variety of fluid-solid systems.

Qu and Mudawar (2002) investigated the incipient heat flux required for boiling in an array of rectangular microchannels. It was shown that this heat flux is dependent on the mass velocity. Additionally, boiling incipience was observed to be different from large channels, such that bubble departure occurred, rather than growth and collapse at incipience. A mechanistic model based on bubble departure criterion was developed to predict the boiling incipience from the flat surface or a corner and showed good agreement with the experimental results. Regarding single tubes, Kennedy et al. (2000) studied boiling incipience in 1.448 mm and 1.168 mm circular copper tubes with water as the working fluid. Their results for the larger tube were in good agreement with macro tube correlations, whereas the smaller tube was underpredicted. An estimation of the Confinement number for their case, taken at 50 °C (from experimental conditions) is calculated to be 0.46 for the larger tube and 0.57 for the smaller tube. Hapke et al. (2000) investigated boiling incipience in a 1.5 mm nickel alloy tube with water as the working fluid and a mass flux range from 100 kg/(m^2 · s) to 500 kg/(m^2 · s). Their results showed wall superheat dependency at incipience on mass flux.

Ghiaasiaan and Chedester (2002) developed a model for predicting boiling incipience in microchannels based on the assumption that the thermocapillary force suppressing the bubble plays a crucial role. Their model showed the incipience heat flux to be dependent on channel diameter (results for 0.75 mm to 1.45 mm diameter), however this was not experimentally verified and the results were for turbulent flows. Yen et al. (2003) experimentally investigated boiling heat transfer in tubes 0.19 mm to 0.51 mm with FC-72 and HCFC123 and at low mass fluxes of 50 kg/(m$^2 \cdot$ s) to 300 kg/(m$^2 \cdot$ s). The maximum wall superheat was found to be dependent on the tube diameter and nucleation site distribution.

2.2.4 Boiling Instabilities

Boiling instabilities in macro-systems have been extensively studied in the past and may be classified as static or dynamic (Bergles, 1981; Kakac and Veziroglu, 1983). Static instabilities are those whose cause may be related through steady state laws. During such instability the fluid may change to another steady state point or oscillate between two steady state points. An example is the Ledinegg instability which, by definition, occurs when the pressure gradient with respect to mass flow of the internal flow system is less than that of the pressure supply system. Inertia or other feedback effects cause dynamic instabilities and the steady state laws are not enough to predict them. These instabilities may be initiated by a static instability. Density waves have a low frequency that is on the order of a particle traveling through the system. Their mechanism is related to delay and feedback between the flow, pressure drop and

density. Other types of dynamic instabilities may include thermal oscillations, which are observed during dryout, and parallel channel instabilities, which are related to interactions between a small number of channels. In this case, various modes of flow redistribution may be observed. A third type of dynamic instability, which occurs as a secondary phenomenon, is the pressure drop oscillation. This type of instability is found to occur when there is a compressible volume upstream of the heated section. Similar to the Ledinegg instability, it occurs just after the minimum in the pressure drop versus mass flow curve. The frequency of oscillation is much lower for the pressure drop type instabilities compared to density wave instabilities and is on the order of 0.1 Hz.

A comparison of flow stability regions for single, parallel, and cross-connected parallel channels has been summarized by Kakac and Veziroglu (1983). The data were compiled from a number of experiments from a single test facility investigating boiling instabilities in vertical pipe systems using Freon-11. The pipe inner diameters were 7.5 mm (0.295 inches). The study found that for density-wave type instabilities, single channel, parallel channel and two parallel cross-connected channels all presented similar performance. For pressure-drop type instabilities the most stable system was provided by the 4 parallel cross-connected channel system. The parallel channel systems with unequal heat inputs showed the smallest stability regions with respect to pressure-drop type instabilities.

Related to microchannel flows, few studies have documented the characteristics of the flow boiling instabilities. Some studies have observed different flow pattern characteristics in the boiling instabilities depending on the imposed conditions, and

14

have classified them as such. Wu and Cheng (2004) investigated boiling instabilities in a parallel channel system with eight trapezoidal channels. The channels were fabricated in a silicon wafer 525 μm thick and had a hydraulic diameter of 186 μm. They used a microscope and a high-speed camera for bubble visualization and placed thermocouples at the base of the wafer. The authors observed three instability modes consisting of liquid to two-phase alternating flow (LTAF), continuous two-phase flow (CTF), and liquid to two-phase to vapor alternating flow (LTVAF). For the LTAF case, bubbly flow dominated with wall temperature fluctuations of 20 °C to 46 °C. The oscillation frequency was 0.065 Hz and was characterized as large-amplitude/long period. Pressure and mass flux oscillations were almost out of phase. With an increase in heat flux and decrease in mass flux, the CTF case was observed. Temperature fluctuations decreased to 7 °C to 20 °C and the pressure and mass flux were almost in phase. Finally with additional increase in heat flux and decrease in mass flux, the LTVAF case was observed. Wall temperature fluctuations were highest in this case at 66 °C to 230 °C and the pressure and mass flux were almost out of phase. These oscillations were also classified as having a large-amplitude over a long period.

Xu et al. (2005) carried out a study of flow boiling instabilities in a copper test section of 26 channels, 300 μm wide and 800 μm deep. By gradually decreasing the mass flux, they were able to initiate flow instability. Two periodic instabilities were observed, large amplitude long period instabilities oscillations (LALPO) and small amplitude small period oscillations (SASPO). These were accompanied by thermal oscillations with fluctuations of up to 20 °C (peak to peak) in the first case and up to 4 °C (peak to peak) in the second. The SASPO instability was characterized by bubble

growth at channel exit, followed by the liquid-vapor interface moving upstream. When the interface reached the inlet plenum for a number of channels, the vapor fronts moved forward into the channels. The growing vapor front increased the temperature while decreasing the heat transfer coefficient. The working fluids were water and methanol. Similar behaviors were observed for both fluids, however, due to methanol's lower latent heat the frequency was lower.

Hetsroni et al. (2005a) investigated water boiling in 21 isosceles triangle channels with a base of 250 μm and an angle of 55°, fabricated in a silicon substrate. At boiling onset, bubble growth rapidly filled the entire channel cross-section, then grew lengthwise both upstream and downstream. The other channels accounted for the liquid that was pushed upstream. A time instant later, the bubble was vented from the channel and a brief period of vapor with liquid droplets commenced. This boiling process was described as "explosive" due to its short time period. The pressure drop amplitude was found to increase with quality and the oscillation frequency in a single channel increased with increasing heat flux. In a recent study by the same authors (Hetsroni et al., 2006), further characterization of the boiling instabilities, termed explosive boiling oscillations (EBO) was provided. They found an increase in the amplitude of bulk system parameters such as the pressure drop and the inlet and outlet fluid temperature with increasing heat flux. Additionally, they found a decrease in the frequency of the bulk system properties with heat flux. This is notably different from the characteristic of individual channels within the same system. Steinke and Kandlikar (2004a), while studying flow boiling heat transfer in six parallel channels

16

(214 μm $\times$ 200 μm) in a copper substrate test section, observed flow reversals in individual channels. The fluid was water and the channels were slightly trapezoidal. The flow reversals were found to occur during the onset of the annular-slug flow regime. Flow reversals were similarly observed by Balasubramanian and Kandlikar (2005) who investigated flow boiling in six parallel copper channels, 990 μm wide and 207 μm deep. The authors noted that while bubble nucleation was the dominant flow pattern (at low surface temperatures), the pressure drop dominant frequency increased with increasing surface temperature. However, with further increase in temperature, the slug flow pattern dominated and the pressure drop dominant frequency decreased. Qu and Mudawar (2004) studied flow boiling in 21, 215 μm $\times$ 821 μm (width $\times$ depth) copper channels, with water as the working fluid. Two oscillation type instabilities were observed. In the first case, the liquid-vapor interface changed position drastically from close to the exit, to close to the inlet. This was accompanied with high pressure drop and temperature fluctuations. The temperature fluctuations reached 15 °C and caused premature critical heat flux (CHF). Installing a throttle upstream of the test section remedied this and it was classified as a pressure drop oscillation. The second case was a result of installing the throttle valve and was characterized by the liquid-vapor front alternating positions between channels. This was characterized as parallel channel instability and was accompanied by mild pressure drop and temperature ($<$1 °C) fluctuations.

2.2.5   Novel Multi-Channel Concepts

Two-phase flow novel configurations have aimed at increasing heat transfer and minimizing instabilities. Kosar and Peles (2006b), introduced restrictors at the channel inlets to suppress flow boiling oscillations. The restrictors had a diameter six times smaller than the channels. They studied the influence of the restrictor length, and observed that with increased length, the instabilities were less severe. Pressure drop fluctuations were on the order of 2 to 7 kPa with no restrictor, whereas they were less than 1 kPa with the restrictors. For heat transfer enhancement under two-phase conditions, Kosar and Peles (2005) utilized re-entrant cavities. When used in macro-sized systems, such structures are known to act as artificial nucleation sites, which can enhance flow boiling. However due to the large discrepancies in two-phase heat transfer results in microchannels, the authors were unable to ascertain the benefit of this configuration. Kandlikar et al. (2006) utilized a combination of inlet flow restriction elements and fabricated nucleation sites, to stabilize the flow boiling process. The study considered restrictors with 51 percent and 4 percent of the flow area, with and without artificial nucleation sites. With the 4 percent flow area restrictor, no flow reversals were observed and the addition of the fabricated nucleation sites produced the best thermal performance. However, the penalty of this was an increase in pressure drop of almost double.

2.3 Heat Transfer Measurement in Microsystems

Most work regarding experimental heat transfer measurements in microchannels use thermocouples (point sensors) for wall temperature measurements, due to their accessibility and relatively low cost. Current fine gage wire thermocouples on the market have diameters as small as 0.013 mm for K and E-Type and 0.025 mm for J and T-Type (OMEGA, 2006). Thermocouple diameters for specialized hypodermic probes are as small as 0.200 mm, while standard small size probes have diameters as low as 1.5875 mm (OMEGA, 2006). One problem with such sensors is their large size compared to the channel dimensions and hence their potential influence on the flow characteristics. This may be alleviated by placing the sensors at a distance from the fluid-wall interface and assuming one-dimensional heat transfer, or by using a fin analysis method (Qu and Mudawar, 2003). These approximations, however, introduce inaccuracies in the internal wall surface temperature measurement. Also, the relative size of these sensors, if discreetly placed at the wall, gives only an area averaged temperature measurement. Another inconvenience of such point sensors is the need for an array of sensors to obtain full surface temperature measurements.

An overview of the various possibilities of micromachined thermal sensors may be found in Kovacs (1998). Many macro size thermal sensing concepts have been fabricated as micro transducers. These include thermo-mechanical sensors, which rely on thermal bimorph of two dissimilar metals, thermo-resistive transducers where temperature is related to change in resistance, and thermocouple type sensors, which rely on the Seebeck and Peltier effect. Self-heating, however, becomes a significant

19

problem as the size reduces for resistive sensors due to the excitation required. If the thermal time constants are known for the system, pulsed measurements may be incorporated to minimize this self-heating and increase accuracy. A recent example of the fabrication of an integrated resistive sensor was presented by Liu et al. (2004). For thermocouple type sensors it is attractive to manufacture them from semiconductor materials, as the Seebeck coefficient is generally larger ($\sim 10^{-3}$ V/K as opposed to 10^{-8} V/K), providing a more sensitive sensor from readily available material. Also common for micromachined thermal sensors are junction-based sensors utilizing diodes or transistors.

Three novel thermometry techniques have been described by Cahill et al. (2002) for temperature measurement at the micro and nano-level. The first is scanning thermal microscopy. In this case, a sharp tip is placed on the surface, and the surface temperature may be derived from the localized heat transfer between the surface to the tip. Most common setups utilize a cantilevered tip on an atomic force microscope. Spatial resolutions in the range of 30 to 50 nm have been obtained. Applicable areas in need of improvement are acquiring fundamental understanding of the tip-sample heat transfer, as well as designing and fabricating integrated multifunctional probes. Additional information on the scanning thermal microscope may also be found in Gu et al. (2002). The second method is pico-second reflectance thermometry, which is similar to reflectance thermometry but extended to pico-second time scales. This method involves generating laser pulses and directing them at the surface of interest. These pulses diffuse heat into the surface and the decay of the reflected light is used to obtain measurements. Nanometer scale resolution is possible with this method.

The third technique is scanning optical thermometry, where through the use of solid immersion lens technology, spatial resolution of optical measurements can be increased past the diffraction limit.

2.3.1 Thermography

Non-intrusive techniques such as infrared (IR) thermography, laser induced fluorescence (LIF) and liquid crystal thermography have traditionally been employed (Goldstein et al., 1998) for macro size experiments. There are a variety of challenges associated with IR thermography, which include accurately characterizing its performance and calibration, determining the measured body's surface emmisivity, identifying the measurement point, and accounting for radiation losses and additional optical equipment (Hetsroni et al., 2003). In addition, for the measurement of micro objects, accurately accounting for the background radiation is necessary. Hetsroni et al. (2003) while measuring the surface temperature of a capillary tube, utilized a technique whereby the background temperature was controlled to within that of the tube wall temperature. The aim of this was to minimize the uncertainty in measurement due to background radiation during IR measurement. Patil and Narayanan (2006) developed a method on the use of IR thermography for the near wall temperature measurement in microchannels. The system incorporated a microscope with a mid-wavelength IR camera (3.5-4.1 μm, 4.5-5.1 μm), and details on the radiation accounting procedure were provided.

Thermochromic liquid crystal (TLC) thermometry is a non-intrusive technique

based on the changing pitch size of the helical molecular structure of the material during temperature change. When illuminated with white light, TLC's will reflect light of wavelength proportional to the temperature they are experiencing. This reflected wavelength is proportional to the instantaneous pitch between molecular layers. Additional information about the characteristics of liquid crystal and their use in thermometry and heat transfer may be found in Ireland and Jones (2000) and Hallcrest (2000). The TLC technique has been used by many researchers since the late 1960's when it was first applied to non-destructive testing and flow visualization (Fergason, 1968).

The successful use of TLC's on a micro-geometry has been demonstrated by Höhmann and Stephan (2002), while investigating evaporation from a liquid meniscus. In their work, they utilized the un-encapsulated form of TLC's applied to the backside of a 20 μm stainless steel foil. They were able to obtain spatial resolutions of 0.83 μm, where the uncertainty in temperature was 0.51 °C or 7.5%. The use and limitations of TLC's in boiling heat transfer has been investigated and has been discussed by Kenning et al. (2001) and Klausner et al. (1995). These studies determined that in many instances, due to the thermal lag between the liquid crystal and the inner wall surface, the response time of the liquid crystal is not sufficient to capture all the unsteady phenomena occurring during nucleation boiling. A recent example on the use of the un-encapsulated TLC form for its high spatial and temporal resolution, during pool boiling experiments may be found in Wagner et al. (2006).

A first glimpse at the use of TLC's in mini-channels with boiling has been recently presented by Chin (1997) and Chin et al. (2002) during an investigation of boiling

incipience and convective heat transfer in narrow vertical channels. These authors used the TLC's in their common encapsulated (as opposed to un-encapsulated) form, which due to capsule diameters of 10 to 25 μm, restricts the spatial resolution capability of the TLC material. The use of un-encapsulated TLC's for quantitative, high resolution heat transfer measurements in small channels has, to a limited extent, been investigated (Aligoodarz et al., 1998). This is likely due to the difficultly in handling un-encapsulated TLC's, since they are easily contaminated by solvents or dust, and prolonged exposure to ultraviolet (UV) light can disturb their calibration and even destroy their response (Hallcrest, 2000).

In the work of Aligoodarz et al. (1998), rectangular channel geometries 2×1 mm and 2×2 mm, with three walls made of 75 μm thick stainless steel, were studied for boiling flows. The fourth wall was made of glass, which was used for visualization while the opposing stainless steel wall was coated with un-encapsulated TLC. The authors document difficulties in obtaining a continuous coating of the TLC on the surface, as well as difficulties in accounting for its stringent requirements for a contaminant free area. Their choice of the un-encapsulated form, however, was motivated by the ability to apply it in thinner layers than the encapsulated form, hence obtaining an improved response time, which was approximately 4 ms. Another benefit of the un-encapsulated form is that the spatial resolution is now restricted to the optical configuration (Azar et al., 1991), thus sub-micron resolution is possible. Overall, TLC's offer the potential for improved temperature measurements in micro-channels due to their non-intrusive character and possibility for high spatial resolution measurements.

2.3.2 Summary

Heat transfer in mini and microchannels is a recent area of study and although the number of researchers in this area has increased significantly over the last decade, a significant amount of research is still needed. Novel microchannel heat sinks using single phase flows have been proposed and investigated with the aim of increasing heat transfer while minimizing pressure drop. In particular, channels with slowly varying cross-sections have had limited heat transfer investigations.

Considering flow boiling heat transfer in small diameter channels (<2 mm), due to the complexity of the process, the number of parameters involved and the lack of correspondence with existing larger channel correlations, more data are still required considering a variety of conditions and fluids. Further, for realizing practical flow boiling microsystems, the characteristics of boiling incipience, including input parameters of influence, and the characteristics of the wall superheat and heat transfer coefficients need to be investigated. For conventional size channel systems, flow boiling instability characteristics can be significantly influenced by modification of the configuration, from single channels to parallel channels and to cross-connected parallel channels. This influence has to the author's knowledge, yet to be investigated for microchannel configurations relevant to micro heat sink applications.

Finally, very few studies have been carried out using thermographic techniques for microsystem thermal investigations. These techniques, however, such as liquid crystal thermography, offer the opportunity for non-intrusive, high resolution measurements.

Chapter 3

Test Facility and Test Methods

The initial stage of this work required the design, procurement and construction of the test facility presented in this chapter. The aim in the design was for a state-of-the-art facility to perform single phase and flow boiling heat transfer experiments using liquid crystal thermography in microgeometries. The facility is composed of three main sections, which are, a flow loop, a data acquisition system and an image acquisition system. Over the course of the investigations, a number of additions have been made to the original layout and the final facility configuration is discussed here.

3.1 Flow Loop

A schematic of the main components used in the closed loop test facility are shown in Figure 3.1. The facility has been designed to handle a number of working fluids, which include FC-72, distilled water and air. FC-72 is a perfluorocarbon fluid manufactured by 3M and some relevant properties of this fluid at room temperature are

25
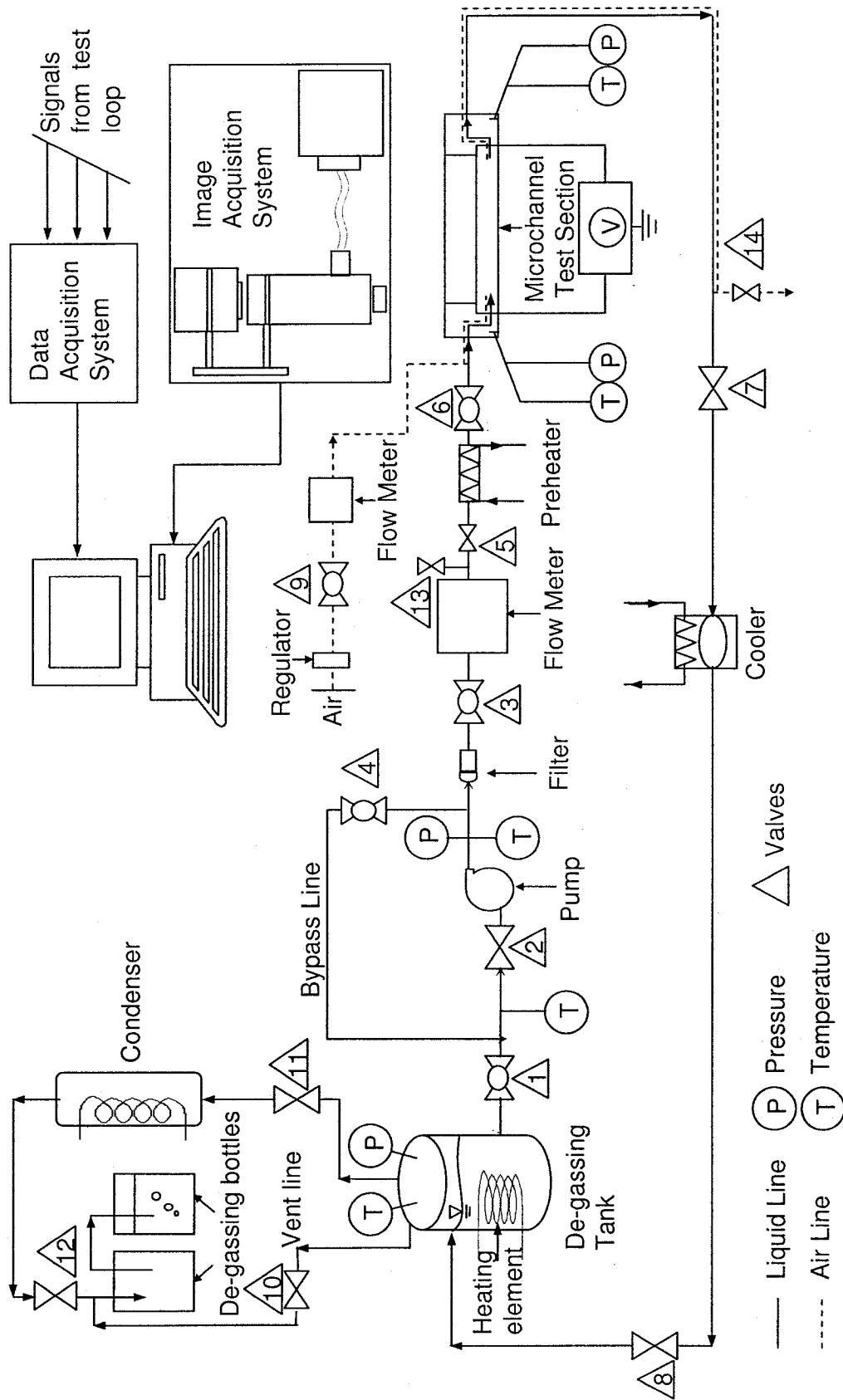
Figure 3.1: Schematic of the experimental test facility.

listed in Table 3.1. It was selected due to its lower saturation temperature compared to water. This is advantageous for the TLC measurements as the material is commercially available with a maximum temperature of about 120 °C. Additionally, FC-72 is considered an electronics cooling fluid and is therefore relevant to the applications of the present work. With reference to Figure 3.1, FC-72 or water (liquid) enters the loop from the main tank and is continuously circulated by a magnetically coupled gear pump. The pump is equipped with a variable speed drive allowing for a flow range up to 300 ml/min, with a maximum pressure of 517 kPa (75 psi). The tank is a one gallon stainless steel pressure vessel, with a number of ports for fluid transfer and process monitoring. The pressure and temperature in the tank are monitored with an absolute pressure gage and a thermocouple. A 1000 W screw plug immersion heater is installed for fluid temperature control via a variac.

A nutating digital output flowmeter provided by DEA Engineering is used to monitor the flowrate. This meter outputs a 5 V square wave signal at a frequency proportional to the time for the nutator to complete one cycle. The flowmeter has been calibrated using the weighing method, and has a reliable range from 10 ml/min to 250 ml/min. Upstream of the flowmeter is a filter which is used to remove any accumulating particles. A 25 μm disposable filter was used for the microtube experiments and this was later changed to a 15 μm tee-type filter (Swagelok, SS-4TF-15) for the heat sink experiments. In addition, a preheater is located at the inlet of the test section for additional flow temperature control. For the microtube experiments, this preheater consisted of a 2.743 m (9 ft) length of 12.7 mm (0.5 inches) OD serpentined copper piping. Three 0.914 m (3 ft) rope heaters rated at 125 W, were wrapped

Table 3.1: FC-72 properties at 25 °C and 1 atm (3M, 2000).

Property	Value
ρ	1680 kg/m^3
μ	0.00064 Ns/m^2
σ	0.01 N/m
C_p	1100 J/kg°C
Pr	12.35
T_{sat}	56 °C

around the piping. This was later modified to a tube-in-tube heat exchanger for the heat sink experiments as it can provide better protection from boiling in the preheating section. This heat exchanger unit consists of a secondary tank similar to the main tank. The secondary tank is equipped with distilled water and has a 1500 W screw plug immersion heater controlled via a variac. A secondary gear pump circulates the water to the tube-in-tube preheater.

At the exit of the test section is a water-cooled heat exchanger unit, which is used to restore the temperature of the fluid. For the air line, the air enters from the building's source with a pressure of approximately 552 kPa (80 psi) after being filtered and dried. A regulator reduces the pressure to the range applicable for the experiments (34 to 69 kPa). The flow rate is adjusted by a needle valve and a mass flowmeter (Omega model FMA-1609) tracks the air flowrate. The air exits to the atmosphere just after exiting the test module. Teflon tubing (1/4") is used throughout for fluid transfer, combined with compression fittings and standard pipe fittings. Additionally, pipe fittings in contact with FC-72 utilize a refrigerant sealant paste (Leak Lock by Highside Chemicals and Pro-Tite by Wagner Manufacturing) rather than Teflon tape, for compatibility. The flow loop components are mounted on a MayTec aluminum extrusion benchtop.

3.1.1 Degassing Procedure

Prior to flow boiling measurements with FC-72, the fluid is degassed to purge the system of non-condensables, particularly oxygen. Due to the limited supply of FC-72

fluid available, it is important to utilize a procedure which minimizes the loss of the fluid vapor to the environment. A procedure similar to that by Ammerman (1997) has been incorporated. The fluid is circulated through the system and the degassing tank at a high flowrate (~150 ml/min for microtube experiments). The degassing tank is heated until the fluid in the tank boils. With reference to Figure 3.1, valves 11 and 12 are open, allowing for the vapour to travel through the condenser and condense. The air escapes as bubbles through the second degassing bottle, which is filled with water. This acts as a visual technique to track the process. The fluid is circulated for one hour after the temperature in the degassing tank has exceeded 50 °C. The preheater is turned on to maintain the fluid at this high temperature throughout the system. This duration, coupled with the flowrate, allows for the entire fluid in the system to pass through the degassing tank. After this time period, bubbling in the degassing bottles is practically non-existent. At this point valve 11 is closed and the system is shut off from the environment. The flowrate is lowered to the desired setpoint and the tank heater is adjusted to maintain the tank temperature between 50 °C to 56 °C. The fluid in the tank therefore remains in a two-phase state throughout the experiment and the system pressure may be changed by adjusting the tank's temperature. To begin measurements, the flowrate is set by adjusting the motor speed and the preheater is adjusted to obtain the desired sub-cooling at test section entry.

For flow boiling measurements with distilled water, a modified procedure is utilized. The fluid in the secondary tank is heated above 90 °C while the excess vapor is expelled to the environment. The fluid is then circulated at a high flowrate for one hour, allowing the entire fluid to pass through the secondary tank twice.

3.2 Instrumentation and Data Acquisition

The facility is equipped with Type-T thermocouples, as denoted in Figure 3.1, to monitor temperature. Two 1.5 mm diameter Type-T (Omega special error limits material) thermocouples are placed in the various microchannel test section plenum chambers to measure the bulk fluid temperature at entry and exit. Pressure taps are installed in the microchannel test section plenum chambers to track the inlet and outlet gage pressures. They include two 517 kPa transducers (75 psig, Omega model PX01C1) used in Section 5.1 for inlet and outlet measurements, and inlet measurements in Section 5.2. A 345 kPa pressure transducer (50 psig, Omega model PX821) is used in Section 5.2 for outlet pressure measurements and in Chapter 6 for inlet pressure measurements. Finally, a 34.5 kPa differential pressure transducer (5 psi, Omega model PX821) is used for differential pressure measurements in Chapter 6. A Vaisala PTB220 barometer is used to obtain the absolute pressure of the surroundings.

The output from the various sensors is monitored through an automated data acquisition system using the LabVIEW$^{\text{TM}}$ software. Code has been developed for various measurement scenarios including microtube experiments and microchannel heat sink experiments under steady state and transient conditions. The data acquisition hardware consists of National Instrument's SCXI 1000 signal conditioning unit with the appropriate modules and the NI 6052E 16-bit 333 kHz data acquisition card. A schematic of the data acquisition system is shown in Figure 3.2. Signals from the transducers were transferred through the signal conditioning unit, then to the computer, whereas the signals from the metering devices were directly transferred
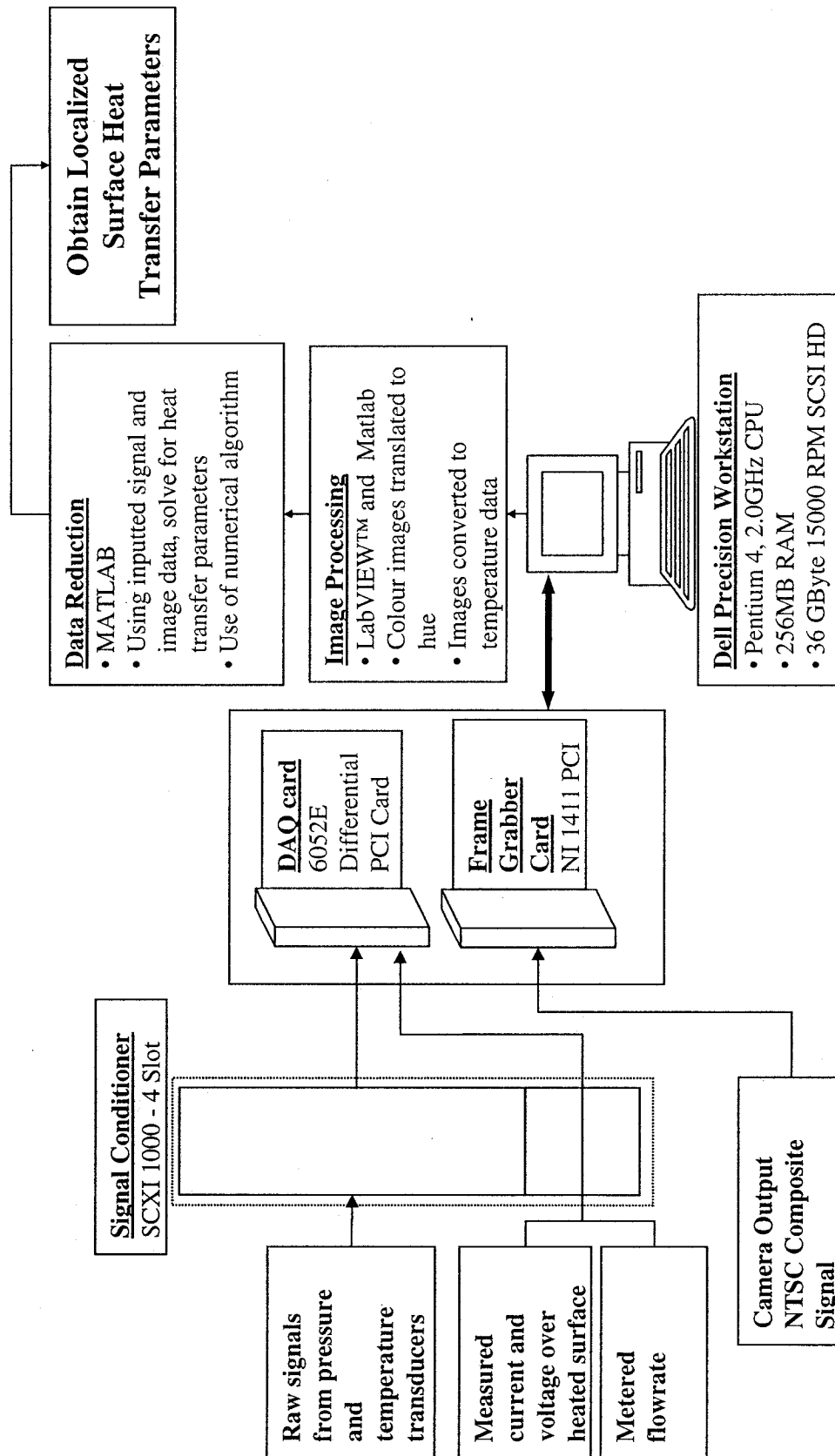
Figure 3.2: Schematic of the data acquisition system.

Obtain Localized Surface Heat Transfer Parameters

Data Reduction
<u>MATLAB</u>
- Using inputted signal and image data, solve for heat transfer parameters
- Use of numerical algorithm

Image Processing
<u>LabVIEW™ and Matlab</u>
- Colour images translated to hue
- Images converted to temperature data

Dell Precision Workstation
- Pentium 4, 2.0GHz CPU
- 256MB RAM
- 36 GByte 15000 RPM SCSI HD

DAQ card
<u>6052E Differential PCI Card</u>

Frame Grabber Card
<u>NI 1411 PCI</u>

Signal Conditioner
<u>SCXI 1000 - 4 Slot</u>

Raw signals from pressure and temperature transducers

Measured current and voltage over heated surface

Metered flowrate

Camera Output
NTSC Composite Signal

32

through the data acquisition card to the computer.

For heat transfer investigations in the microtubes, heater power was provided by a BK Precision switch mode DC power supply (Model 1692) and a Good Will Instruments DC power supply (Model GPC-1850). Their ratings were a voltage range of 2.7 V to 15 V, with a maximum current rating of 40 A, and a voltage range of 0 V to 5 V with a maximum current rating of 20 A, respectively. For the heat sink experiments, heater power is provided by two BK Precision DC power supplies (Model 1623A) operating in parallel mode, each with a voltage range of 0 V to 60 V and a maximum current rating of 1.5 A.

3.3   Image Acquisition

Image acquisition was performed in LabVIEW™ and the images were captured with a size of 640 × 480 pixels in Red-Green-Blue (RGB) format. The Hue planes were simultaneously extracted and saved in tagged image file format (TIFF). Post-processing of the images and acquired data was performed in MATLAB. Sample code is presented in the appendix. A detailed view of the image acquisition apparatus is shown in Figure 3.3. Light originating from the illuminator box is directed through a single fibre optic cable. This has the advantage of keeping any heat generated by the light source away from the TLC coated surface. An EKE configured lamp was used, with a colour temperature rating of 3250 K. Light passes through a polarizer just before entering the zoom lens casing. Within the casing, it is deflected to the test surface by a beam

33
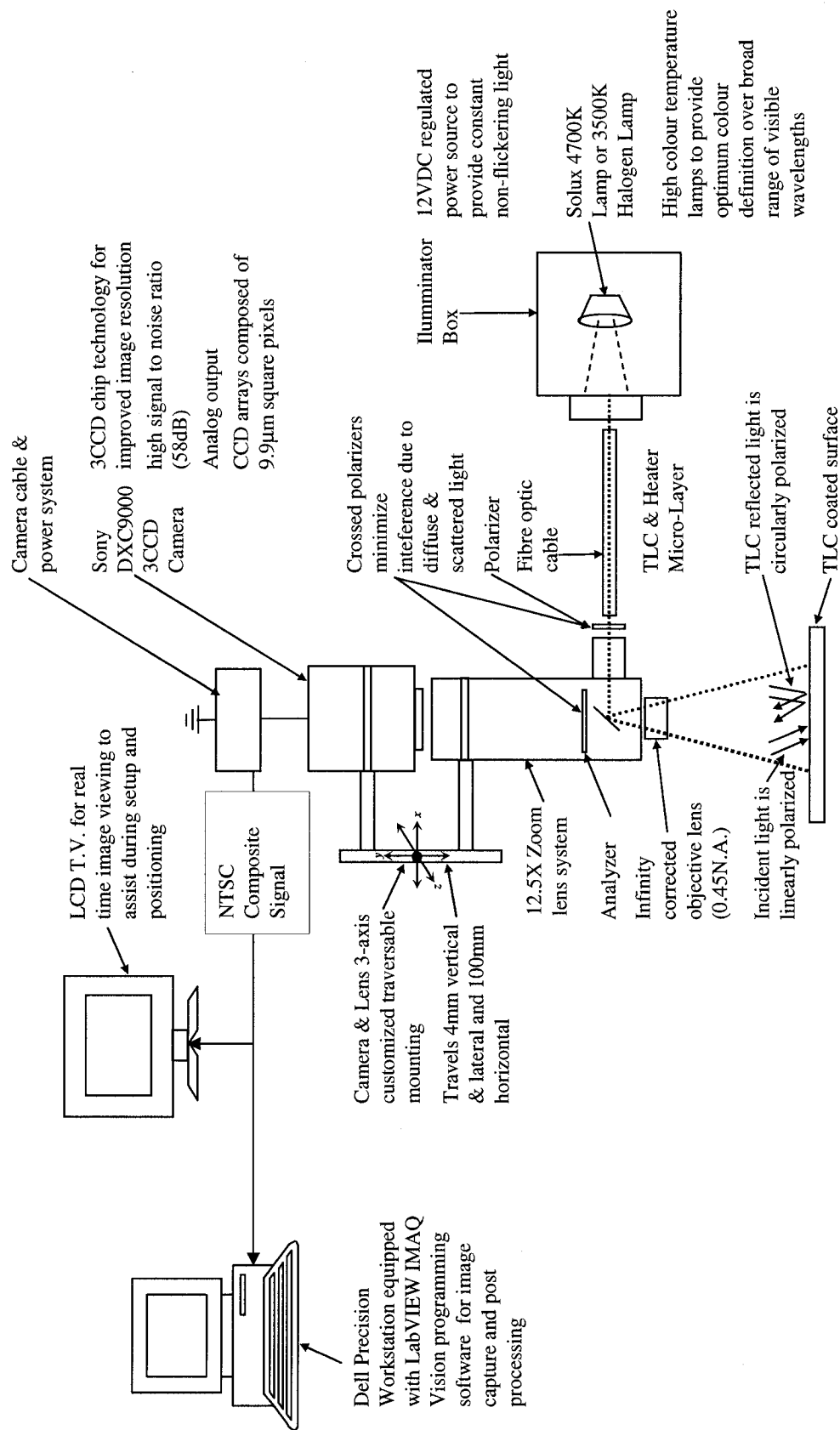
Figure 3.3: Schematic of the image acquisition system.

Camera cable & power system

Sony DXC9000 3CCD Camera

3CCD chip technology for improved image resolution high signal to noise ratio (58dB)

Analog output

CCD arrays composed of 9.9μm square pixels

Crossed polarizers minimize inteference due to diffuse & scattered light

Polarizer

Fibre optic cable

TLC & Heater Micro-Layer

Illumminator Box

12VDC regulated power source to provide constant non-flickering light

Solux 4700K Lamp or 3500K Halogen Lamp

High colour temperature lamps to provide optimum colour definition over broad range of visible wavelengths

LCD T.V. for real time image viewing to assist during setup and positioning

NTSC Composite Signal

Camera & Lens 3-axis customized traversable mounting

Travels 4mm vertical & lateral and 100mm horizontal

12.5X Zoom lens system

Analyzer

Infinity corrected objective lens (0.45N.A.)

Incident light is linearly polarized

TLC reflected light is circularly polarized

TLC coated surface

Dell Precision Workstation equipped with LabVIEW IMAQ Vision programming software for image capture and post processing

splitter. Depending on the magnification required, the light may pass through an infinity corrected objective for high resolution measurements or else through the default auxiliary lens. Upon reflection from the surface, the light is circularly polarized. It passes into the zoom lens through the analyzer and is directed to the CCD camera. The crossed polarizing lens pair is available to obtain improved image quality. The light reflected by the TLC material is circularly polarized and thus travels through the crossed polarizing pair essentially unaffected. The acquired image is then transferred directly to the computer as an NTSC signal through a single BNC cable. An LCD television was used for real time monitoring and for positioning. The video signal used in the television loop comes from a separate output line in the camera. The benefit of this is to minimize the accumulated noise that can occur by transferring the desired video signal through many components. Image acquisition is obtained using a Sony 3-CCD analog camera. The camera was connected to a variable zoom microscopic video lens. The camera lens combination was mounted onto a 3-axis traverse through variable length stages each with approximately a 1 μm resolution. The lateral and vertical axis stages allow for fine tuning of the position and focusing. Although the facility has the capability of a crossed polarizing illumination setup, this was not utilized for the microtube experiments due to the reduced intensity obtained when voltage was applied to the tubes. The fibre optic illumination source was instead fixed onto the zoom lens at a fixed angle and directly illuminated the surface.

3.4 Uncertainty

Uncertainty estimates for the various signals are presented in Table 3.2. For the pressure transducers they are based on manufacturer specifications, whereas for the thermocouples they are based on manufacturer specifications and the combined measurement system. Uncertainty in derived parameters are presented throughout this document where applicable and have been calculated using similar methods to those described by Kline and McClintock (1953).

Table 3.2: Sensor uncertainty.

Sensor	Uncertainty
Thermocouple temperatures	0.7 °C
Pressure transducer (PX01)	0.45 kPa
Pressure transducer (PX02)	0.57 kPa
Pressure transducer (PX821)	0.03 kPa
Barometric pressure	0.015 kPa
Liquid flowrate	2.25 ml/min
Air flowrate	0.5 SLPM

Chapter 4

Un-encapsulated Liquid Crystal Thermography for Mini and Micro Geometries

The general classification of matter is of solid, liquid and gas. For solids a further classification is crystalline and amorphous solid. Crystalline solids are characterized by their ordered molecular structure, which is maintained over a long range. Upon heating a crystalline solid past its melting point, one arrives at an isotropic liquid. The liquid phase, unlike its solid counterpart, does not display any long range ordered structure at its molecular level (Chandrasekhar, 1977).

The term liquid crystal is assigned to a group of intermediate phases, or mesophases, encountered while melting some organic crystalline solids to their isotropic liquid phase. This transitioning process, due to thermal means, is termed thermotropic

mesomorphism, and liquid crystal mesophases obtained in this manner are likewise termed, thermotropic liquid crystals. Another means of transitioning through various mesophases would be due to solvents and the resulting intermediaries are called lyotropic liquid crystals. In general, the main characteristics of these mesophases are their strongly anisotropic tendency combined with a high degree of fluidity. They were first observed by Reinitzer and Lehmann in the late 1800's, during their investigation of some esters in cholesterol (Chandrasekhar, 1977). Since then, an enormous amount of research has followed with experimental measurement applications utilizing liquid crystals emerging over the last 20 years (Ireland and Jones, 2000).

Thermotropic liquid crystals (LC's) may be loosely classified as nematic, cholesteric and smectic. These liquid crystals are composed of molecules shaped in a rod-like manner. Figure 4.1 illustrates the various mesophases as described in the following. Nematic LC's exhibit a preferred molecular order in their orientation direction, but no order in their position. This orientation direction is called the director. Another type of liquid crystal may be formed by the addition of a chiral molecule to the nematic LC. This form, called the chiral nematic liquid crystal, is different from the nematic in that its orientation order is periodic normal to the director. Furthermore, the intermediate layers transform in a helical fashion, which gives the crystals their optical activeness. This same structure is observed in cholesterol esters and hence the coining of the term, cholesteric liquid crystals. Chiral nematic and cholesteric liquid crystals are synonymous in structure. Smectic liquid crystals come in a variety of forms (for example Smectic A and Smectic C), and their main characteristic is their high degree of long range order in both position and direction.
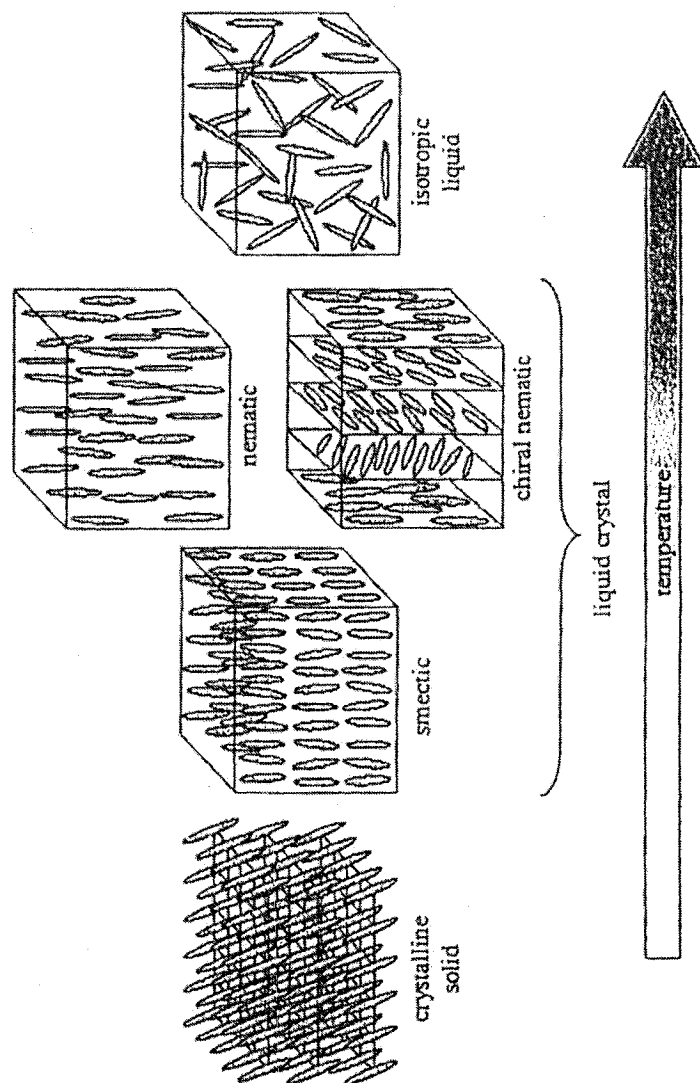
Figure 4.1: States of liquid crystal substances, from Anderson (1999).

A typical phase transformation of liquid crystals can be described as follows. At the melting point one arrives at one form of the smectic mesophase. With further heating one then arrives at the cholesteric mesophase. This mesophase as described earlier and as depicted in Figure 4.2 (a), exhibits optical activity. If viewed during this heating process one would observe the liquid crystal to gradually change color from red to blue. Finally, past the cholesteric mesophase is the clearing point and then the liquid phase. Cooling the liquid crystals produces the reverse effects of heating them, however with hysteresis effects if encapsulated (Anderson, 1999).

4.1 Liquid Crystals for Temperature Measurement

The term *Thermochromic* liquid crystal (TLC) is assigned to the chiral nematic / cholesteric liquid crystals, since they display color change during a thermal process. This optical activity is brought about by their helical molecular configuration. A TLC substance can be modeled as several layers or sheets, each containing uni-directional molecules. The distance between identical directors is termed the pitch and represents a 360-degree helical rotation of the director between layers (Figure 4.2 (b)). The pitch is the parameter that determines the specific wavelength of light that is reflected. As the liquid crystal is heated the separation between the sheets increases due to increased molecular activity, causing the pitch to increase. Simultaneously and with an opposing effect, the relative angular displacement between sheets increases, which decreases the pitch. The dominant effect for most liquid crystals is the increase in

41

(a) Typical diagram of wavelength of light reflected with increased temperature.

(b) Pitch diagram from Chandrasekhar (1977).
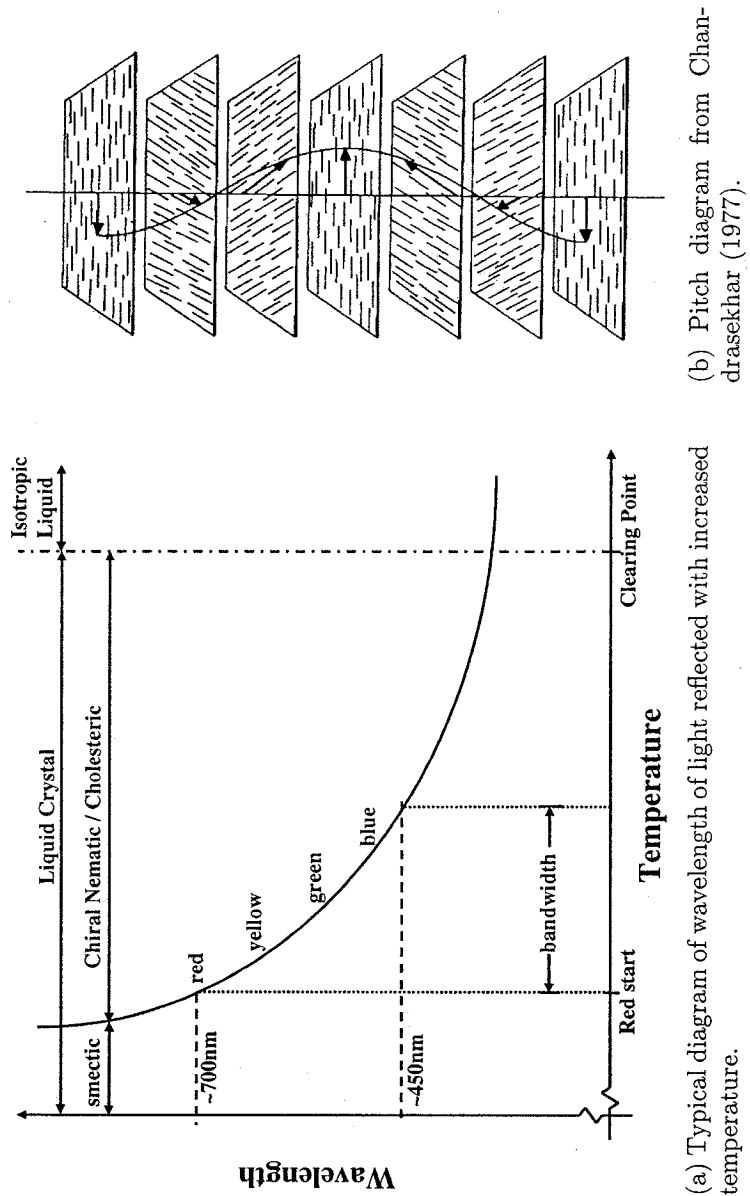
Figure 4.2: Thermochromic liquid crystal characteristics.

angular displacement, and therefore as the temperature is increased, a decreasing

pitch occurs. This translates into a decreasing wavelength of light being reflected.

4.2 Color Temperature Interpretation

As has been shown, the TLC's color temperature dependency makes them ideal for

qualitative surface temperature mapping. However, in order to obtain quantitative

information, a data acquisition and interpretation method is required. According to

Moffat (1990) there are three broad classes of image interpretation methods available:

1. Human observers,

2. Intensity-based image processing systems, and

3. True-color processing systems.

Early researchers such as Clifford et al. (1983) and Jones and Hippensteele (1987) ac-

quired images using a video camera and a video tape recorder. Temperature isotherms

denoted by constant color lines, were then isolated by a human observer based on

replays of the recording. Although the results obtained in this manner were of rea-

sonable accuracy, one can imagine that this was a very tedious and time consuming

process.

In order to discuss the intensity and true-color methods a brief summary on com-

puter vision follows. A color may be represented as a combination of three color

primaries. This is called the tristimulus decomposition of light. The most famil-

iar method developed by the Committee de l'Ecliarge (C.I.E) in 1931 is the RGB

(red, green, blue) decomposition. The RGB model gives us the relative brightness or luminance of the source. In fact, the luminance of a light source is defined as a proportional summation of the three primaries. Two other descriptors of a light source are its hue and saturation value. Hue is the property that distinguishes color, for example, red light from a green light. Its value depends directly on the wavelength of a color. Saturation is the attribute that describes the relative 'whiteness' of a light. In most electronic image acquisition devices the intensity is captured and converted to an electronic signal. Through filters of various transmissivities the intensity can be converted to its R, G and B values. Finally, if required, computer algorithms can convert the RGB values to hue values.

4.2.1 Intensity Based Image Processing

In the intensity-based image processing methods, two different techniques may be employed, depending on whether a monochrome or color recorder is available. A typical intensity response to temperature change of TLC's is shown for a transient heating test in Figure 4.3(a). The peak of the intensity plot provides the correlation with temperature as it is a fixed value depending only on the liquid crystal type. On acquisition of images, one could then track each pixel of an image acquisition series for its intensity. Pixels within a specified band of the peak intensity would then have an associated temperature for the corresponding time instant. This single temperature will be unique for the TLC's and is determined through a calibration. Figure 4.3(b) shows the color primaries intensity response to temperature change of
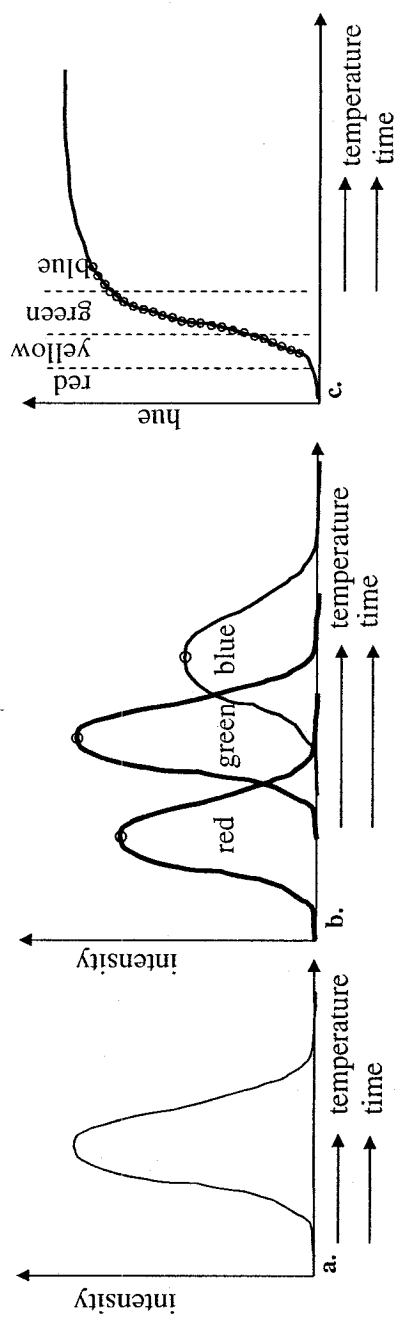
Figure 4.3: Color descriptor response versus temperature a)intensity of monochrome system, b)intensity of color primaries and c)hue angle.

a TLC. This is similar to the monochrome intensity method except that now up to three temperatures may be associated.

4.2.2 True Colour Image Processing (Hue Method)

The most prevalent method used in true color processing of TLC images is the hue method. A typical hue response of TLC's is shown in Figure 4.3(c). Curve fitting may be applied to the data points acquired and used as the calibration template. Unlike the intensity method whereby only a single point gives the color temperature relationship, with the hue method the entire curve may be used. This alleviates the need for the entire surface to undergo full color change. For example, if using the green peak in the intensity method, all points on the surface would need to clear the green peak temperature in order to convey quantitative surface temperature information. This is difficult to design for, particularly when testing complex geometries. Based on the aforementioned characteristics, the hue method has been selected as the color descriptor for the present work.

4.3 TLC Material

TLC's come with active temperature ranges of approximately -30 °C to 115 °C and color change bandwidths ranging from about 1 °C to 20 °C. Material with a bandwidth less than 5 °C is typically termed a narrow band TLC, and greater than or equal to 5 °C, a wide band TLC. Both types have their advantages and disadvantages depending on the image processing method used. The un-encapsulated liquid crystal material

used in the present investigations is a chiral nematic blend provided by LCR-Hallcrest. Acquisition sources for the un-encapsulated form of TLC material are limited and the user is subsequently limited in the formulations and volumes available. Three different formulations were purchased during the course of the investigations. Their nominal properties included, a red start of 40 °C with a bandwidth of 10 °C (R40C10W), a red start of 70 °C with a bandwidth of 20 °C (R70C20W) and a red start of 75 °C with a bandwidth of 20 °C (R75C20W). The cost per unit volume of the un-encapsulated material is substantial and more so when compared with the encapsulated form. The cost and formulation restrictions require that experiments be uniquely tailored around the available TLC material. Additionally, surface temperature predictions should be performed to identify the appropriate formulation required.

4.4   Coating Application

The aim of the TLC application procedure is to prepare a uniform coating, which will produce vibrant colors. A thicker coating will improve the vibrancy, while too thick of a coating may start to produce non-negligible temperature gradients through the TLC layer. Additionally, a variably thick layer will introduce uncertainty into the observed temperature field. A uniform coating has traditionally been applied through the use of an airbrush for the encapsulated TLC's (Ireland and Jones, 2000). Application of the un-encapsulated TLC's as documented by Höhmann and Stephan (2002); Aligoodarz et al. (1998); Kenning et al. (2001) has been through use of a paint brush. However, Aligoodarz et al. (1998) mentioned significant difficulties in

obtaining a continuous layer through this application method. According to Hallcrest (2000), the LC's may be applied in their un-encapsulated form through dilution with an appropriate solvent, such as acetone. They then may be sprayed through an airbrush, resulting in an improved thin uniform layer. This approach, however, is usually not recommended due to the hazardous nature of most solvents. Similar methodologies of applying un-encapsulated LC's with an airbrush have been used for obtaining shear stress measurements. In these cases, the researchers diluted the LC's with petroleum ether (Fujisawa et al., 2003) or with Freon (Reda et al., 1994) before applying them with an airbrush. No literature, however, to the author's knowledge demonstrates the application of TLC's in their un-encapsulated form via an airbrush.

Through trial runs of applying the TLC's with a paint brush, the difficulties observed by Aligoodarz et al. (1998) were confirmed and therefore this methodology was considered inadequate for producing reliable results. The use of an airbrush was then selected and a variety of trials both of mixture concentration and of application were then performed to produce a sound application methodology. A Badger Model 100 independent action airbrush was used for application as it allowed for variation of the air to coating material concentrations independently during spraying. The solvent used was acetone and concentrations by weight of 20:1 (solvent to TLC) based on the suggestions of Hallcrest (2000) were incorporated. This approach produced highly improved results in terms of coating uniformity and control. Subsequent trials have shown that concentrations as high as 5:1 (acetone to TLC) may also be used. It was necessary to apply the coating within a vented environment due to the toxic nature of the solvent used. Additional solvents tried included isopropyl alcohol and distilled

water. However, both required much larger amounts of solvent proportions to dilute the TLC material and both had significantly longer evaporation times. To improve the color vibrancy of the TLC response, it is common to apply a coat of black paint before the TLC layer. This was incorporated in the current coating application using a water-based black paint and also applying through the airbrush.

4.5 Calibration

To obtain quantitative thermal data from the TLC response, a calibration of the material is required to quantitatively relate the observed color to the material temperature. The definition of hue in the current work is the same as that recommended by Hay and Hollingsworth (1996), which is

$$Hue = \arctan\left(\frac{\sqrt{3}\,(G-B)}{2R-G-B}\right). \tag{4.1}$$

The perceived color of a TLC will depend upon the primary and background light spectral characteristics, the camera viewing angle and distance, the primary lighting angle and distance, the lights optical path, and the instance of the TLC application. For a calibration to be fully valid the above must be maintained between the calibration and the experiment. This is usually done through an in-situ calibration (Anderson, 1999). Choices for calibration include a linear temperature gradient (Chan et al., 2001), a liquid bath or circulated liquid (Hay and Hollingsworth, 1996), or an isothermal block (Anderson, 1999). A linear temperature gradient applied to a metal

block is advantageous in providing a quick calibration, however, the amount of calibration points is dependent on the number of sensors employed along the gradient. An isothermal bath or circulated bath provides the best means of obtaining a truly isothermal surface, however it does require a liquid supply that is either stirred or circulated. A constant temperature block is usually difficult to work with in maintaining the full viewing surface isothermal and hence not recommended. For the present study, a calibration based on circulating the fluid through the channel was selected due to its ease of incorporation into the setup. For the remainder of this section the calibration procedure described is based on evaluations with the microtube test section described in Chapter 5. Similar methods are then utilized for the heat sink calibration (Ch. 6). The temperatures at the tube inlet and outlet were measured and remained within 0.5 °C of each other. The fluid was slowly heated via the pre-heater and images captured at incremental changes in temperature. One of the main observations from this work is that the response of the un-encapsulated TLC under increasing magnification will contain varying degrees noise and scatter. Figure 4.4 shows the histogram of a color response from a constant temperature region 30×600 pixels.

To address this in an automated fashion, an intelligent calibration process is introduced. To start, a region of interest (ROI) needs to be selected to base the calibration curve on. Lighting, viewing angle, and coating uniformity may all influence the calibration between two different regions on the tube. To eliminate such influences a calibration curve was produced for a number of regions in the image. The minimum
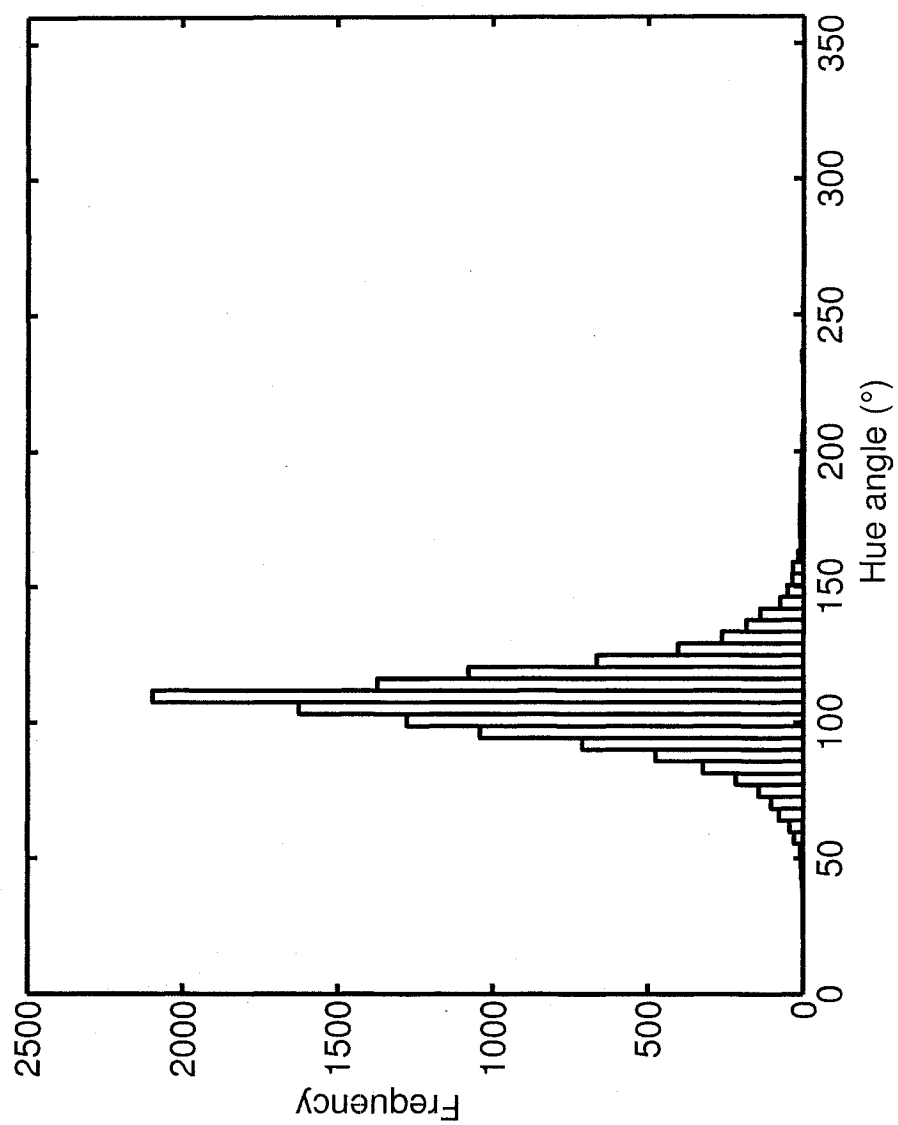
Figure 4.4: Constant temperature region hue angle histogram.

size for a given ROI is a single pixel, however to account for noisy pixels using statistics, an ROI size greater than one pixel was utilized. Since the camera was traversed this meant that the ROI would be a particular tube location and that high accuracy in traversing between set locations was pertinent. The ROI should not be too large, since local variations will not be captured and for the present work, an ROI of 4×3 pixels was typically used. A typical image size then of the cropped microtube region of 60×640 pixels, produces 3200 calibration curves. It was intended to use a 5th order polynomial to fit the calibration data, which is typical in TLC measurements. To manually verify the goodness fit of each curve would be too time consuming and hence two automated approaches that consider extraneous cases were incorporated with the second being an improvement from the first. Figure 4.5 provides a depiction of the calibration data processing and details on the automated curve fitting procedure are presented in the next two sections.

4.5.1 Stage I Calibration

In the first, the fluid was incrementally heated and at each increment images were captured at each of the locations. This method produced only a few calibration points for each location. The number of calibration points was few due to the fact that traversing occurred while the temperature was slowly rising. By the time the camera was returned to a given location, the temperature had risen significantly. If an assumption is made that within the valid calibration range the hue response will increase monotonically with increasing temperature, the main point to verify is that

640 pixels

480 pixels

Y pixels
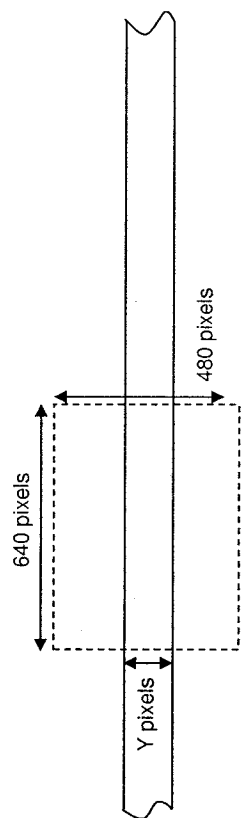
i. Image surface at a given traverse location.

640 pixels

1 2 3 4 ... N

Y pixels
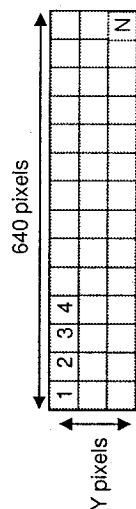
ii. Crop tube section, convert from RGB to hue and define ROI size to produce N calibration curves.

⊥

Hue
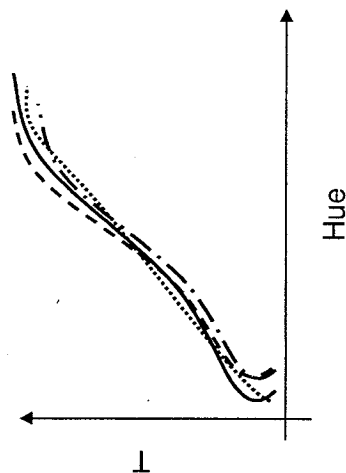
iii. Generate N calibration curves using polynomial fits.

Figure 4.5: Depiction of calibration data processing.

there are no maxima or minima occurring. If a minima or maxima is present, modification of the calibration curve needs to be addressed. It was found that using a third order polynomial will produce a reasonably accurate calibration curve without these minima or maxima locations. An automated calibration curve fitting was utilized with an initial polynomial order of five, but if any local minima or maxima were present within a predefined region, its order was reduced to three. Figure 4.6 (a) shows a calibration fit with a fifth order polynomial. Figure 4.6 (b) shows a calibration curve with data points originally set to a 5th order fit then corrected to a 3rd order fit.

4.5.2   Stage II Calibration

The second approach consisted of heating incrementally at a fixed location and capturing the full bandwidth before moving to the next location. This method is implemented for all the microtube measurements using FC-72 and the heat sink measurements. The main issue is to minimize the calibration time and capture as many points as possible. In the first approach calibration time was on the order of three hours and few data points were captured. In the second approach the fluid's inevitably increasing temperature was taken advantage of, and therefore since the camera was at a fixed location, it would continuously capture images as the temperature slowly rose. The rate of heating was approximately 0.5 °C per minute. The aim of the curve fit is to produce a monotonically increasing relationship. Depending on the quality of the data points for each ROI, this was not always possible. Extraneous cases would
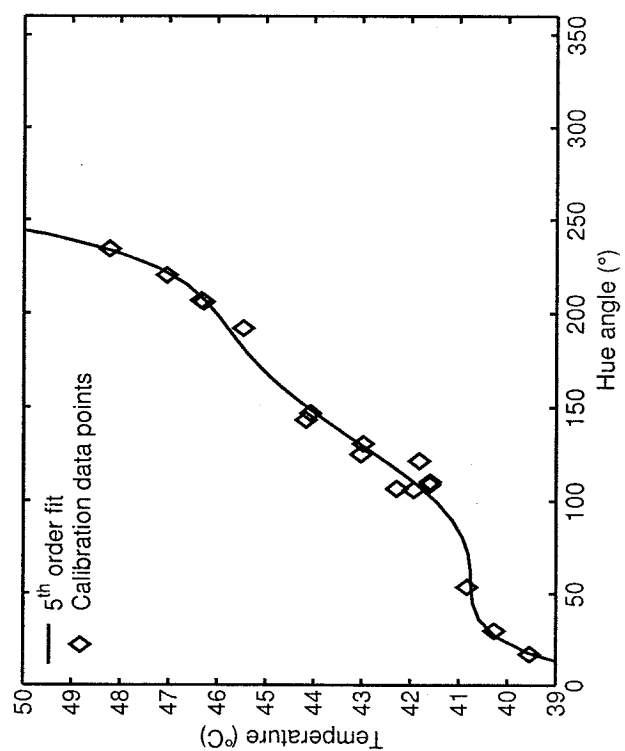
(a) Fifth order fit.
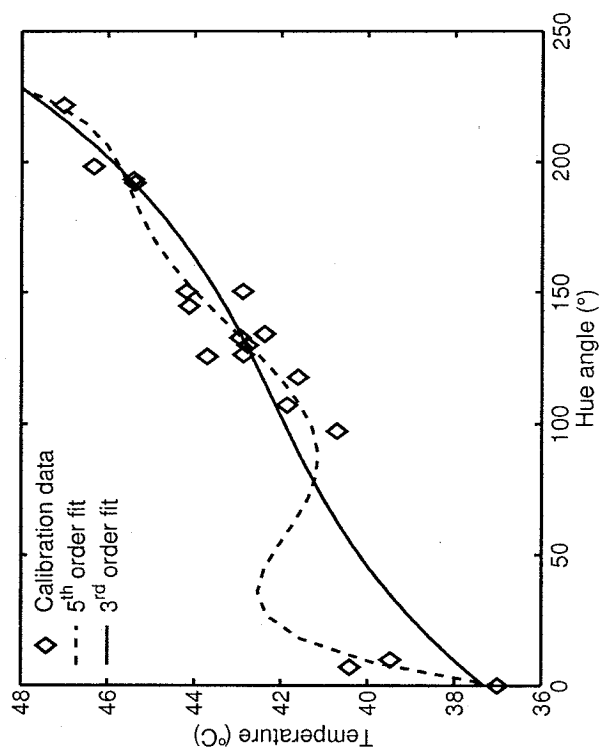
(b) Fifth to third order fit.

Figure 4.6: Stage I corrected calibration curves.

have maxima or minima locations in the curves. To automatically determine a calibration data curve-fit that did not contain extraneous regions, the following logic was implemented:

1. Sort the data set with respect to increasing hue.

2. Starting from the minimum hue value, only keep data points that have a positive change in temperature with respect to increasing hue.

3. Fit a fifth order polynomial curve to the modified data set.

4. If any maxima or minima exist in the hue range of 25 to 175 discard the fifth order polynomial curve and fit a third order polynomial curve.

5. If any maxima or minima exist in the hue range of 25 to 225 modify the data sets zero location to a predefined temperature. If any maxima or minima exist in the hue range of 100 to 175, abandon curve fitting and use the neighboring ROI instead.

The ranges were selected based on repeated observations of curve fits, however depending on the experiment type and conditions, they may be adjusted. The change of hue range between steps 4 and 5 was due to the change in characteristics of the two polynomial types applied to the same data set. The change of hue range between steps 5 and 6 was because once a third order fit was applied and the zero location fixed, if an extremity in the curve occurred in the hue range of 25 to 100, it was a very slight minima that could be disregarded. That is the temperature dip at the minima was less than 0.1 °C.

56

4.5.3 Additional Corrections

The hue angle is defined on a polar system and hence due to scatter, hue values close to 0° may be present in the 300° to 360° range and vice versa for hue values close to 360°. Compensation similar to that of Hay and Hollingsworth (1996) is incorporated whereby the negative angle was used when such scatter occurs. This can be identified, for example, when at high temperatures a low hue value is obtained, or at low temperatures, a high hue value is obtained. The ROI will have a particular scatter in the hue values and for the present study, the nominal hue value was based on the median of the hue values. With the above three conditions incorporated, Figure 4.7 shows typical calibration curves for a given traverse location. Each calibration curve is for is for a ROI. The symbols in the figure only differentiate the curves and are not calibration data points. Figure 4.8 (a) shows a good fifth order curve fit. The circles are the section of the data set that is kept after sorting. Figure 4.8 (b) shows the modification of a fifth order fit to a third order fit due to a maximum in the curve-fit. Once again the circles are the section of the data set that are kept after sorting. Such good fits were not always possible due to scatter and noise as described previously.

The TLC calibration may change slightly over time. It was important then to verify that over a measurement run, which could be as long as three hours, the calibration curve would not shift significantly. To verify this, calibration data at a fixed location were obtained at two different times 3.5 hours apart. Figure 4.9 shows the data obtained from these two calibration runs, determined from a ROI size of
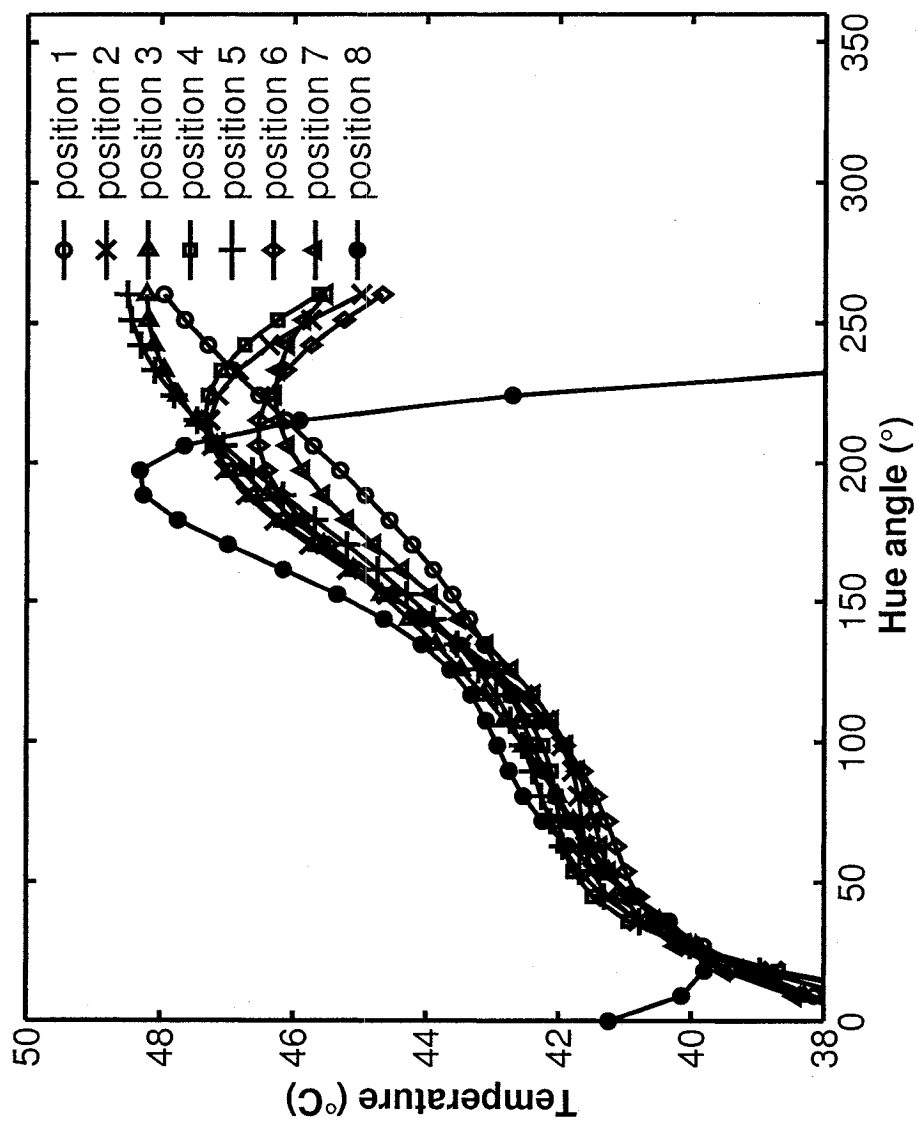
Figure 4.7: Typical calibration curve fits for various ROI positions at a given traverse location.
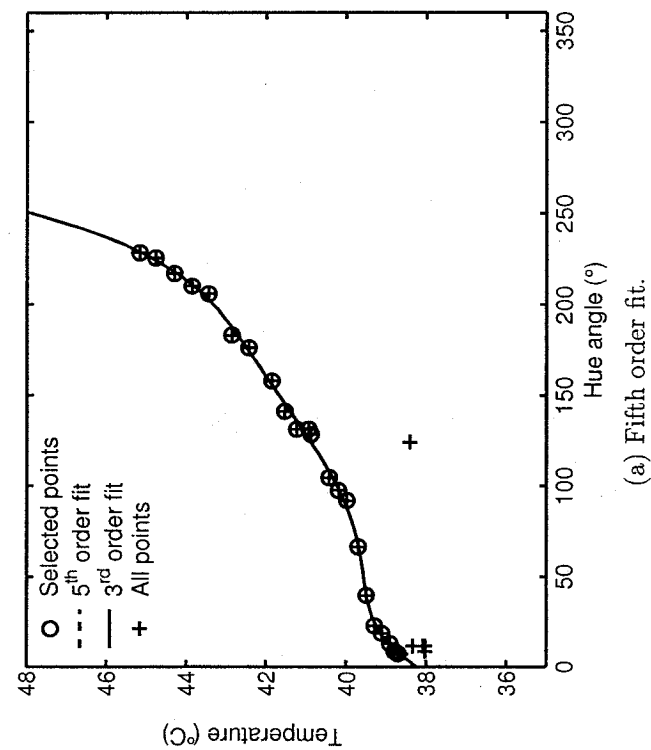
(a) Fifth order fit.
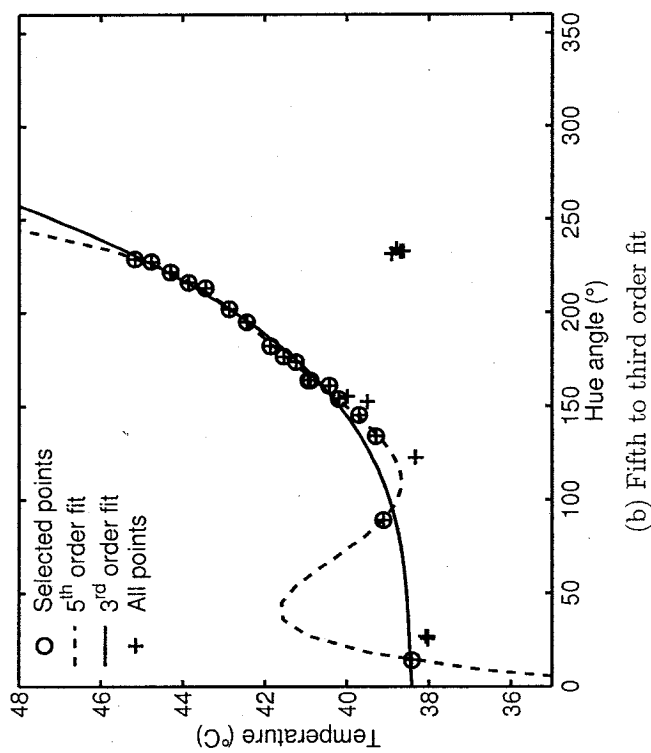
(b) Fifth to third order fit.

Figure 4.8: Stage II corrected calibration curves.
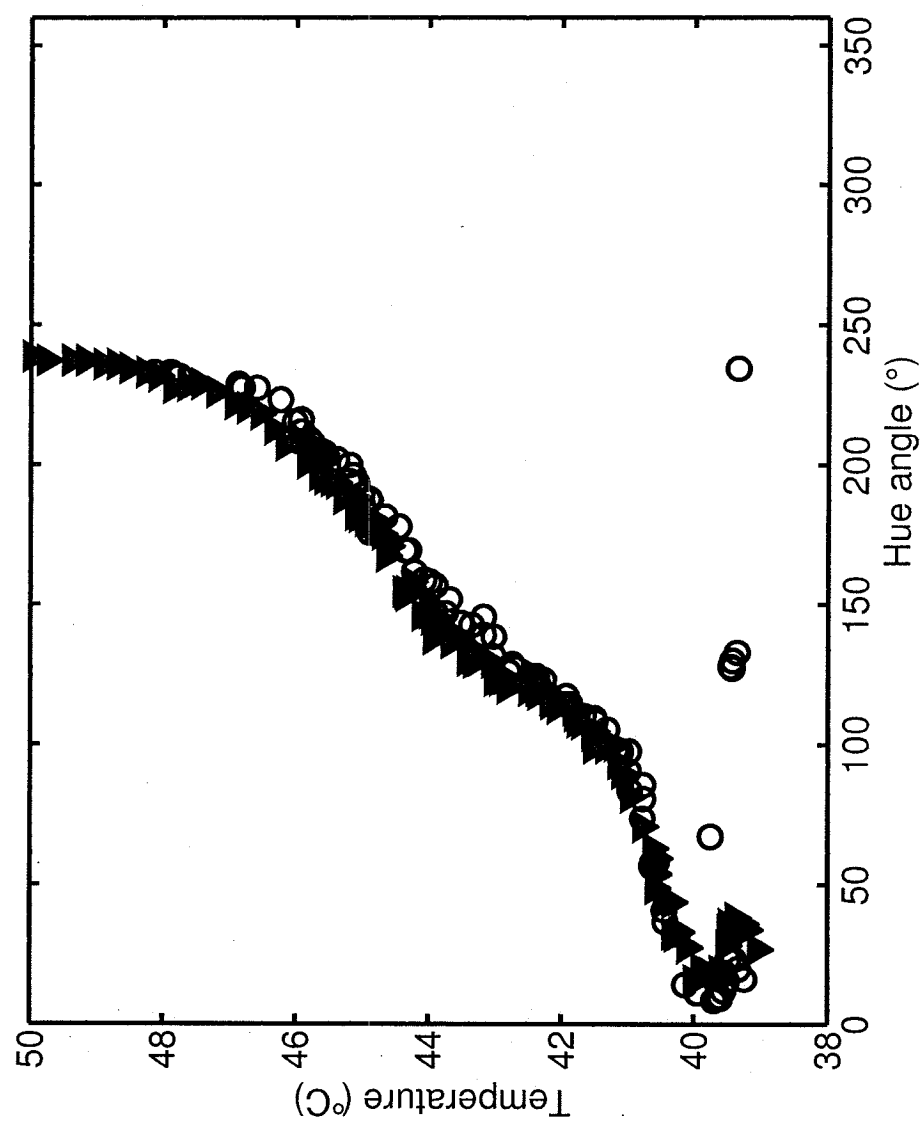
Figure 4.9: Calibration curves at different time periods.

4×3 pixels. As can be seen in Figure 4.9, the change in the calibration curve is insignificant, with a maximum temperature change of approximately 0.5 °C. Hence, the calibration taken prior to the measurements runs can be used over the entire measurement period.

4.6 Methodology Validation

4.6.1 Test Module Selection

Heat transfer in mini and microchannels is the main motivation for the experimental methods developed in the present study. Such channels will come in many shapes, which are predominantly dictated by the manufacturing processes available. An additional constraint will be the measurement technique utilized in the experiments. To design a heated channel test module utilizing TLC's for measurement, a primary criterion is optical access to the measured surface. In the most basic case, a flat surface is utilized with the camera at its normal. Three test module designs were investigated during validation of the test facility, with each subsequent design being a consequence of shortcomings in the previous configuration. They are described hereafter and results are presented for the final design.

Heat transfer from a single-wall heated rectangular mini channel with TLC's has been investigated by Chin et al. (2002) and Piasecka and Poniewski (2004) for boiling flows. The channels had widths of 20 mm and 40 mm and heights from 0.5 mm to 2 mm. The test modules were manufactured from aluminum with the channels

milled in a slot, while the fourth wall was produced from a metallic foil. Air gaps were machined on the side and bottom walls to produce approximately adiabatic conditions. The backside of the foil was coated with encapsulated liquid crystal and bolted closed with a transparent cover. The initial validation test concept, utilized similar characteristics of the above design. The base of the channel was manufactured from G-10 fiber-glass with three of the four channels produced from a milled out slot. The materials low conductivity allowed for approximately adiabatic conditions. The fourth wall was provided via a 25 μm thick and 1 mm wide foil supported on a polycarbonate cover. A schematic of this setup is shown in Figure 4.10.

The TLC material was applied on the backside of this foil before it was placed on the cover. Several difficulties were encountered with this approach. First, the use of un-encapsulated TLC's directly in the channel caused the coating to erode over time. Unlike the encapsulated form typically used by previous researchers, the un-encapsulated TLC material does not solidify, but rather remains in an oily state. Therefore, any air pockets present on the backside of the foil where the TLC coating is located, will draw fluid and/or will allow for the TLC material to escape over the course of an experiment. Attempts to squeeze out all the air bubbles are difficult since too much pressure will force out the TLC material and create a discontinuous measurement surface. A second drawback of this design was the use of a thin foil, which was very difficult to handle and to produce accurately. In addition, alignment of the foil with the channel was challenging and each failed alignment trial required the coating to be re-applied, as it was destroyed due to contact with the cover. The use of the thin foil highlighted how any minor local fault in the foil would produce
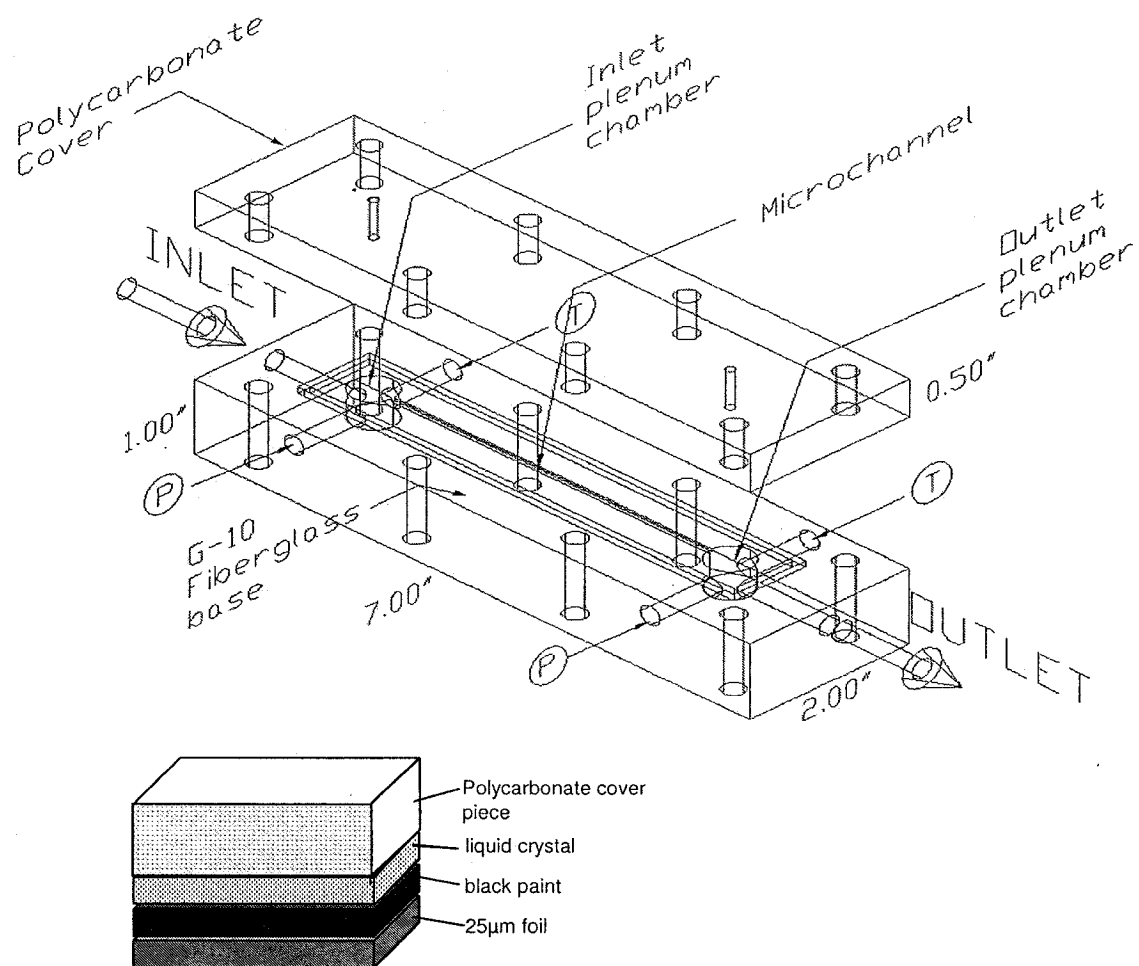
Figure 4.10: Configuration for Test Module 1.

localized hot or cold spots, characterizing a non-uniformly heated surface. A third drawback of this design was the use of an o-ring for sealing. This seal introduced additional uncertainty into the height of the channel as well as produced secondary paths for the fluid flow. It was noted that these difficulties were likely not encountered in the works of Chin et al. (2002) and Piasecka and Poniewski (2004) to this extent, due to the width of their channels (20 mm and 40 mm as opposed to 1 mm) and their use of encapsulated TLC's (as opposed to the un-encapsulated form). The primary conclusion from the above design was that if the TLC coating could be isolated from the flow path, it could be an effective measurement tool.

A second test module design was investigated to address the above drawbacks. In this concept, a wide thin foil was used rather than a narrow thin foil. The wider foil was easier to handle and minimized local faults produced during its slitting to size. Its size was based on the power available, since too wide a foil would draw too much current. The foil was permanently secured to the base using an epoxy and thus eliminated the need for an o-ring seal. It was important to prevent the epoxy, prior to drying, from seeping into the channel while under compression. To prevent this, a layer of double-sided tape was placed at the channel edge as a barrier. This had the added advantage of keeping the channel height fixed rather than the height being dictated by the dried epoxy, which would make it uneven. The height of the channel was increased however, so selection of a thin tape was necessary. A drawback of this semi-permanent sealing method, was that it was semi-destructive if resealing was necessary. In addition, lead-time for each new seal including drying time was about two days. Finally, each new sealing added uncertainty into the pressure the channel

could withstand due to unforeseen random errors, which occurred during assembly.

The foil required cooling in the section not exposed to the channel. A cooling sink of copper blocks with water running in a copper pipe over-top was incorporated. An added advantage of the copper blocks was that they could be bolted to the test base providing additional pressure for sealing. This was necessary since the epoxy tack to the foil or to the base was not even in all regions and had limited strength. Also, the region where the foil tacked onto the double-sided tape was prone to becoming loose with increased channel pressure, which would subsequently change the dimensions of the channel. However, even with the copper blocks the test piece was sensitive to increased channel pressure depending on how well it was sealed. The use of a metallic heat sink required electrical isolation from the foil, while minimizing thermal resistance. An alumina based epoxy that fit this requirement was utilized. It was necessary though to control the flow of the epoxy before it dried, as it was under pressure and so it may flow onto the measurement region. Once on the measurement region, it is difficult to remove without affecting the surface texture and sometimes destroying the foil. A schematic of the channel is shown in Figure 4.11.

Identification of the channel underneath the foil was challenging and it was necessary to utilize a microscope. Nusselt number measurements utilizing this test set up were found to be high in comparison to a number of correlations. After consideration of the test set up, it was concluded that these high Nusselt values were due to an inaccurate measure of the heat transfer from the top wall to the fluid. In calculating the heat transfer coefficient, the enthalpy change of the fluid was used rather than the power applied to the foil. When these two values are compared the enthalpy
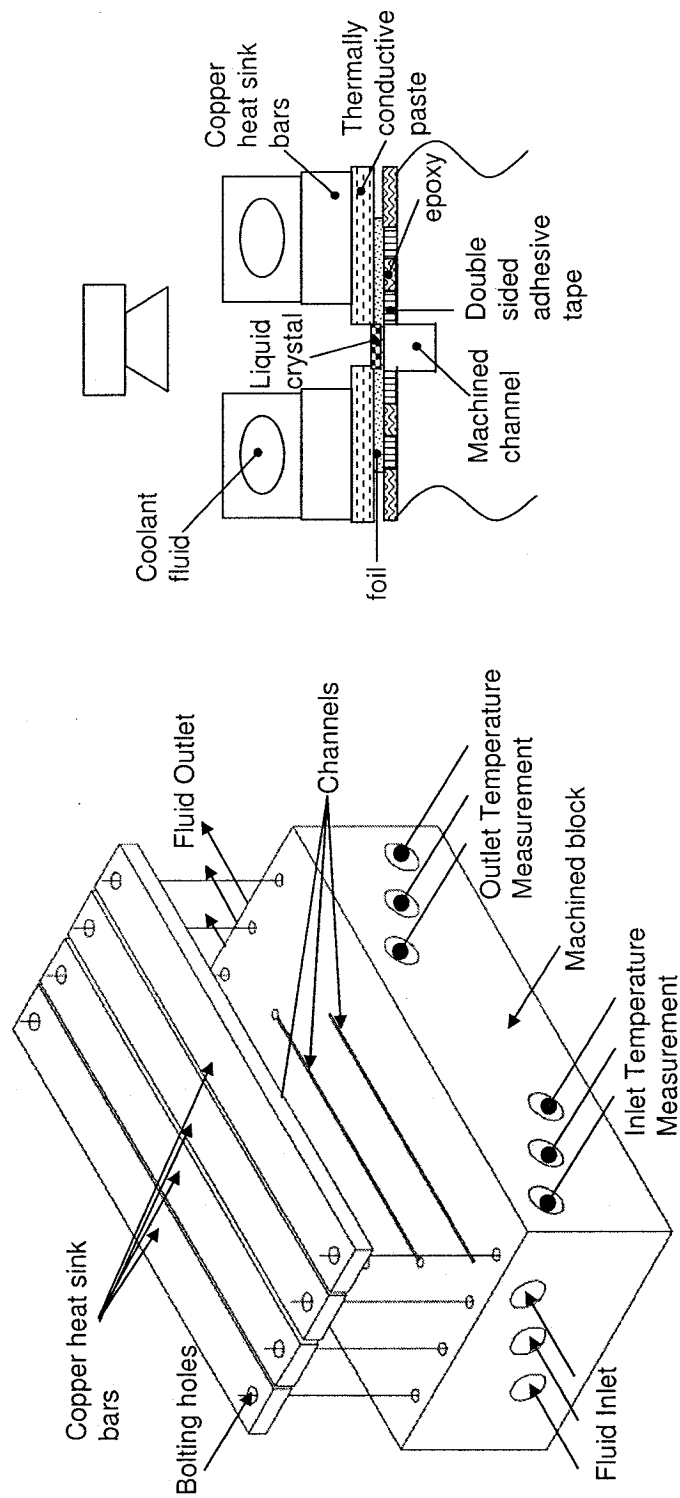
Figure 4.11: Configuration for Test Module 2.

change is much higher for the fluid than the energy from the foil over the channel area, which suggests an alternative source of energy. It was observed that the foil surfaces adjacent to the channel had extremely high temperatures in comparison to the surface above the channel. Therefore, although the base material had a low conductivity, heat transfer through the sidewalls produced the additional energy to the fluid. Furthermore, this meant that cooling of the foil was not as effective as it was designed for.

The Joule heating produced in the foil was not used to calculate the heat transfer since the foil surface and dimensions were not uniform, and hence the foil resistance was not uniform everywhere. This occurred since it was necessary to roughen the foil in regions where epoxy was applied for adhesion. Another source of excess energy transfer to the fluid occurred at the connection of the electrodes to the foil surface. This occurred, as the region where the two were connected was very small and difficult to reach, and hence inadequate connections produced high resistance causing this unwanted energy dissipation. Overall, assembly of this second design was difficult at all stages particularly due to the small size of the regions being worked on. This second design, however, demonstrated the assumption from the previous design that with the TLC isolated from the flow, effective measurements could be produced. However, it also demonstrated that application of accurate boundary conditions was difficult as the size was reduced.

4.6.2 Circular Tube Test Module

The main difficulties with the previous two concepts were the sealing and the application of a controlled heat load. Many setbacks were observed due to the extensive in-house assembly required, which produced many failed trials. In conceiving the third design, this point was of primary concern. Readily available on the market are relatively thin-walled stainless steel circular tubes, usually produced as hypodermic needles. Tube inner diameters are available as low as 0.254 mm and with wall thicknesses as low as 0.051 mm (Small Parts). Rectangular tubing is also available and can be custom made with inner cross sections as low as 0.510 mm (Microgroup). The use of custom-made tubing is, however, expensive and requires minimum orders not necessary for small-scale experiments. For this reason, a circular tube was selected as the channel configuration for the third design. The recent use of circular steel tubes in heat transfer studies of mini and microchannels has been performed by Lelea et al. (2004) and Owhaib and Palm (2004) using thermocouples, as well as Hetsroni et al. (2003) and Hapke et al. (2000) using infrared measurement.

A schematic of the circular tube test module used is shown in Figure 4.12. A polycarbonate sheet was machined to produce the measurement chambers for pressure and temperature and a detailed CAD drawing is presented in the Appendix. The tube had a 1.0668 mm (0.42") inner diameter and an outer diameter of 1.27 mm (0.5"). It was connected to these chambers using standard 1/16" stainless steel compression fittings with specialty ferrules to accommodate the small diameter tubing. The ferrule material is a composite of graphite and polyimide, which has a high
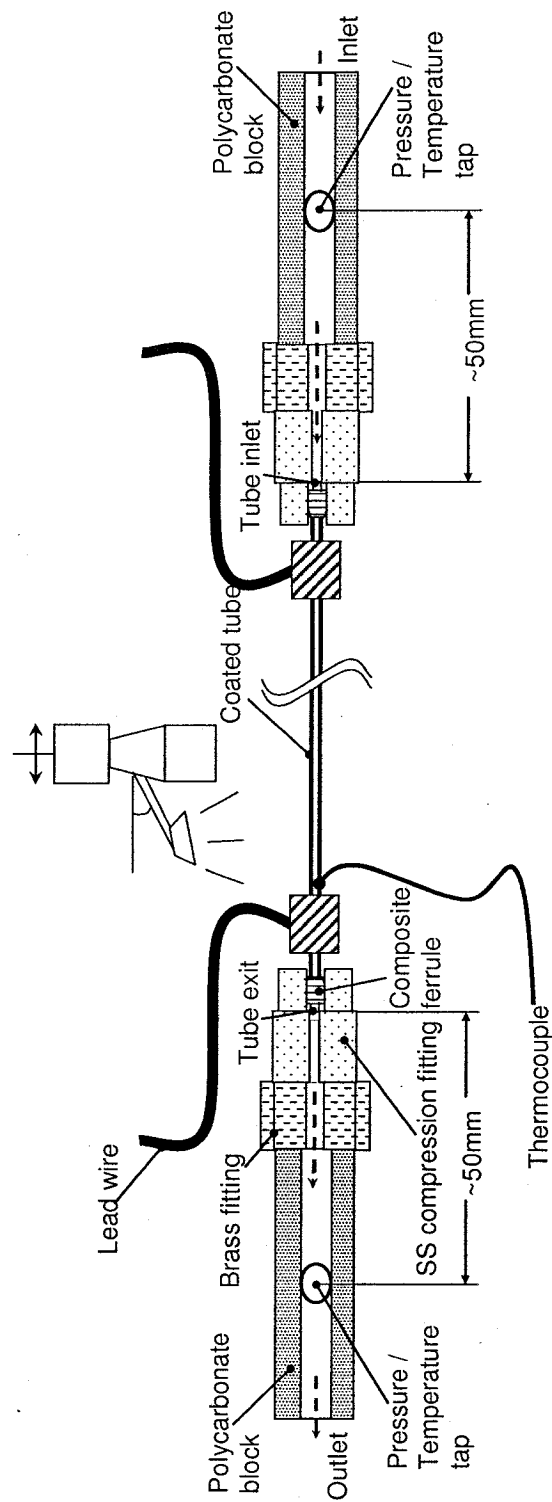
Figure 4.12: Configuration for Test Module 3.

electrical resistance. The advantages of the compression fittings are that they are resealable and can withstand high pressures (100 psi rating). Copper stranded wire (14AWG), was used for the electrical lead connection. It should be noted that the present set-up did not utilize any cover directly in contact with the TLC surface due to the small size of the tube. Attempts were made to utilize optically transparent epoxies to encapsulate the tube, however, none of the ones tried were compatible with the TLC material. Trials were also performed with transparent heat shrink tubing. This, however, produced localized air pockets and the heated TLC would easily be expelled. As well, for smaller tube sizes, as will be presented in Chapter 5, appropriate heat shrink tube sizes were not available. Rather then, a non-contacting cover was placed over the tube to protect the TLC coated surface from dust and the room lights. The cover was an opaque plastic half tube which is open at both ends. The main drawback of this was the reduced color vibrancy. Future studies with geometries such as microtubes may consider the use of glass capillary tubes for in-contact covers.

4.6.3 Procedure

Prior to each experiment, the TLC material was calibrated as described in Section 4.5.1. To begin measurements, the flow rate was set and the system was then left to run for about ten minutes. Measurements were carried out over a flow range of 20 to 160 ml/min, with inlet temperatures ranging from 28.4 °C to 31.9 °C and outlet temperatures ranging from 32.9 °C to 38.3 °C. The room lights were dimmed and the tube was kept covered. Traversing began at the rear of the tube where the wall

temperature would be the highest. The configured magnification provided a field of view of 10.233 mm $\times$ 7.671 mm, which translated into 15.53 μm/pixel for the CCD sensor size. Although the facilities magnification capabilities are much larger, a higher magnification would have required more traversing in order to capture the entire tube. This would require more time and provide additional information unnecessary for the purpose of the present work. After running flow through the system, measurements were ready to be taken and the cover was removed. The illumination system was turned on and the voltage was slowly adjusted until the TLC color response was in the predominantly green range ($\sim$41 °C to 46.0 °C). The system was then allowed to come to equilibrium, which spanned 5 to 10 minutes and afterwards a measurement was taken.

Three images were captured at a speed of 30 frames per second. These colour images were converted to hue angle, scaled on an integer range from 0 to 255, and then averaged for each pixel location. Simultaneously, the fluid temperature at inlet and outlet, as well as the flow rate measurements were captured. For each traversed location, two to four measurements were captured at a given flowrate, though the heater power may be adjusted between image capture. During data reduction, the best images by visual inspection were selected for final presentation. Whenever the voltage was adjusted, the illuminating system was turned off in order to minimize any degradation to the TLC and external heat addition to the tube as the system approached equilibrium.

4.6.4 Data Reduction

The local Nusselt number was calculated as

$$Nu_z = \frac{h_z D}{k_{loc}}. \tag{4.2}$$

The local heat transfer coefficient (h_z) was obtained through the convective heat transfer relation with the following parameter definitions:

$$h_z = \frac{q''}{(T_{w,zy} - T_{b,z})}. \tag{4.3}$$

The heat flux was calculated based on the fluid enthalpy change given by

$$q'' = \frac{\dot{m}Cp(T_{out} - T_{in})}{\pi D L_{heated}}. \tag{4.4}$$

The local fluid bulk temperature $(T_{b,z})$ was determined from an energy balance and at each streamwise location was

$$T_{b,z} = T_{in} + \frac{\pi D q''}{\dot{m}Cp} \cdot z. \tag{4.5}$$

Properties for the above calculations, except the local Nusselt number, were based on the average fluid temperature between inlet and outlet. The properties were obtained from Kays and Crawford (1993) and were interpolated between temperatures. $T_{w,zy}$ was based directly on the TLC measurement. Estimation of the internal wall temperature assuming 1-D heat transfer gave a wall temperature gradient less than

72

0.3 °C. This was well within the wall temperature uncertainty and not incorporated at this stage.

4.6.5 Uncertainty

The uncertainty in the TLC temperature was calculated similar to the methods discussed in Hay and Hollingsworth (1996) and in Chin (1997). The wall temperature uncertainty was taken to be:

$$\delta T_w = \sqrt{\left(\frac{dT}{dHue}\delta Hue\right)^2 + \delta T_{fluid}^2 + (2 \times SEE)^2}, \qquad (4.6)$$

where $dT/dHue$ is the sensitivity in the temperature hue curve, which was either a fifth or third order polynomial as discussed earlier. Also, δHue represents the standard deviation in hue for the ROI, and since the ROI's were small (around 12 pixels), a constant value of 1° was selected instead. An additional 2° bias was added for the RGB to composite signal conversion uncertainty. In addition, δT_{fluid} was the uncertainty of the thermocouple probes used to measure the fluid temperature during calibration. Finally, the standard error estimate (SEE) takes into account the error in the polynomial curve fit and is typically defined as

$$SEE = \left[\sum_{k=1}^{n} [T_k(Hue) - T_{fit,k}(Hue)]^2 \Big/ (n - j - 1)\right]^{1/2}, \qquad (4.7)$$

where n is the number of data points, and j is the polynomial fit.

The calibration yielded only a few points for each tube section and sometimes produced points with large scatter that may significantly alter the *SEE* unreasonably. A constant value was instead selected for the *SEE* based on repeated observations of the calibration curves of 0.5 °C. A typical wall temperature uncertainty for the TLC's of 1.02 °C was estimated and is similar to that of other researchers (Chin et al., 2002). Typical uncertainties for other parameters considered in the results are listed in Table 4.1. The uncertainty in the local Nusselt number is high, but this is due to the use of a heat flux derived from the fluid enthalpy change which is a function T_{fluid}. This was initially selected to alleviate the need for estimating the energy loss to the environment. If instead the measured power was used, an estimate of typical uncertainty in Nusselt number showed that it decreased from 23.2% to 12.7%. This value is typical of what is quoted in most works.

4.6.6   Results

Figure 4.13 shows a sample of the surface temperature variation observed as well as the corresponding fluid bulk temperature deduced from Equation 4.5. This dataset is from a condition whereby the heater flux was kept constant at each traverse. The data is from six separate images, for a range of 40 to 100 z/D and is for a Reynolds number of 610. The wall temperature rises with an approximately constant slope from 41 °C to 44 °C, as would be expected for a constant heat flux boundary condition. Such a distinct wall temperature slope was not always observed, particularly for the higher flow rates whereby the wall temperature rise was much smaller. The wall temperature

Table 4.1: Typical parameter uncertainty for results.

Parameter	Uncertainty
Local Nusselt number, Nu	23.2 %
Reynolds number, Re	7.78 %
Flowrate	7.60 %
$z/RePrD$, z^*	9.60 %
Normalized distance, z/D	16.20 %
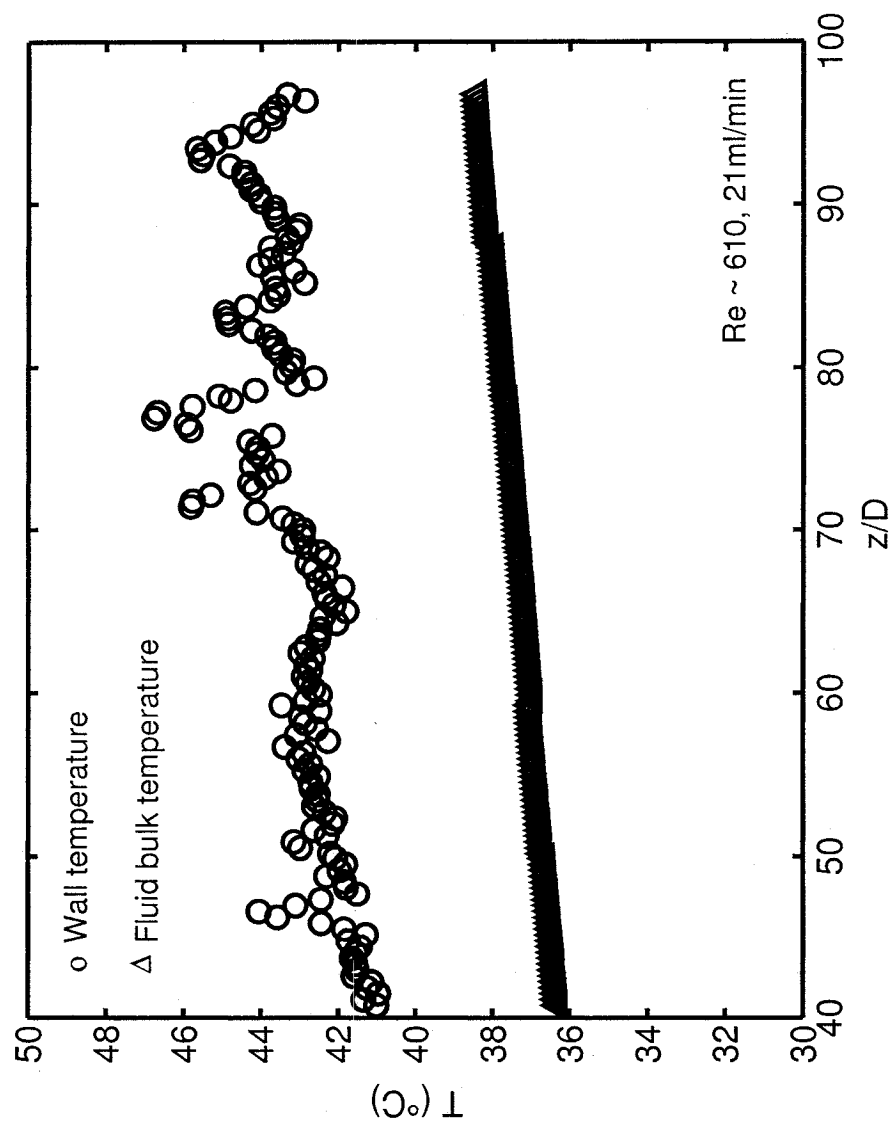
Figure 4.13: Sample measured wall temperature and calculated fluid bulk temperature.

data is a streamwise average over the visible surface and has been down-sampled for clarity. Figure 4.14 shows the streamwise averaged variation of the Nusselt number for the laminar flow cases, which was generated by considering approximately 90 diameters of tube length and which is a combination of nine adjacent tube sections imaged separately. For each tube section, there is a calibration curve for a region size of 4×3 pixels and each averaged data point consisted of 60 spanwise pixels. The data is compared with the analytical solution for laminar thermally developing flow in a circular tube, with a constant heat flux boundary condition (Shah and London, 1978). This solution has been demonstrated to have good agreement with other experimental data for tube flows down to 125 μm (Lelea et al., 2004). The results presented in Figure 4.14 are in good agreement with this solution, showing a decreasing trend towards the fully developed value of 4.364. There is some scatter between the cases, which is partially due to the noisy response of the liquid crystal. Other discrepancies will arise from the ability to repeatedly traverse to a given section both during calibration and experimentation.

In Figure 4.15, the streamwise averaged Nusselt number is plotted for the laminar and turbulent flow rate cases. Each streamwise plot is a combination of nine tube sections imaged separately. For the laminar flow cases, the Nusselt number trend is relatively smooth, showing a slight decrease in the initial length, followed by a constant trend for the remaining length. For the turbulent cases, however, the Nusselt number is slightly oscillatory, particularly farther downstream. These oscillations are not physical phenomena, rather they are due to noise in the images and local non-uniformities in the coating. It was observed that the application of the voltage had
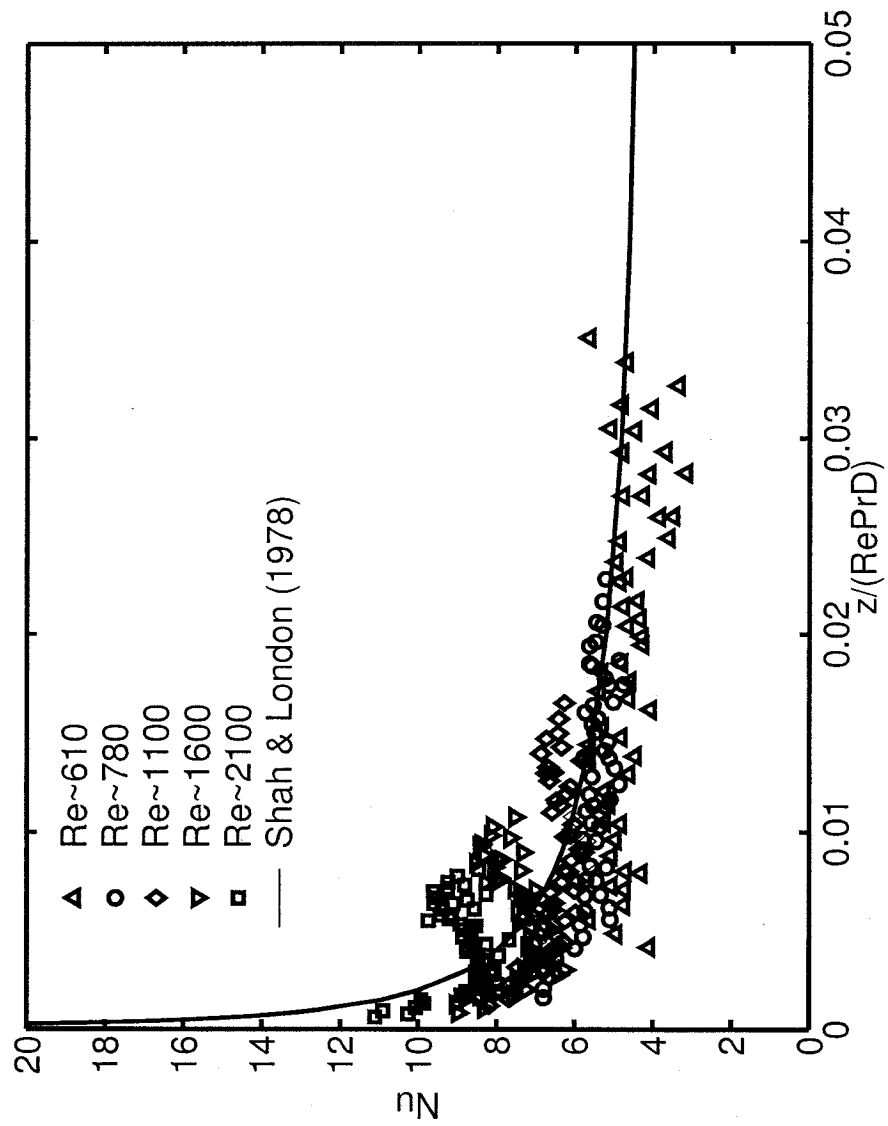
Figure 4.14: Streamwise averaged Nusselt numbers for laminar flow cases.
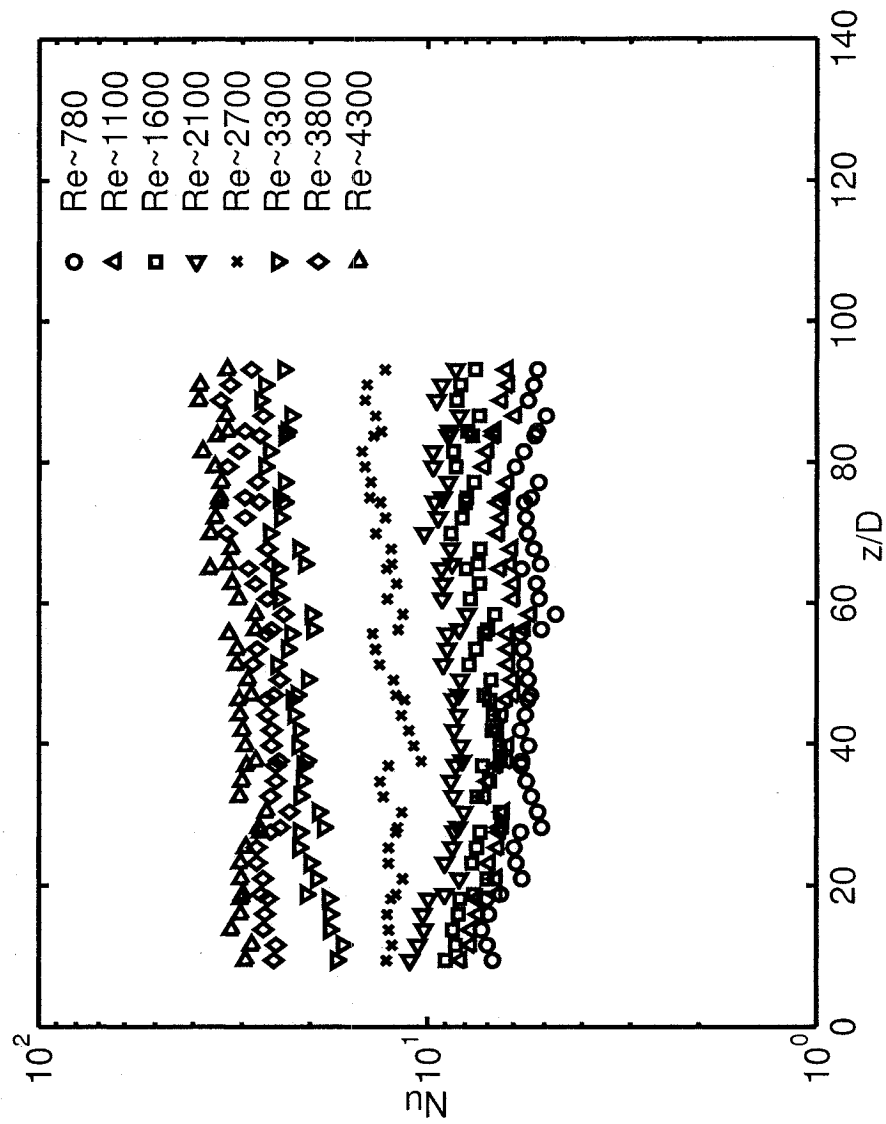
Figure 4.15: Streamwise averaged Nusselt numbers for various flowrates.

a minor influence on the TLC's and produced some coalescing of the coating, hence some of the local non-uniformities. Local non-uniformities also arose due to dust particles settling on the coating over time. This was a further reason for the localized calibration methodology developed. Variation between tube sections will be due to minor fluctuations during measurement in parameters such as the flow rate as well the inability to reproduce the original positions during traversing. In addition, between traversing for a fixed flow rate, the heat flux was sometimes adjusted as mentioned earlier to have the wall temperature within the TLC's active and reliable range.

The averaged Nusselt number for the laminar and turbulent flow cases is shown in Figure 4.16. Two sets of data are presented from experimental runs on different days. The turbulent results are compared with two heat transfer correlations for fully developed flow in smooth circular tubes. The laminar results are compared with an analytical solution for thermally developing flow with a constant heat flux boundary condition in a circular tube. For the turbulent results, one correlation is given by Gnielinski (1976) for macro size tubes as

$$Nu = \frac{(f/8)(Re - 1000)Pr}{1 + 12.7(f/8)^{1/2}(Pr^{2/3} - 1)}, \tag{4.8}$$

where

$$f = [1.82 \cdot \log(Re) - 1.64]^{-2}. \tag{4.9}$$
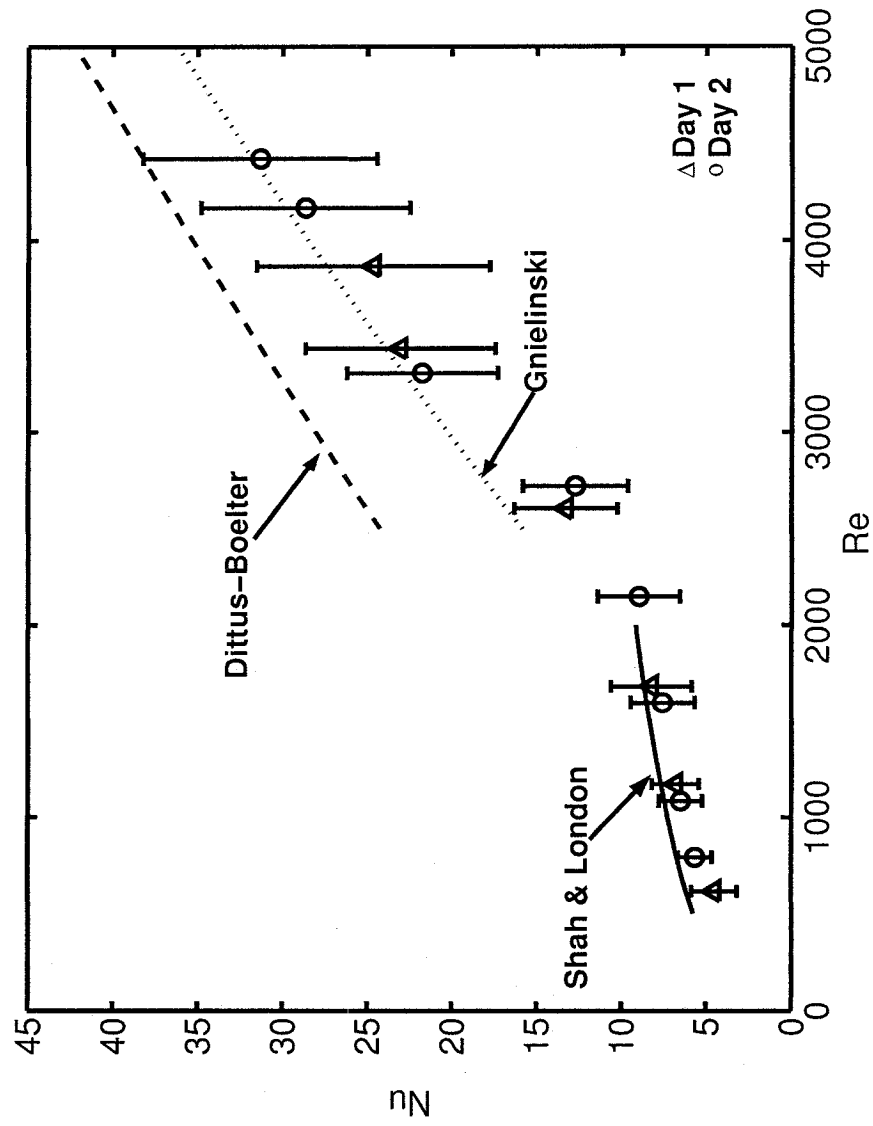
Figure 4.16: Variation of the averaged Nusselt number with Reynolds number, with comparison to correlations.

The second is the Dittus-Boelter (Rosenhow et al., 1998) correlation also for macro size tubes and given by

$$Nu = 0.024 Re^{0.8} Pr^{0.4}. \tag{4.10}$$

For the laminar results, the following solution which gives the averaged Nusselt number at a streamwise location for laminar flow was used (Shah and London, 1978),

$$Nu = 4.364 + \frac{0.046}{(z^*)^{1/3}}. \tag{4.11}$$

The turbulent results are in very good agreement with the correlation given by Gnielinski (Equation 4.8), whereas the Dittus-Boelter (Equation 4.10) correlation appears to over predict the heat transfer. Equation 4.10 is in the functional form for which most experimental correlations of turbulent heat transfer are based (Holman, 2002). Whereas, Equation 4.8 has a similar functional form as the analytically derived relation for turbulent flow heat transfer inside tubes (Kays and Crawford, 1993). Both relations however have constants derived from empirical methods. The data suggests that the combination of the functional form and the empirically derived constants of Equation 4.8, provide a better prediction for turbulent heat transfer in smooth tubes, under the present conditions. Additionally, it is noted that Equation 4.8 is the recommended choice for turbulent heat transfer predictions in smooth tubes for the present flow ranges (Kays and Crawford, 1993; Rosenhow et al., 1998). The figure also shows data from two separate days demonstrating the good repeatability. The laminar results are also in very good agreement with the analytical solution and

this was expected since it is derived from the same solution used in the comparison for Figure 4.14.

4.7 Summary

The development of a method utilizing un-encapsulated thermochromic liquid crystals for local heat transfer measurements in microgeometries has been described. To the authors' best knowledge, this is the first use of this form of liquid crystal for heat transfer measurements in a channel this small. The un-encapsulated TLC form is difficult to handle and significant scatter and noise may be present in measurements with increased magnification. A localized calibration is utilized to minimize the influence of lighting, viewing and local variability's. A large number of calibration curves are obtained from this approach and so automation, as well as logical filtering are necessary. The calibration data generated are demonstrated to be insignificantly un-altered over the course of an experimental run. The use of an airbrush is found to produce a significant improvement in coating uniformity and thickness control as compared to application with a paintbrush.

The motivation for the methods developed was the need for increased and improved measurement in mini and microchannels. Three channel configurations were discussed and due to difficulties in the first two arrangements, attributed to the combination of the TLC's and small size, results are presented for only the third configuration, which is a circular tube. The results demonstrate that the conventional size analytical solution for laminar flow is adequate for predicting the local heat transfer in

thermally developing flows inside a 1 mm nominally sized circular tube. In addition, the Gnielinski correlation for conventional size channels is adequate for predicting the average heat transfer in a 1 mm nominal size circular tube.

The circular tube design was easily configured from readily available parts and is an effective approach for channel heat transfer studies of diameters down to 250 μm. Some of the scatter and noise in measurements was introduced due to the need to traverse the test surface. It is noted that during application of the voltage on the circular tube geometry, the TLC material coalesced in some regions altering the surface uniformity and a slight dimming of the response intensity occurred. This was not observed in the other two geometries and was not documented in previous heat transfer experiments utilizing the un-encapsulated TLC's. This observation highlights the need for additional work related to the use of the un-encapsulated form of TLC's for engineering thermometry applications, as they are a promising potential for micro thermography applications. Overall, the methods developed and utilized have been shown to provide the local heat transfer coefficient in a micro geometry of 1 mm nominal size, and they are a viable approach for geometries of smaller sizes.

Chapter 5

Transport Phenomena in

Microtubes

Limited data is available on the thermo- fluid transport characteristics in sub-millimeter channels particularly under flow boiling conditions. This chapter presents pressure drop and heat transfer measurements in microtubes ranging from 0.25 mm to 1.00 mm nominal inner diameters. Single phase and flow boiling conditions are both considered separately. Single phase flow covers both the laminar and turbulent regimes. The test section configuration is as depicted in Figure 4.12 and described in Section 4.6.2. The un-encapsulated TLC methods developed and validated in Section 4.6 are utilized for measurement.

5.1 Single Phase

5.1.1 Data Reduction

The friction factor is obtained from the pressure drop relation,

$$\Delta P = \left(f\frac{L}{D} + K_{loss}\right)\frac{\rho u^2}{2}.$$ (5.1)

The losses at the entrance and exit (K_{loss}) are estimated from Streeter (1961), considering the area changes at each location between the pressure port and the tube entrance and exit. The local Nusselt number and local heat transfer coefficient are obtained as previously defined in Equations 4.2 and 4.3. The heat flux to the fluid is calculated based on the power applied to the tube and corrected for losses to the environment. This is given by,

$$q'' = \frac{\tilde{P}_{tube} - h_\infty A_{o,heated}\left(T_{w,TLC} - T_\infty\right)}{A_{i,heated}}.$$ (5.2)

The external heat transfer coefficient (h_∞) is obtained from tests with no fluid circulating and a constant power applied to the tube. The power to the tube is the measured voltage and current, corrected for power loss across the lead connections. Comparisons were made between the fluid enthalpy rise based on measured inlet and outlet temperature differences versus the electrical power applied to the tube. These differences were found to be within 5 % of each other for the majority of the cases. However, in a few cases where the fluid bulk temperature rise was low, differences were

on the order of 20 to 40 %, this can be attributed to fluid temperature measurement uncertainty. The internal wall temperature was calculated assuming one-dimensional radial heat conduction through the wall, with the outer wall temperatures measured by the TLC's as boundary conditions. That is given,

$$\frac{1}{r}\frac{\partial}{\partial r}\left(r\frac{\partial T}{\partial r}\right) + \frac{\dot{q}}{k} = 0 \qquad (5.3a)$$

$$T\left(r_o\right) = T_{w,TLC} \qquad (5.3b)$$

$$-k\frac{\partial T\left(r_o\right)}{\partial r} = h_\infty\left(T_{w,TLC} - T_\infty\right) \qquad (5.3c)$$

then the inner wall temperature $T_{w,i}$ is given by,

$$T_{w,i} - T_\infty = -\frac{r^2}{4}\frac{\dot{q}}{k} + C1\cdot\ln\left(r\right) + C2 \qquad (5.4a)$$

$$C1 = -\frac{r_o h_\infty}{k}\left(T_{w,TLC} - T_\infty\right) + \frac{r_o^2\dot{q}}{2k} \qquad (5.4b)$$

$$C2 = \left(T_{w,TLC} - T_\infty\right) + \frac{r_o^2}{4}\frac{\dot{q}}{k} - C1\ln\left(r_o\right). \qquad (5.4c)$$

The difference between inner and outer wall temperatures were minor, however, and typically less than 0.3 °C. The local fluid bulk temperature $(T_{b,z})$ was determined from an energy balance and at each streamwise location was as defined in Equation 4.5. Properties for the above calculations, except the local Nusselt number, were based on the average fluid temperature between inlet and outlet. The properties

were obtained from Kays and Crawford (1993) for water and 3M (2000) for FC-72.

Uncertainty estimates for the TLC measured wall temperature are similar to those presented in Section 4.6.5. Uncertainty in measured signals is presented in Section 3.4. Diameter dependent uncertainties included the tube inner and outer diameter, the flowrate and the Nusselt number, and they are listed in Table 5.1. Note, the diameter uncertainties are based on manufacturing tolerance.

5.1.2 Friction Factor

The friction factor results are shown in Figure 5.1. They are compared with the friction factor for fully developed laminar flow in a pipe given by (Shah and London, 1978),

$$f = \frac{64}{\text{Re}}, \tag{5.5}$$

and Equation 4.9 for fully developed turbulent flow. Equation 4.9 was selected due to its use in the average Nusselt number relation. Very good agreement is observed for all diameters in the laminar range. In addition, the predicted curves show very good agreement for the 1 mm diameter tubes in the turbulent regime. For the 0.5 mm case the results are under predicted by Equation 4.9. This equation though is valid for smooth tubes with a $Re > 10^4$. This may suggest an increasing tube roughness influence with decreasing diameter, however, as seen later for the average Nusselt number results, no benefit in heat transfer is gained from the higher friction factor. Rather, it suggests that the estimated entrance and exit loss factors are the cause of the differences observed. The transition for both the 1 mm and the 0.5 mm

Table 5.1: Typical uncertainties for diameter dependent parameters.

Nominal Tube Diameter	Inner Diameter	Outer Diameter	Flowrate	Nusselt Number
0.254 mm	±0.0254 mm	±0.0127 mm	±0.5 ml/min	±14-17%
	+0.0254 mm	+0.0127 mm	±1.5 ml/min	±8-18%
0.508 mm	-0.0127 mm	-0.0000 mm	±1.5 ml/min	±8-18%
1.067 mm	±0.0254 mm	±0.0127 mm	±1.5 ml/min	±9-18%
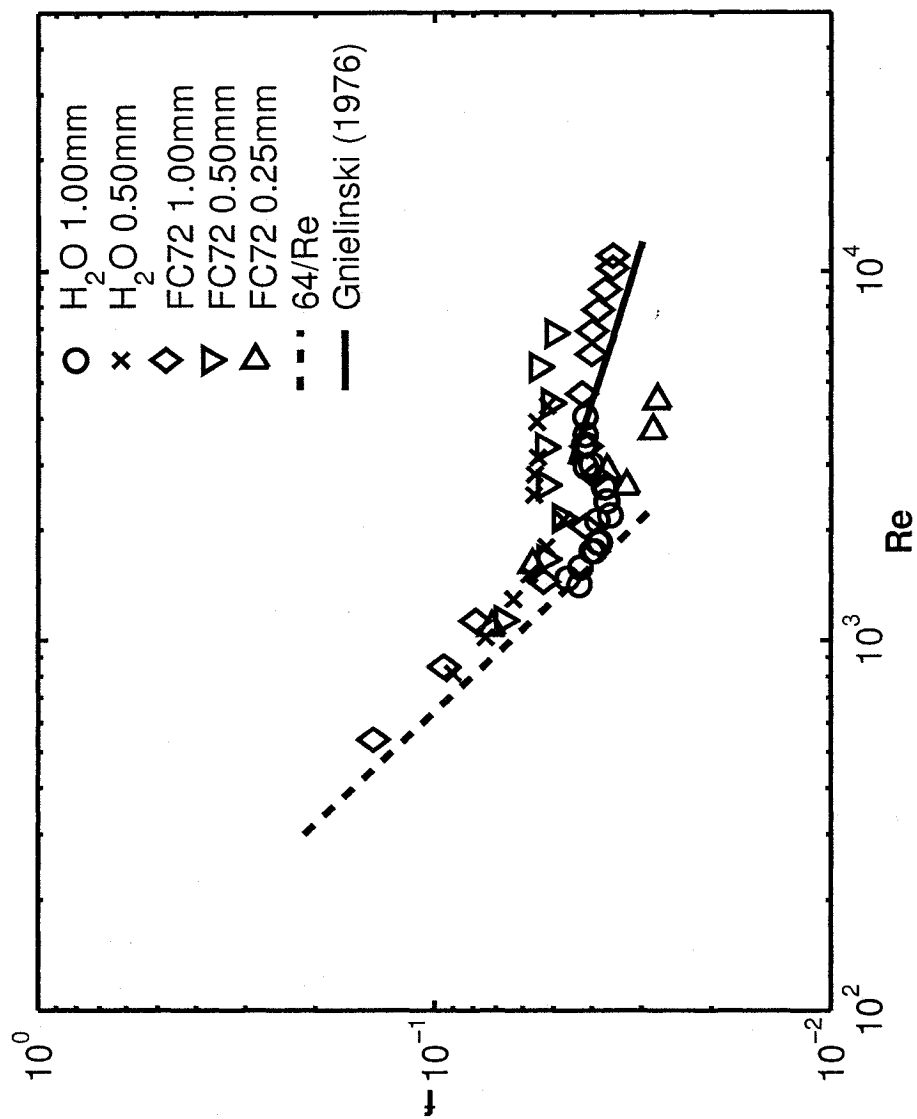
Figure 5.1: Microtube friction factors versus Reynolds number.

tubes is observed between a Reynolds number of 2000 and 4000. This is observed for both fluids and shows that the conventional value of 2300 is reasonable for these two diameters. For the 0.25 mm case, however, a delayed transition is observed and the curve appears to be changing direction at a Reynolds value of about 5000.

5.1.3   Heat Transfer Coefficient

Figure 5.2 shows a pair of data sets from raw image to processed data. Figure 5.2 (a) is considered a good data set and is typical of the data presented in this section. In the figures the temperature is rising from left to right and covers a distance of approximately 10 mm. In Figure 5.2 (a), there is some minor scatter in the red range due to the large light intensity, however, in the green/blue range the response is much better. Most of the data presented is derived from images that fell in this green/blue range. Figure 5.2 (b) only has a small useful region, therefore such a data set is not considered for final presentation. Figures 5.3 to 5.7 show the circumferentially averaged streamwise Nusselt number. The data are compiled from a number of traversed locations and the heat flux used was not always constant. For the majority of the plots in the laminar regime (taken as Re < 2300) a decreasing Nusselt trend is observed with increasing distance, approaching an asymptotic value. Although for some laminar cases the downward slope is minimal, their slope tends to be more significant than for the turbulent and transitional cases. For the remaining cases the Nusselt number is constant. The decreasing versus constant trend of laminar versus turbulent flows are as expected based on physical considerations and observations in

(a) Adequate data set.

(b) Inadequate data set.
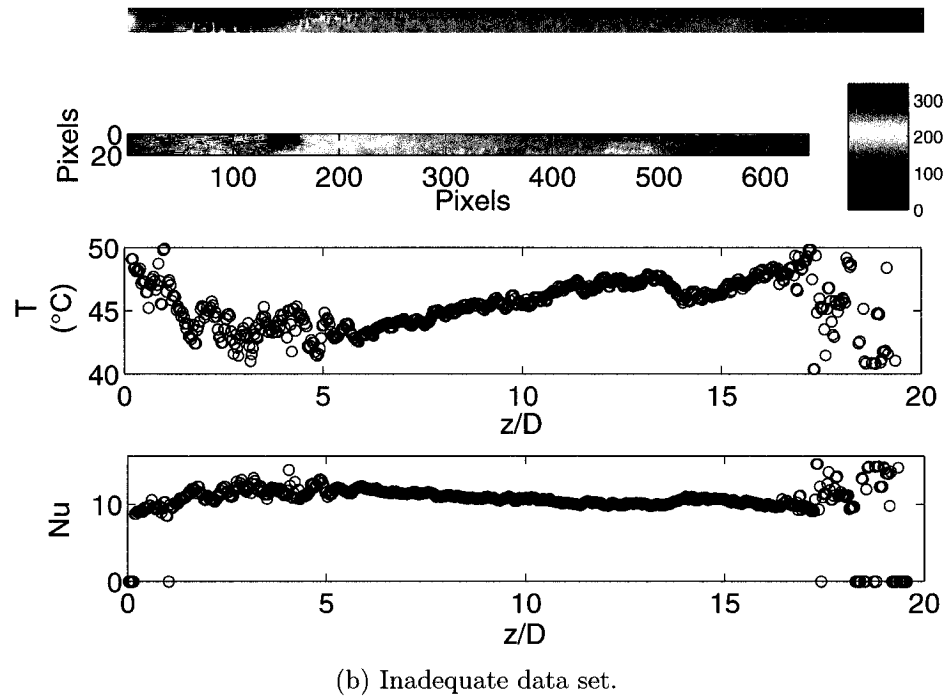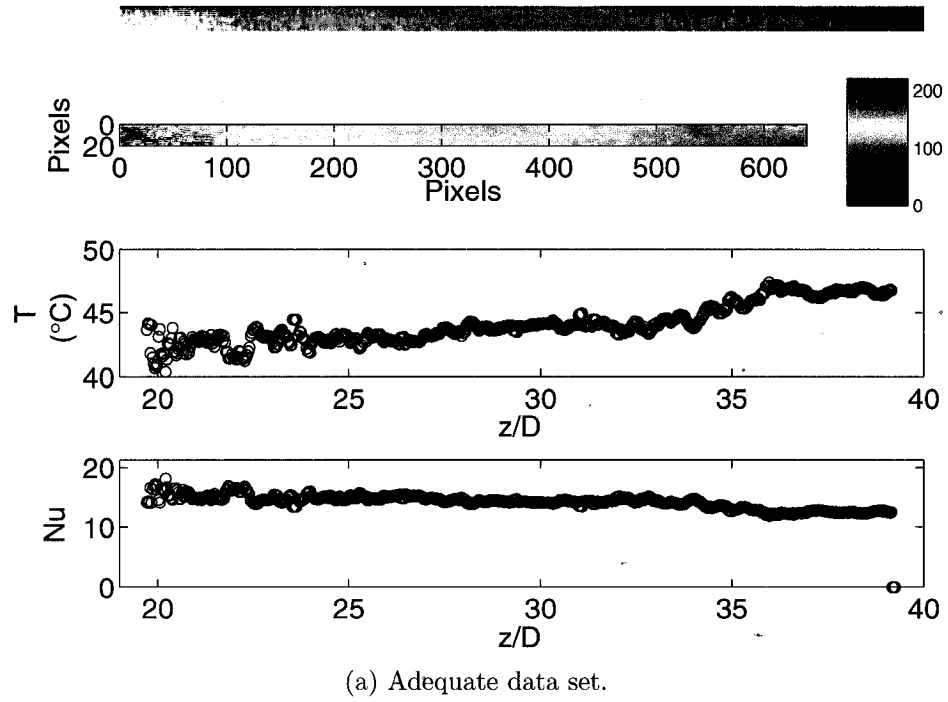
Figure 5.2: Typical raw to processed results.

larger tubes (Holman, 2002). For data in the turbulent regime, a short developmental length is observed, which can be generalized as being less than 10 hydraulic diameters.

Shown in Figures 5.8 to 5.11 are the local heat transfer results for the laminar regime data. The results show that the developmental length for the laminar results are well represented by the analytical solution given in Shah and London (1978). In the fully developed region, the Nusselt number tends to the analytical result of 4.364, which is for constant heat flux in a circular tube. The results show no unexpected trend related to decreasing tube diameter.

The average Nusselt number for all the tube diameters and the two fluids is shown in Figure 5.12. These data are obtained from the average of the farthest downstream image captured to allow for thermal development. The Nusselt number is divided by $Pr^{0.4}$ to account for the two differing fluids, with the Prandtl number taken at room temperature. The data are compared with two correlations, one the Gnielinski (1976) correlation (Equation 4.8) representing large tubes. The second, a correlation given by Adams et al. (1998) and representing small diameter channels. It is based on Equation 4.9, with a slight modification as follows,

$$Nu_{Adams} = Nu_{Gniel}\left(1 + F\right)$$

where ,   (5.6)

$$F = 7.6 \times 10^{-5}\mathrm{Re}\left[1 - \left(\tfrac{D}{1.164}\right)^2\right].$$

The data are well correlated between each other particularly between the 0.5 mm
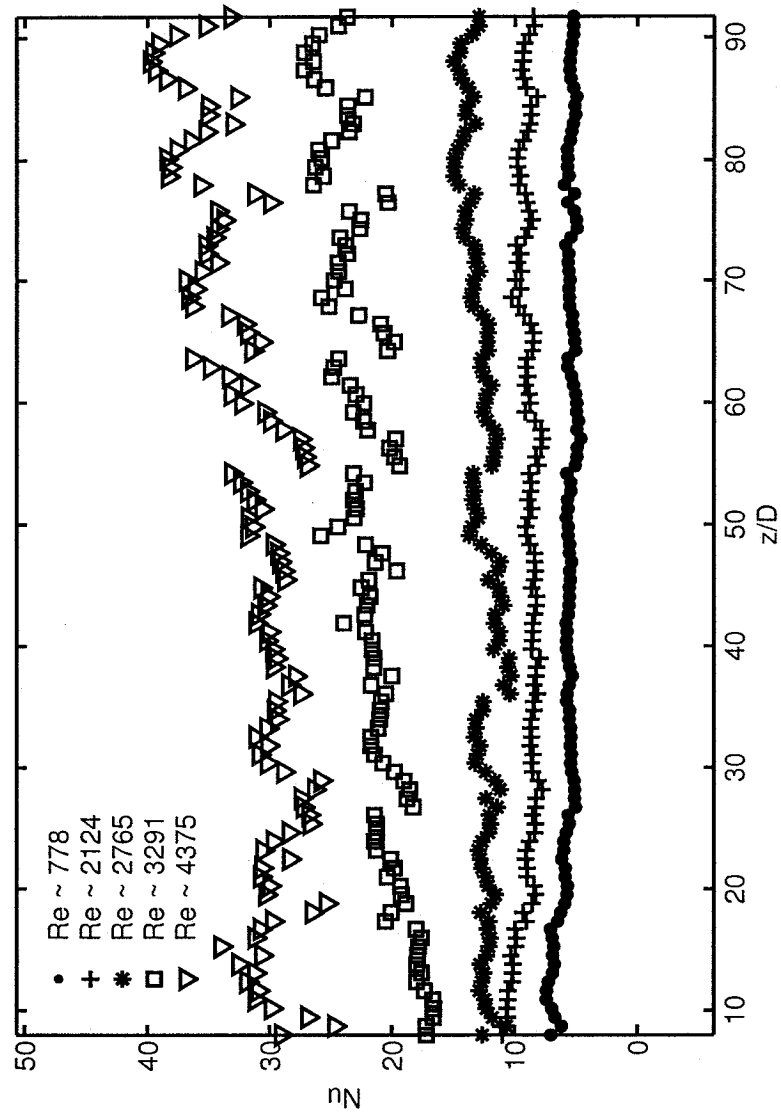
Figure 5.3: Streamwise Nusselt numbers - 1.0 mm, H_2O.
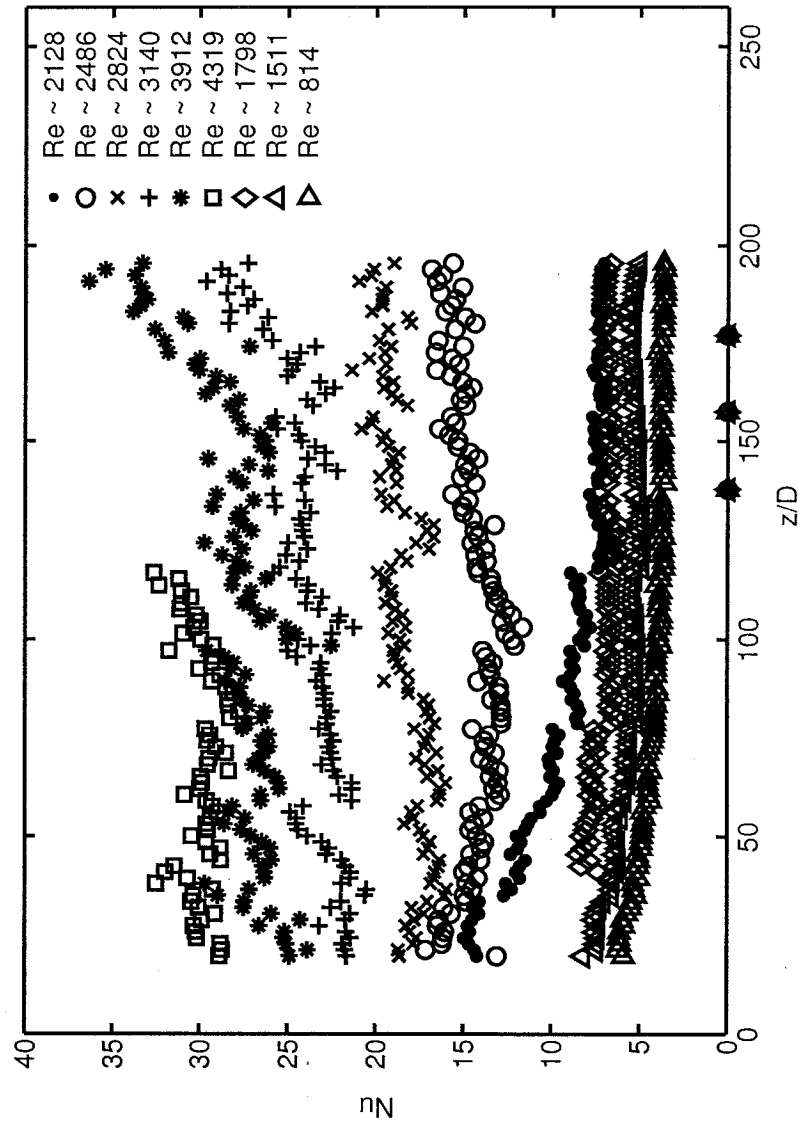
Figure 5.4: Streamwise Nusselt numbers - 0.5 mm, H_2O.
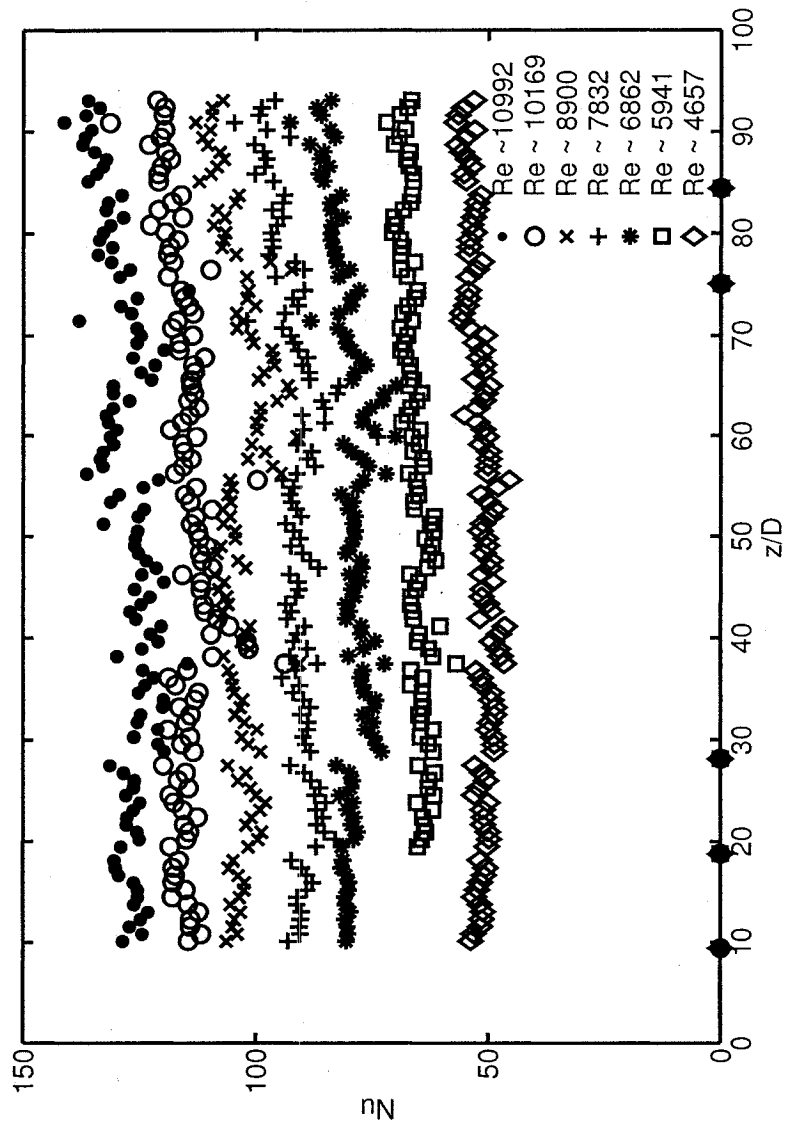
Figure 5.5: Streamwise Nusselt numbers - 1.0 mm, FC-72.
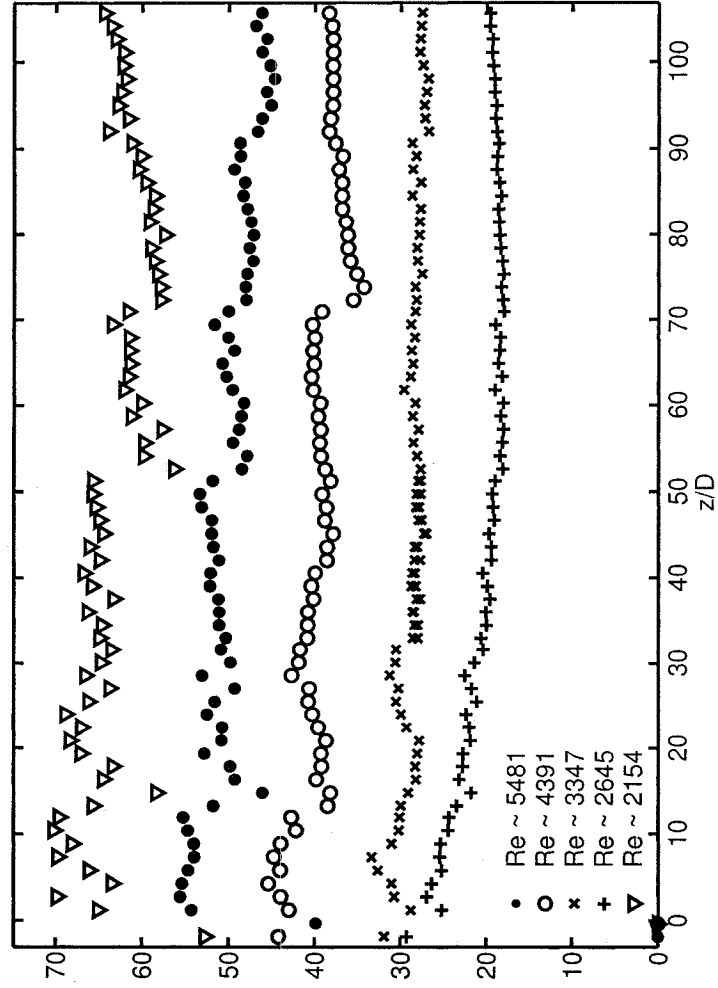
Figure 5.6: Streamwise Nusselt numbers - 0.5 mm, FC-72.
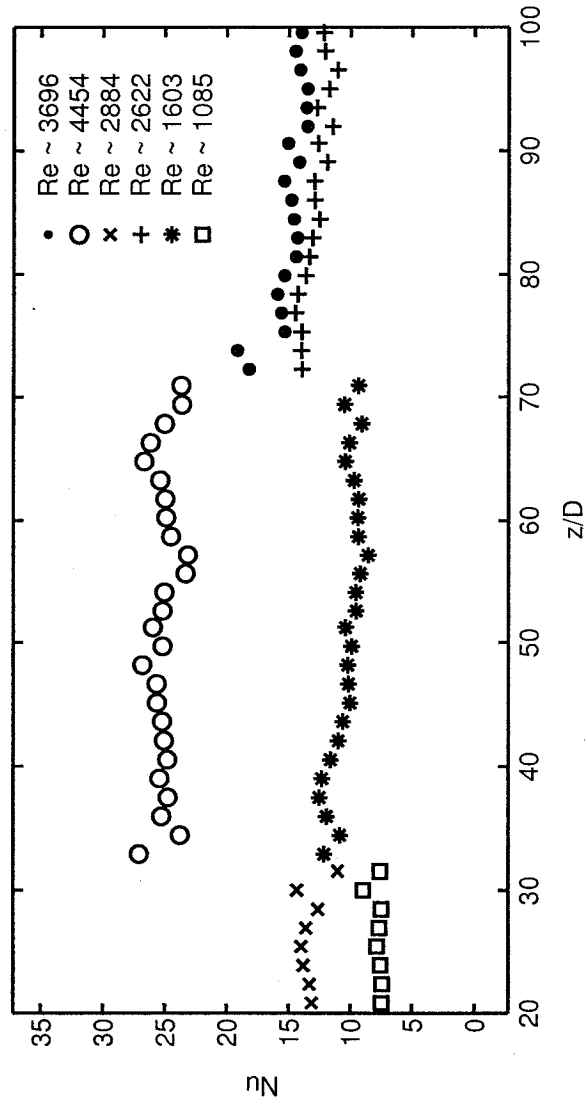
Figure 5.7: Streamwise Nusselt numbers - 0.25 mm, FC-72.
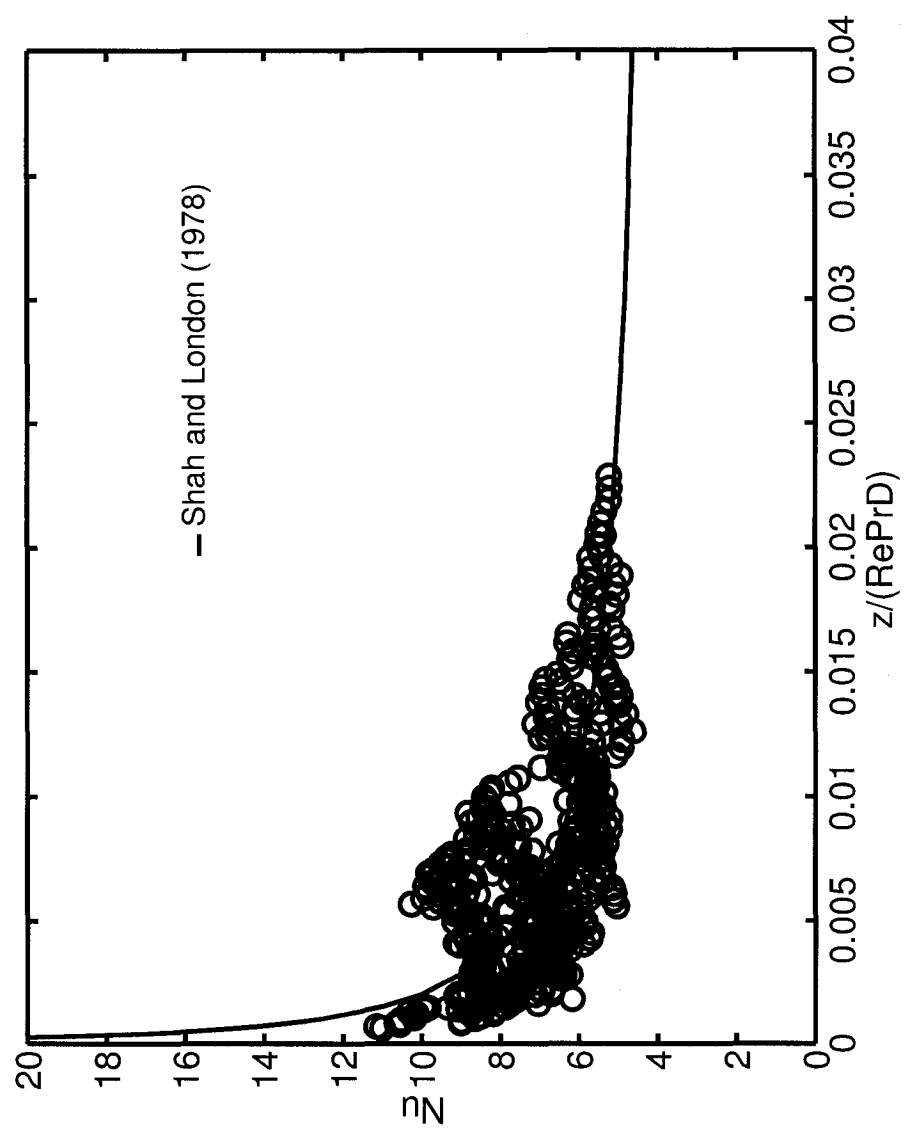
Figure 5.8: Laminar streamwise Nusselt number - 1.0 mm, H_2O.
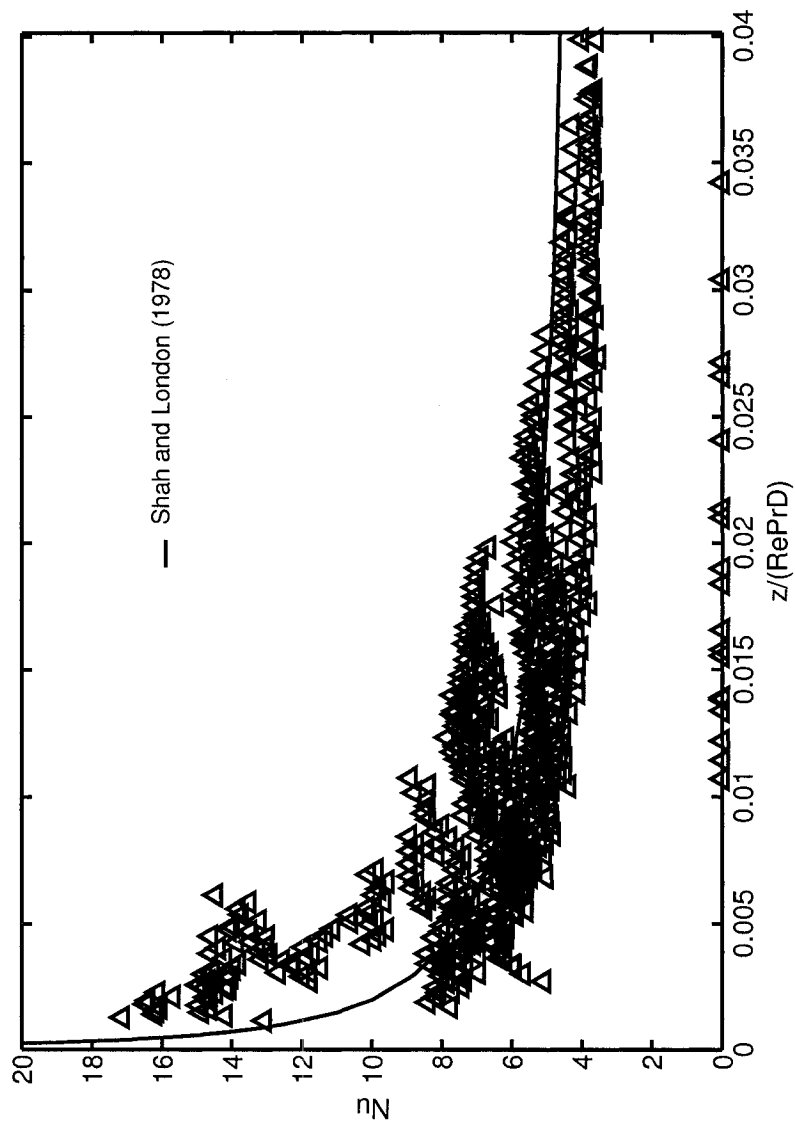
Figure 5.9: Laminar streamwise Nusselt number - 0.5 mm, H_2O.
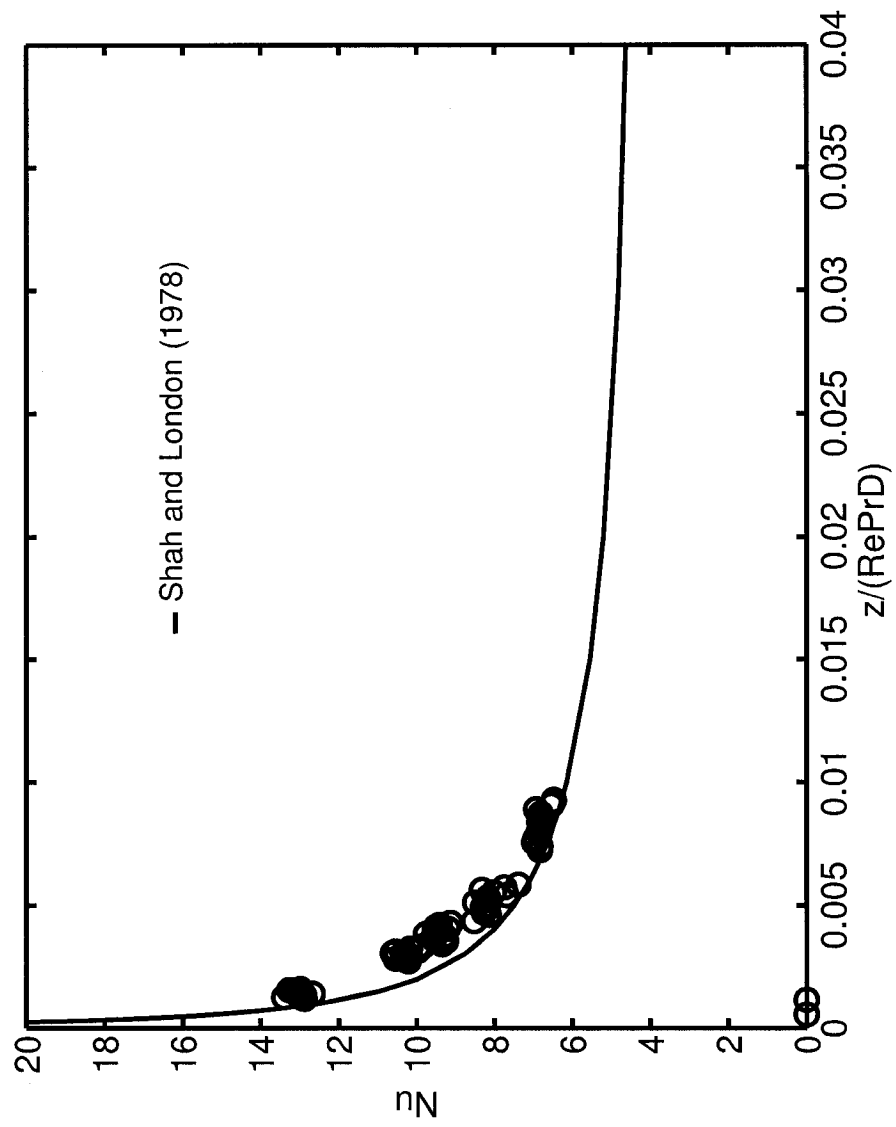
Figure 5.10: Laminar streamwise Nusselt number - 1.0 mm, FC-72.
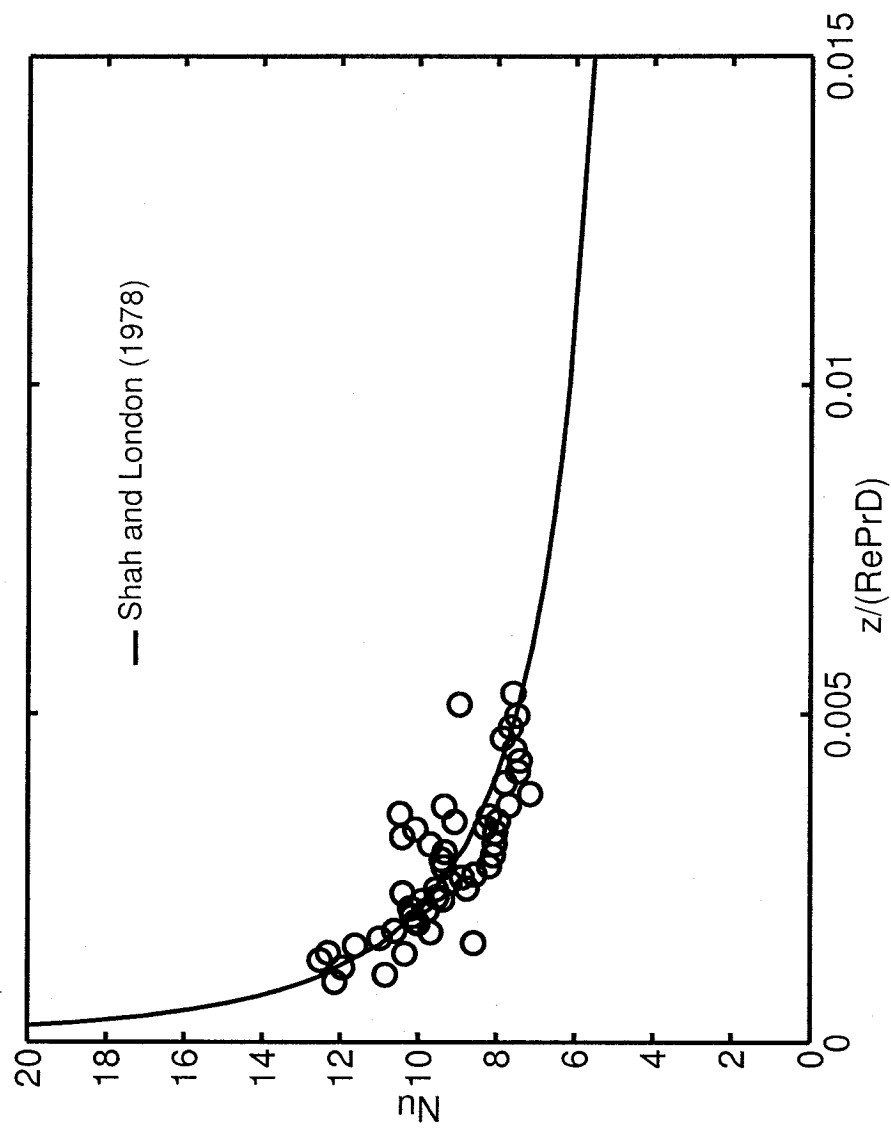
Figure 5.11: Laminar streamwise Nusselt number – 0.25 mm, FC-72.
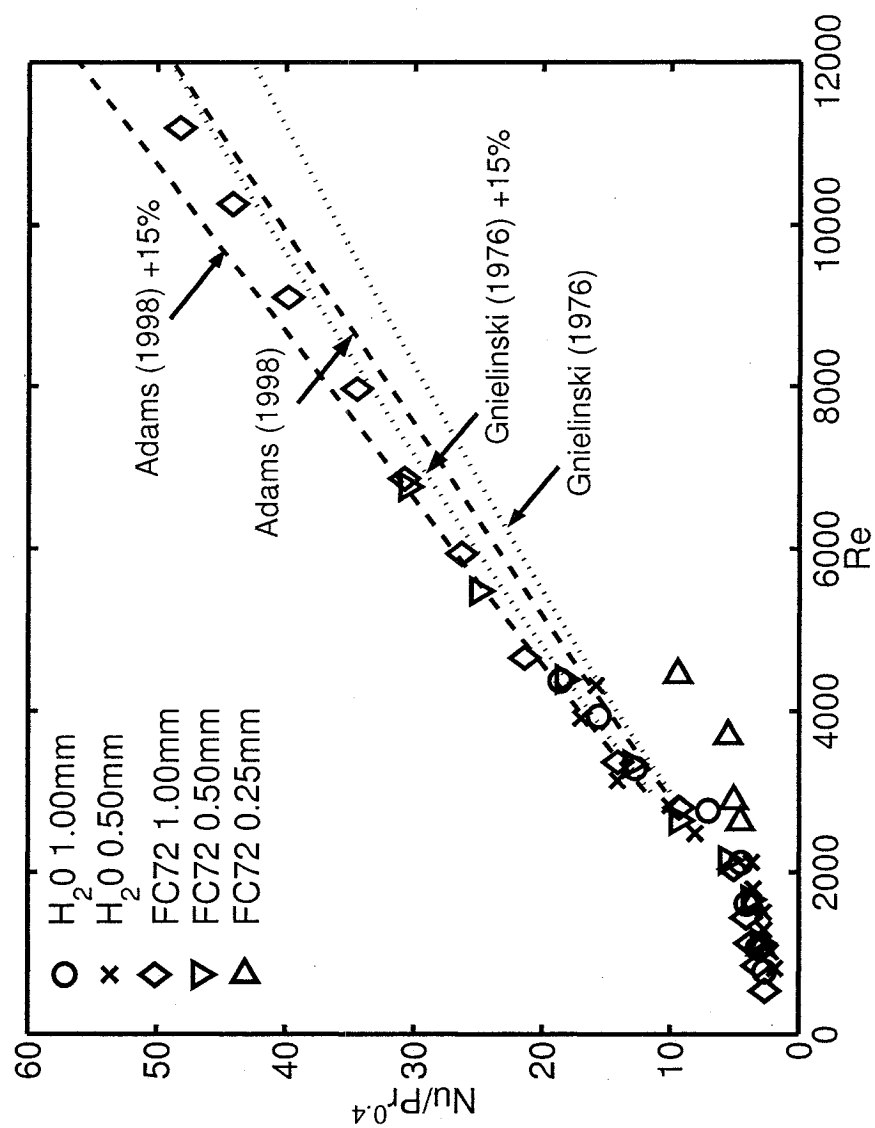
Figure 5.12: Average Nusselt numbers.

and 1.0 mm tubes at higher Reynolds. The influence of the delayed transition for the 0.25 mm FC-72 case is reflected also in the average Nusselt number (Figure 5.1). Comparing the data to the correlations, at first glance the Adams et al. (1998) correlation appears to be the better choice. However when considering experimental uncertainty of the experiment, correlation, or both (taken as 15%), the Gnielinski (1976) correlation also demonstrates an adequate comparison. Tube roughness is not considered a major influence as both tubes showed differing friction factors yet similar Nusselt numbers. The conclusion therefore is that in the operational range considered of $Re < 1.2 \times 10^4$ and Prandtl number ranging from 5.4 to 11.5, and with experimental uncertainties kept in mind, both the Gnielinski (1976) correlation for large tubes and the Adams et al. (1998) correlation suggested for small tubes are adequate. Further as a conservative design guideline, when determining the heat load applied, the Adams et al. (1998) correlation should be used, whereas when estimating the cooling benefit gained, the Gnielinski (1976) correlation should be used. These guidelines are deemed general, as there will be few applications of tubes in the sub-millimetre range with Reynolds numbers exceeding 10^4, as the pressure drop becomes unrealistically large.

5.2 Boiling

5.2.1 Data Reduction

The local heat transfer coefficient (h_z) is obtained as defined in Equation 4.3. The heat flux to the fluid is calculated based on the power applied to the tube and corrected for losses to the environment as defined in Equation 5.2. The internal wall temperature is calculated from Equation 5.4. The difference between inner and outer wall temperatures was minor and typically less than 0.3 °C.

In order to determine the local heat transfer coefficient, the local bulk temperature is required. In the single phase region it is based on an energy balance from the inlet, whereas in the saturated flow boiling region, it is determined from the local saturation pressure. The local saturation pressure is assumed to be linearly decreasing within the two-phase region. This method is similar to that adopted by many recent works (Qu and Mudawar, 2003; Yen et al., 2003; Lee and Lee, 2001; Tran et al., 1996). The local quality is then calculated as,

$$x\left(z\right) = \frac{q''\pi D\left(z - z_0\right)}{\dot{m}h_{fg}}.$$

(5.7)

Uncertainty estimates for the various sensors is presented in Section 3.4. Typical uncertainty in the two-phase heat transfer coefficient was estimated to be 9.9%.

5.2.2 Measurement Scope

Measurements were carried out at three flowrates, two low flowrates in the laminar regime and a high flowrate in the turbulent regime. For the low flowrates, the mass flux was nominally 770 kg/(m² · s) and 1040 kg/(m² · s), with inlet subcooling ranging from 7 °C to 18 °C. For the high flowrate, the mass flux was nominally 2050 kg/(m² · s) and the inlet subcooling ranged from 5 °C to 18 °C. Details of the conditions investigated are listed in Table 5.2.

At the high mass flux, onset of nucleate boiling characteristics such as increased pressure drop and large wall temperature drop, were not observed for the heat flux range covered. Additionally, with increased heat flux the exit fluid temperature could sustain temperatures higher than the saturation temperature for small time periods before dropping to the saturation temperature. With a drop in the exit fluid temperature to its saturation temperature, vapour was observed in the tubing downstream of the test section. However, the wall temperature and pressure drop characteristics were virtually unchanged. Figures 5.13 (a-d) compares the wall temperature and pressure drop characteristics at different levels of inlet subcooling for both the high and low mass fluxes. These figures show the differences in initiating boiling at a mass flux of 770 kg/(m² · s) and 2050 kg/(m² · s). It is important to note that the temperature for these plots is measured by the thermocouple bonded to the tube wall close to the exit. This temperature is not representative of the actual wall temperature, due to the thermal resistance of the electrically resistive epoxy used. However, it is presented since it effectively highlights the wall temperature trend. The TLC's are not

Table 5.2: Tube boiling measurement conditions.

Volumetric Flow Rate (ml/min)	Descriptor	Nominal mass flux (kg/(m²·s))	$T_{in}(°C)$	$\Delta T_{sub}(°C)$	P_{out} (bar)	N_{conf}
68	$\Delta T_{sub,low}$	2050	59	5.2	1.25	0.66
	$\Delta T_{sub,med}$		56	9.9	1.33	0.55
	$\Delta T_{sub,high}$		46	18.4	1.26	0.70
			48	16.3	1.26	0.69
26	$\Delta T_{sub,low}$	770	56	6.7	1.20	0.55
	$\Delta T_{sub,high}$		48	17.8	1.32	0.69
35	$\Delta T_{sub,low}$	1040	55.5	7.8	1.21	0.64
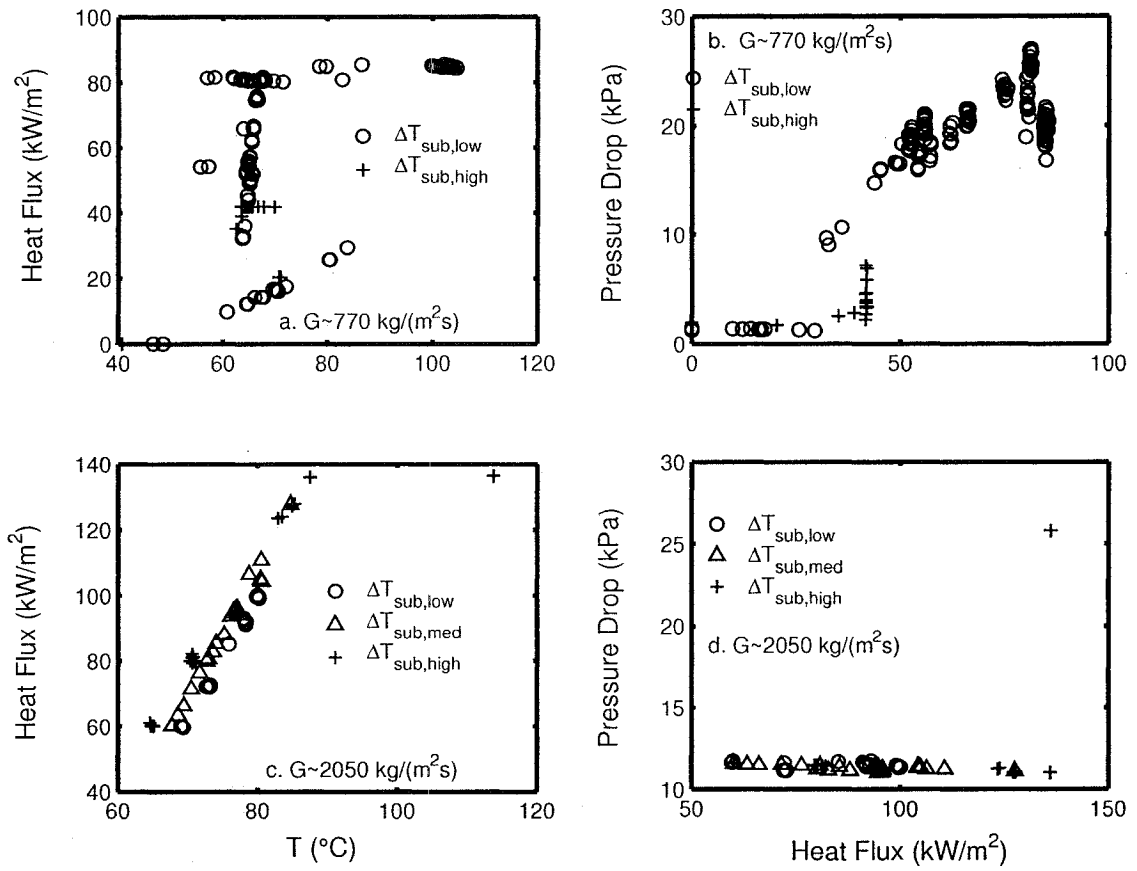
Figure 5.13: (a,c) Heat flux versus wall temperature, measured by embedded thermocouple. (b,d) Pressure drop versus heat flux.

presented at this point since the wall temperature was not always within their active range. In Figure 5.13 (a), for the low mass flux, the wall temperature increases in the single-phase regime until about 30 kW/m^2 when boiling is initiated. At this point, there is a large wall temperature drop. With increased heat flux the wall temperature rises slightly with increased heat flux. At a high heat flux of about 42 kW/m^2 for the high subcooling case and 80 kW/m^2 for the low subcooling case, further increase in heat flux causes a drastic wall temperature rise. The wall temperature through a large part of the boiling region fluctuates and is likely the reason for some of the scatter in the data at lower heat flux. Although the cause of the large temperature rise appears to be due to a critical heat flux condition, it needs to be investigated further as the trend is counter to the trends observed in many other works. That is, if it is a critical heat flux condition, the lower critical heat flux should be observed in the lower subcooled case (Bowers, 1994). Figure 5.13 (b) shows the pressure drop characteristics at the low mass flux case. The pressure drop slightly decreases with increasing heat flux in the single phase regime, as would be expected. At onset of boiling, the pressure drop increases, though this increase is more significant for the low inlet subcooling case.

Figure 5.13 (c) shows the wall temperature characteristics for the highest mass flux case. Unlike the low mass flux case, increased heat flux continually increases the wall temperature at an almost constant rate. For the case of high inlet subcooling, a threshold heat flux was observed, at which point further increase in heat flux caused a wall temperature jump. As the setup was not configured for critical heat flux experiments, power to the system was immediately shut down to prevent damage to

the tube. Figure 5.13 (d) shows the wall pressure drop characteristics for the high mass flux case. Similar to what is observed for single phase flows, the pressure drop slightly decreases with increasing heat flux for the range covered. For the high inlet subcooling case at a threshold heat flux of about 138 kW/m^2, a significant rise in pressure drop is observed, signifying two-phase or superheated flow.

For the wall thermocouple temperature measurements presented above, a wall temperature of 87 °C signifies a tube outer wall temperature greater than 100 °C. This high temperature caused vaporization of the TLC coating and long periods at this temperature would completely eliminate the TLC coating. This highlights one of the two drawbacks in utilizing un-encapsulated TLC's for boiling measurements. That is, when using the material in conditions that require high wall superheats to initiate boiling, there is a potential that the wall temperature can be too high for the TLC material and thus erode or completely eliminate the coating. The second drawback is related to effectively utilizing the TLC active range. The measurements were restricted to a system pressure that would provide wall temperature conditions in the active TLC range during boiling. This range was determined through a number of trials and is not an effective approach for a full parametric study.

From the above, boiling was only initiated at the low mass flux conditions. Detailed experimental measurement and analysis are therefore carried out at these conditions and more specifically at the low inlet subcooling condition. The remainder of this section provides results from these test conditions of low mass flux and low inlet subcooling.

5.2.3   Boiling Onset at Low Mass Flux

Flow boiling was initiated by incrementing the applied heat flux. While in single phase, the wall temperature constantly rose and this was observed with the TLC color changing from red to blue at a given location. With further increase of heat flux downstream locations of the tube past the clearing point of the TLC and wall temperature monitoring was restricted to the thermocouple embedded close to the tube end. The demarcation to the clearing point was a long smooth color change implying a low temperature gradient. With further increase, the TLC clearing point moved further upstream, signifying an increased wall temperature. No bubbles or vapour were observed in the tubing downstream of the test section, or in the outlet instrumentation chamber. At a threshold heat flux, a fast moving front with a large temperature gradient was observed to travel towards the exit of the tube. Additionally, just prior, the TLC coating was observed to partially vaporize suggesting an instantaneous wall temperature rise. A sample of this fast moving front is shown in Figure 5.14. The red region is the cooler temperature region, whereas the black is the higher temperature region, since it is past the TLC clearing point. The velocity of the front was estimated to be approximately 1.4 m/s to 1.7 m/s, which is higher than the all liquid fluid velocity of 0.58 m/s and much lower than the all vapour velocity of 47.95 m/s. Immediately following the front, the wall temperature is significantly lower than under single-phase conditions, and remains relatively constant over the two-phase length. The location of this front initiation was not identified exactly on the tube, but was approximately 1/5th to 1/4 downstream of the inlet. The large

111
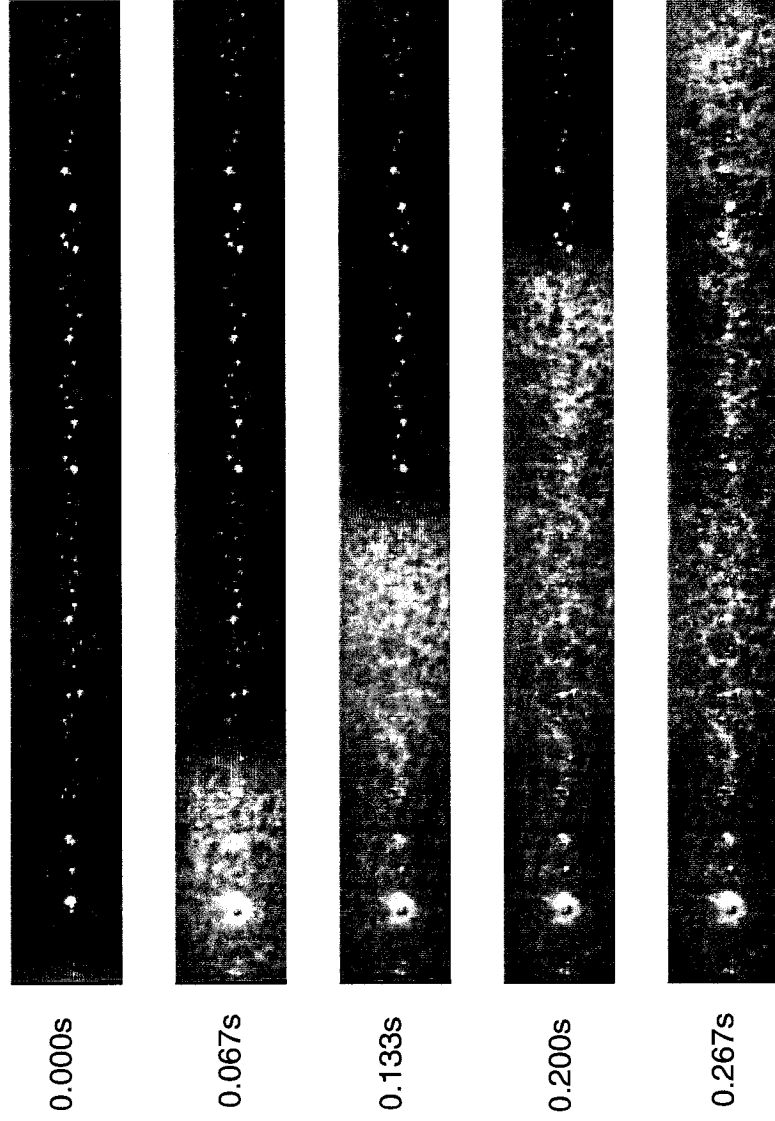
Figure 5.14: TLC wall temperature visualization over time during boiling onset, 79 to 88 z/D, $q'' = 30.4$ kW/m^2, $G = 770$ kg/(m$^2 \cdot$ s). Red is lower temperature region, and flow is from left to right.

temperature spike at onset suggests a transition from all liquid to significant vapour flow. The moving wall temperature gradient further suggests that this condition is unstable, causing an immediate purging of the high vapour region by a two-phase region with better heat transfer characteristics. This onset phenomenon was found to be repeatable over the same experimental run by turning on and off the power to the tube, and was also observed on different experimental days. Its occurrence is likely function of the tubes inner surface, the tube diameter and the working fluid characteristics. Further studies are recommended to clearly identify this phenomenon.

5.2.4 Wall Temperature Visualization and Measurement During Flow Boiling

With boiling initiated at a low heat flux, the wall temperature remained stable. The TLC color was at the red-start of the bandwidth and hence it was difficult to obtain measurements at this condition. With an increase in heat flux the wall temperature slightly increased and the TLC color response was clearly in the red range. With further increase in heat flux wall temperature oscillations were observed. Far downstream the oscillations were in the red range signifying a low wall temperature and far upstream they were in the yellow to green range signifying a higher wall temperature. With further increase in heat flux, a large increasing wall temperature gradient was observed downstream, past the clearing point of the TLC in the form of a front. This front would periodically oscillate and its color would fluctuate.

Figure 5.15 presents sample data of these oscillations taken at a low heat flux
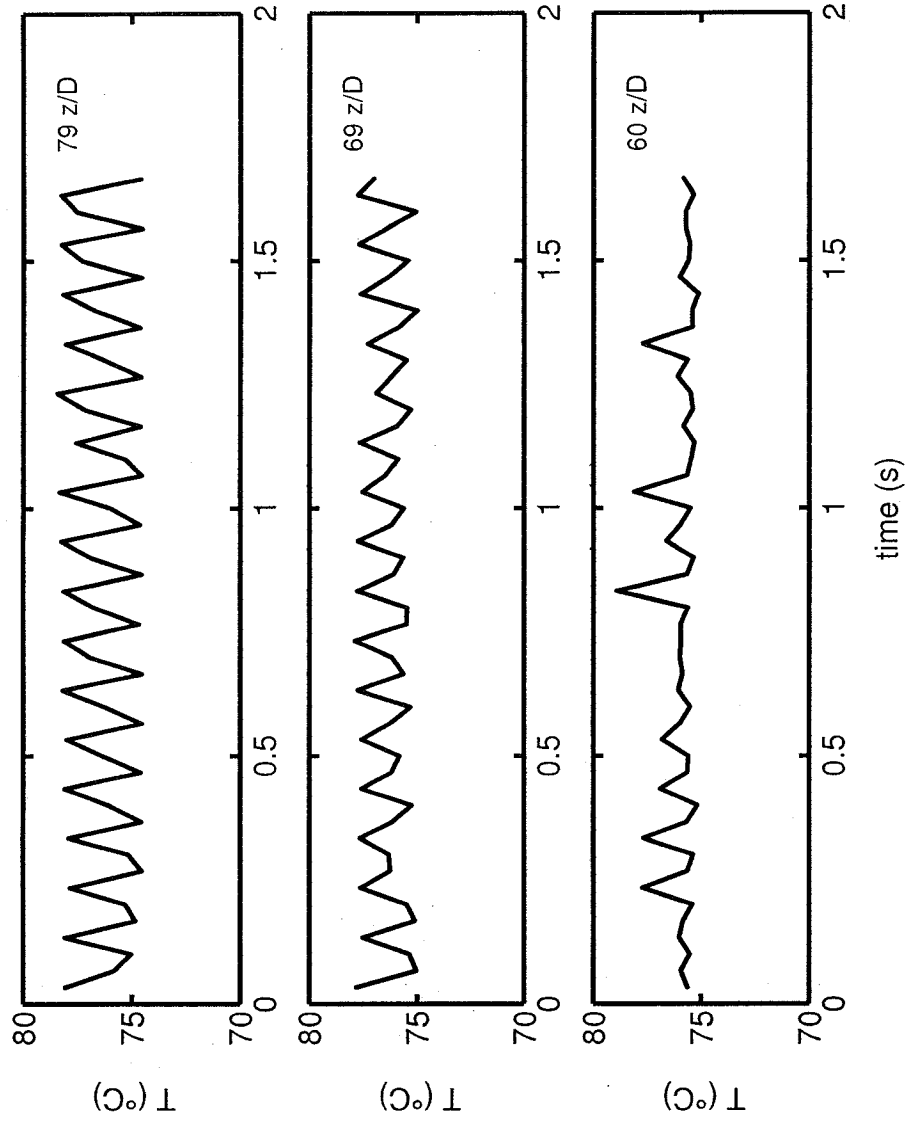
Figure 5.15: TLC wall temperature time trace - 3 separate locations imaged at separate time instants, $q'' = 50.7$ kW/m^2, $G = 770$ kg/(m$^2 \cdot$ s).

and at a far downstream location of 60 z/D to 79 z/D. The time traces are produced from considering the median value of a region of 20 pixels in the streamwise direction and 72 pixels in the circumferential direction. Prior to this the images are filtered to exclude pixels that appear white or black based on consideration of their intensity, hue and saturation. The wall temperature fluctuations in Figure 5.15 are observed to be semi-periodic with amplitudes ranging from 1 °C to 5 °C. Based on this figure and other data, it was not clear the influence of variable distance on the amplitude at a given heat flux. Figure 5.16 shows a frequency spectrum of the signal typical of a variety of far downstream locations along the tube. The fundamental frequency is approximately 10 Hz. With the temporal resolution available, a constant frequency was observed across the length of the tube for a fixed heat flux. Figure 5.17 shows a second sample of the wall temperature fluctuations at low heat flux for a location close to the inlet (18 z/D) and close to the outlet (83 z/D). The mean wall temperature decreases by about 2 °C, but the frequency and amplitude of the oscillations remain similar. The influence of the heat flux on the wall temperature amplitude was not clear. Figure 5.18 shows a sample of data taken at 8 z/D with increasing heat flux. The amplitude clearly increases from 64.6 kW/m^2 to 73.5 kW/m^2, however, with further increase, the amplitude slightly decreases then remains at the same magnitude.

As the heat flux was increased the wall temperature fluctuations appeared to increase in frequency based on real-time visual inspection of the TLC color change. However, frequency spectrums of signals captured during these conditions suggest a decrease in frequency to about 6 Hz to 8 Hz. This decreasing trend however, may be caused by aliasing due to the limitation in the frame capture rate of approximately
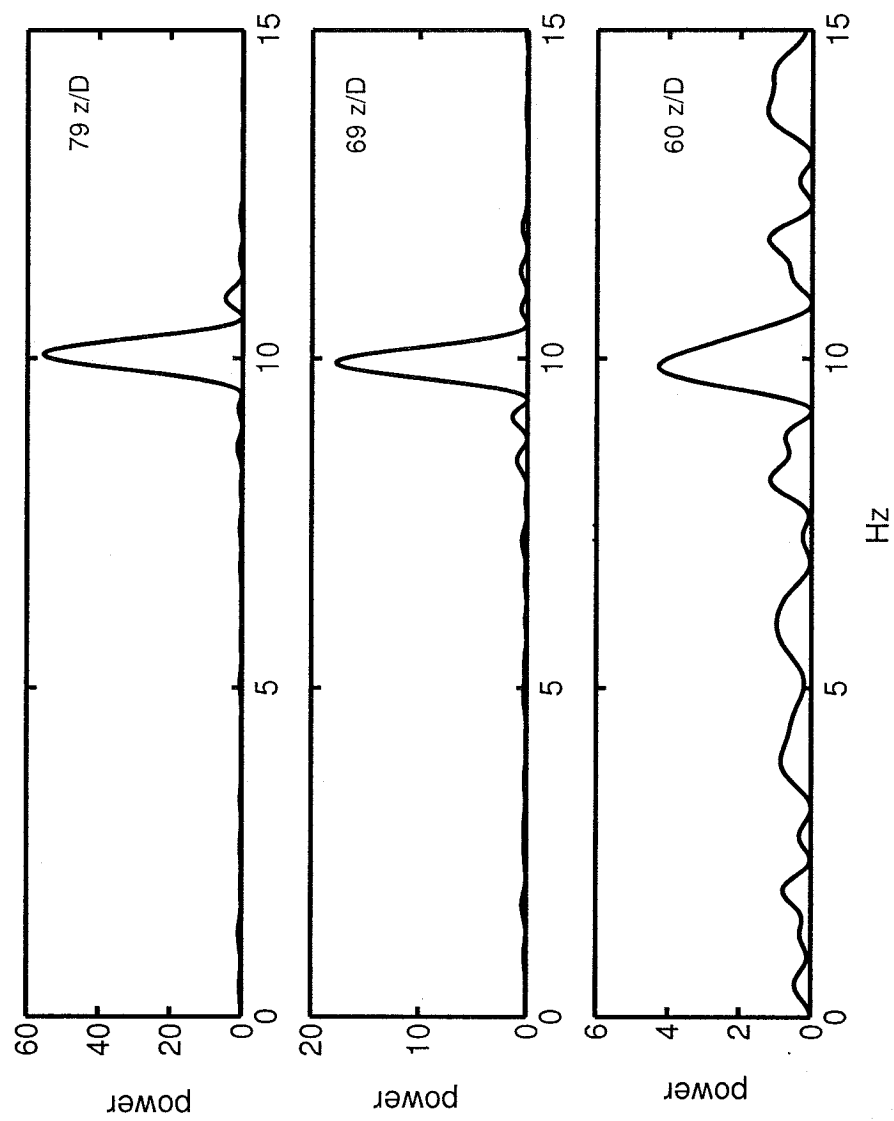
Figure 5.16: Typical power spectrum of oscillating wall temperature as measured by TLC, for corresponding waveforms in Figure 5.15, $q'' = 50.7$ kW/m^2, $G = 770$ kg/(m$^2 \cdot$s).
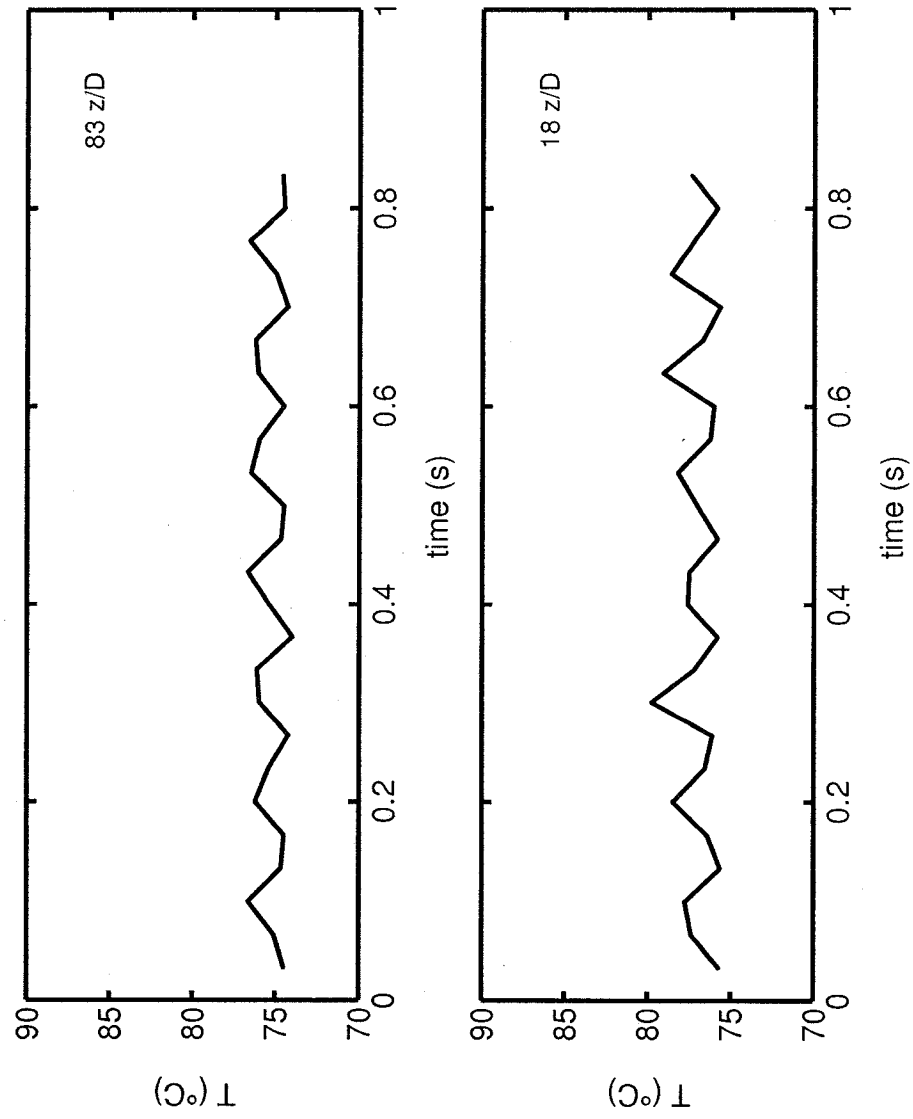
Figure 5.17: Wall temperature time trace at a far downstream (83 z/D) and an upstream (18 z/D) location, $q'' = 54.1$ kW/m².
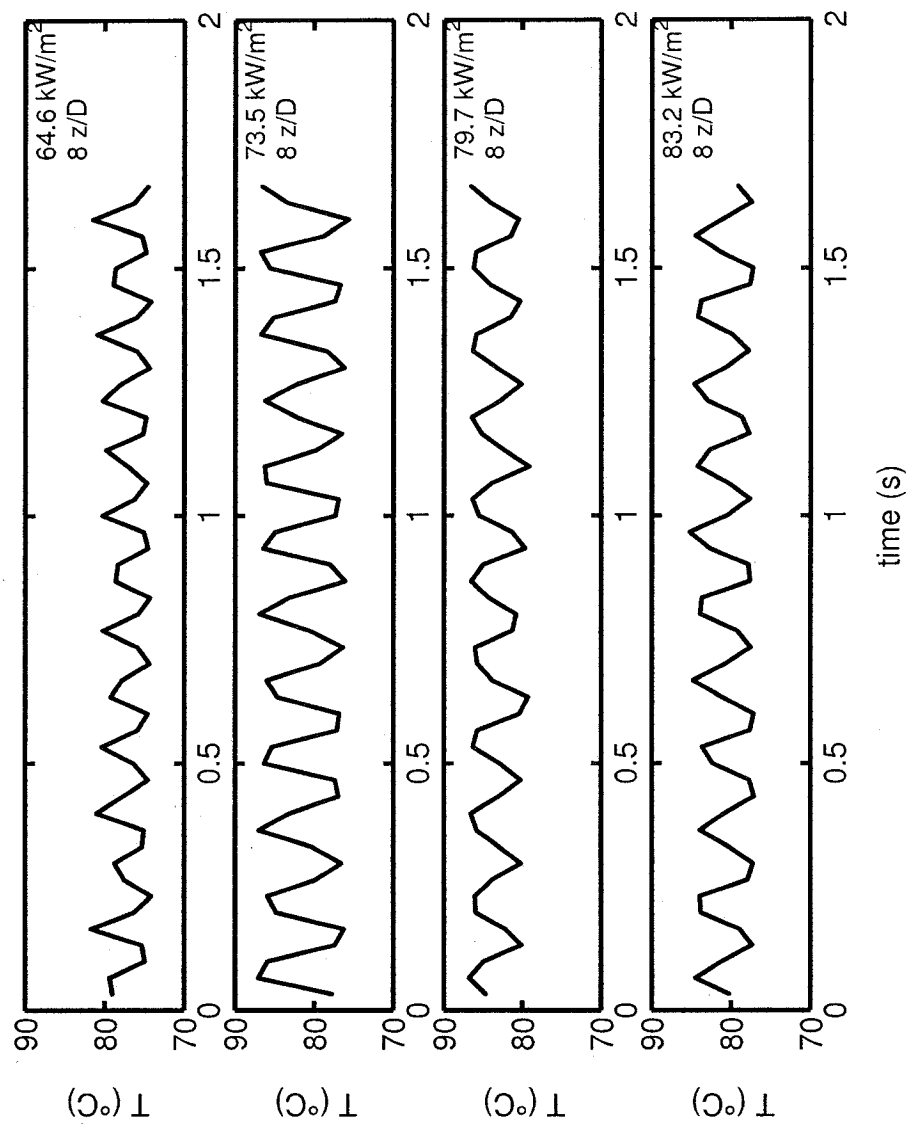
Figure 5.18: Wall temperature time trace at a fixed location with increasing heat flux.

30 Hz. Image capture at higher frequencies is therefore required to ascertain the correct trend. Figure 5.19 shows a sample of data at two different heat fluxes at the same location of 32 z/D. The frequency spectrum show a decrease with increased heat flux. At this high heat flux, the response still remains periodic, however, at the same condition far downstream, there is a significant rise in wall temperature and a large fluctuating wall temperature gradient front is observed. Figure 5.20 shows a sample of this front over a time period of 0.3 s. From 0 to 0.167 s wall temperature fluctuations are observed within the range of the TLC. The wall temperature gradient at this point is mild. From 0.2 s to 0.3 s a rapid rise in temperature is observed as the clearing point of the TLC is exceeded. This signifies a large temperature gradient. These conditions are observed at the point where the wall temperature begins to increase after the constant wall temperature region in Figure 5.13. With a further increase in heat flux the large temperature gradient front continues to move further upstream. Figure 5.21 shows a sample of the temperature gradient front at a higher heat flux and thus moved further upstream. For the duration of the time period it remains at the same location, however, a few milliseconds later its position may shift and return to the location. Upstream of the front location, however, change in the color of the TLC is observed showing that the wall temperature is fluctuating at a lower level. This large temperature gradient front suggests conditions of partial dryout inside the tube in the vicinity of the front. An important point to note during these oscillations is that there were no oscillations in mass flux, and the fluid bulk temperature at inlet and outlet remained relatively constant. The pressure, however, fluctuated at relatively small amplitude. The low pressure drop fluctuations, as well the lack of mass flow

119
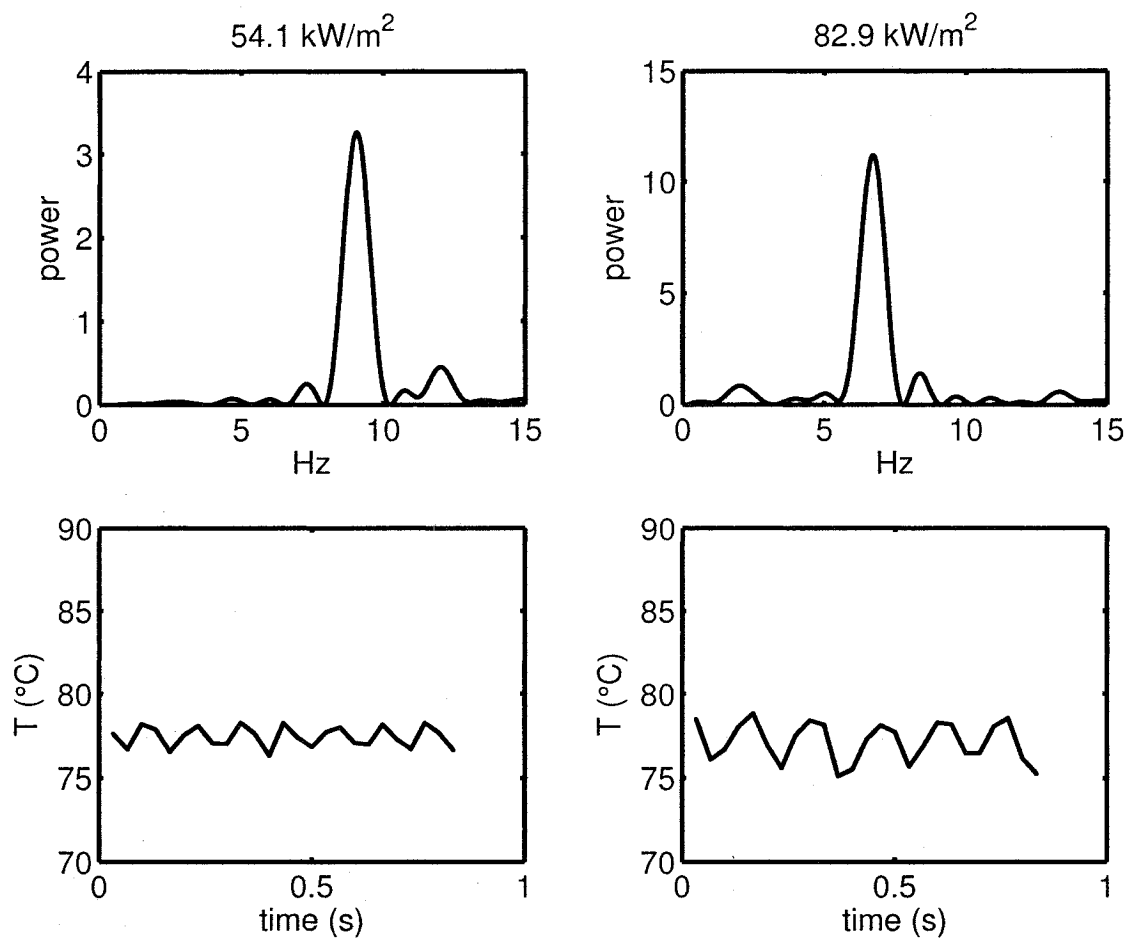
Figure 5.19: Wall temperature oscillations and corresponding power spectrum with increasing heat flux, taken at a distance of approximately 32 z/D.
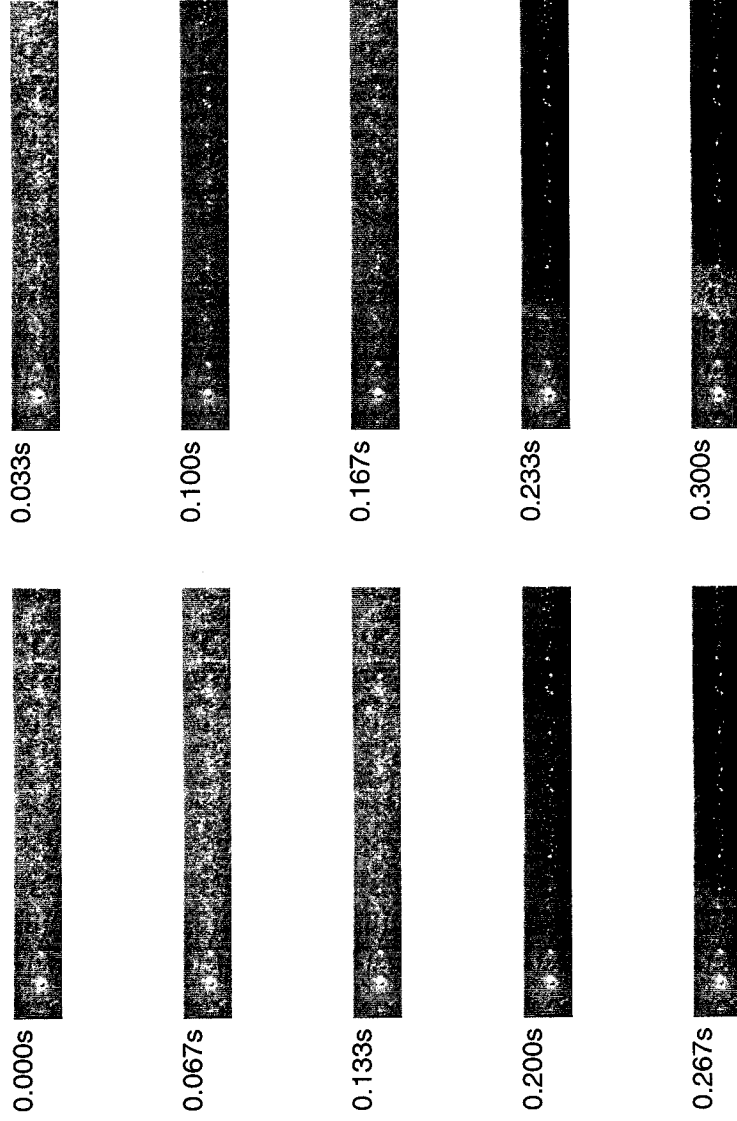
Figure 5.20: Wall temperature fluctuations highlighting oscillatory behaviour and high wall temperature gradient front. Red is cool and blue is hot, black is high temperature past the clearing point of the TLC. Covering a time span of 0.3 s, at 78 z/D to 88 z/D and $q'' = 79$ kW/m^2, $G = 770$ kg/(m$^2 \cdot$ s), and flow is from left to right.
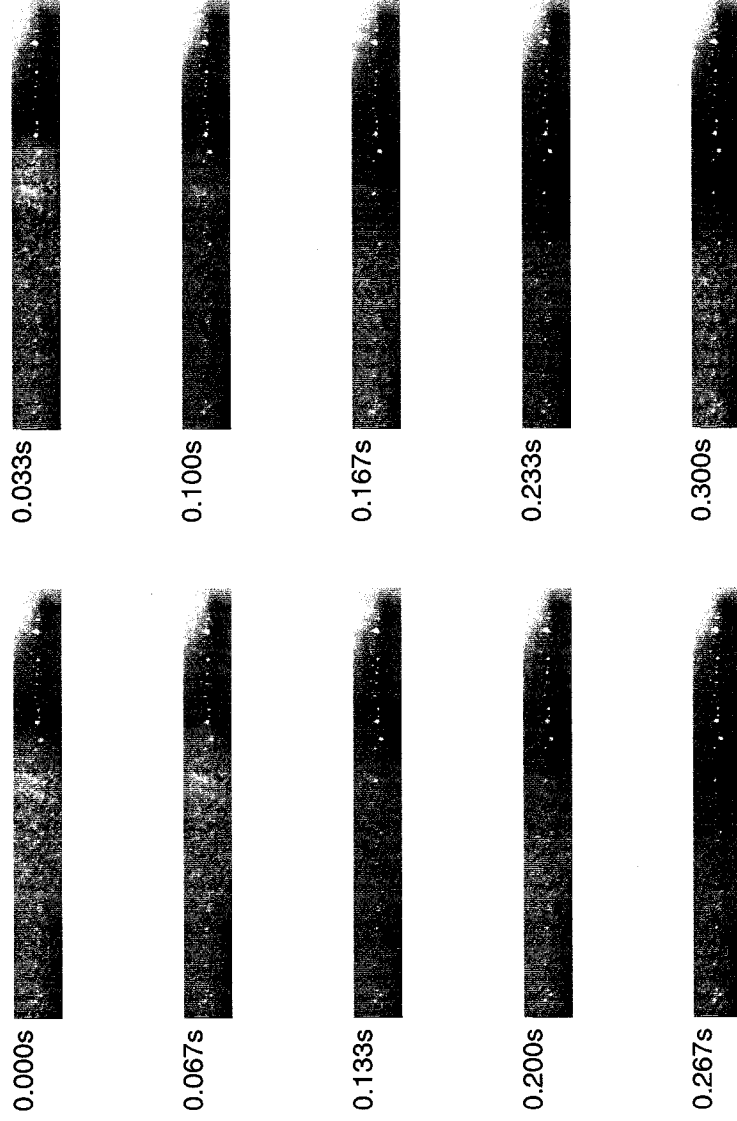
Figure 5.21: Wall temperature fluctuations highlighting oscillatory behaviour and high wall temperature gradient front. Red is cool and blue is hot, black is high temperature past the clearing point of the TLC. Covering a time span of 0.3 s, at 70 z/D to 78 z/D and $q'' = 83$ kW/m^2, $G = 770$ kg/(m$^2 \cdot$ s), and flow is from left to right.

fluctuations, suggest that these are neither pressure drop nor density instabilities. Ding et al. (1995) presented the various dynamic instabilities that may be present in a horizontal tube. Their discussion on thermal oscillations suggests that high wall temperature fluctuations will be present. Additionally, the characteristics of the thermal oscillations are initiated at the transition from a thin liquid film to an all vapour region that may oscillate due to frequent impulses of purged vapour slugs from upstream. Although at upstream locations the wall temperature oscillations are on the order of 10 °C at maximum, at the oscillating front the wall temperature gradient is likely greater than 20 °C, which is high and therefore more representative of thermal oscillations. This suggests that the mechanism responsible for the oscillations is similar to that for thermal oscillations, whereby there exists a thin film of liquid that oscillates due to bubbles being purged at the interface. This is corroborated by the fact that just upstream of the interface the wall temperature fluctuates suggesting a passing vapour slug. These observations, however, need further verification by means such as flow visualization. Nevertheless, the advantage of a thermographic technique has been highlighted in the present measurements. The spatial correspondence of discrete fluctuating signals (pixels) over time could be observed and their relationship identified as a likely vapour liquid interface. Therefore the TLC's have inadvertently provided a means of flow visualization.

5.2.5 Two-Phase Flow Heat Transfer Coefficient

To determine the two-phase heat transfer coefficient, accurate wall and fluid bulk temperature measurements are required. As mentioned earlier, determination of the fluid bulk temperature in the two-phase region is based on a linear pressure drop assumption. Additionally, accurate determination of the zero quality location requires an effective energy balance. Figure 5.22 (a-e) presents samples of the wall temperature, as well as the calculated fluid bulk temperature at incremental levels of heat flux and at a mass flux of 770 kg/(m² · s). The wall temperature is a spanwise average of 72 pixels and has been down sampled for presentation. It is compiled from snapshots at a number of locations along the tube with each location spanning 640 pixels or approximately ten diameters. Identified in the figure is the zero quality location calculated based on an energy balance. Typical in all figures is an almost constant, but slightly decreasing wall temperature in the two-phase region. In the single phase region of Figures 5.22 (d) and (e), the wall temperature rises then falls, typical of what is seen during onset of subcooled boiling. There is scatter within the data and this is partially due to the time variance of the data. The data during high heat flux when significant wall temperature variations were present and where the liquid crystal clearing point was exceeded are not included.

Figure 5.23 presents the heat transfer coefficient at two different heat fluxes and mass fluxes as a function of quality. Similar to the wall temperature measurements, they are determined by a spanwise average of 72 pixels and down sampled for presentation. In the region leading up to the zero quality location, the heat transfer

124
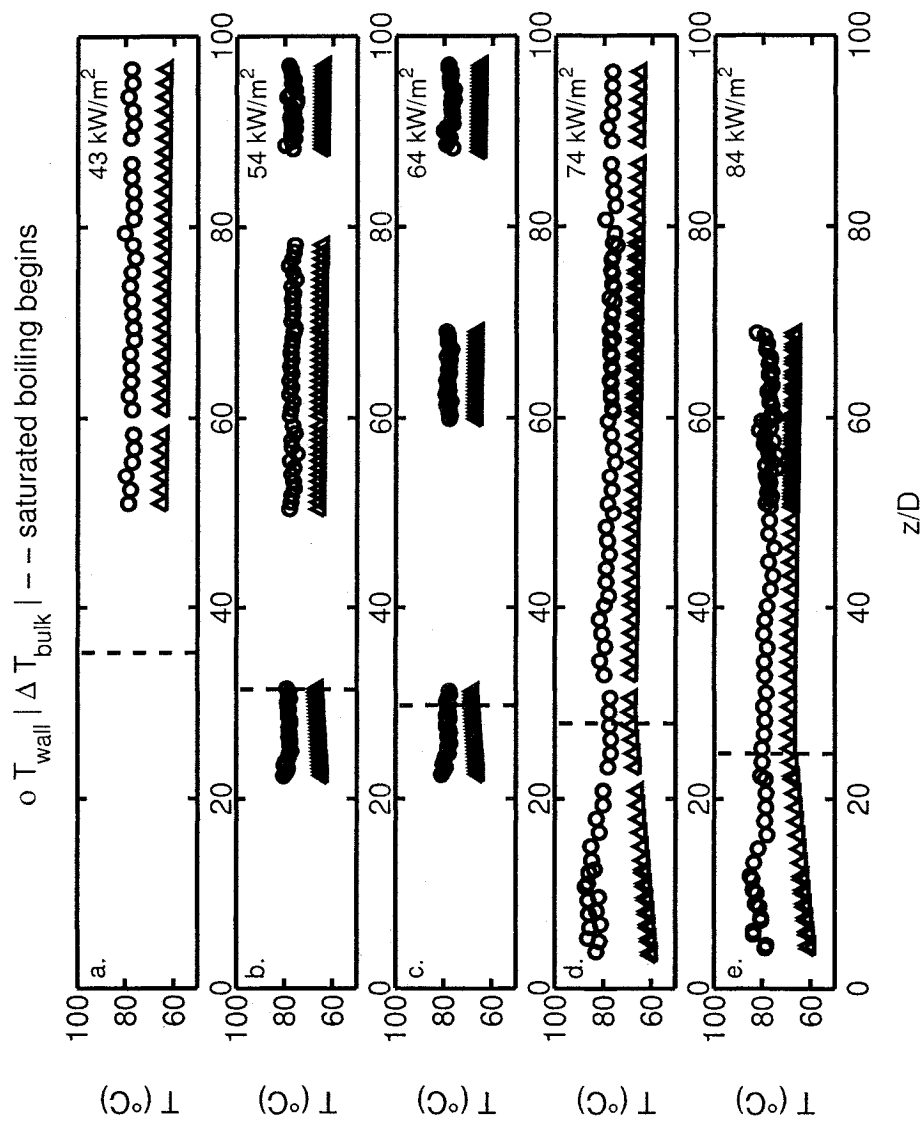
Figure 5.22: Measured circumferentially averaged wall temperature and calculated fluid bulk temperature along tube for varying heat fluxes, $G = 770$ kg/(m² · s).

125
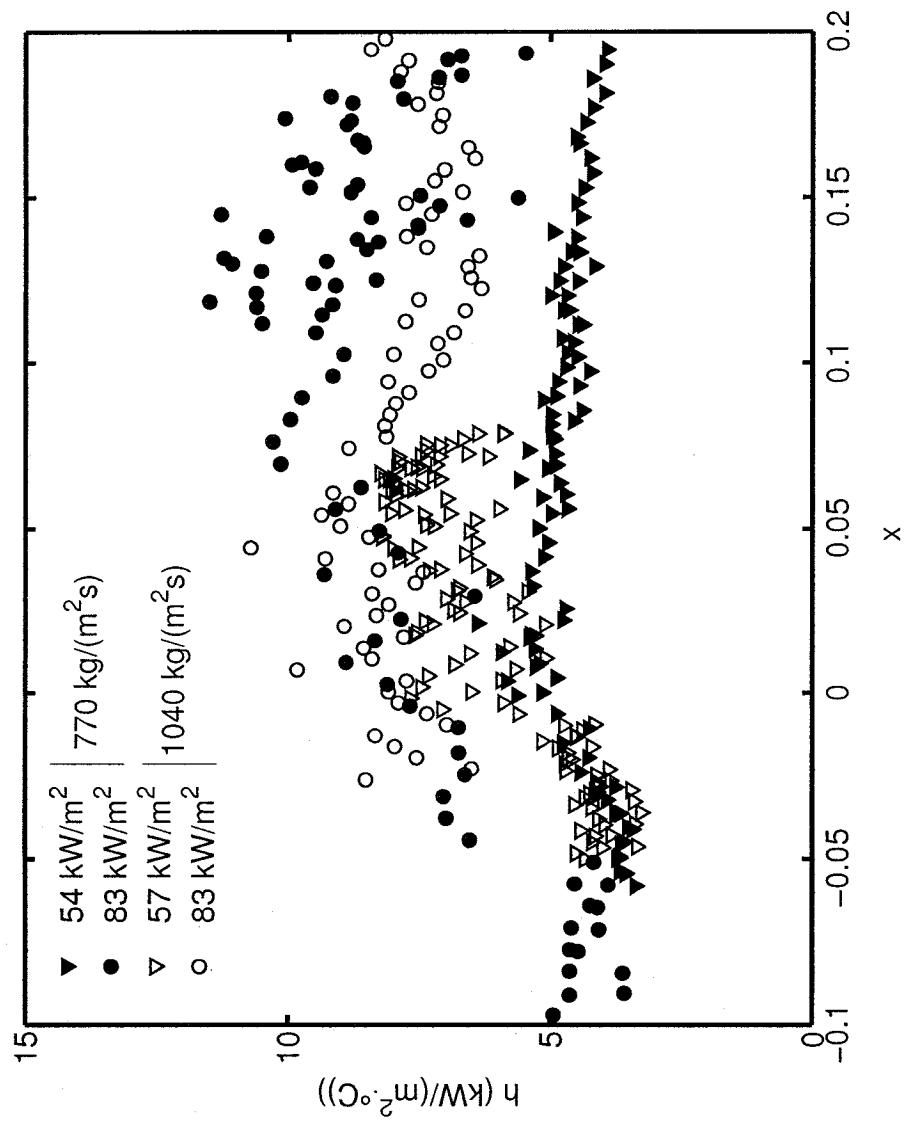
Figure 5.23: Local heat transfer coefficient as a function of quality, effect of heat flux and mass flux.

coefficient rises rapidly. With increasing heat flux, the heat transfer coefficient increases when the quality is greater than zero. The increase for a mass flux of 1043 $kg/(m^2 \cdot s)$ is not as significant for as for the lower case of 770 $kg/(m^2 \cdot s)$. With the exception of the low mass flux, high heat flux case ($q'' = 83$ kW/m^2, $G = 770$ $kg/(m^2 \cdot s)$), the heat transfer coefficient has a mild decrease with increasing quality. Finally, at a given heat flux the influence of mass flux is mild. For the low heat flux case, the heat transfer coefficient increases slightly with increased mass flux, whereas for the high heat flux case there is a slight decrease in the heat transfer coefficient with increased mass flux. However, at this high heat flux case, there is significant scatter in the dataset, and looking back at the wall temperature trend in Figure 5.22 (e), it is expected that the heat transfer coefficient should be displaying the same trend as the other higher mass flux dataset.

In observing the trends of the lower mass flux case ($G = 770$ $kg/(m^2 \cdot s)$), these data suggest a nucleation dominated region at low quality, with the heat transfer coefficient being a strong function of the heat flux and a weak function of the mass quality. These trends were typical for the other heat flux values at this mass flux. For the higher mass flux case ($G = 1040$ $kg/(m^2 \cdot s)$), the heat flux influence on the heat transfer coefficient is less significant, however, and this was typical for other heat flux cases at this mass flux. It is noted that the data obtained during the large temperature gradient fronts are not presented as they are out of range of the TLC, as well they would be accompanied with significant time variance. However, if wall temperature measurements were available they would show a significant decrease in the heat transfer coefficient in the range of quality greater than 0.35.

127

Figures 5.24 and 5.25 compare the measured heat transfer coefficient with three different correlations. The first correlation is given by Kandlikar (1990) and Kandlikar and Balasubramanian (2004). It is based on a variety of working fluids and working conditions, and for channel diameters ranging from 4 mm to 32 mm (Kandlikar, 1990). It has been modified from its original form to account for flow in minichannels $(0.20 \text{ mm} \leq D_h \leq 3.0 \text{ mm})$ in the laminar and transitional range (Kandlikar and Balasubramanian, 2004). Flow is considered in the transitional range if $1600 \leq Re_f \leq 3000$, which are the conditions of the presented data. The correlation is,

$$h_{tp} = \text{larger of } (h_{tp,NBD} \text{ and } h_{tp,CBD}), \tag{5.8}$$

where, NBD denotes nucleation boiling dominated and CBD denotes convection boiling dominated. Each term is,

$$h_{tp,NBD} = 0.6683 Co^{-0.2} (1-x)^{0.8} h_f + 1058.0 Bo^{0.7} (1-x)^{0.8} F_{Fl} h_f \tag{5.9a}$$

$$h_{tp,CBD} = 1.136 Co^{-0.9} (1-x)^{0.8} h_f + 667.2 Bo^{0.7} (1-x)^{0.8} F_{Fl} h_f \tag{5.9b}$$

$$Co = \left(\frac{1-x}{x}\right)^{0.8} \left(\frac{\rho_v}{\rho_f}\right)^{0.5} \tag{5.9c}$$

where, F_{fl} is a fluid to surface relating term and for stainless steel tubes with any fluid is 1.0 (Kandlikar and Balasubramanian, 2004). For the transitional regime, it is recommended to use a single phase heat transfer coefficient based on a linear interpolation between laminar and turbulent flow. In the present work, h_f has been
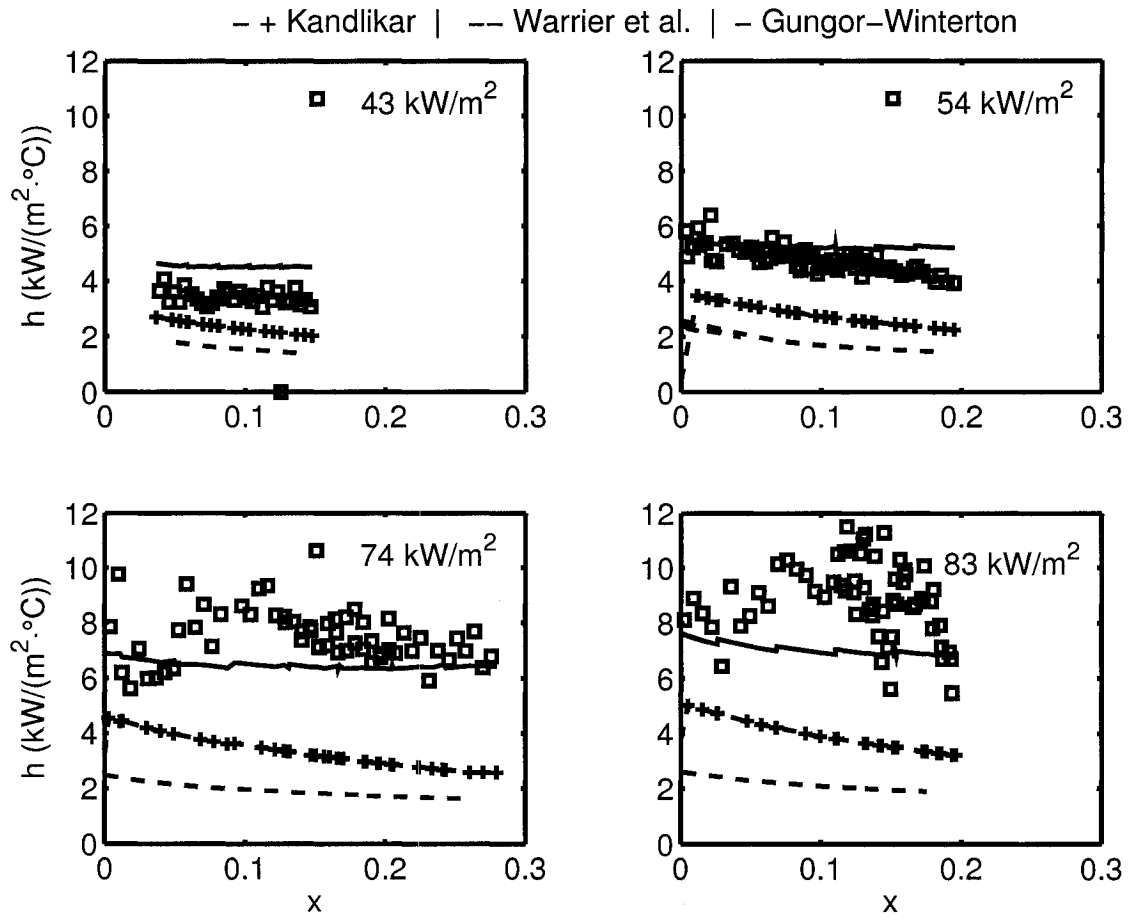
Figure 5.24: Local heat transfer coefficient, comparison with correlations at various heat fluxes, $G = 770 \text{ kg}/(\text{m}^2 \cdot \text{s})$.
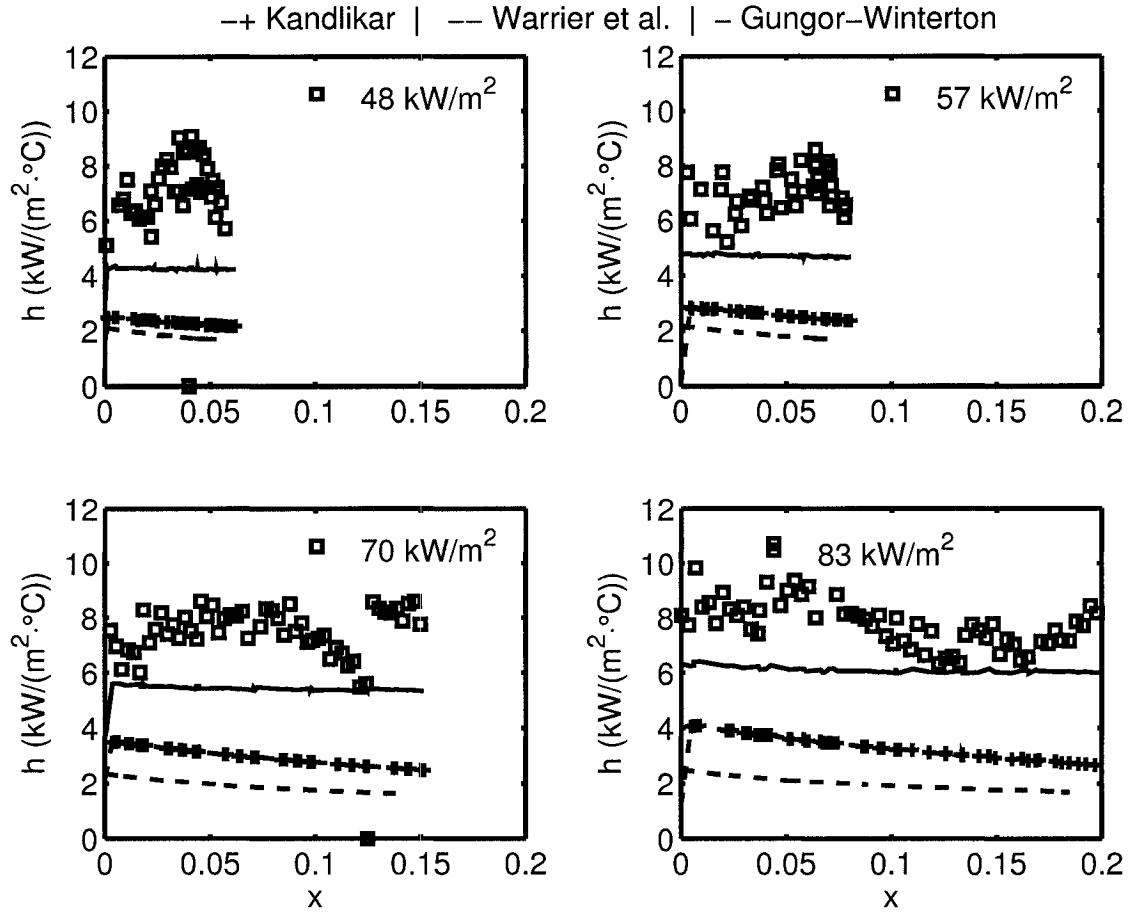
Figure 5.25: Local heat transfer coefficient, comparison with correlations at various heat fluxes, $G = 1040$ kg/(m$^2 \cdot$ s).

taken as that based on the analytical solution for laminar thermally developing flow.

The second correlation by Warrier et al. (2002) was selected as it is based on a working fluid with similar chemical structure, FC-84. However, the geometry used in the study was composed of five parallel rectangular channels of 0.75 mm hydraulic diameter. The correlation is given by,

$$\frac{h_{tp}}{h_f} = 1 + 6.0 Bo^{1/16} \left[-5.3 \left(1 - 855 Bo \right) \right] x^{0.65}. \tag{5.10}$$

The single-phase liquid heat transfer coefficient (h_f), is for fully developed flow, however, it was taken as the thermally developing value for the present analysis. The third correlation by Gungor and Winterton (1986) is based on a database covering a variety of fluids for channel diameters ranging from 2.95 mm to 32.00 mm, and under a variety of channel orientations. It is,

$$h_{tp} = E h_f + S h_{ncb} \tag{5.11a}$$

$$h_{ncb} = 55 P_r^{0.12} \left(-0.4343 \ln \left(P_r \right) \right)^{-0.55} M^{-0.5} \left(Q/A \right)^{0.67} \tag{5.11b}$$

$$E = 1 + 24,000 Bo^{1.16} + 1.37 \left(\frac{1}{X_{tt}} \right)^{0.86} \tag{5.11c}$$

$$S = \left(1 + 1.15 \times 10^{-6} E^2 \mathrm{Re}_f^{1.17} \right)^{-1} \tag{5.11d}$$

$$X_{tt} = \left(\frac{1-x}{x} \right)^{0.9} \left(\frac{\rho_v}{\rho_f} \right)^{0.5} \left(\frac{\mu_f}{\mu_v} \right)^{0.1}. \tag{5.11e}$$

The parameter E is an enhancement factor of the single phase heat transfer and S is a suppression factor for the pool boiling term. The single phase heat transfer coefficient (h_f) is defined based on the Dittus-Boelter correlation (Gungor and Winterton, 1986) for turbulent flow. However, in the present as with the previous cases, it has been modified with the thermally developing laminar flow analytical solution. Due to lack of data on vapour phase viscosity of FC-72, this term was taken as 1.0. As shown in Figures 5.24 and 5.25, both the correlation of Equations 5.8-5.9 and Equation 5.10 under predict the heat transfer coefficient for all cases of heat fluxes, though Equations 5.8-5.9 are closer in magnitude. The trends presented by both correlations however are very similar to that observed in the data of Figure 5.24 ($G = 770$ kg/(m$^2 \cdot$ s)), showing a slight decrease in heat transfer coefficient with increasing quality. For this lower mass flux case also, the correlation by Equation 5.11 provides a good measure of the magnitude of the heat transfer coefficient for the middle range of heat fluxes, however, it over predicts and slightly under predicts the data for the low and high heat flux cases respectively. For the higher mass flux case shown in Figure 5.25 however, the correlation from Equation 5.11 consistently slightly under predicts the heat transfer coefficient. The correlation of Equations 5.8-5.9 contains a nucleate boiling dominated form $(h_{tp,NBD})$ and a convective boiling dominated form $(h_{tp,CBD})$. For the conditions in the present work it was found that the nucleate boiling dominant form of the equation prevailed for the majority of the instances, particularly at the lower mass flux case (770 kg/(m$^2 \cdot$ s)). On the other hand, the correlation in Equation 5.11 contains a nucleate boiling component (Sh_{ncb}) and a convective boiling component (E_{hf}) and in general had the best agreement with the results in terms of magnitude.

It was found that the total heat transfer coefficient from this correlation was dominated by the convective boiling component which accounted for 60 to 70% of its value. The lack of correspondence of the correlations confirms that additional studies are still required as has been mentioned by many other researchers. Additionally with a variety of fluids to expand the correlation versatility, as has been demonstrated by the lack of fit with present data.

5.3 Summary

Through use of un-encapsulated liquid crystals, local single phase heat transfer measurements have been performed in small diameter tubes of nominal size 0.254 mm, 0.512 mm and 1.067 mm, covering the laminar, transitional and turbulent regimes. The results demonstrate that the conventional size channel analytical solution for laminar flow is adequate for predicting the local heat transfer in thermally developing flows inside sub-millimeter size circular tubes over the range studied.

Local Nusselt numbers in the turbulent regime are shown to have a developmental length less than approximately 10 z/D, which is similar to conventionally sized tubes in this Prandtl number range. Considering uncertainties in Nusselt number correlations and the present data, both the conventional correlation by Gnielinski (1976) and the microchannel correlation by Adams et al. (1998) are adequate for predicting averaged Nusselt numbers in circular tubes with diameters ranging from 0.25 mm to 1 mm, for $2500 \leq Re \leq 10^4$ and Prandtl numbers ranging from 5.4 to 11.5. Finally, the choice of the correlation should be based on the amount of conservatism required

in the design.

The investigation of flow boiling heat transfer of FC-72 in a 1.067 mm tube through use of liquid crystal thermography has been presented. Local heat transfer data are presented for a low mass flux (770 kg/(m$^2 \cdot$ s) and 1040 kg/(m$^2 \cdot$ s)) and a low inlet subcooling, partially because boiling initiation was not observed at other conditions. At these low mass flux cases, a unique phenomenon at boiling onset was observed, whereby a large temperature gradient front moved towards the exit of the tube with a cooler wall temperature behind it. This observation was enabled due to the use of a thermographic technique for wall temperature measurement.

Under two-phase conditions the wall temperature was observed to oscillate for a wide range of heat fluxes. The amplitude ranged from 1 °C to 7 °C for a low heat flux with the frequency around 10 Hz. At high heat flux, large oscillatory wall temperature gradients were observed in the form of wall temperature gradient fronts. The nature of these large gradient oscillations suggests an oscillating partial dryout regime. Although flow visualization was not directly performed, the use of a thermographic technique has inadvertently provided a means for partial flow visualization.

Local heat transfer coefficient data were presented for a quality up to approximately 0.3. In the range of heat flux covered, the heat transfer coefficient is dependent on heat flux, but only mildly influenced by quality at a lower mass flux of 770 kg/(m$^2 \cdot$ s). At a higher mass flux of 1040 kg/(m$^2 \cdot$ s), the heat transfer coefficient is less dependent on heat flux. When compared with some relevant correlations, none can accurately predict the observed magnitude and trend over the entire range of heat fluxes.

Chapter 6

Transport Phenomena in a

Cross-Linked Heat Sink

This chapter presents the flow and heat transfer characteristics in a cross-linked microchannel heat sink. The aim of the cross-links is to address the issue of flow boiling instabilities and flow maldistribution. The cross-linked geometry is similar to a standard microchannel heat sink with parallel channels, except that cross-linked paths are introduced at three locations along the channels. The purpose of the gaps is to allow fluid communication between channels at additional points other than entry or exit of the channels.

6.1 Design

For the detailed design and sizing of the cross-linked heat sink concept, a one-dimensional thermal resistance model was utilized based on a design target. Additional constraints are introduced based on manufacturing limitations. The design target is motivated by thermal control for micro/nano- spacecrafts. From Paris et al. (2002), who developed a pumped cooling loop for this application, future demands will be required to manage power densities of 25 W/cm^2, over a 3.5 cm^2 footprint area (87.5 W over the footprint), while maintaining a chip temperatures below 85 °C. The footprint area is considered in the present work as the area directly above the microchannels. The channels are to be manufactured via deep reactive ion etching (DRIE) as it allows for a wider variability of shapes. The manufacturing constraints are a silicon wafer thickness of 550 μm and a maximum DRIE etch depth of 300 μm, with an aspect ratio of width to depth not exceeding 1:50. Additional constraints are that the working fluid is single-phase water and a maximum pressure of 34.5 kPa (5 psi) is available for the entire loop.

Within the model, the heat transfer coefficient is calculated considering steady, laminar, hydrodynamically and thermally fully developed flow, in a rectangular duct with constant wall temperature at three walls and the fourth wall adiabatic. The Nusselt number, which is based on the wetted perimeter hydraulic diameter, is obtained from Shah and London (1978) in tabular form, and intermediate values are based on interpolation. The pressure drop is modeled considering only the channels, that being the heat sink channel core, the channel inlet and the channel outlet. Similar to

136

the heat transfer results, the flow is considered fully developed, laminar and steady. In addition, entry and exit loss factors are included.

The parameters to be determined include the channel width, and the length and width of each cross-linked section. The number of channels is determined from the channel width. From the literature, the influence of the cross-links on pressure drop and heat transfer compared to a straight channel is not clear and so a conservative approach is taken. In doing so, each length of channel section is considered a new channel and therefore has an inlet and outlet pressure loss attributed. For the thermal component, the area comprising the gap space is considered to have a heat transfer coefficient equivalent to 50% of the main passages. Results from the analysis are shown in Figure 6.1. Comparing the pressure drop (Fig. 6.1 (a)) and maximum surface temperature (Fig. 6.1 (b)) for different cross-link widths and number of cross-links, only very slight differences are observed. In both cases, however, minimizing the number of cross-links results in better performance. As an initial iteration for the research program, the number of cross-links has been set to three, with the width of the cross-links equal to the determined channel width.

Figure 6.1 (c) and 6.1 (d) show the resulting pressure and temperature isotherms as a function of the channel width and flowrate, at heat fluxes of 25 W/cm^2 and 50 W/cm^2. At the lower heat flux, a wide range of channel widths meet the design target of 85 °C with a pressure drop less than 5 psi. At the higher heat flux, channel widths less than 300 μm with flowrates greater than 100 ml/min meet the target. Although the pressure penalty with increasing flowrate is not significant, the benefit gained for the target isotherm of 85 °C is limited for widths greater than 300 μm. A channel

137
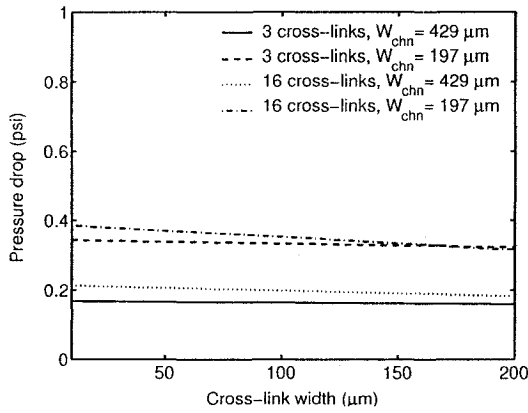
(a) Pressure drop versus cross-link, width, 30 ml/min.
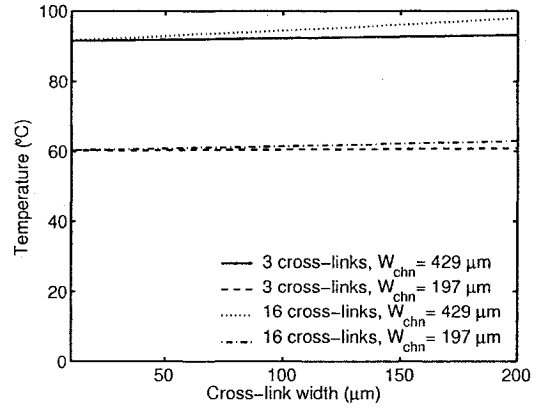
(b) Maximum surface temperature versus cross-link width, 30 ml/min.
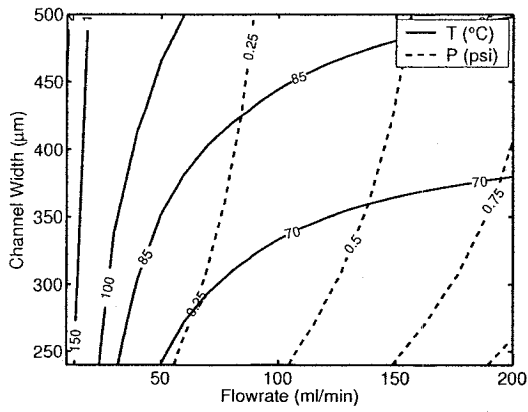
(c) Channel width versus flow rate, $q'' = 25$ W/cm^2.
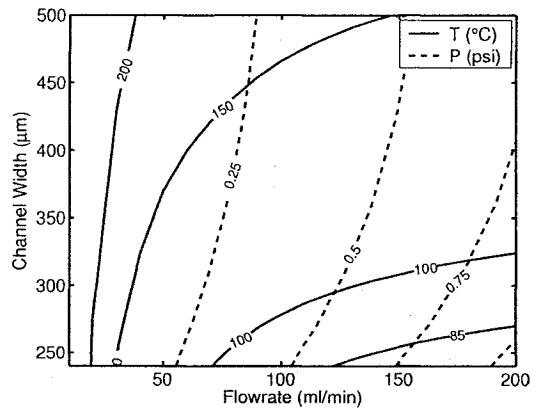
(d) Channel width versus flow rate, $q'' = 50$ W/cm^2.

Figure 6.1: Cross-link concept analysis results.

width of 250 μm is selected as it can comfortably meet the design target and future requirements.

The finalized design is presented in Figure 6.2. The heat sinks were fabricated at the Washington Technology Center's Microfabrication Lab. They are are fabricated from silicon wafers 500 μm thick. A silicon dioxide (SiO_2) layer is deposited on the backside for electrical isolation. A serpentined platinum heating element, 1 mm wide and 186 mm long, is deposited on the backside of the channel base to simulate the heated chip. The heating element has been designed for a nominal resistance of 90 Ω, with a potential applied serially through the entire length of the serpentine. However, the actual resistance was found to be approximately 16 times greater. To account for this, the potential is applied in parallel through the 11 strips of the serpentine. A Pyrex wafer (Corning 7740) of thickness 350 μm seals the chamber and is bonded to the silicon base piece containing the channels. The cover has eight 1 mm diameter holes etched for flow inlet and outlet.

6.2 Heat Sink Packaging

6.2.1 Packaging Method I

Figure 6.3 shows the first heat sink support with the inlet and outlet chambers, and the pressure and temperature taps. The support is fabricated from Teflon due to its high temperature limits, as well as its low thermal conductivity and high electrical resistance. The chips were originally intended to be directly mounted to the Teflon
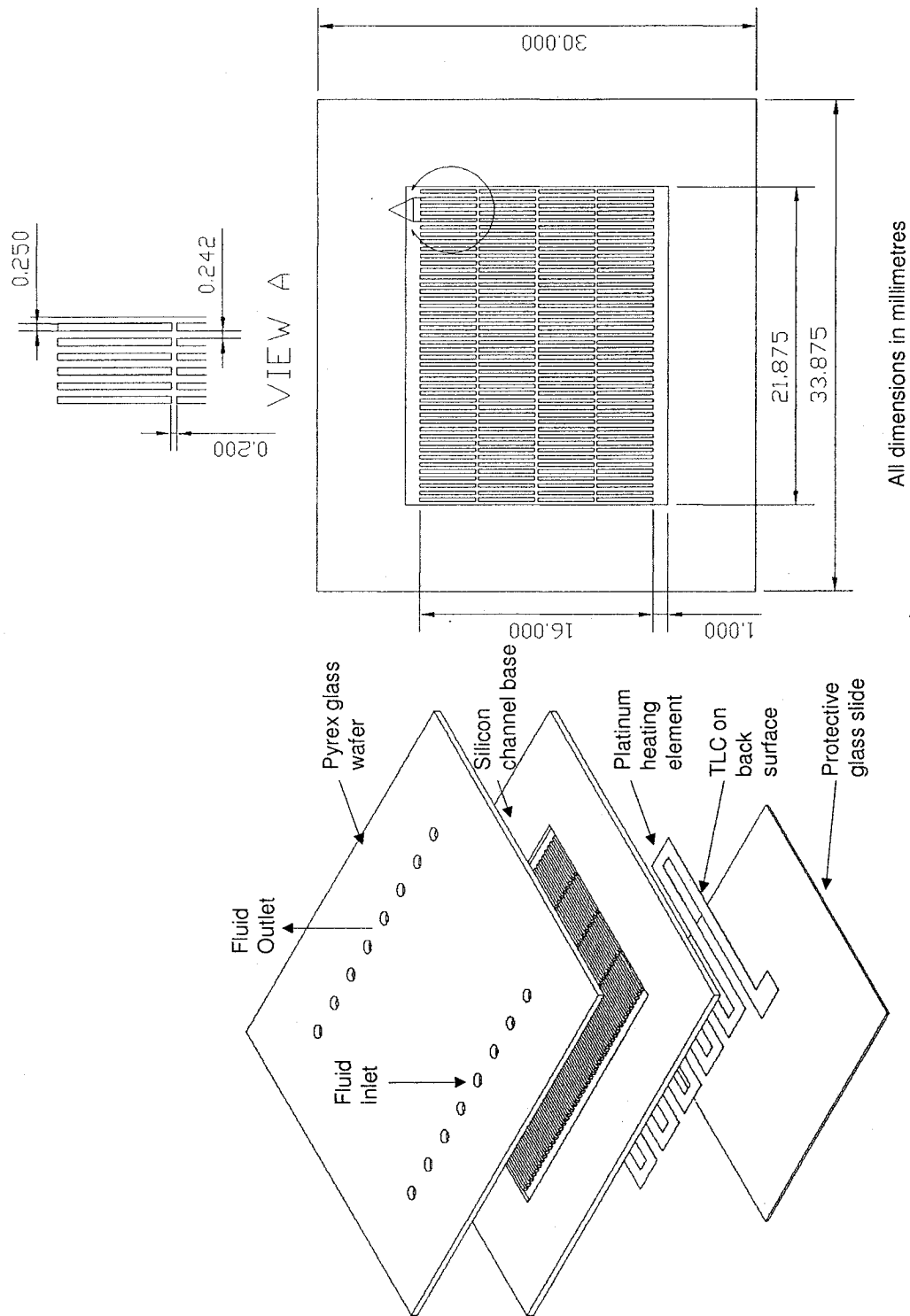
Figure 6.2: Cross-linked heat sink.

Polycarbonate Midplate
(12.7 mm thick)

From
Heat
Sink

To
Heat
Sink

Fluid
Outlet

8.5 mm

Inlet / Outlet
Temperature
and Pressure
ports on both
sides

24 mm

Fluid
Inlet

Teflon
Support
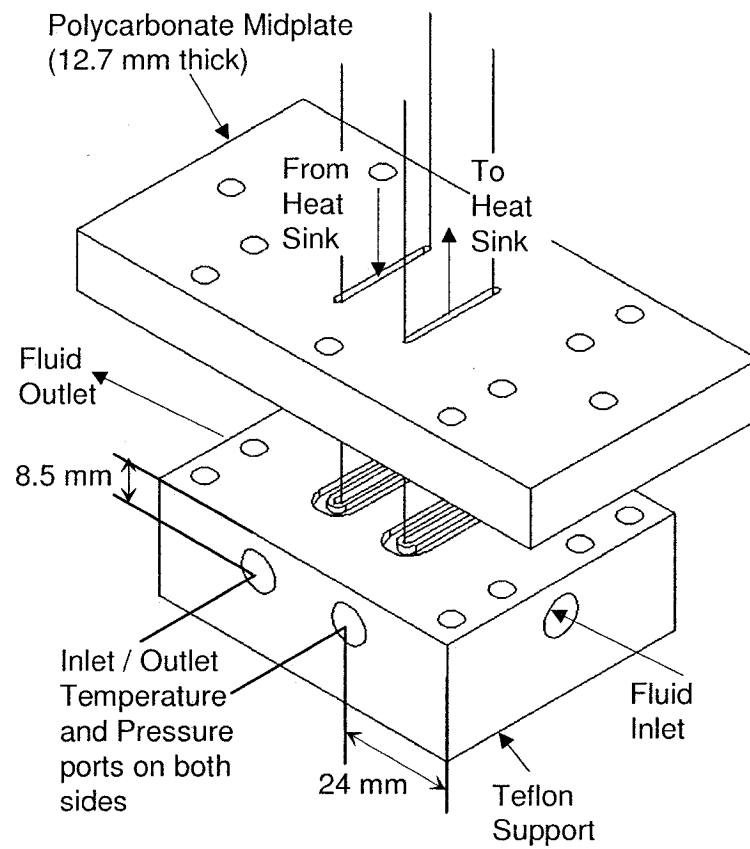
Figure 6.3: Heat sink support I.

base piece with gaskets for sealing. However, during sealing attempts the chips easily broke, if misaligned when applying the required compressive loading for the gaskets. Rather then, a rigid midplate with two slots for fluid transfer is introduced for the chips to be permanently bonded onto, before transferring to the Teflon base. This midplate, which is easily handled, is sealed to the Teflon base using a silicone based adhesive with a high temperature limit, or gaskets. The midplate is transparent to verify that the sealant between the chips and the midplate does not leak into the heat sink port holes. Clear polycarbonate is selected due to its higher temperature limits. The vertical distance from the sensor ports to the heat sinks is 21.2 mm.

6.2.2 Packaging Method II

The second support, shown in Figure 6.4, was designed to allow for flow visualization and micro-PIV experiments. All parts are manufactured from transparent polycarbonate to provide sufficient temperature limits with optical access. A top plate, 3.18 mm (1/8" sheet) thick, supports the heat sink. A second base plate, also 3.18 mm thick, has a 1.59 mm slot machined to allow fluid transport from the pressure / temperature measurement ports to and from the heat sink. Thin plates are utilized to accommodate the working distance of the microscope objectives available. The plates and the instrument chambers are bonded together using a polycarbonate cement (SC-325 Cadillac Plastic and Chemical Company) and a transparent UV curing adhesive recommended for elevated temperatures with moisture content. The heat sinks are bonded to the top plate using the same UV curing adhesive.
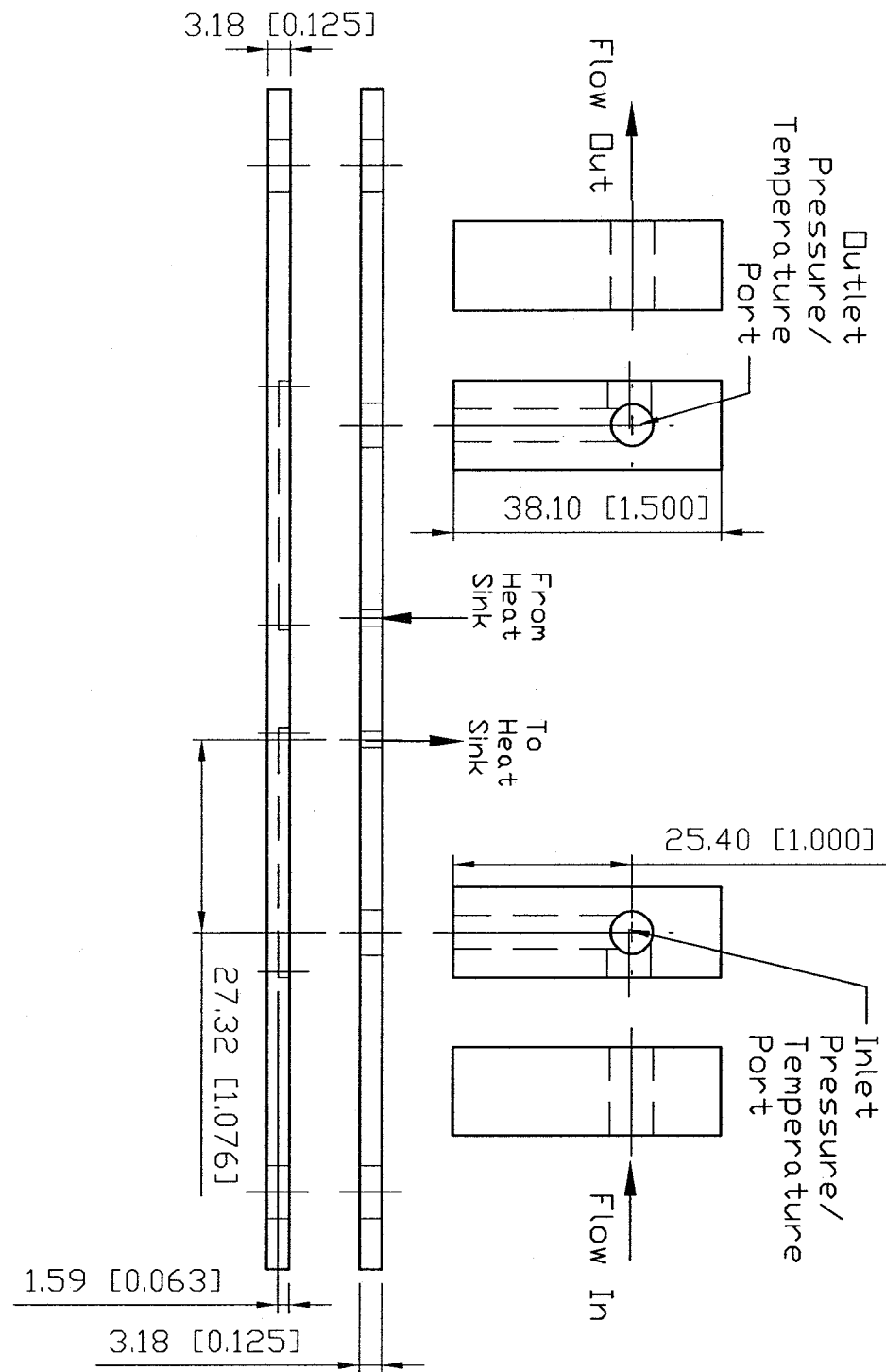
Figure 6.4: Heat sink support II, millimeters [inches].

6.3 Single Phase Flow

6.3.1 Methods and Data Reduction

Pressure Drop

The pressure taps are located at some distance from the channel inlets and exits, and so contain additional pressure components due to the inlet and outlet chamber circuitry. These are accounted for through loss factors (K_i) for area changes and bends and are obtained from Munson et al. (2002). Additional losses will be incurred due to the channel entry and exit and flow acceleration. These are estimated using the methodology outlined by Kays and London (1964) for flows in compact heat exchangers. Finally, as the flow at entry is not fully developed, this is also considered. In summary the pressure drop in the channels (ΔP_{chn}) is obtained as follows,

$$
\begin{aligned}
\Delta P_{Measured} \quad = \quad & \Delta P_{chn} \\
& + \left[\xi_{in} + 2 \left(\frac{\rho_{in}}{\rho_{out}} - 1 \right) - \frac{\rho_{in}}{\rho_{out}} \xi_{out} + K_\infty \right] \frac{(\rho u^2)_{chn,in}}{2} \\
& + Minor\, Losses
\end{aligned} \tag{6.1}
$$

where,

$$
\xi_{in} = K_c + 1 - \sigma_{por}^2 \tag{6.2a}
$$

$$
\xi_{out} = 1 - \sigma_{por}^2 - K_e \tag{6.2b}
$$

and

$$\sigma_{por} = \frac{N_{chn} W_{chn} H_{chn}}{W_{total} H_{chn}} \tag{6.3}$$

and where,

$$Minor\,Losses = \sum_j K_j \frac{(\rho u^2)_j}{2} \tag{6.4}$$

The loss factors utilized in the above are from experiments in macro size configurations. These may not be fully appropriate for all the present conditions, particularly for the channel inlet and exit losses. Nevertheless, they are used as there are currently no correlations for micro configurations readily available. For comparison with theoretical predictions, the pressure drop across the channels may be obtained from

$$\Delta P_{chn} = 4f \frac{L}{D_h} \frac{\rho_{in}}{\rho_{mean}} \frac{(\rho u^2)_{chn,in}}{2} \tag{6.5}$$

The friction factor is obtained from Shah and London (1978) for a rectangular duct of fixed aspect ratio as,

$$fRe = 24 \left[1 - 1.3553\alpha + 1.94673\alpha^2 - 1.7012\alpha^3 + 0.9564\alpha^4 - 0.2537\alpha^5\right]. \tag{6.6}$$

The aspect ratio is denoted by α and fRe was calculated to be approximately 14.25 for an aspect ratio of 0.95.

For accurate prediction of the pressure drop, accurate determination of the channel dimensions is required, particularly the cross-section. This may be done through non-destructive and destructive optical measurement, and both are utilized in the present

investigations. In the first case, the width is obtained from a top view image and the depth is obtained from focusing on the top and bottom surfaces. This approach can be expected to provide good measurement of the width, however, the depth measurement will be slightly subjective. The alternative approach is obtaining the dimensions from cross-sections of the heat sink. However, this approach is destructive and therefore not favorable. Both approaches were explored and were found to be in good agreement with each other. Further, significant discrepancies were observed between the design and fabricated heat sink dimensions. A comparison of the design and measured dimensions is shown in Table 6.1. Inspection of the channel cross-sections showed that they are not purely rectangular as assumed in the prediction calculations. At the inlets and exits, the channels have a slight flare as shown in the heat sink top view of Figure 6.5 (a). Due to this flare, the cross sections at the inlet and exits are trapezoidal with taper angles as low as 85 degrees. This characteristic is depicted in Figure 6.5 (b). In the channel core however, the channels are found to not have a strongly tapered angle, but do have curved edges. Figure 6.5 (c) shows a cross section of the core and shows the locations used for approximating the dimensions. These deviations in fabrication have been noted by some other researchers such as Steinke and Kandlikar (2005b), and the present inspection shows the importance of determining the 'as fabricated' channel dimensions. In addition, it is preferable to perform such measurements prior to sealing the heat sink so that destructive testing does not have to be performed, unless the sealing process has an influence on the final dimensions.

Table 6.1: Comparison of design and measured parameters.

	Design	Measured
Channel width	242 μm	269 μm
Channel depth	300 μm	283 μm
Cross-link width	200 μm	269 μm
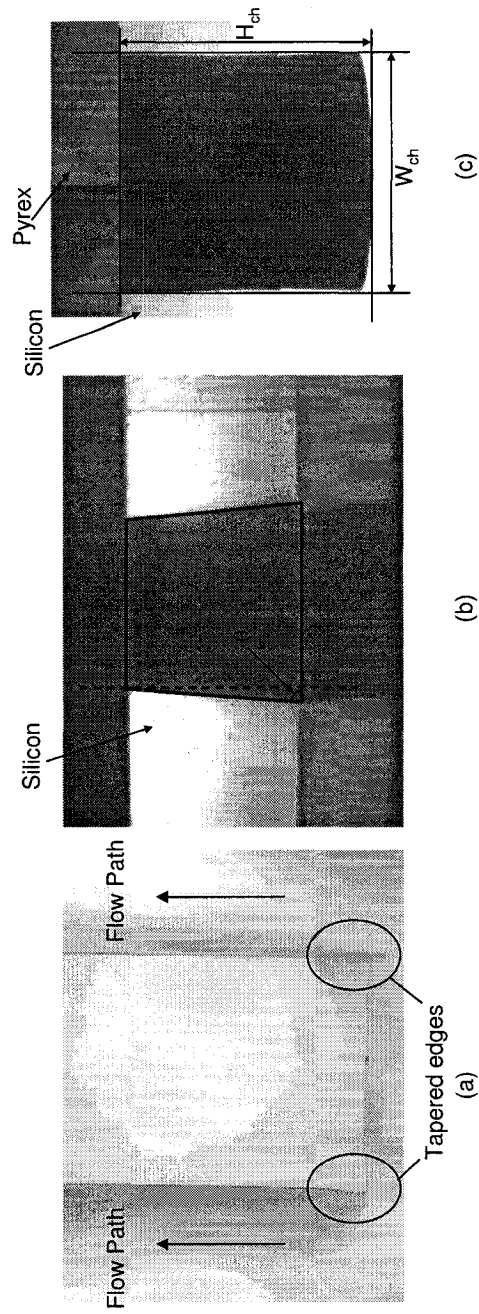
Figure 6.5: Channel inspection (a) Tapered edges, (b) Trapezoidal cross-section at entry/exit, (c) Cross-section in core.

Heat Transfer

The TLC material used has a nominal red start of 40 °C with a bandwidth of 10 °C. Image capture covers a region of 9.94 mm × 7.45 mm yielding a resolution of 10 μm/pixel. To map the entire heat sink, three locations are traversed in the spanwise direction. To enable automated image pre-processing and presentation, regions of the image not active had their pixel values set to zero. This is done by applying a binary filter with the regions marked up manually. On completion, the images from a single case at all four locations are joined in an automated procedure. Where there is overlap, the average pixel value is used. Figure 6.6 shows sample pre-processed TLC mappings of the heated surface. The locations where the image is joined can be observed at $\sim$28 and $\sim$52 y/D_h for some cases and is due to minor error in traverse. The TLC map shows some non-uniformity in the wall temperature. There is a wavy profile in the spanwise direction, and this is due to the heating elements underneath. The color response in Figure 6.6 is highly vibrant when compared to measurements on the microtubes (e.g. Fig. 5.14). This is primarily due to the use of a cover in direct contact with the TLC (glass slide) and also because no overheating of the coating occurred to vaporize it.

Evaluation of the local heat transfer coefficient is through assuming the heat sink to behave as a one-dimensional fin with insulated ends. Such an approach has been presented by Qu and Mudawar (2003), and a similar approach is utilized as follows:

$$q'' W_{cell} L_{plan} = h \left(T_{w,i} - T_b \right) \left(W_{chn} + 2\eta H_{chn} \right) \left(4 L_{chn,sec} \right) \tag{6.7}$$
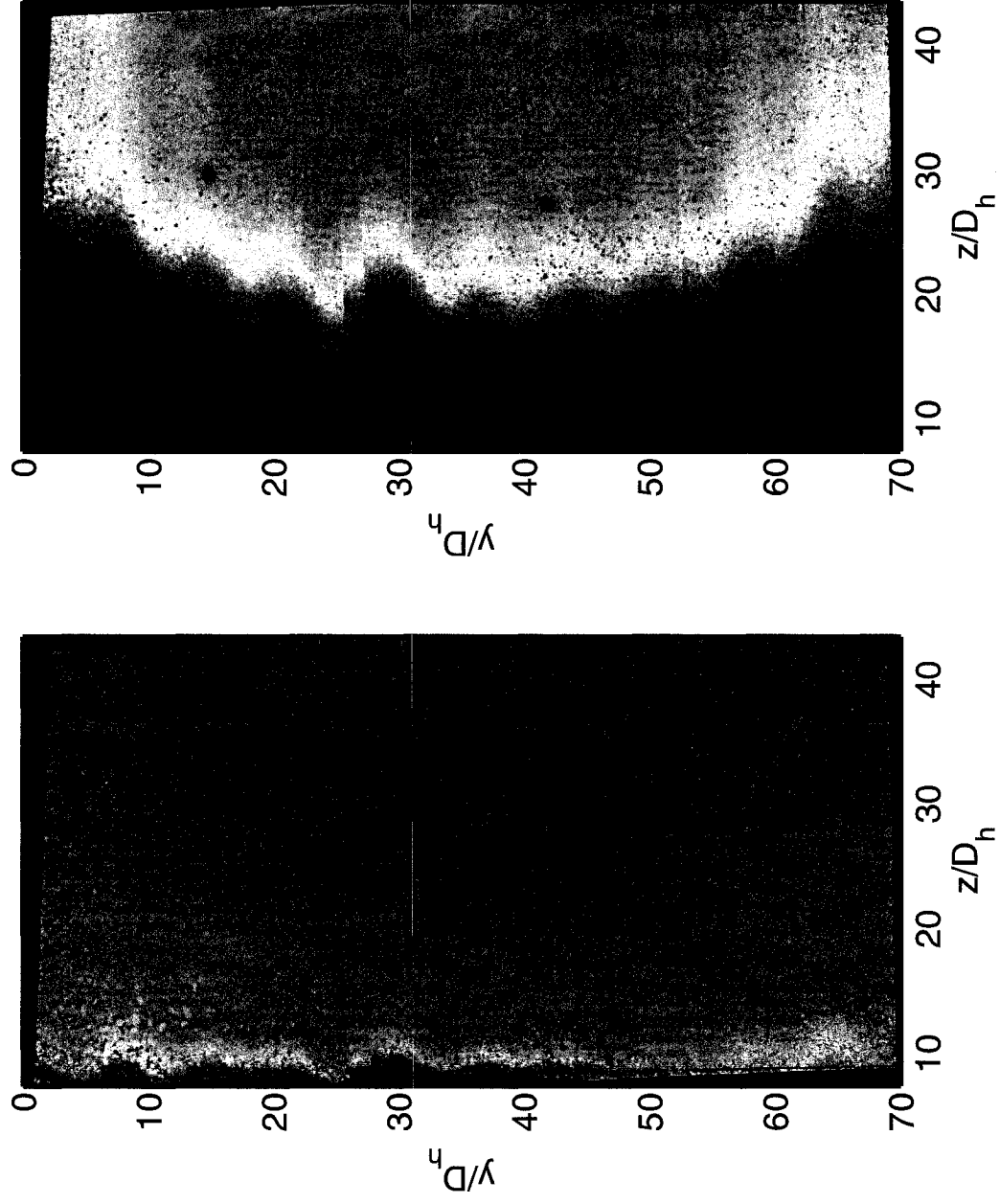
(a) $Re = 210$, $q'' = 3.11 \text{W/cm}^2$.

(b) $Re = 563$, $q'' = 2.38 \text{W/cm}^2$.

Figure 6.6: Preprocessed heat sink TLC thermal maps, consist of 3 images joined and binary filtered.

$$\eta = \frac{\tanh{(mH_{chn})}}{mH_{chn}} \qquad (6.8)$$

$$m = \sqrt{\frac{h}{k_{Si} W_w/2}} \qquad (6.9)$$

$$W_{cell} = W_{chn} + 2\left(W_w/2\right) \qquad (6.10)$$

A unit cell ($W_{cell}/2$) consists of a single channel with half the wall thickness on either side ($W_w/2$). The above neglects the heat transfer contribution within the cross-link paths and is utilized out of convenience. The heat transfer coefficient is evaluated iteratively to an accuracy of $1e^{-3}$. The inner wall temperature is obtained from a one-dimensional heat transfer approximation as follows,

$$T_{w,i} = T_{w,o} - \frac{q''\left(\delta_{Si} - H_{chn}\right)}{k_{Si}} \qquad (6.11)$$

Energy losses are found to be at maximum 5%, but in most cases less than 1% and hence deemed to be negligible. The power to the fluid is obtained from the fluid enthalpy rise given by,

$$q'' = \frac{Q_{vol}\left(\rho_{out}Cp_{out}T_{out} - \rho_{in}Cp_{in}T_{in}\right)}{A_{plan}} \qquad (6.12)$$

TLC temperature measurement uncertainties are estimated to range from ± 1.1 °C to ± 1.5 °C. Typical uncertainty in the Nusselt number are estimated at 9%.

6.3.2 Pressure Drop Measurements

Pressure drop measurements are carried out with both air and water in a flow range of 1 to 5 standard LPM and 10 to 200 ml/min, respectively. These measurements were carried out with the support system in Figure 6.3. Initial liquid pressure drop results showed a significant deviation from theoretical predictions at low Reynolds numbers. Comparison with the air data suggested that the deviations are not likely due to channel dimensions or sensors. A physical difference between the water and air, is the existence of surface tension in the case of water. Some recent works have shown that the congestion of a bubble in microchannels can pose a significant increase on the pressure drop (Kim et al., 2002). If this is indeed the case, methods to alleviate it are through applying a high liquid pressure, vibration of the channels, or a deaerating technique such as heating the flow. The chosen approach was to run at high flowrate to increase the pressure, with the fluid at an elevated temperature. Figure 6.7 compares the results before and after deaerating the flow. The large difference in pressure drop results before and after, confirm that in large, the deviation from theoretical is due to bubble congestion in the channels. Visualization would have also verified this, however in cases as in the present where this was not possible, the above procedure proved to be a valuable approach.

Figure 6.8 compares the water and air friction factors with the theoretical predictions. Good agreement is observed in both cases with a deviating trend in the lower Reynolds number ranges. In case of the air measurements, the deviation is likely due to the sensor accuracy at the low flowrates. In case of the water measurements, the
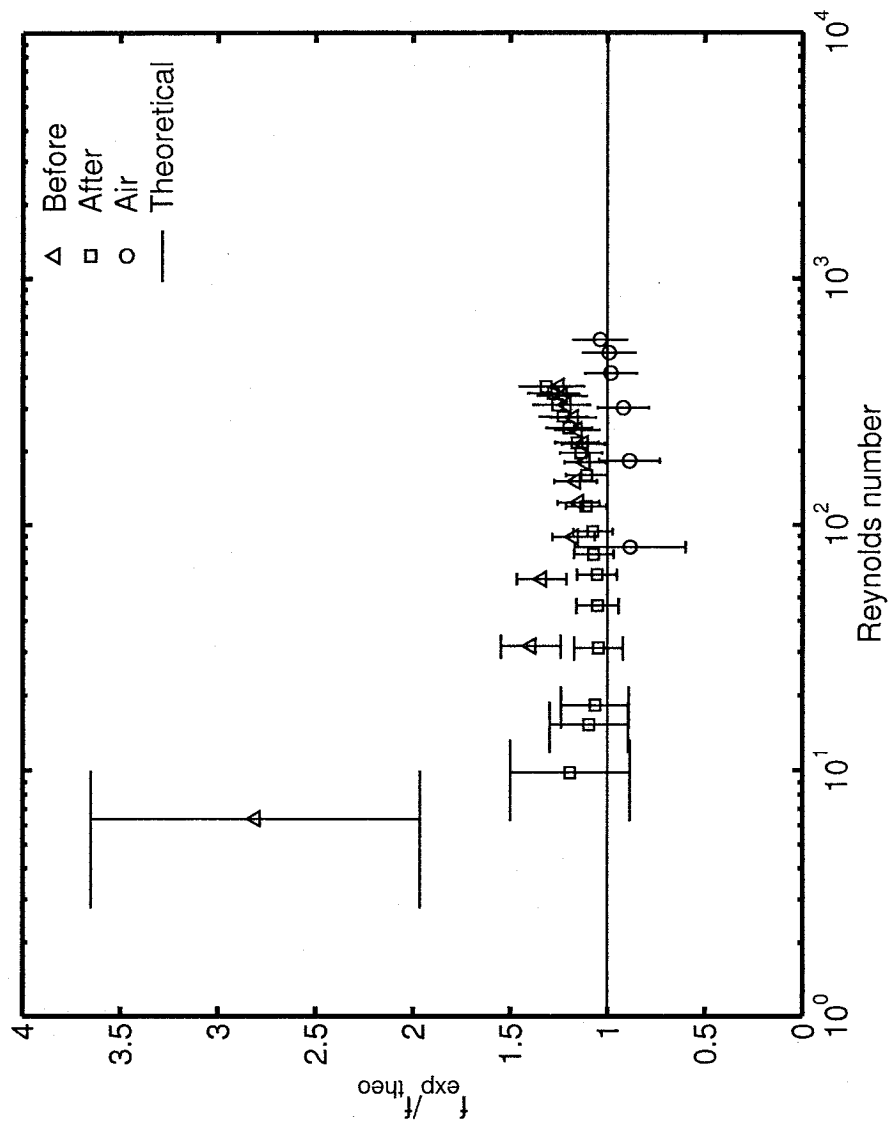
Figure 6.7: Ratio of experimental to theoretical friction factor versus Reynolds number, before and after rapid heating at high flowrate, STR01.

153
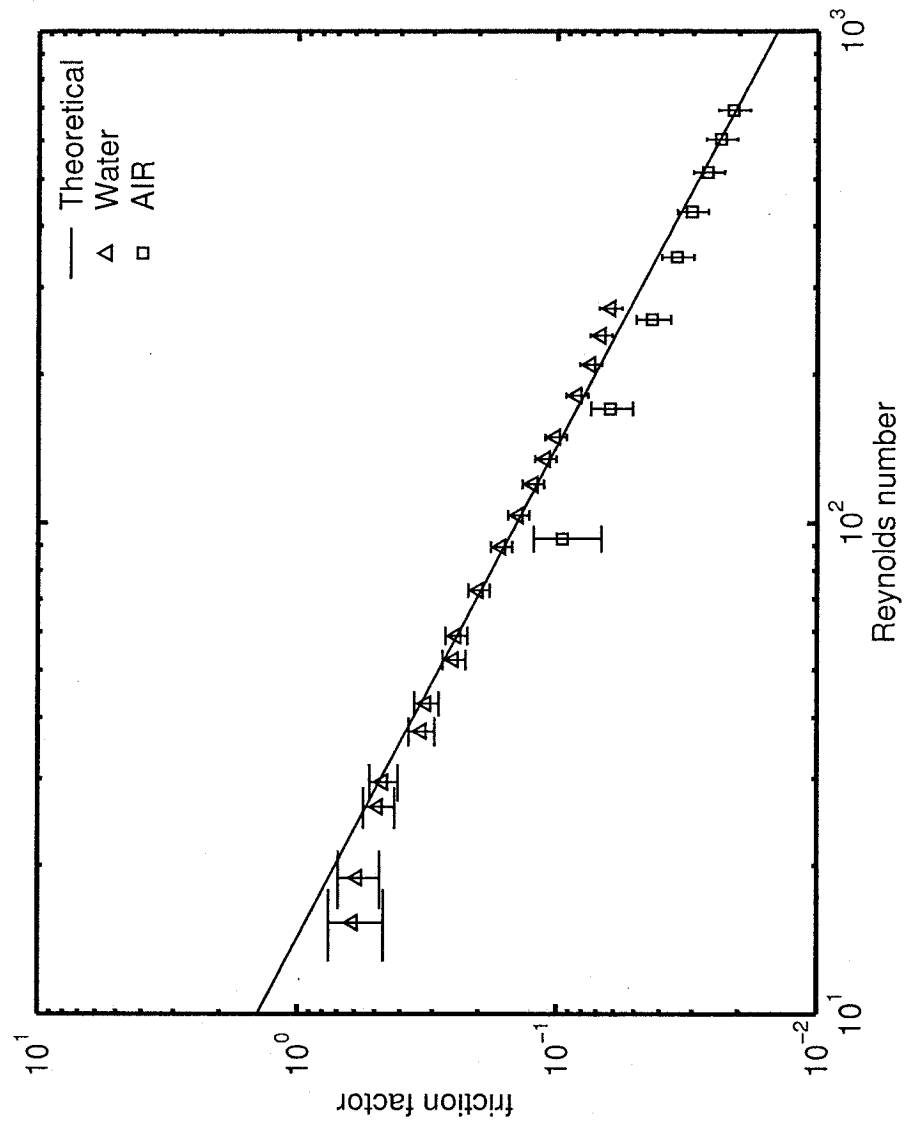
Figure 6.8: Friction factor versus Reynolds number, STR02.

deviation is likely a combination of the flowrate sensor and the pressure drop sensor uncertainties, while in their low ranges. Although the air and water show differences between each other, this is still close to their uncertainty limits. Figure 6.9 compares the difference between measured and predicted friction factors from a number of microchannel studies (Steinke and Kandlikar, 2005a,b; Harms et al., 1999; Tuckerman, 1984). All studies used parallel silicon channels flowing water and accounted for entrance and exit losses in a manner similar to what has been presented. The present measurements are found to be within the range of those obtained by other researchers. At higher Reynolds numbers there is a consistent trend of an increasing deviation from predictions. This is likely due the loss factors not being fully appropriate for parallel microchannel configurations. Future works should look into obtaining loss factors appropriate for microgeometries. Figures 6.10 (a) and (b) compare the pressure drop characteristics between the standard and cross-linked heat sinks. The difference in pressure drop is observed to be negligible over the flow range investigated and no discernible benefit or detriment of the cross-linked scheme is observed.

6.3.3   Local Heat Transfer Measurements

Heat transfer measurements were carried out using FC-72, at Reynolds numbers ranging from 142 to 559, using the support system of Figure 6.4. Successful measurements were obtained only with the cross-linked heat sink, due to leakage and fracture of the standard heat sinks. Local wall temperatures and Nusselt values are presented in Figures 6.11 to 6.14. Also presented in the figures are the calculated local fluid bulk
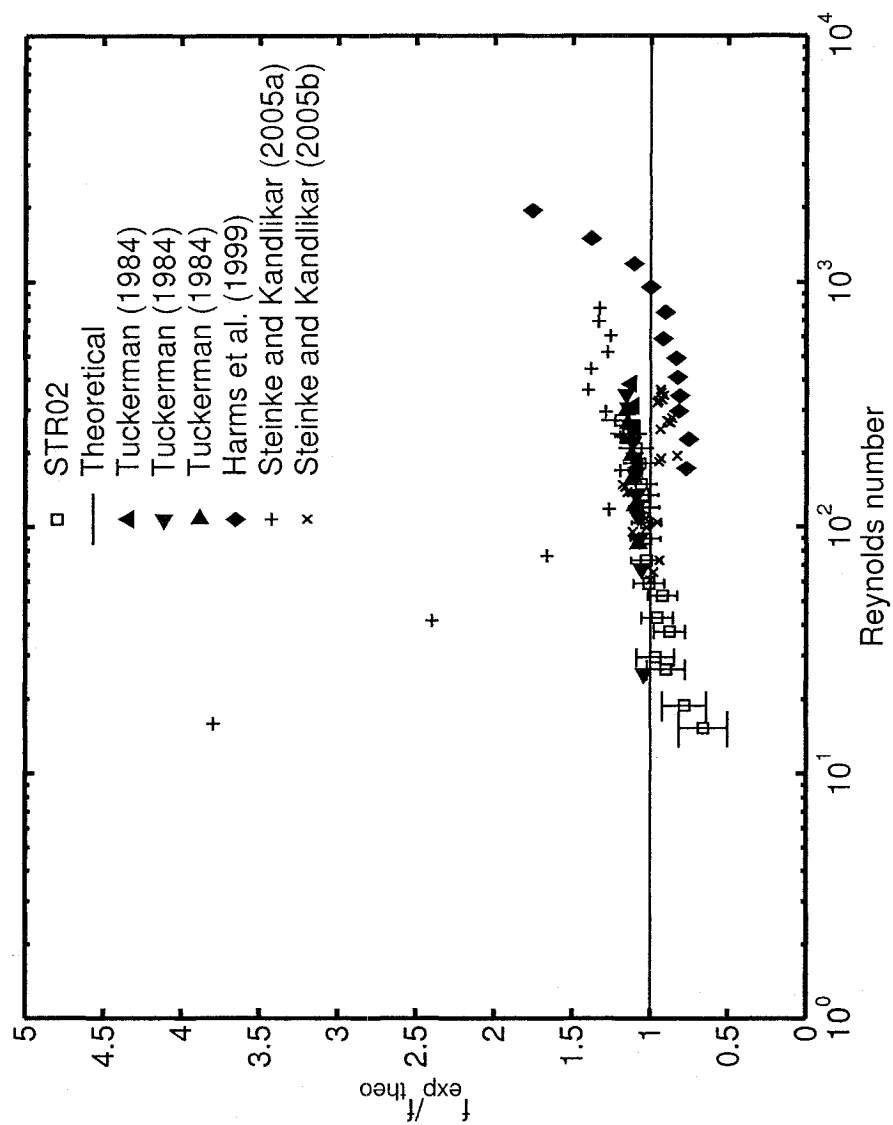
Figure 6.9: Ratio of experimental to theoretical friction factor versus Reynolds number, comparison with other researchers flowing water in parallel silicon microchannels.
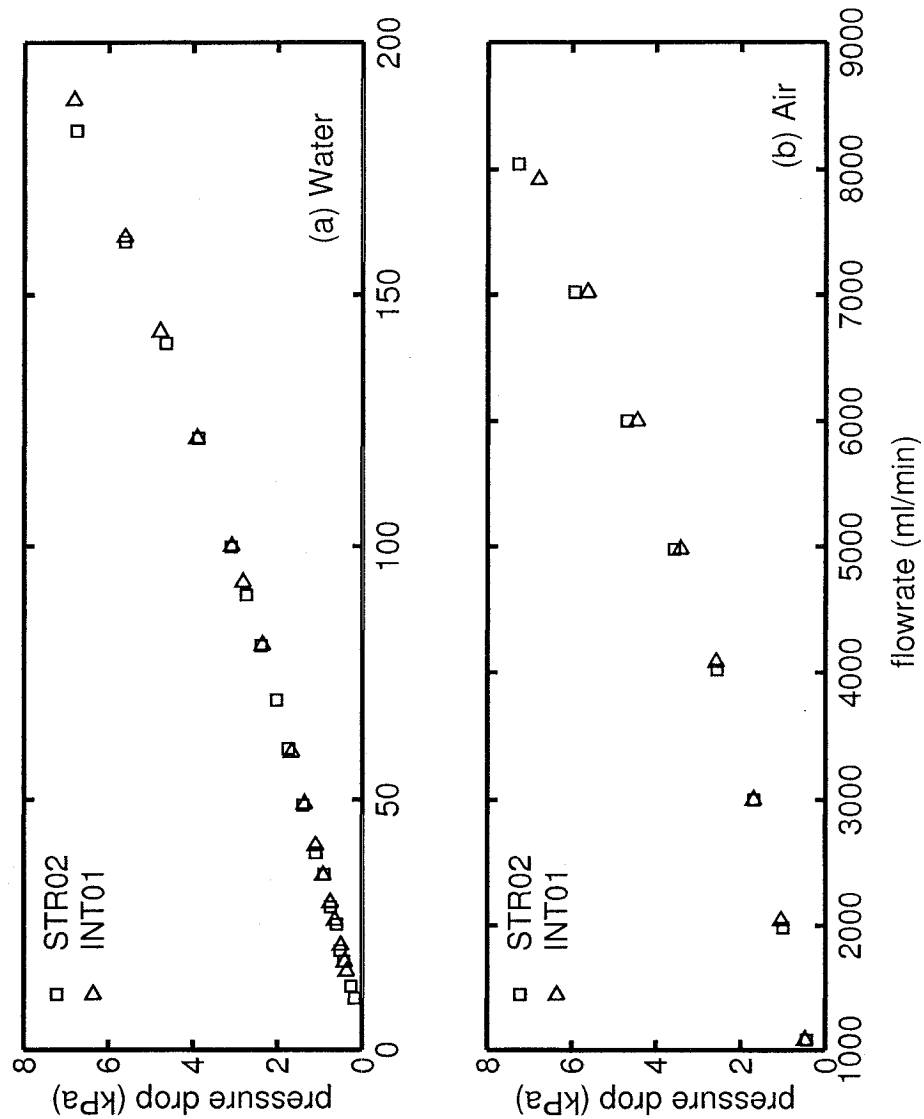
Figure 6.10: Pressure drop versus flowrate for standard versus cross-linked microchannel heat sinks flowing water and air.

temperatures and the approximate location of the cross-links. The results are span-wise averages centered at 17.6 y/D_h, 35.3 y/D_h and 52.9 y/D_h. They are averaged over 250 pixels which corresponds to 1/5th of the height. Negligible differences are observed in the wall temperatures and Nusselt values between the different spanwise locations considered. For the Reynolds range covered, the wall temperature rises non-linearly and peaks just after the second cross-link. In all cases, a slight drop in wall temperature is observed at the third cross-link. Finally, a slight change in slope is observed at the first cross-link. Overall, the cross-link influence on heat transfer for the present configuration and Reynolds number range is observed, however it is minimal. Xu et al. (2005) observed a dramatic change in their averaged streamwise wall temperature and Nusselt values from their experiments with cross-linked trian-gular channels. This was attributed to a re-developing thermal boundary layer. Their cross-link widths, however, were approximately three times wider than the channel width and their configuration included five cross-link paths. Thermal boundary layer re-development is similarly the likely cause of the observed inflections in temperature and Nusselt number profiles. However, given the narrower cross-link widths in the present work (cross-link width $\approx$ channel width), minimal influences are observed.

Figure 6.15 compares the averaged streamwise Nusselt number based on the cen-tral region (35.3 y/D_h), with the theoretical solution for a 4-wall heated channel with constant heat flux and fully developed flow (Shah and London, 1978). This solution assumes hydrodynamically fully developed flow. From this figure, it is observed that the results correlate similarly with the non-dimensional parameters of laminar ther-mally developing flows. The Nusselt number trend, however, has inflections caused
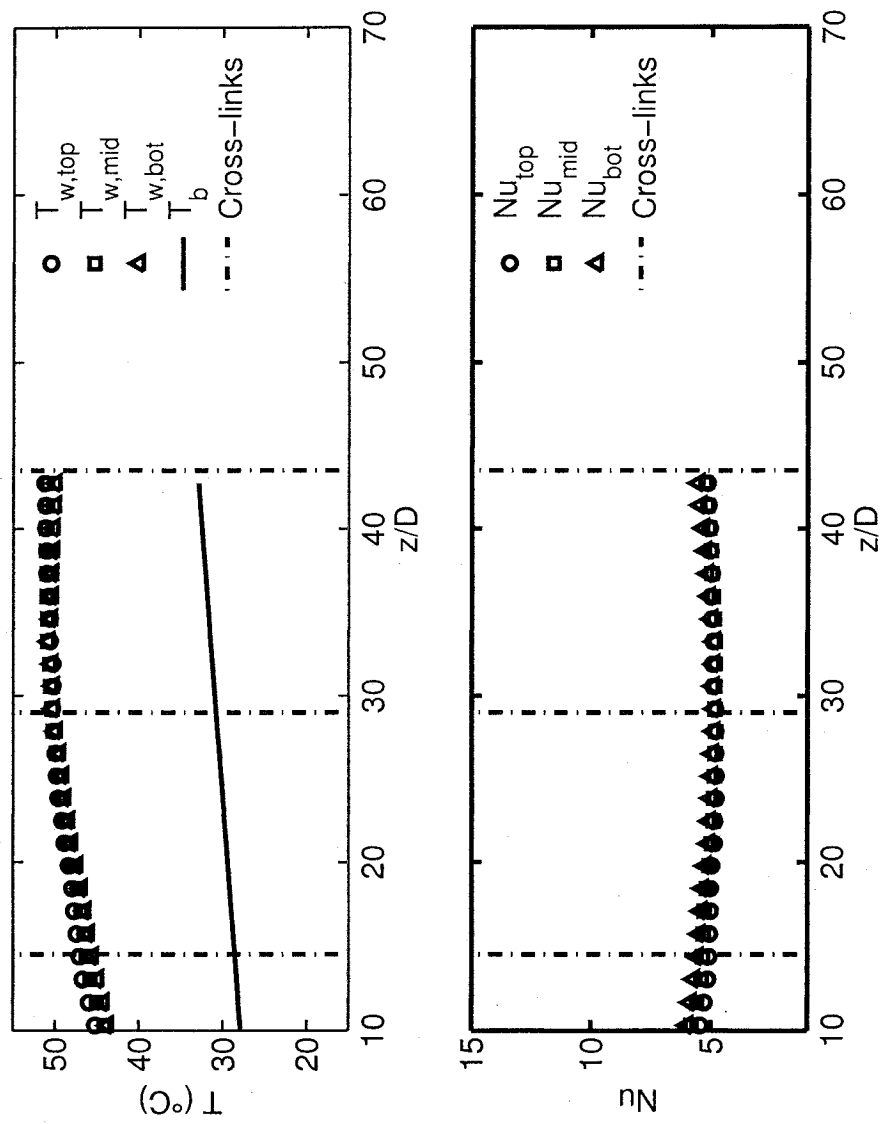
Figure 6.11: Local wall temperatures and Nusselt numbers at various spanwise locations, Re = 142, INT02 flowing FC-72.
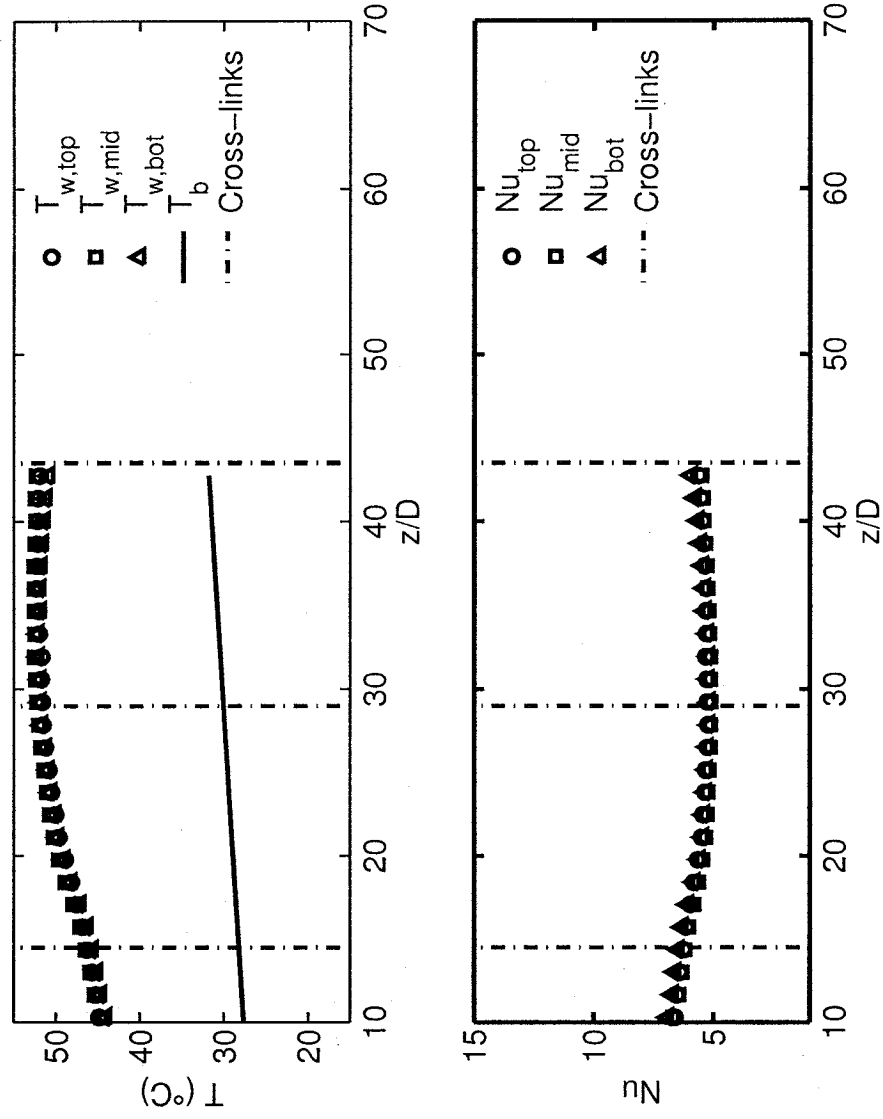
Figure 6.12: Local wall temperatures and Nusselt numbers at various spanwise locations, Re = 210, INT02 flowing FC-72.
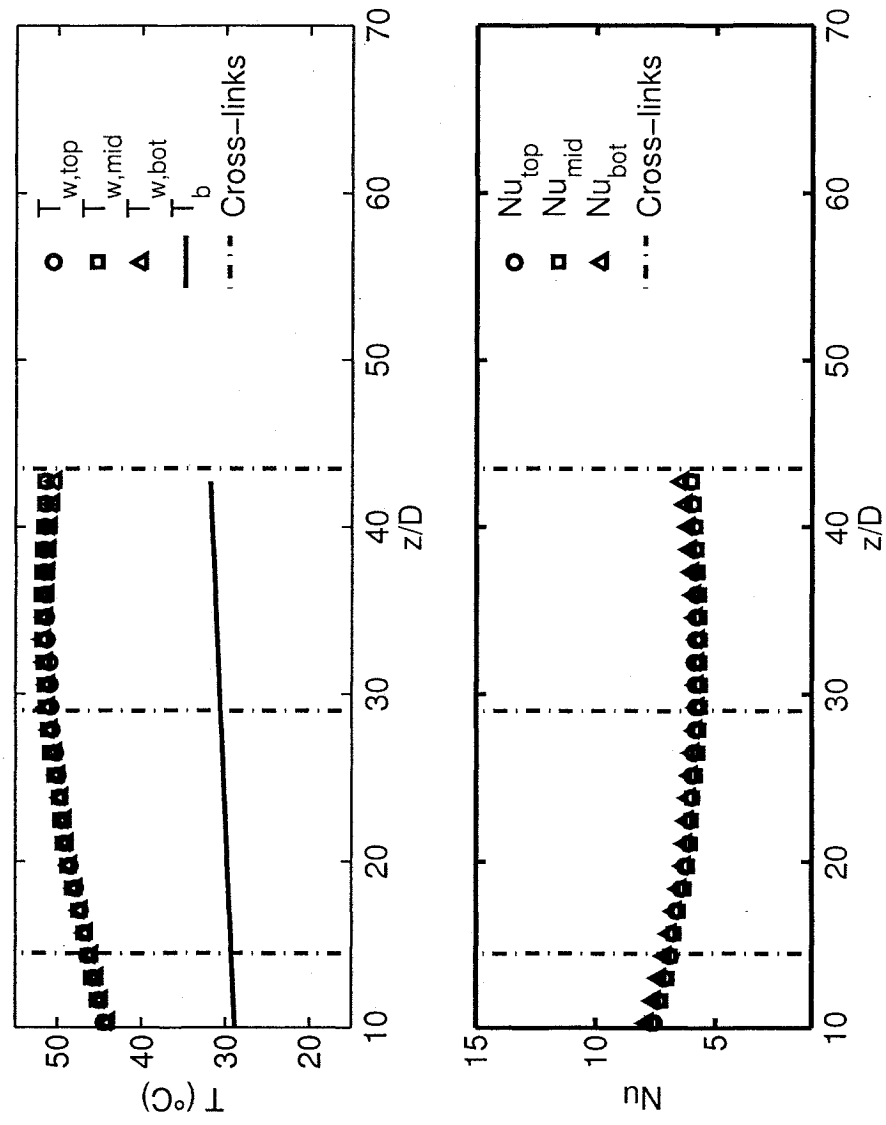
Figure 6.13: Local wall temperatures and Nusselt numbers at various spanwise locations, Re = 307, INT02 flowing FC-72.
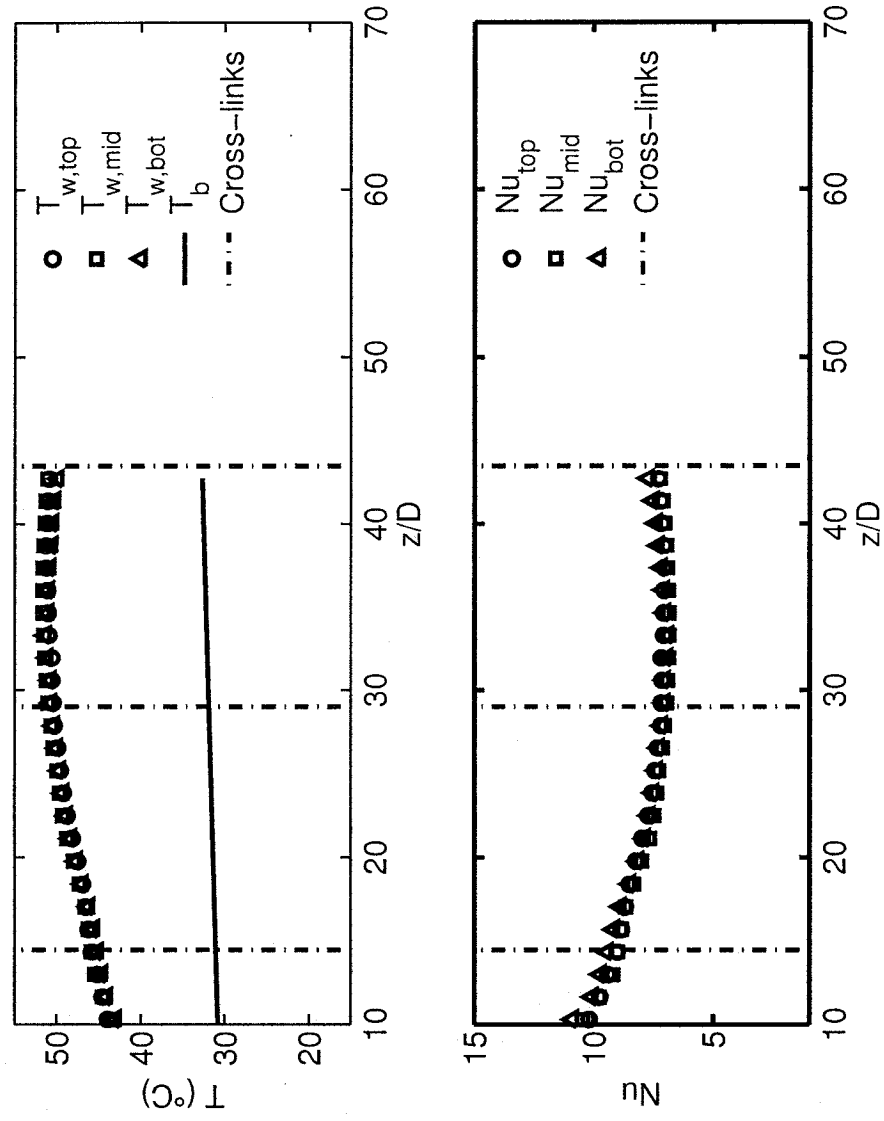
Figure 6.14: Local wall temperatures and Nusselt numbers at various spanwise locations, Re = 559, INT02 flowing FC-72.
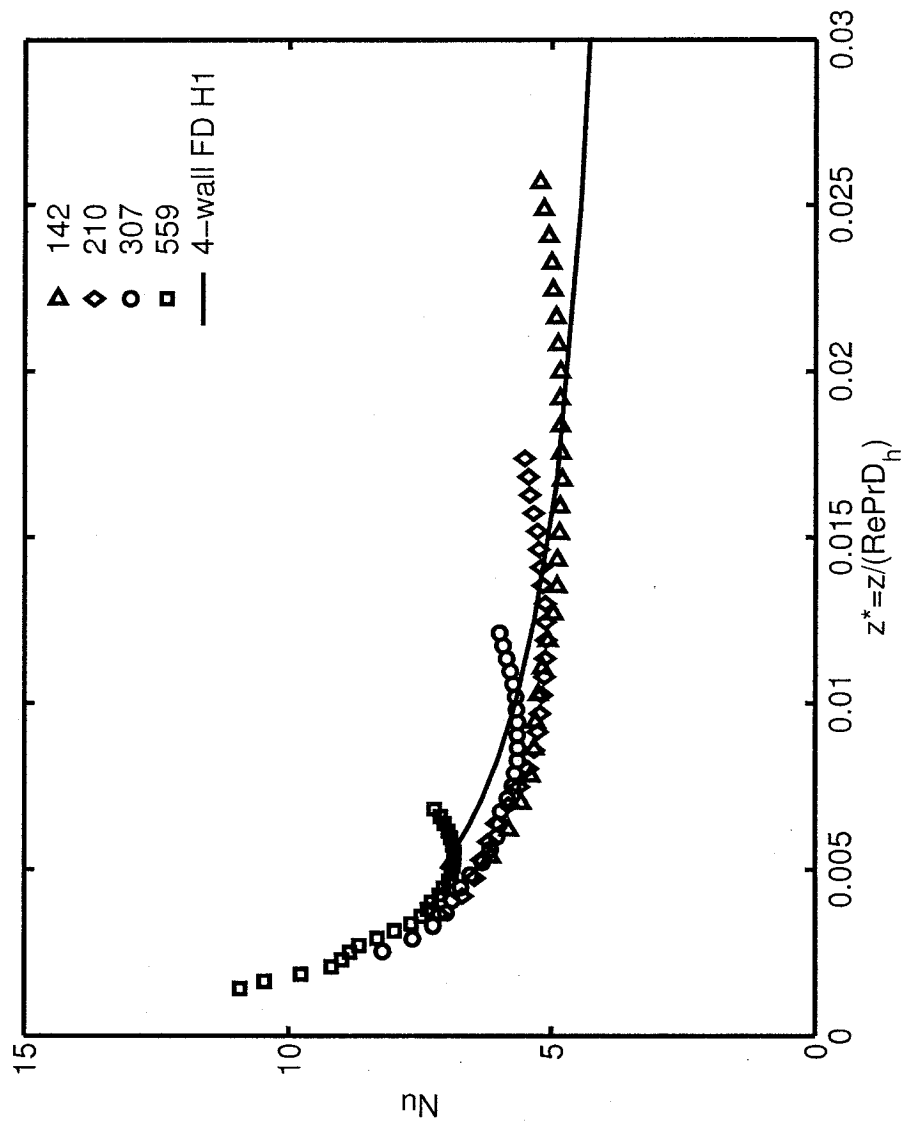
Figure 6.15: Local Nusselt numbers versus non-dimensional streamwise distance at various Reynolds numbers, INT02 flowing FC-72.

by the cross-links.

6.4   Flow Boiling

The prevalence of boiling instabilities in parallel microchannel systems was discussed in Section 2.2.4. Compared to conventional size channels, understanding of their mechanisms and characteristics is still in its infancy. Additionally, boiling oscillations in literature have only been presented for straight, standard, parallel microchannel systems. The following presents characteristics of boiling instabilities in a cross-linked microchannel heat sink and a standard microchannel heat sink, to better understand their mechanisms. The aim of the cross-links is to interrupt any rapidly expanding bubble and prevent it from engulfing the entire channel length up to the inlet.

6.4.1   Procedure and Data Reduction

Flow boiling measurements were performed using distilled water with the first support system (Fig 6.3). Before commencing experiments, the fluid is degassed as outlined is Section 3.1.1. After this, the desired flowrate is set and the preheater is adjusted to obtain the inlet temperature setpoint. Data is obtained at incremental levels of heat flux. Flow boiling measurements for the standard heat sink (STR02) have been obtained at flowrates of 20 to 50 ml/min (91 to 228 kg/(m$^2 \cdot$s)) and inlet temperatures of 70 °C and 80 °C. For the cross-linked design (INT01), however, only one flowrate and inlet temperature is investigated due to difficulties with leakage in the setup.

164

Power to the fluid under single phase conditions is obtained from an energy balance as shown in Equation 6.12. During flow boiling, the heat flux was obtained from the heater power generated and corrected for losses to the environment using a power ratio factor, γ. This results in,

$$q'' = \frac{(VI) \cdot \gamma}{A_{heated}}.$$

(6.13)

Ideally, the power ratio factor, γ, may be estimated from an energy balance through estimation of convective losses to the environment and axial conduction losses, as was shown by Hetsroni et al. (2005a). However, this requires measurement of the outer wall temperature which was not available for the boiling measurements. To alleviate this, the present work estimated this factor by combining Equations 6.12 and 6.13 under single phase conditions. For each flowrate, as the heat flux was increased, the power ratio factor reached a limiting value prior to boiling. This limiting value, which ranged from 0.85 to 0.97 for the various flowrates, was taken as the power ratio factor under boiling conditions.

Uncertainty estimates for the various sensors are presented in Section 3.4. Uncertainty estimates for derived parameters are presented in Table 6.2.

6.4.2 Flow Boiling Onset and Limits

The typical inlet pressure trend leading up to two-phase flow is shown in Figure 6.16 for an inlet temperature of 70 °C at a flowrate of 30 ml/min. After boiling occurred, the inlet pressure would rise slightly in some cases, due to increased vapor generation

165

Table 6.2: Uncertainty estimates for derived parameters.

Parameter	Uncertainty
D_h	5.5 μm
G	4.8 - 12.3%
q''	3.4 - 6.2%
Re	7.4 - 27.5%
Bo	7.1 - 13.4%
We_D	12.4 - 24.0%
We_L	12.2 - 23.9%
N_{sub}	2.4 - 4.2%
f^*	0.4 - 2.1%
P^*	1.7 - 4.7%
T^*	5.3 - 21.6%
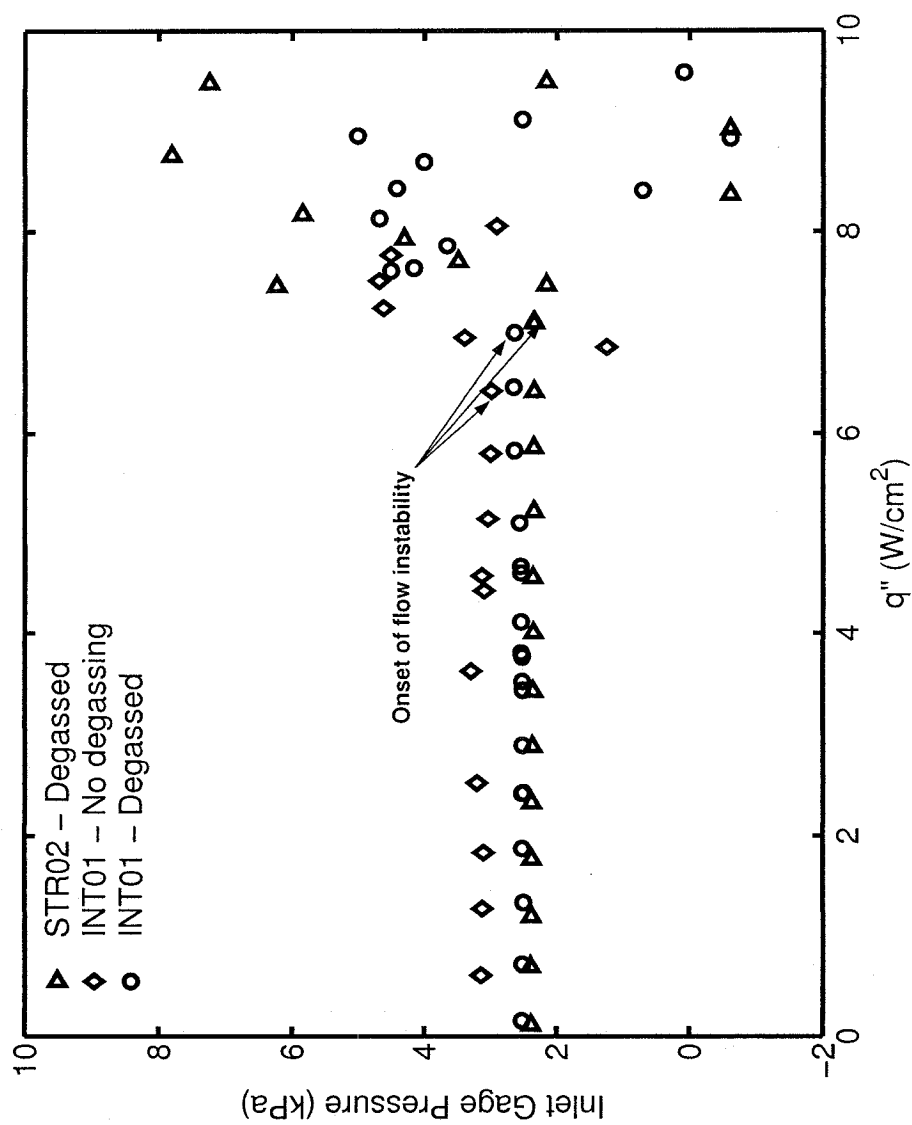
Figure 6.16: Inlet pressure versus applied power, $T_{in} = 70\ °C$, $Q_{vol} = 30$ ml/min.

until instabilities occurred. Figure 6.16 shows that for degassed fluids, the heat flux at which instabilities occur is similar for both cases, at approximately 7.9 W/cm². However, for a non-degassed fluid as shown for the cross-linked design, the onset of flow instabilities occurs earlier, and at approximately 66 % of the heat flux for the degassed fluid. Early onset due to a non-degassed fluid has been observed by prior investigations, and this highlights the importance of utilizing a well prepared fluid for predictability Steinke and Kandlikar (2004b). Additionally, this latter point has recently been reiterated by Chen and Garimella (2005) who investigated flow boiling of a degassed and non-degassed dielectric fluid in a microchannel heat sink.

The demarcation between relatively stable flow boiling and large boiling oscillations is sometimes considered the onset of premature critical heat flux, due to the uncertain flow characteristics under such conditions. With such an assumption, the approximate heat flux demarcating stable to unstable flow boiling is plotted in Figure 6.17 in non-dimensional form, with the Boiling number (Bo) dependent on the Weber number (We). Identification of the onset of instability was based on monitoring the fluctuations of flow parameters as well as observation of the flow in the tubing downstream. The data are from the STR02 heat sink at inlet temperatures of 70 °C and 80 °C and are compared with proposed critical heat flux correlations from both microchannel (Qu and Mudawar, 2004) and conventional channel (Katto, 1981) flows. These correlations are listed in Table 6.3.

Fluid properties are taken as the saturation temperature at the exit of the system, which is taken as 100 °C. The correlation by Katto (1981) is based on conventional size

168
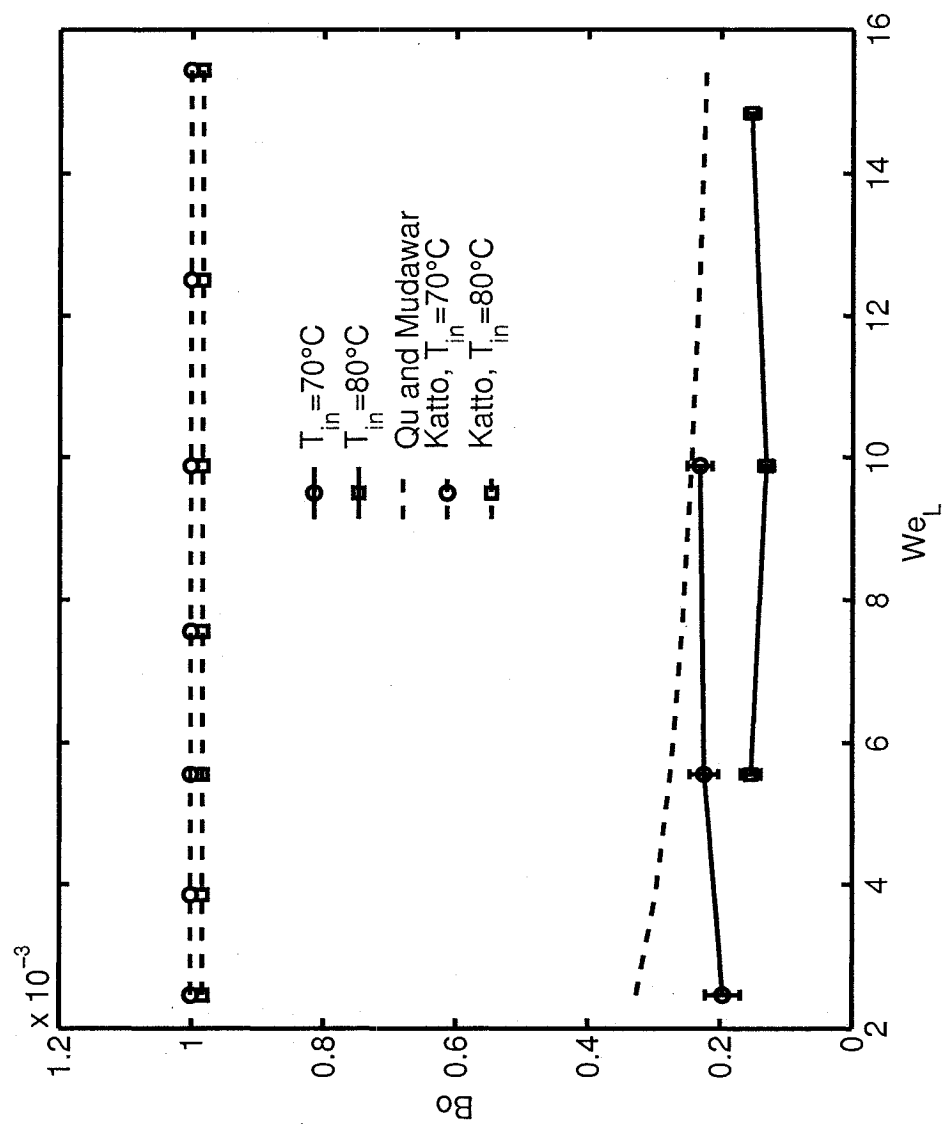
Figure 6.17: Limiting Boiling number of STR02 heat sink for different inlet temperatures and compared to correlations.

Table 6.3: Critical heat flux correlations.

Reference	Conditions	Correlation
Conventional Size Channels Katto (1981)	- rectangular ducts - water and R113 - $D_h \sim 2.1$ mm – 20.5 mm single wall heated or double opposite wall heated	$q''_{crit} = q''_{crit0} \left(1 + K \frac{\Delta h_{sub,in}}{h_{fg}}\right)$ $q''_{crit01} = 0.25 \left(Gh_{fg}\right) \left(\frac{1}{L_{chn}/d_{heated}}\right)$ $q''_{crit02} = C\left(Gh_{fg}\right) We_L^{-0.043} \left(\frac{1}{L_{chn}/d_{heated}}\right)$ $q''_{crit03} = 0.15 \left(Gh_{fg}\right) \left(\frac{\rho_g}{\rho_f}\right)^{0.133} We_L^{-1/3} \left(\frac{1}{1+0.0077 L_{chn}/d_{heated}}\right)$ $q''_{crit04} = 0.26 \left(Gh_{fg}\right) \left(\frac{\rho_g}{\rho_f}\right)^{0.133} We_L^{-0.0433} \left(\frac{L_{chn}/d_{heated}}{1+0.0077 L_{chn}/d_{heated}}\right)^{0.171}$ $C = 0.25 \ for \ \frac{L_{chn}}{d_{heated}} < 50, \ C = 0.34 \ for \ \frac{L_{chn}}{d_{heated}} > 50$ $K_1 = 1; \ K_2 = \frac{0.261}{CWe_L^{-0.043}}; \ K_3 = \frac{0.556(0.0308+d_{heated}/L_{chn})}{(\rho_g/\rho_f)^{0.133} We_L^{-1/3}}$ Similar to Qu and Mudawar (2004) the coefficients are determined as follows, When $q''_{crit01} < q''_{crit02}$, $q''_{crit0} = q''_{crit01}$, $K = K_1$ When $q''_{crit01} > q''_{crit02}$ if $q''_{crit02} < q''_{crit03}$, $q''_{crit0} = q''_{crit02}$, $K = K_2$ if $q''_{crit02} > q''_{crit03}$ and $q''_{crit03} < q''_{crit04}$, $q''_{crit0} = q''_{crit03}$, $K = K_3$ if $q''_{crit03} > q''_{crit04}$, $q''_{crit0} = q''_{crit04}$
Microchannels Qu and Mudawar (2004)	- rectangular and circular parallel channels - water and R113 - $D_h \sim 318$ μm – 2.54 mm	$q''_{crit} = 33.43 \left(\frac{\rho_g}{\rho_f}\right)^{1.11} We_L^{-0.21} \left(\frac{L_{chn}}{d_{heated}}\right)^{-0.36}$

rectangular channels with one or two walls heated, from a variety of studies that predominantly used water. The hydraulic diameters in the developed correlation ranged from 2.1 mm to 20.5 mm. The correlation by Qu and Mudawar (2004) was developed for an array of 21, 215 μm wide $\times$ 821 μm deep parallel microchannels flowing water and single mini and microchannels (2.54 mm and 510 μm hydraulic diameters respectively) flowing R-113. Assuming instabilities to signal premature critical heat flux, the present data show a much reduced CHF limit on the order of 5 times, compared to conventionally sized channels denoted by the Katto (1981) correlation. However, in comparison with the correlation by Qu and Mudawar (2004) for microchannels the difference is much less. The data from this correlation showed no dependence of the critical heat flux on inlet subcooling. The present data, however, shows a dependency on the inlet subcooling. This dependency is similar to that for conventionally sized channels, in that the critical heat flux is decreased with an increase of inlet subcooling. However, the degree of influence of subcooling is more significant for the microchannels (45% and 75% increase from 80 °C to 70 °C) compared to the conventional channels (1.8% increase from 70 °C to 80 °C). The remainder of this section details the characteristics of flow under unstable conditions to better understand their source and mechanisms. Also, this section looks at the influence of cross-links to evaluate how they compare to standard straight parallel channel heat sinks under unstable boiling conditions. A summary of the flow conditions leading to unstable flow and the boiling oscillation measurement conditions are listed in Table 6.4.

Table 6.4: Measurement conditions and stability limits.

Heat sink configuration	T_{in} (°C)	Q_{vol} (ml/min)	G (kg/(m² · s))	Conditions at onset of instability	
				q'' (W/cm²)	Bo
STR02	70	20	91	4.1	$1.958 \times \times 10^{-4}$
		30	140	7.1	2.247×10^{-4}
		40	186	9.7	2.316×10^{-4}
	80	30	140	4.9	1.540×10^{-4}
		40	185	5.5	1.312×10^{-4}
		50	228	7.9	1.538×10^{-4}
INT01	70	30	140	7.0	2.215×10^{-4}

6.4.3 Flow Boiling Oscillations

Once the stable threshold was crossed, sustained oscillations in flow parameters were observed. These were relatively periodic fluctuations in various sensors including the inlet and outlet temperature and the inlet and differential pressure sensors. Samples of these signal fluctuations, for a given heat flux and flowrate, are presented in Figure 6.18. They are presented both for the STR02 and INT01 heat sinks. The oscillations are captured at a rate of 5 to 10 Hz over a 20 s to 50 s span. The time traces show relatively large amplitude oscillations. This is likely due to periodic refilling of the channels, typical of what has been observed by other researchers working with boiling in parallel channel microsystems (Hetsroni et al., 2005a, 2006; Qu and Mudawar, 2004). A characteristic trend in the flow oscillations captured, is that the dominant frequency is the same for all the sensors, and they are in phase. This is a relatively low frequency on the order of 10^{-1} Hz. No discernible trends are observed between a pressure time trace versus inlet or outlet temperature time trace. The inlet temperature, however, is always observed to oscillate with a smaller amplitude than the outlet temperature. Its amplitude though, grows more significantly with increased heat flux and details of these amplitude characteristics are presented later. Through performing a Fast-Fourier Transform on the time traces and parsing for the largest peak, the dominant frequency of the signals is obtained. Figure 6.19 shows the variation in the inlet temperature oscillation frequencies, comparing both heat sink configurations. For STR02, the frequency is higher than INT01 and decreases with increasing heat flux. For INT01, the frequency also decreases with increasing
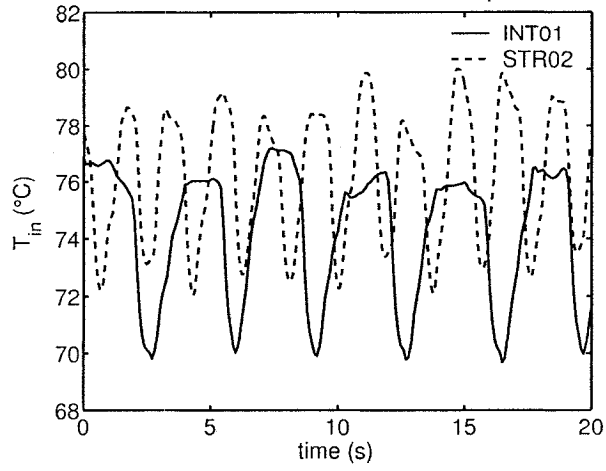
(a) Inlet temperature sample transient behaviour.
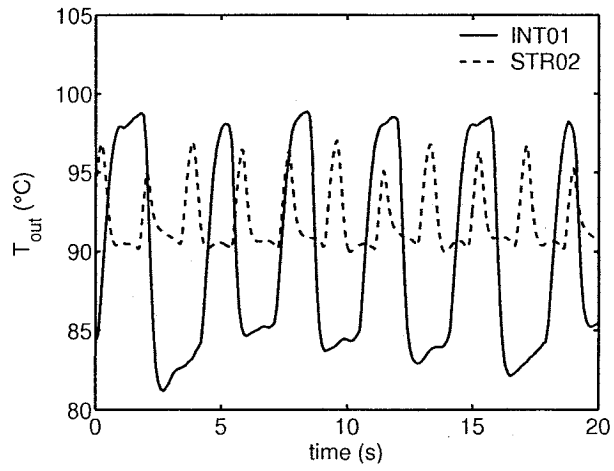
(b) Outlet temperature sample transient behaviour.
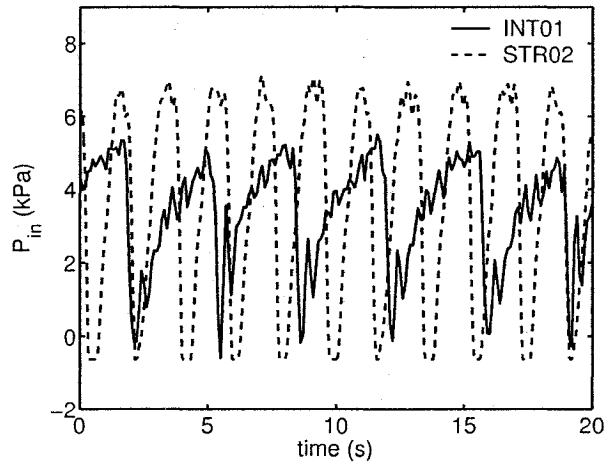
(c) Inlet pressure sample transient behaviour.

Figure 6.18: Sample transient behaviour of various signals, $q'' = 7.9 \text{ W/cm}^2$, $\text{T}_{in} = 70$ °C, $Q_{vol} = 30$ ml/min.
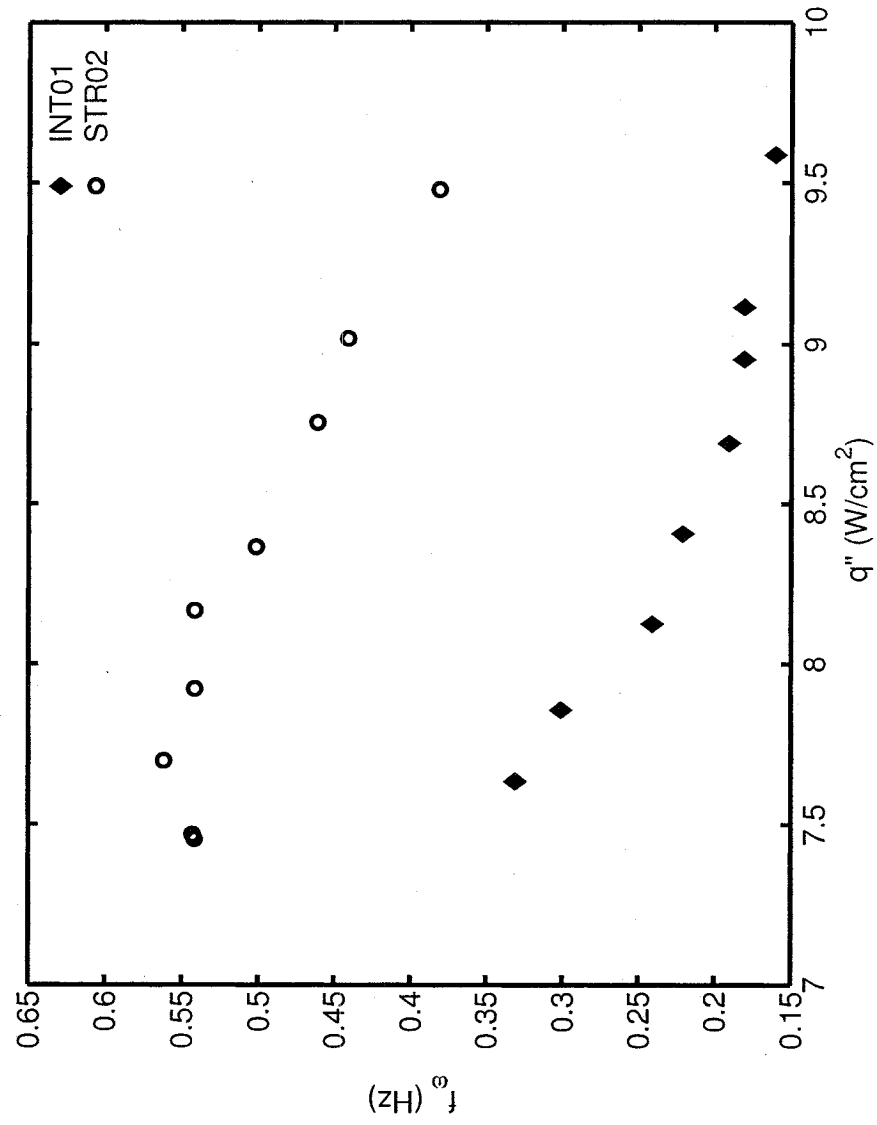
Figure 6.19: Inlet temperature oscillation frequency versus power, $T_{in} = 70\ °C$ for different heat sinks at $Q_{vol} = 30$ ml/min.

175

heat flux.

Figure 6.20 (a) shows the variation in frequency for the STR02 heat sink as a function of inlet temperature, flowrate and heat flux. For a higher temperature, the frequency is lower for the same flowrate and with a lower flowrate, the frequency is also lower. It is observed that the frequency of oscillations is dependent not only on the heat flux, but the flowrate and the inlet subcooling. Also included in Figure 6.20 (a) is the frequency data obtained from Hetsroni et al. (2006). The heat sinks in this work contained 13 triangular cross-section channels, fabricated in a silicon substrate and with a hydraulic diameter of 220 μm. The mass flux range of the data was 63.3 kg/(m$^2 \cdot$ s) to 127 kg/(m$^2 \cdot$ s)and the heat flux ranged from 17 W/cm^2 to 32 W/cm^2. Similar trends to the present data are observed, in that the frequency decreases with increasing heat flux and lower mass fluxes have lower frequencies. A correlation has been developed to compile these observations. The frequency is non-dimensionalized with the heated length and the channel inlet velocity, assuming all liquid flow at entry,

$$f^* = f_\omega{}^{L_{chn}}\!/\!u_{chn,in}. \tag{6.14}$$

A number of length scales exist to non-dimensionalize the frequency, and they include the boiling length, the full channel length and the hydraulic diameter. Based on the performance of a number of correlation fit trials, the channel length was chosen as opposed to the boiling length. The hydraulic diameter is accounted for through inclusion of the Weber number based on hydraulic diameter. Since the frequency is a function of the heat flux and subcooling, we may utilize the Boiling number
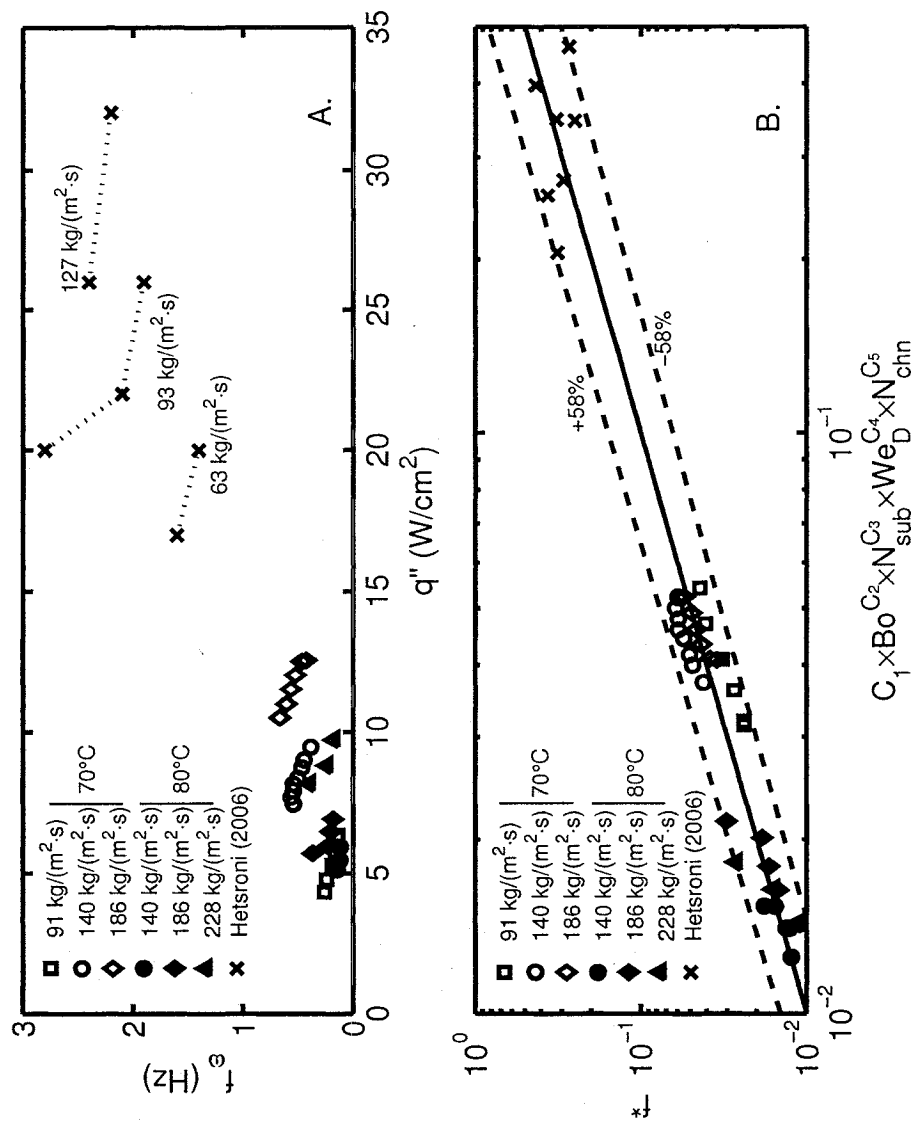
Figure 6.20: Inlet temperature oscillation frequency versus power for STR02 at different flowrates and inlet temperature.

as the non-dimensional heat flux and the Subcooling number (N_{sub}) to account for inlet subcooling. Finally, the number of channels is also included as an independent parameter. Based on these parameters, the following relationship was developed to correlate the data in Figure 6.20 (a),

$$f^* = C_1 Bo^{C_2} N_{sub}^{C_3} We_D^{C_4} N_{chn}^{C_5}, \tag{6.15}$$

where, $C_1 = 3.383 \times 10^{-15}, C_2 = -1.408, C_3 = 4.328, C_4 = 0.144$ and $C_5 = -0.137$, or in dimensional form as,

$$
\begin{aligned}
f_\omega = {} & 3.383 \left(10^{-15}\right) \frac{u_{chn,in}}{L_{chn}} \left(\frac{q''}{Gh_{fg}}\right)^{-1.408} \\
& \times \left[\frac{Cp\left(T_{sat} - T_{in}\right)}{h_{fg}} \cdot \frac{\rho_f - \rho_g}{\rho_g}\right]^{4.328} \left(\frac{G^2 D_h}{\sigma \rho_f}\right)^{0.144} \left(N_{chn}\right)^{-0.137}. \tag{6.16}
\end{aligned}
$$

Fluid properties in the above are calculated from saturation conditions at the tube exit. Equation 6.15 fits the data with a standard deviation of 25.4%. Figure 6.20 (b) compares the correlation fit with the data and includes the 95% confidence intervals based on the standard deviation. The Boiling number exponent shows that f^* is inversely proportional to the heat flux and hence a decreasing frequency with increasing heat flux will be obtained. As well, the magnitude of the Subcooling number exponent is over double that of the Boiling number, suggesting a stronger dependency of the oscillation frequency on the subcooling compared to heat flux.

Figure 6.21 shows the variation in the peak to peak amplitude of various sensor signals with increasing heat flux. In all cases (P_{in}, T_{in}, T_{out}) the amplitude increases
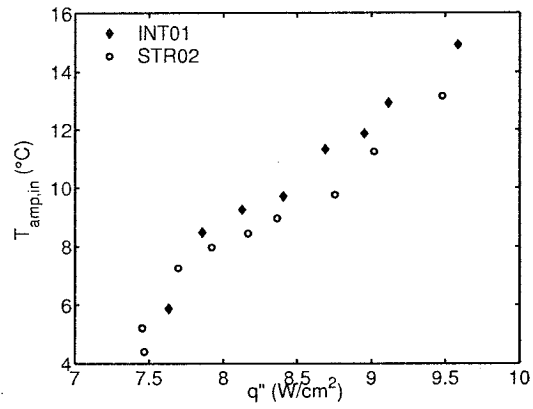
(a) Inlet temperature oscillation amplitude versus power
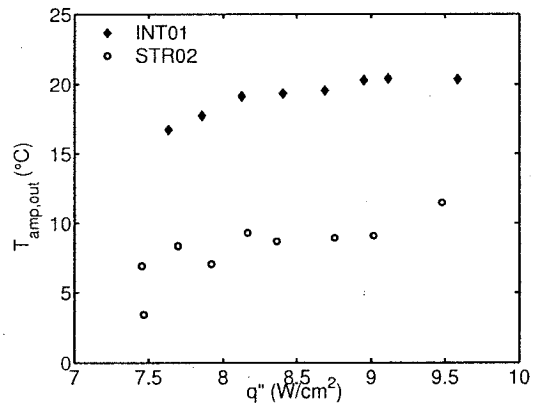
(b) Outlet temperature oscillation amplitude versus power
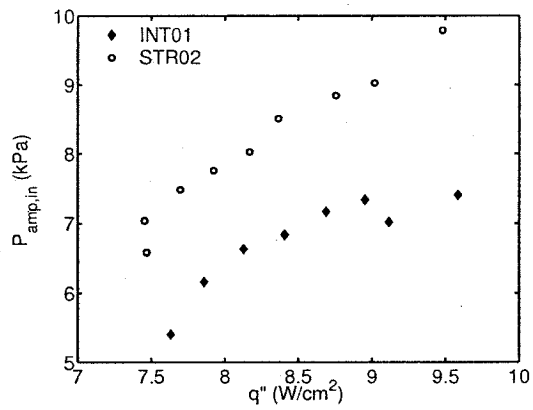
(c) Inlet pressure oscillation amplitude versus power

Figure 6.21: Oscillation amplitude versus power of various signals, $T_{in} = 70\ ^\circ\text{C}$ for different heat sinks at $Q_{vol} = 30$ ml/min.

with increasing heat flux. Fluctuations in the inlet temperature are likely due to flow reversals traveling as far upstream as the inlet plenum chamber. Such observations have been described in some recent studies (Hetsroni et al., 2005a, 2006; Qu and Mudawar, 2004). Comparing inlet pressure amplitude for heat sinks STR02 and INT01 in Figure 6.21, we observe a consistently lower amplitude for INT01. However, looking at the inlet and outlet temperatures, the behavior is opposite, whereby, STR02 has a lower amplitude than INT01. Further, the difference in the amplitude is only 1 °C to 2 °C at the inlet whereas it is as high as 10 °C at the outlet. Such a large variation, if translated to the wall temperature, could be extremely detrimental and it is recommended for future works to investigate it further.

Figure 6.22 (a) shows the variation of the inlet pressure amplitude for the STR02 heat sink at different flowrates and inlet temperatures. With increased flowrate, the amplitude of the pressure fluctuations increases, but this is also related to boiling onset and instabilities occurring at a higher heat flux. With decreased inlet temperature, the pressure amplitudes are higher. Overall, the pressure amplitude correlates relatively well with the heat flux, showing an increasing trend. To provide a more universal representation in non-dimensional form, the pressure may be non-dimensionalized with the liquid density and the inlet velocity, assuming all liquid flow at entry. This may then be set, similar to the frequency case, as a function of the Boiling number, Subcooling number and Weber number. The following correlation
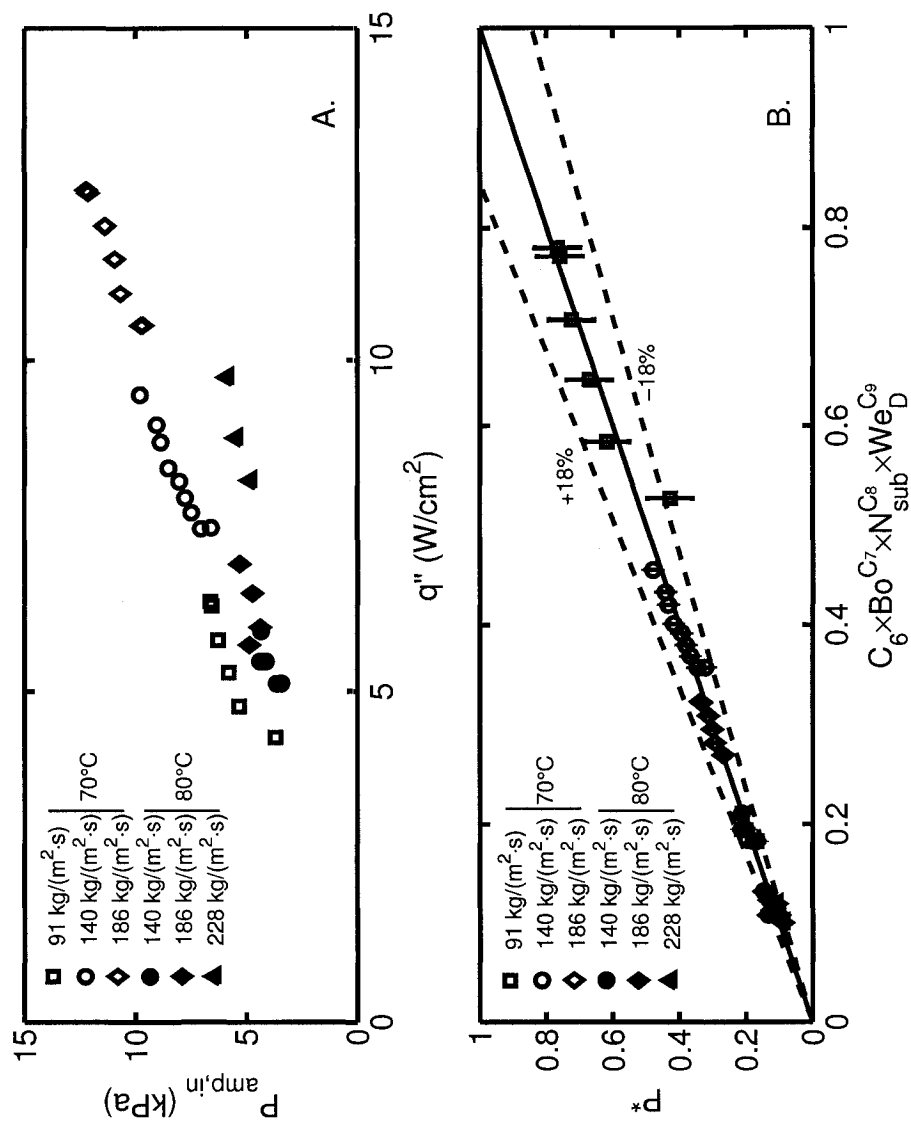
Figure 6.22: Inlet pressure oscillation amplitude versus power for STR02 at different flowrates and inlet temperature.

with the fluid properties calculated at saturation conditions at exit is obtained,

$$P^* = \frac{P_{amp}}{G^2/\rho_f} = C_6 Bo^{C_7} N_{sub}^{C_8} We_D^{C_9}, \qquad (6.17)$$

with the coefficients determined as, $C_6 = 17.600, C_7 = 1.016, C_8 = 0.714$ and $C_9 = -0.588$, or in dimensional form as,

$$
\begin{aligned}
P_{amp} &= 17.600 \frac{G^2}{\rho_f} \left(\frac{q''}{G h_{fg}} \right)^{1.016} \\
&\times \left(\frac{Cp\,(T_{sat} - T_{in})}{h_{fg}} \cdot \frac{\rho_f - \rho_g}{\rho_g} \right)^{0.714} \left(\frac{G^2 D_h}{\sigma \rho_f} \right)^{-0.588}.
\end{aligned}
\qquad (6.18)
$$

The correlation fits the data well with a standard deviation of 8.4%. Figure 6.22 (b) compares the fit with the experimental points and shows the 95% confidence intervals based on the standard deviation.

The outlet temperature amplitude for the STR02 heat sink for various flowrates and inlet temperatures is presented in Figure 6.23 (a) as a function of the heat flux. In general, the temperature amplitude increases with increasing power as mentioned previously. The data has been correlated as a non-dimensional temperature utilizing the saturation temperature (in Kelvin) and set once again as a function of the Boiling number and Subcooling number. Fluid properties, as previously, have been calculated at the exit saturation temperature taken as 100 °C. From this, the following is obtained,

$$T^* = \frac{T_{amp}}{T_{sat}} = C_{10} Bo^{C_{11}} N_{sub}^{C_{12}}, \qquad (6.19)$$
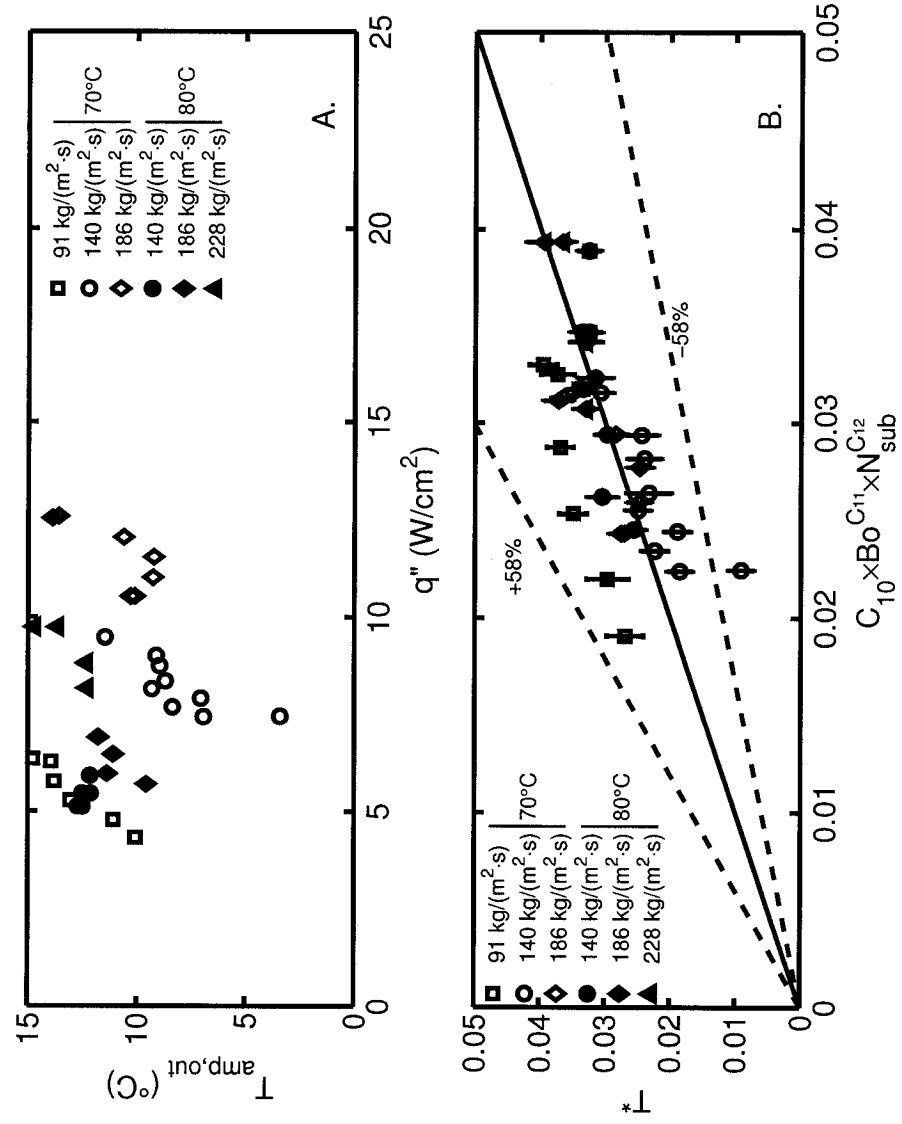
Figure 6.23: Outlet temperature oscillation amplitude versus power for STR02 at different flowrates and inlet temperature.

with the coefficients determined as, $C_{10} = 5.493 \times 10^7, C_{11} = 1.421$ and $C_{12} = -2.169$, or in dimensional form as,

$$T_{amp} = 5.493 \times 10^7 \times T_{sat} \left(\frac{q''}{Gh_{fg}} \right)^{1.421} \left[\frac{Cp\,(T_{sat} - T_{in})}{h_{fg}} \cdot \frac{\rho_f - \rho_g}{\rho_g} \right]^{-2.169} \quad (6.20)$$

in degrees Kelvin. Although there is a large degree of scatter, the correlation (Eq. 6.19) fits the data with a standard deviation of 25.5%. Figure 6.23 (b) compares the correlation fit with the experimental data and shows the 95% confidence intervals based on the standard deviation. The exponents show that increasing the Boiling number and hence the heat flux, will increase the inlet temperature amplitude, whereas an increased subcooling will have decreased amplitude.

6.4.4   Discussion

Although flow visualization was not performed, some conclusions on the type of oscillations may be obtained when compared with other recent findings. The frequency and amplitude data by Hetsroni et al. (2006) shows similar trends as the present. Additionally, these authors were able to track the period of oscillation of flow patterns in individual channels. The period of oscillation of the system, versus an individual channel from their work, has been calculated to range from 5 to 15 times. For the present data, the period of oscillation for the system ranged from 1.5 s to 10 s, compared to the liquid particle travel time, which was estimated to range from 0.06 s to 0.16 s, for a flowrate of 20 to 50 ml/min. This ratio of the system's oscillation period to the particle travel time, is on the order of 10 times and is similar to the range

184

of the data by Hetsroni et al. (2006). These qualitative and quantitative similarities lead to the conclusion that the present oscillation phenomena are explosive boiling oscillations, as described by Hetsroni et al. (2005a, 2006) and also observed by some other researchers (Steinke and Kandlikar, 2004a).

A note on the correlations presented follows. According to Yadigaroglu and Bergles (1972), density wave oscillation characteristics are governed by the combination of a variety of auxiliary phenomena. These include the heat capacity of the walls, the saturation enthalpy's dependency on the system pressure, the gas phase compressibility, the variation in heat transfer and the relative velocity between the phases. Although these auxiliary phenomena have been described for density wave oscillations, they are expected to also have some significance during explosive boiling oscillations. The correlations presented, are then considered applicable to parallel silicon wafer substrate microchannel systems flowing water, with a system pressure of 1 atm and for low mass flux ranges.

The flow boiling results presented did not include local heat transfer measurements for two reasons. First, the measurements with the first support used water. This was necessary, as the bond for the chip to the mid-plate was silicone based, a compound not compatible with FC-72 (as opposed to the element Silicon used for the heat sink fabrication). Boiling heat transfer measurements with water would require TLC's with temperatures greater than 100 °C which were not available. Secondly, flow boiling heat transfer measurements were indeed attempted with the second support using FC-72. However, during a degassing run, whereby significant vapour may be generated, a leak was produced in the bond between the heat sink and the top plate.

This leak was likely due to a combination of the moisture limits and rigidity of the UV adhesive utilized. Additionally, the large surface area which required bonding due to the multiple hole arrangement, also likely contributed to a weaker bond. For future investigations, a compliant adhesive is recommended. As well, using a single hole entry rather than multiple hole entry will eliminate the requirement for a transparent adhesive.

6.5 Summary

The flow and heat transfer characteristics of a cross-linked silicon microchannel heat sink have been presented. Relatively good agreement was obtained between air and water adiabatic pressure measurements compared with theoretical predictions, after accounting for inlet and outlet losses. No significant flow differences were observed between a standard and a cross-linked heat sink scheme for the cross-linked spacing investigated (cross-link width $\approx$ channel width).

Heat transfer measurements under single phase conditions were successfully obtained using the liquid crystal thermography methods developed in Chapter 4. Variations in the streamwise thermal profiles were observed due to the cross-links. These variations, however, were minor due to the narrow width of the cross-links used.

Flow boiling oscillations pose a restriction on the realization of MEMS based two-phase flow heat sinks for thermal management in demanding applications, for both terrestrial and extra terrestrial applications. The detailed flow characteristics of flow boiling instabilities in two different silicon microchannel heat sinks were presented.

186

One is a straight standard microchannel configuration, whereas the second contains cross-links along the channels. There were similarities in the characteristics of the flow boiling oscillations for both configurations and these may be summarized as follows,

1. Both configurations show a decreasing frequency of oscillation with increasing heat flux.

2. Flow oscillations for inlet temperature, outlet temperature and inlet pressure are at the same frequency.

3. In both configurations, the peak to peak amplitude for the oscillations increased with increasing heat flux.

The qualitative and quantitative characteristics of these oscillations are similar to the explosive boiling oscillations described in recent literature. Instability data were presented at two different inlet temperatures and a range of flowrates for the straight standard heat sink. The data showed that with increasing flowrate, the frequency of oscillations increased, whereas with decreasing inlet temperature, the oscillation frequency increased. The frequency and amplitude characteristics of these oscillations, for the standard heat sink at two different inlet temperatures, have been correlated with the Boiling number, the Subcooling number and Weber number. These correlations provide an intuitive means of interpreting the frequency and amplitude characteristics as a function of flowrate, inlet subcooling and heat flux, combined with a quantitative measure of their relation.

Chapter 7

Investigating a Radial Flow

Microchannel Heat Exchanger

This chapter investigates the heat transfer characteristics in a radial microchannel heat exchanger scheme. Radial flowing heat exchangers are of interest in scenarios of thermal management for other radially flowing microdevices. An example is the radial micro fuel cell presented by Pattekar and Kothare (2005). In this design, radial outward flow was utilized due to the use of varying channel cross-sections, for control of the chemical reaction. For thermal management of the fuel cell a radial heat exchanger may be utilized. Another prevalent radially flowing microdevice is the microturbine (Epstein, 2003). To improve thermal efficiency, reheat or intercooling stages can be introduced, and radial flow would be advantageous to accommodate the inherent radial flow of these devices.

7.1 Design and Fabrication Trials

A radially flowing heat exchanger was designed using similar criterion as the cross-linked heat sink. This criterion was that given a 3.5 cm foot print area with a heat flux of 25 W/cm^2, maintain a maximum temperature of 85 °C with a maximum 5 psi supply of single phase water. A similar thermal resistance analysis as described for the cross-linked heat sink was performed to size the radial design. The channel height was fixed at 300 μm, with a central plenum of 1 mm and a minimum wall thickness of 50 μm. Results from this analysis are presented in Figure 7.1. The figure compares the resulting maximum temperature and pressure demands for a variety of channel widths and flowrates. From the figure it is observed that to meet a maximum temperature of 85 °C, a channel width just over 100 μm is required, with a pressure supply just under 3 psi.

The designed heat sink is shown in Figure 7.2. It is a three-wafer stack consisting of a 550 μm thick silicon wafer base with a SiO_2 layer on its backside for electrical isolation. This base piece contains the microchannels fabricated via DRIE. A middle wafer, also fabricated from silicon and 330 μm thick, acts to isolate the incoming and outgoing flow streams. It is adhered to the base silicon wafer using a gold eutectic bonding technique. A Pyrex glass cover 500 μm thick is anodically bonded to the silicon stack. Eight circumferential holes are located on the glass cover for flow transfer. The holes are fabricated via drilling with a high speed diamond tipped drill. Flow may then enter radially inward or outward. Similar to the parallel channel design, a platinum heating element 1 mm wide and 186 mm long is deposited on

189
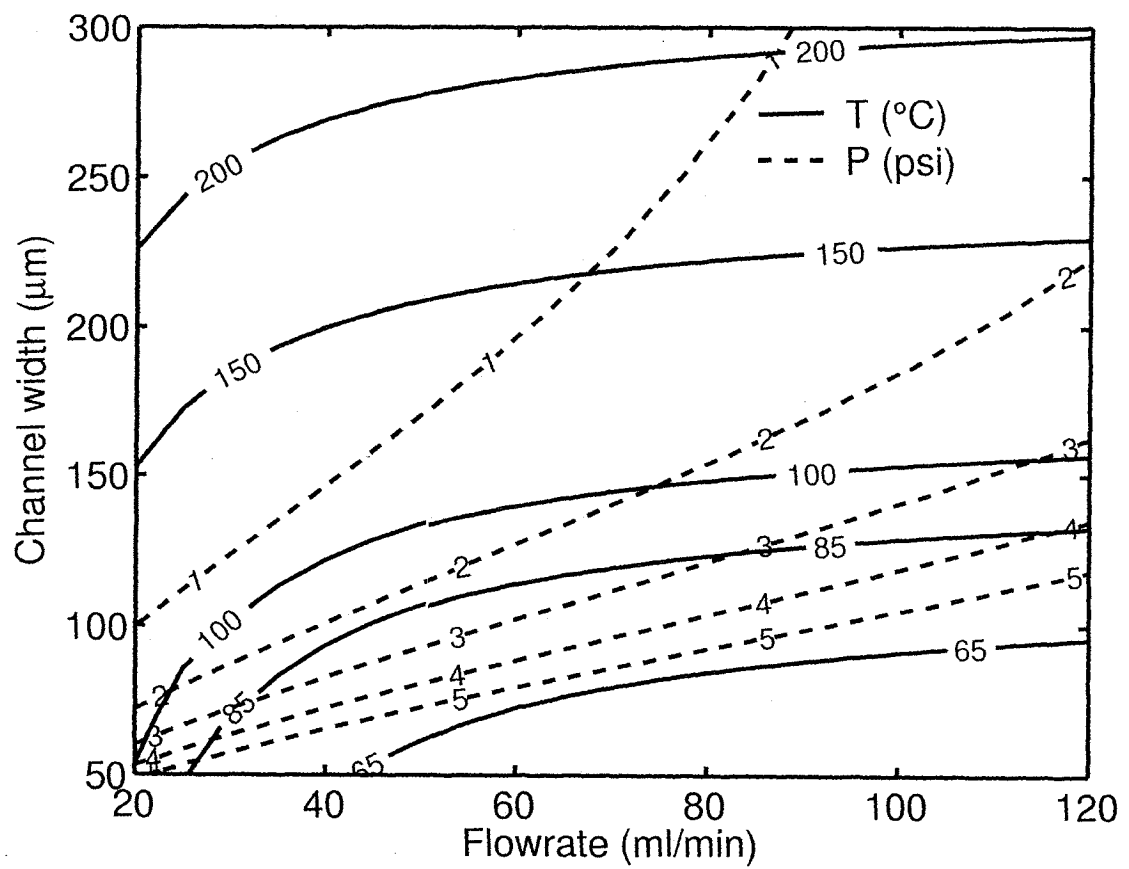
Figure 7.1: Radial concept analysis results.
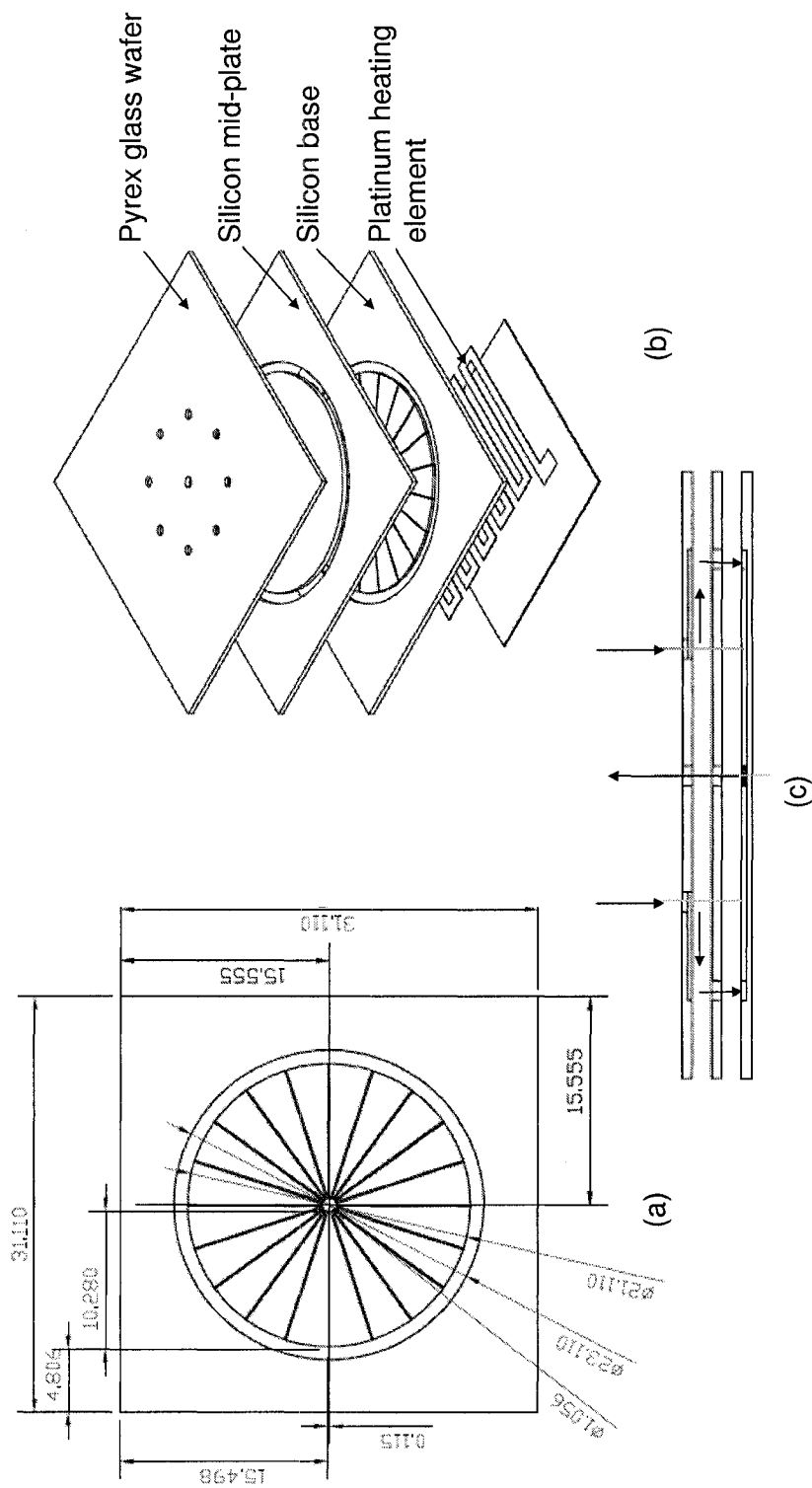
Figure 7.2: Radial heat sink.

191

the backside of the channel base to simulate the heated chip. Thermochromic liquid crystal material may then be deposited on top of the heating element, followed by a glass slide.

Fabrication trials were performed for this design by the Washington Technology Center's Microfabrication Lab. Unique in this design is the three-wafer stack composed of silicon to silicon to Pyrex. This posed unique challenges for its fabrication, particularly with respect to bonding the different layers. Additionally, drilling of the holes was difficult due to their close spacing and fractures between two holes would easily occur. One chip managed to pass through all the fabrication phases, and was provided for testing. During handling of this chip, however, the Pyrex to silicon bond delaminated. An attempt was made to seal it and continue with the testing. The seal, however, did not provide adequate support and during testing leaks between the Pyrex and silicon mid-plate were present. Further experimental work with the radial design was discontinued at that point until a reliable chip could be fabricated.

A potential benefit of a radially flowing heat exchanger is the geometries ability to easily incorporate varying cross-sectional area channels. For example, linearly converging channels for radially inward flow or linearly diverging channels for radially outward flow. As highlighted in the literature review, few works are available on the convective heat transfer characteristics of channels with slowly varying cross-sections. In the first part of this chapter, a thermal resistance model is adapted for use with radially inward flow channels with streamwise varying cross-section. The analysis evaluates the benefits and characteristics of flow in channels of varying cross-sections.

The second part of the chapter performs a similar investigation, but with a three-dimensional conjugate heat transfer model. For both analyses, the general heat sink dimensions are based on the fabricated design presented in this section.

7.2   Thermal Resistance Analysis

7.2.1   Mathematical Model

Microfabrication through techniques such as DRIE enables a variety of channel shapes to be fabricated. This section evaluates the possibility of improved performance with a linearly varying channel cross-section. Also considered is the influence of the wall heating condition. The model is an adaptation of the model by Bau (1998), which only considered a 3-wall heated boundary condition under fully developed flow conditions. This model was a one-dimensional thermal resistance network model which assumed steady state, laminar and incompressible flow within a heated parallel channel system. The present adaptations are 4-wall heating, 4-wall heating with thermally developing flow and radially configured channels. Thermally developing flow is more realistic for microsystems, since due to the large pressure drop, short channels are usually encountered. The fluid properties are taken as constant, viscous dissipation and axial conduction are neglected as are heat transfer due to natural convection and radiation.

The modeled region consists of a unit cell which is depicted in Figure 7.3. This cell consists of a single channel with a fixed height (H_{chn}) and length (L_{chn}) which spans the outer (r_{out}) to inner (r_{in}) radius. The wall thickness resistance is neglected
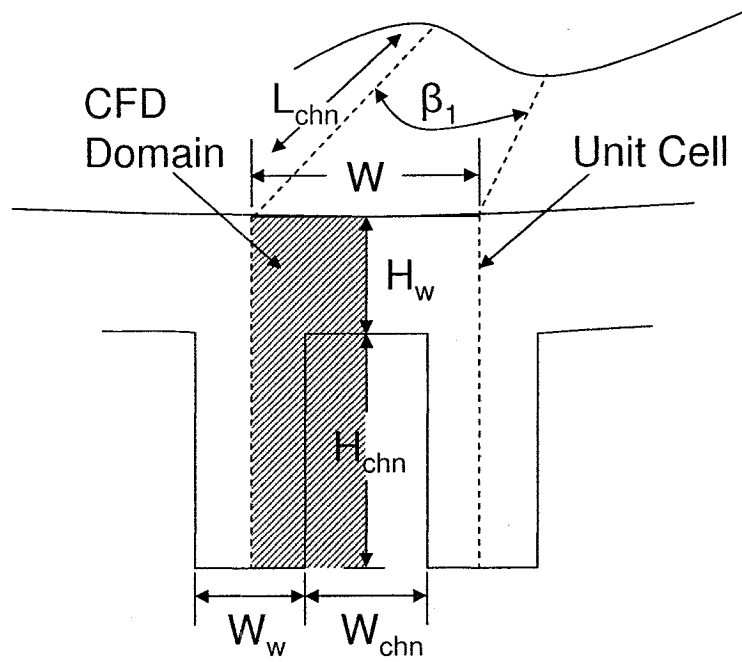
(a) Cross-sectional view.
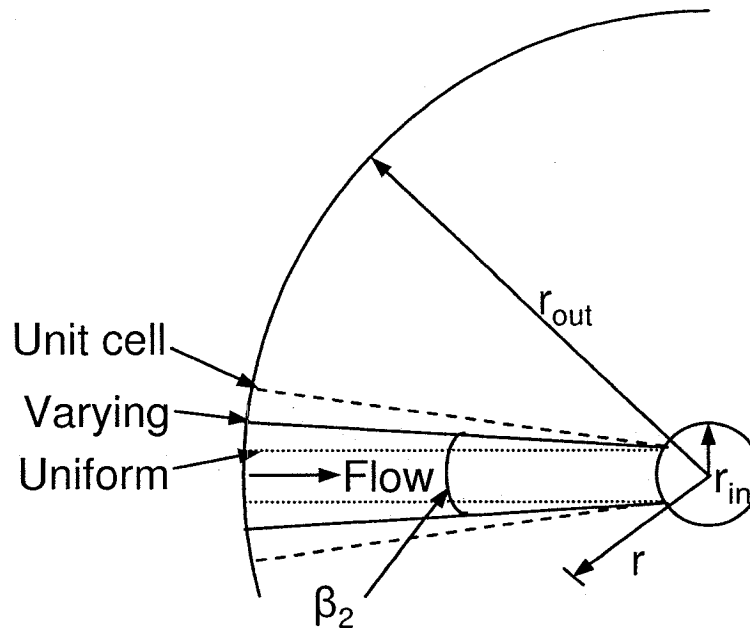
(b) Top view.

Figure 7.3: Modeling domain depiction.

assuming the material to have a high thermal conductivity. The channel width is defined as some continuous function of the axial location $(W_{chn}(r) = r\beta_2)$, whereas the channel height is constant. Correspondingly the channel aspect ratio, defined as the width to height ratio, is a function of the radial location $(\alpha = W_{chn}(r)/H_{chn})$.

The total thermal resistance is a combination of the convective thermal resistance (R_{conv}) and the calorimetric thermal resistance (R_{cal}). Considering convective transport within a single channel and due to a heat flux applied on the top outer wall, we have,

$$\left[\frac{q'' \pi \left(r_{out}^2 - r_{in}^2\right)}{N_{chn}}\right] \bigg/ A_{3/4} = h\left(r\right)\left(T_w\left(r\right) - T_b\left(r\right)\right). \tag{7.1}$$

The convective thermal resistance may then be derived as,

$$R_{conv} = \theta_w\left(r\right) - \theta_b\left(r\right) = \frac{2\alpha\pi \left(r_{out}^2 - r_{in}^2\right)}{Nu\left(r\right)\left(1 + \alpha\right)\left(L_{chn}H_{chn}\left(\frac{(\alpha_o + \alpha_i)}{2} + 2\right)\right)N_{chn}}, \tag{7.2}$$

for a 3-wall heated channel and

$$R_{conv} = \theta_w\left(r\right) - \theta_b\left(r\right) = \frac{2\alpha\pi \left(r_{out}^2 - r_{in}^2\right)}{Nu\left(r\right)\left(1 + \alpha\right)\left(2L_{chn}H_{chn}\left(\frac{(\alpha_o + \alpha_i)}{2} + 1\right)\right)N_{chn}} \tag{7.3}$$

for a 4-wall heated channel. θ is the non-dimensional temperature defined as,

$$\theta = \frac{T - T_{b,in}}{\frac{q'' H_{chn}}{k}}. \tag{7.4}$$

Numerically derived solutions of the Nusselt number under fully developed flow

for cases of 3 and 4 wall heated conditions, may be obtained from Shah and London (1978) as a function of aspect ratio. Similar to Bau (1998), the solutions for periphery constant wall temperature are taken. For thermally developing flow, Lee and Garimella (2006) recently provided a correlation based on numerical solutions for 4-wall heated conditions with constant heat flux. This was selected as data is not readily available for a constant periphery wall temperature, for a variety of aspect ratio channels and under thermally or simultaneously developing flow conditions.

For the calorimetric thermal resistance, an energy balance within the channel gives,

$$\frac{q'' \pi \left(r_{out}^2 - r^2\right)}{N_{chn}} = \dot{m} Cp \left(T_b\left(r\right) - T_b\left(r_{out}\right)\right). \tag{7.5}$$

Following the considerations by Bau (1998), the calorimetric thermal resistance is defined as,

$$R_{cal} = \theta_b\left(r\right) = \frac{\pi \left\{r_{out}^2 - \left(r_{out} - r^+ \left(r_{out} - r_{in}\right)\right)^2\right\}}{N_{chn}} \left(\frac{k_f}{Cp}\right) \left(\frac{1}{\dot{m}^* \cdot \dot{m}_o H_{chn}}\right) \tag{7.6}$$

where

$$r^+ = \frac{r_{out} - r}{r_{out} - r_{in}} \tag{7.7}$$

and

$$\dot{m}^* = \frac{1}{\left(\int_0^1 \frac{1}{8} Po\left(\alpha\right) \frac{(1+\alpha)^2}{\alpha^3} dr^+\right)}. \tag{7.8}$$

The parameter $\dot{m}_o$ is the characteristic mass flowrate parameter given by,

$$\dot{m}_0 = \frac{H_{chn}^4 \Delta P}{\nu L_{chn}}.$$

(7.9)

To obtain the above definition of calorimetric thermal resistance, Bau (1998) assumed the flow to be locally fully developed within the channel and the pressure drop due to acceleration to be negligible. The Poiseuille number ($Po(\alpha)$) has been obtained from Shah and London (1978) and is given by,

$$
\begin{aligned}
Po(\alpha) &= f\mathrm{Re} \\
&= 96[1 - 1.3553\alpha + 1.94673\alpha^2 - 1.7012\alpha^3 \\
&\quad + 0.9564\alpha^4 - 0.2537\alpha^5].
\end{aligned}
$$

(7.10)

This is a correlation for numerical solutions of fully developed flow within a channel of aspect ratio α. The total thermal resistance is then obtained from summation of the calorimetric and convective resistances. This is equivalently the wall temperature,

$$R_{tot} = \theta_w(r) = R_{conv} + R_{cal}.$$

(7.11)

Detailed presentation on the development of these equations may be found in the Appendix (Section C.1).

7.2.2 Problem Analysis

The performance criterion evaluated was the channel configuration which produces the smallest peak wall temperature and defined as,

$$\min\left[\max\left\{\theta_w\left(r\right)\right\}\right].\tag{7.12}$$

The aspect ratio may be defined as an Nth order polynomial,

$$\alpha\left(r\right)=\sum_{k=0}^{N}\alpha_k r^k.\tag{7.13}$$

For the present study, linear, quadratic and cubic polynomials were considered. The minimization of Equation 7.12 was performed using a Golden Section search and parabolic interpolation minimization routine available using the MATLAB `fminbnd` and `fminsearch` functions. The `fminbnd` function is a one parameter minimization routine and was used to optimize the uniform channel configurations. The `fminsearch` function is a multi-parameter minimization routine and was used for the varying cross-sectional channel searches. This function may produce local minima and hence was found to occasionally be start point dependent. For this reason, the channel configurations using this multi-parameter function are not identified as optimum, but improved.

General inputs for the analysis include a channel depth of 300 μm and an outer and inner radius of 11.05 mm and 0.5 mm respectively. The working fluid is water with properties set at 25 °C. Restrictions were placed on the channel width and the

fin width at exit to be at minimum 50 μm.

7.2.3 Results

The resulting channel configurations determined using the developed 1-D analysis for radially inward flowing channels, for a variety of boundary conditions, are presented in Figure 7.4. For the present conditions, at a heat flux of 25 W/cm^2, a difference of $\theta_w = 0.01$ translates into temperature difference of approximately 1.2 °C. In all cases, a lower peak temperature is obtained by using a converging channel. Looking at the uniform cross-sectional area channels, a consistent trend is observed. This trend shows a decreasing channel width with increasing pressure availability. The increased pressure allows for smaller channel diameters, which in turn improves the thermal performance. This is due to both higher heat transfer coefficients and increased convective surface area, due to more channels. For the channels with varying cross-sectional areas, however, such a trend is not readily observed. Comparing the channels with varying cross-sectional areas to uniform channels, in all cases the varying cross-sectional area channels have a wider inlet and a narrower exit for a given pressure drop. This is possible as the wider inlet provides a lower frictional resistance, and this added benefit may then be utilized at the narrower exit. The resulting wall profiles for the fully developed cases approach each other, both for uniform and varying cross-section configurations as the available pressure increases. The resulting non-dimensional temperatures are also similar, however, the magnitudes may vary substantially when considering the dimensional values.
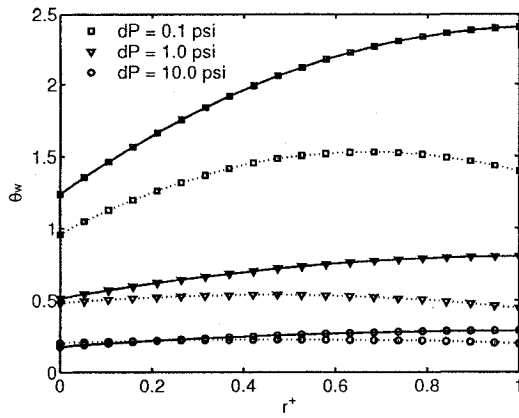
(a) 3-wall heated constant temperature, fully developed.
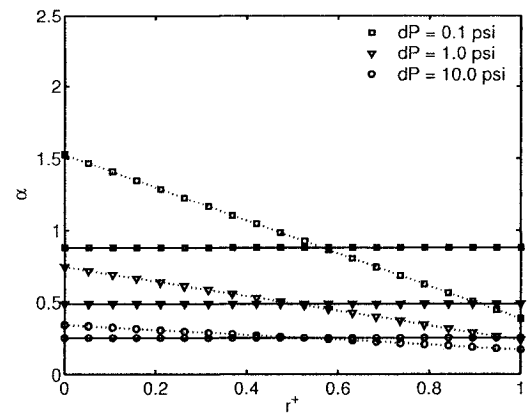
(b) 3-wall heated constant temperature, fully developed.
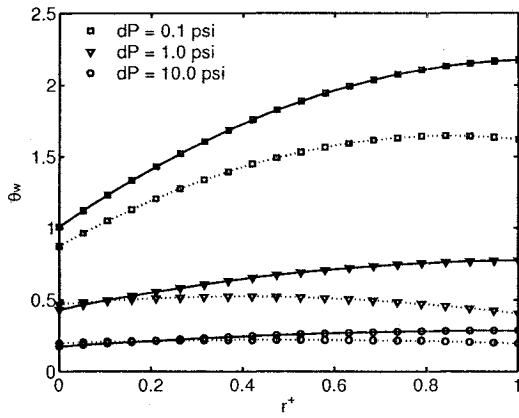
(c) 4-wall heated constant temperature, fully developed.
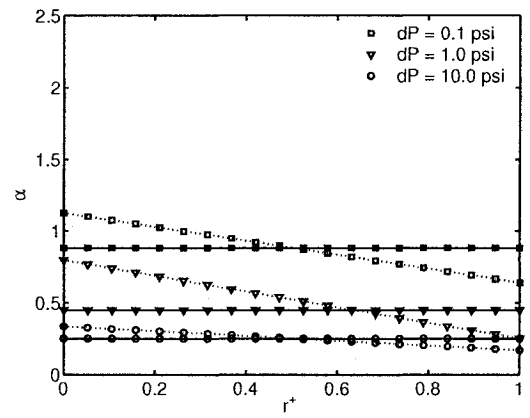
(d) 4-wall heated constant temperature, fully developed.
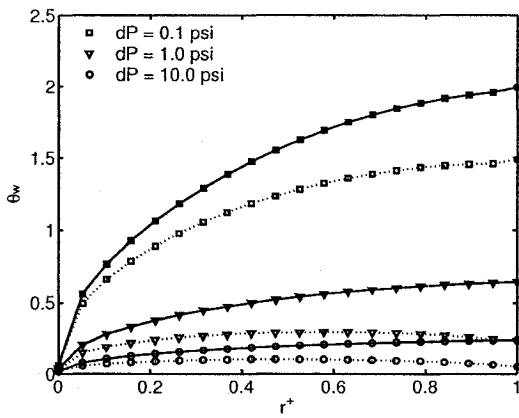
(e) 4-wall heated constant temperature, thermally developing.
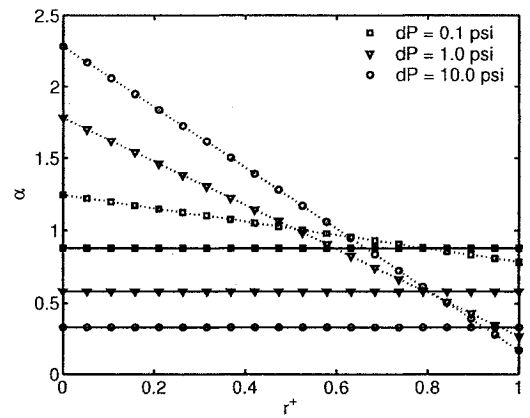
(f) 4-wall heated constant temperature, thermally developing.

Figure 7.4: Minimizing peak temperature: Linear profile. Solid lines are uniform channels and dashed lines are varying cross-sectional area channels.

Observing the wall temperature profiles in all cases, a non-linear rise in wall temperature is obtained. For 4-wall heated fully developed (Fig. 7.4 (c) & (d)) versus thermally developing flow (Fig. 7.4 (e) & (f)), a more realistic temperature profile is obtained whereby the initial wall to fluid temperature difference approaches zero and rises rapidly due to the developing thermal boundary layer. Comparing Figures 7.4 (c) and (e), for the uniform channels, the influence of a fully developed versus a thermally developing profile influences the entrance characteristics. The exit temperatures, however, are similar and the peak occurs at the exit. Therefore, in terms of minimizing the peak temperature, if considering uniform channels, fully developed and thermally developing flows will provide a similar conclusion. However, this is substantially different when considering a channel with linearly varying cross-section in a radial configuration. Although the exit temperatures are similar in magnitude, the peak does not necessarily occur at the exit. Subsequently, the improved configuration can be significantly different depending on whether fully developed or thermally developing flow is used.

The previous case considered a fixed fin width at the channel exit. The exit fin width will depend on fabrication constraints and structural requirements. Figure 7.5 shows the resulting wall temperatures and channel configuration for exit fin widths of 0 μm, 50 μm and 100 μm. No general trend in channel configurations is observed with increasing exit fin width and pressure supply. The wall temperatures, however, increase with increasing exit fin width. This is due to a decreasing number of channels with increasing fin width and is further due to the decreased area available. It would be advantageous to have a zero thickness exit fin width, however based on design
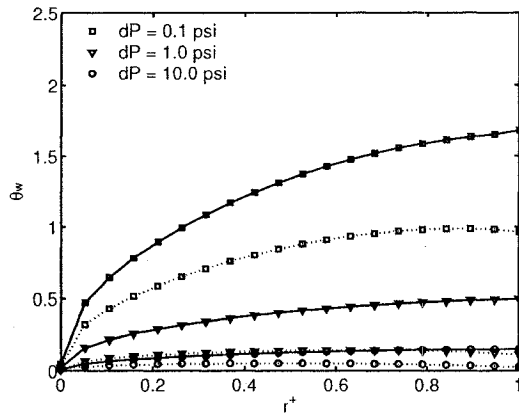
(a) θ_w, Minimum fin width $= 0$ μm.
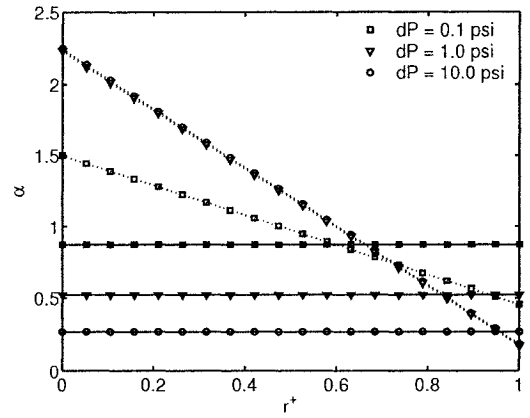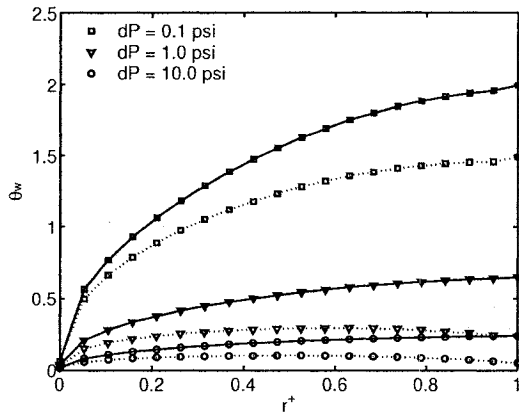
(b) α, Minimum fin width $= 0$ μm.

(c) θ_w, Minimum fin width $= 50$ μm.
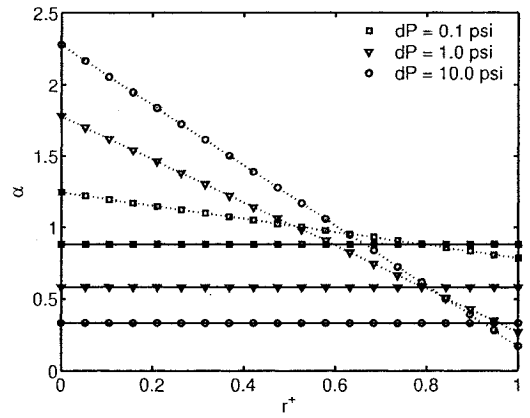
(d) α, Minimum fin width $= 50$ μm.
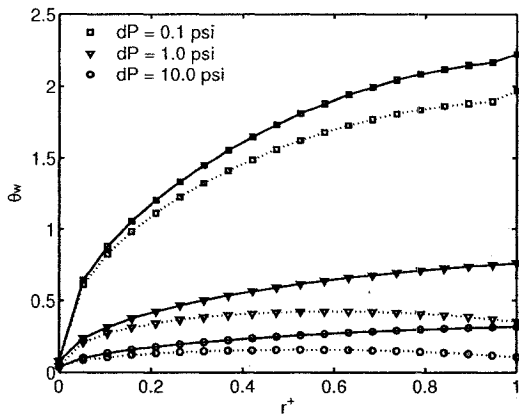
(e) θ_w, Minimum fin width $= 100$ μm.
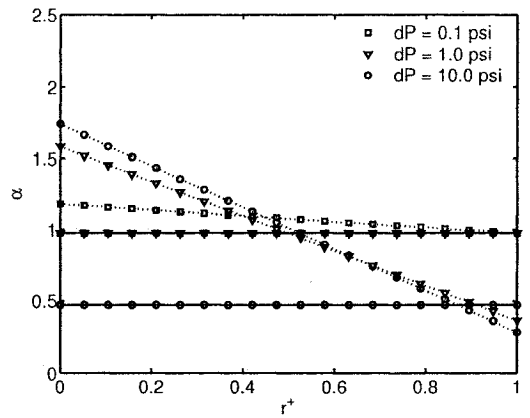
(f) α, Minimum fin width $= 100$ μm.

Figure 7.5: Minimizing peak temperature: Influence of fin width for thermally developing, 4-wall heated channels. Solid lines are uniform channels and dashed lines are varying cross-sectional area channels.

and fabrication constraints, the present results show that the characteristics of the improved channel configuration will be design specific.

7.3   Three-dimensional Conjugate Analysis

The results presented in the previous section are limited by the assumptions incorporated. Particular assumptions that may have significance for actual microchannel systems are the flow development (thermally and hydrodynamically), negligible axial conduction and constant fluid properties. An investigation was carried out on a radially inward flowing micro- heat exchanger, using a three-dimensional conjugate heat transfer model.

7.3.1   Formulation and Solution Methodology

The computational domain is the shaded region depicted in Figure 7.3 (a), spanning the full radius. It is composed of a single half-section of a channel and fin portion, with the adjacent surfaces set to symmetry boundary conditions. The top outer wall is heated by a constant heat flux and the base wall is adiabatic. All other outer walls are also set to adiabatic. The inlet is set to pressure inlet or uniform velocity depending on the case being evaluated, while the outlet is set to zero gage pressure. The solid material is silicon ($k = 157$ W/m·K), while the fluid is water with properties obtained from Collier and Thome (1999). The modeling assumptions were as follows:

- Steady state flow and heat transfer,

- Laminar flow,

- Constant solid properties and temperature dependent fluid properties,

- Negligible radiation heat transfer.

The commercial package Gambit 2.0 is used for grid generation. A structured mesh with hexahedral elements is used in all the test cases.

The analysis is carried out using the commercial package FLUENT 6.1 to solve the continuity, momentum and energy equations within the fluid and given by,

$$\nabla \cdot \left(\rho \vec{V} \right) = 0, \tag{7.14}$$

$$\vec{V} \cdot \nabla \left(\rho \vec{V} \right) = -\nabla P + \nabla \cdot \left(\mu \nabla \vec{V} \right) \tag{7.15}$$

$$\vec{V} \cdot \nabla \left(\rho C_p T \right) = \nabla \cdot \left(k \nabla T \right), \tag{7.16}$$

and the conduction equation within the solid given by,

$$\nabla \cdot \left(k \nabla T \right) = 0. \tag{7.17}$$

Discretization of pressure, velocity and energy terms is through a second order upwind scheme. Coupling of pressure and velocity is performed using the SIMPLE algorithm. Finally, the solution of the equations is through a Segregated solver.

7.3.2   Benchmark Study and Grid Independency Evaluation

A benchmark investigation was performed to evaluate the efficacy of the modeling method and assumptions. The selected case was from the study by Lee and Garimella

(2005). This study involved heat transfer investigations in a copper substrate with 10 channels. The selected case consisted of 194 μm wide by 884 μm deep channels (D_h=318 μm), 25.4 mm long. The simulated domain and boundary conditions are similar to those intended for the radial heat sink. The domain consisted of one half the channel width and wall thickness and the full channel length. Symmetry boundary conditions were applied on the side surfaces, a uniform heat flux on the top surface and adiabatic conditions on the bottom surface. The flow was taken as laminar, with pressure boundary conditions and temperature dependent fluid properties. The double precision form of FLUENT was necessary to produce reasonably decreasing residuals. A number of grid densities were evaluated and by tracking the outlet temperature a grid density of 50 × 220 × 120 was deemed satisfactory. The results from the mesh evaluations are presented in Table 7.1. A comparison of the average Nusselt number from the selected mesh and experimental data are shown in Figure 7.6. The figure shows that satisfactory agreement is obtained when compared to the experimental data. Lee and Garimella (2005) also performed numerical simulation with a half channel section using FLUENT. Satisfactory agreement was obtained with their experimental data using a mesh of 50 × 160 × 100 cells. Their study however neglected the temperature dependence of the fluid properties. Discrepancies between the present numerical results and the experimental data, are likely due to a combination of experimental error and data reduction of the experimentally defined average Nusselt number. Experimental errors were quoted in the range of 6 to 17% and estimates with the present data show differences of about 12% at $Re = 800$ and 4% at $Re = 400$. The average Nusselt number was obtained from four thermocouples located

205

Table 7.1: Benchmark grid study.

Case	Mesh ($W_{chn} \times H_{chn} \times L_{chn}$)	T_{out}	% change
1	$30 \times 40 \times 50$	308.9783	-
2	$40 \times 100 \times 100$	309.1931	0.070
3	$50 \times 160 \times 100$	309.225	0.010
4	$50 \times 220 \times 120$	309.2292	0.001
5	$60 \times 280 \times 150$	309.235	0.002
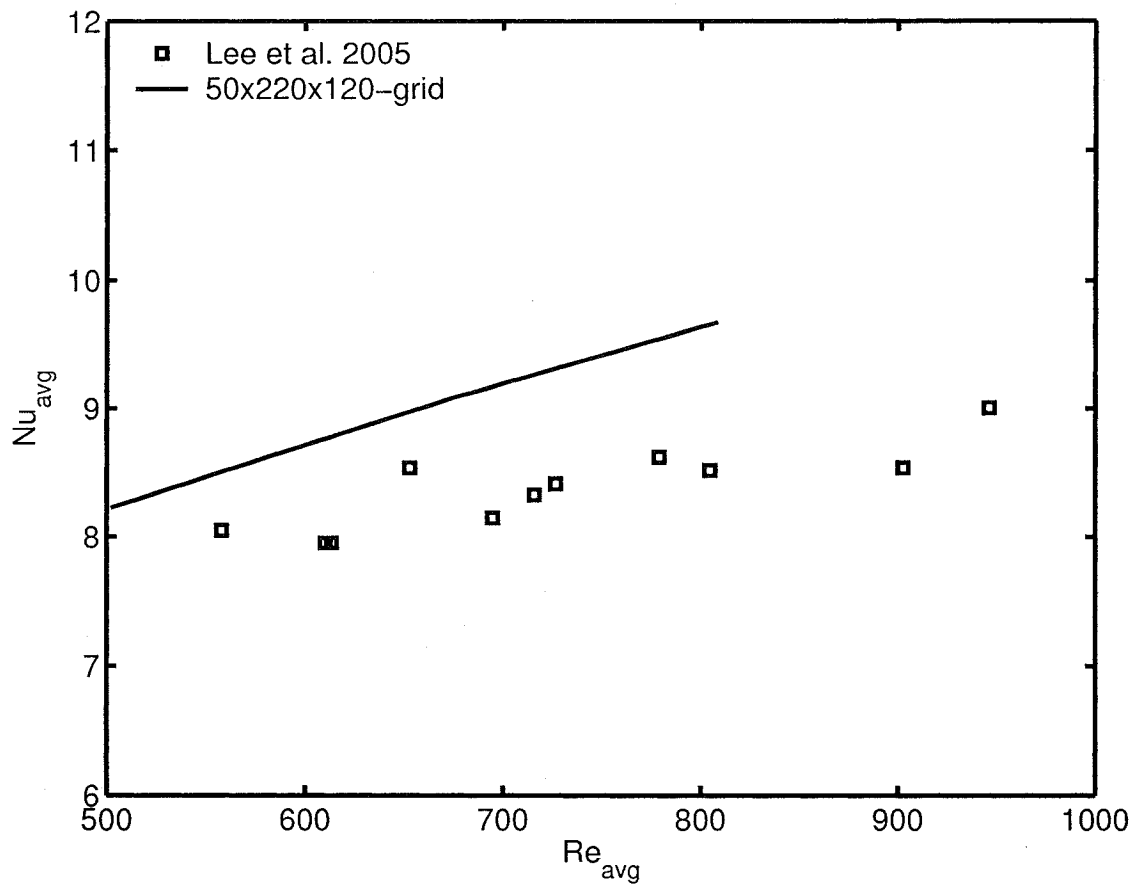
Figure 7.6: Benchmark grid comparison with experimental data.

along the channel and placed a distance from the fluid-wall interface. Additionally the wall temperature was calculated based on a one-dimensional extrapolation of the thermocouple temperature.

Considering now the radial scheme, two grid sizes were evaluated with mesh densities of $50 \times 160 \times 100$ and $50 \times 220 \times 120$. The percent change in outlet temperature was 0.001% and hence the $50 \times 220 \times 120$ grid size was selected for the study.

7.3.3 Results

A number of configurations of varying cross-sectional area channels were analyzed and compared to a uniform channel with an inlet and outlet aspect ratio of 0.5. A summary of the test cases are listed in Table 7.2. For all the test cases the outlet aspect ratio is set to 0.5 with a channel height of 300 μm. The aspect ratio of 0.5 was selected based on the results from the one-dimensional thermal resistance analysis, at a pressure of 6895 Pa (1 psi). The channel height was selected based on the fabrication considerations. The cases considered were the influence of inlet width for aspect ratios ranging from 0.4 to 1.0, for a fixed pressure drop and a heat flux ranging from 25 W/cm^2 to 62.5 W/cm^2 . Similarly the influence of inlet width for inlet aspect ratios ranging from 0.4 to 1.0, but for a fixed mass flowrate and a heat flux of 25 W/cm^2. The influence of inlet height for aspect ratios of 0.4, 0.5 and 1.0 for a fixed pressure drop and a heat flux of 25 W/cm^2. In the last case both the inlet height and width were variable and the inlet aspect ratio fixed at 0.5, for a fixed pressure drop and a heat flux of 25 W/cm^2.

Table 7.2: 3-D CFD simulation test matrix. Below dimensions in millimeters. $W_{out} = 0.15$ mm & $H_{out} = 0.30$ mm throughout. $q_1'' = 25$ W/cm², $q_2'' = 43.75$ W/cm², $q_3'' = 62.5$ W/cm² and $q_3'' = 62.5$ W/cm², $\Delta P_{fixed} = 6.9$ kPa and $\dot m_{fixed} = 2.85 \times 10^{-5}$ kg/s.

α_{in}	$H_{in} = 0.300$				$W_{in} = 0.150$	$\alpha_{in} = \alpha_{out} = 0.5$
	ΔP_{fixed}			$\dot m_{fixed}$	ΔP_{fixed}	ΔP_{fixed}
	q_1''	q_2''	q_3''	q_1''	q_1''	q_1''
0.4	$W_{in} = 0.120$	$W_{in} = 0.120$	$W_{in} = 0.120$	$W_{in} = 0.120$	$H_{in} = 0.375$	$W_{in} = 0.120$ & $H_{in} = 0.240$
0.45	$W_{in} = 0.135$	$W_{in} = 0.135$	$W_{in} = 0.135$	-	-	-
0.5	$W_{in} = 0.150$	$W_{in} = 0.150$	$W_{in} = 0.150$	$W_{in} = 0.150$	$H_{in} = 0.300$	$W_{in} = 0.150$ & $H_{in} = 0.300$
0.55	$W_{in} = 0.165$	$W_{in} = 0.165$	$W_{in} = 0.165$	-	-	-
0.6	$W_{in} = 0.180$	$W_{in} = 0.180$	$W_{in} = 0.180$	-	-	$W_{in} = 0.180$ & $H_{in} = 0.360$
0.8	$W_{in} = 0.240$	$W_{in} = 0.240$	$W_{in} = 0.240$	$W_{in} = 0.240$	$H_{in} = 0.1875$	$W_{in} = 0.240$ & $H_{in} = 0.480$
1	$W_{in} = 0.300$	$W_{in} = 0.300$	$W_{in} = 0.300$	-	-	-

Figure 7.7 presents the maximum surface temperature determined for the various test cases. With increasing inlet width and thus increasing aspect ratio, a decreased maximum temperature is obtained. Equivalently with an increasing inlet height and thus decreasing aspect ratio, decreased maximum temperature is obtained. In the case of a fixed aspect ratio, increasing the inlet area similarly decreases the maximum temperature. The average surface temperature plots showed similar trends to the maximum surface temperature.

The decreasing peak temperature with increasing inlet aspect ratio is primarily due to the increasing flowrate. Figure 7.8 (a) shows the mass flowrate for various heat fluxes as a function of inlet aspect ratio and the thermal resistance also as a function of inlet aspect ratio (Figure 7.8 (b)), for fixed height channels. Note that the total thermal resistance in Figure 7.8 (b) is calculated from the summation of the convective and calorimetric resistances, whereby the convective resistance is based on the channel averaged heat transfer coefficient. Increasing the inlet aspect ratio increases the mass flowrate (Fig. 7.8 (a)) which in turn will decrease the calorimetric thermal resistance (Fig. 7.8 (b)). The diverging channels ($\alpha_{in} < 0.5$) will produce higher heat transfer coefficients and hence lower convective resistance. However, the benefit in heat transfer coefficient due to decreased channel inlet size is not significant compared to the mass flow benefit for increased channel inlet size. This arises due to the restriction on the number of channels, which is subsequently due to the restriction of the exit radius and fin width at the exit.

The mass flow alone, however, is not the only criterion for improved heat transfer. This is observed in the fixed pressure drop case of $\alpha_{in} = 0.6$ (0.3mm×0.18mm) and
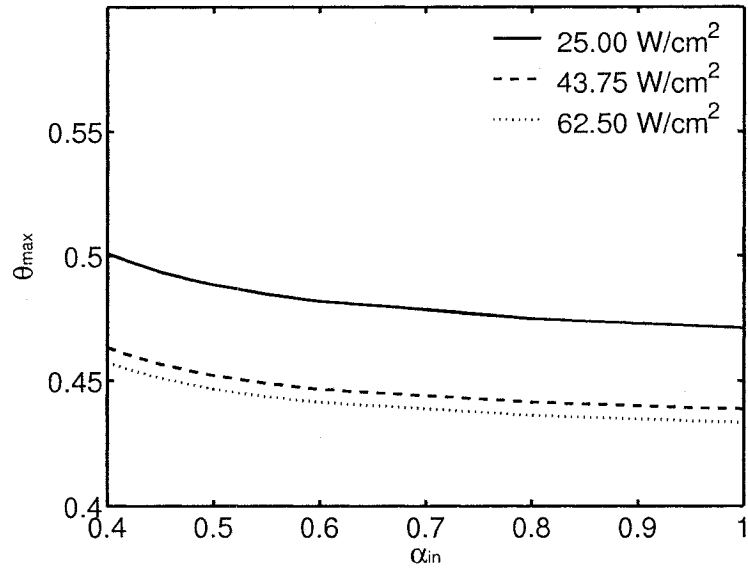
(a) Influence of heat flux.
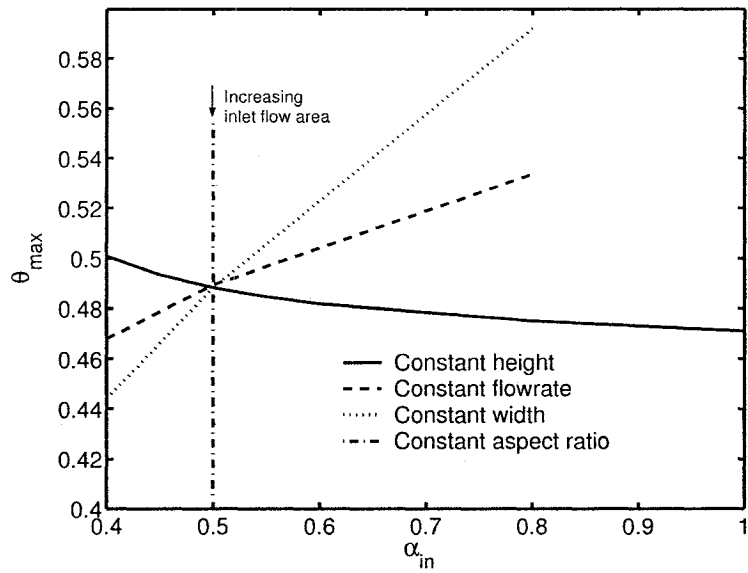
(b) Influence of geometry.

Figure 7.7: Maximum surface temperature versus aspect ratio.
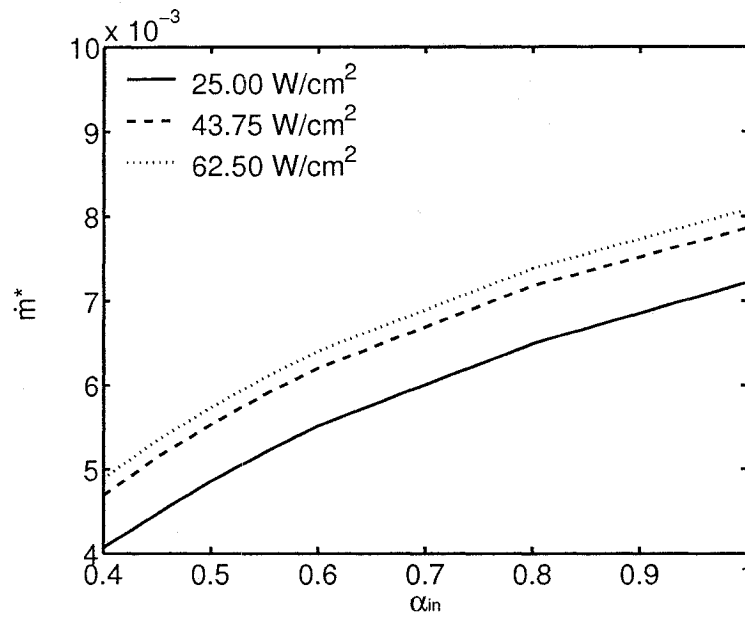
(a) Non-dimensional mass flowrate
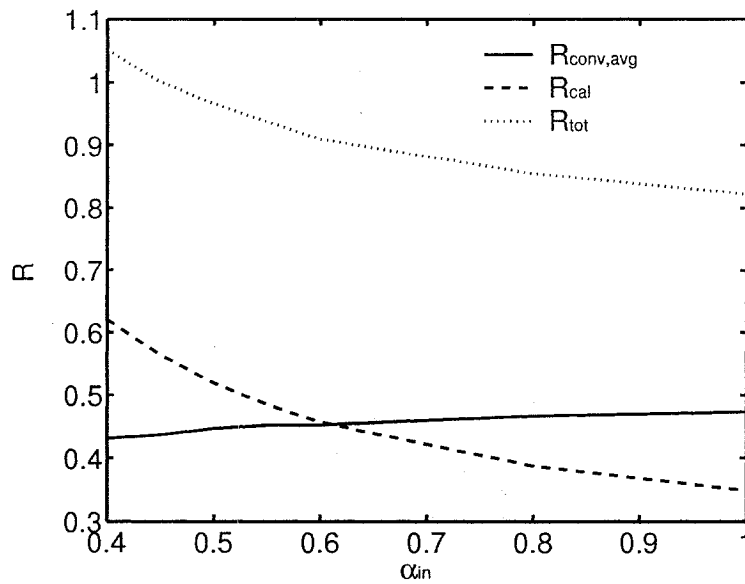
(b) Thermal resistance

Figure 7.8: Evaluation of optimal aspect ratio.

212

$\alpha_{in} = 0.4$ (0.15mm×0.375mm), which are fixed height and fixed width cases. Their inlet cross-sectional areas are within 4.2% of each other, with $\alpha_{in} = 0.6$ having the lower cross-sectional area. The mass flowrates, however, are reversed with $\alpha_{in} = 0.4$ having a mass flowrate approximately 3.8% lower than $\alpha_{in} = 0.6$. Looking at Figure 7.7, however, an aspect ratio of 0.4 produces the lower maximum temperature ($\theta_{max} = 0.44$), compared to an aspect ratio of 0.6 ($\theta_{max} = 0.48$). This is primarily due to the differences in heat transfer coefficients, with the aspect ratio of 0.6 having an average Nusselt number of 8.6, whereas the aspect ratio of 0.4 produces an average Nusselt number of 14.0. Some benefit is also likely gained from a reduced inner to outer wall thickness for the 0.4 aspect ratio case, due to a larger height.

In Figures 7.9 and 7.10, the fluid bulk and inner wall temperature characteristics of the radial heat exchanger are presented. The fluid bulk temperature is calculated based on an energy weighted average, whereas the wall temperature is calculated based on an area weighted average. In all cases, the fluid bulk temperature shows a non-linear rise with increasing distance. A lower fluid bulk temperature rise is observed for cases with lower maximum wall temperatures. This is because the lower maximum temperature was obtained from an increase in mass flow. Due to a balance of energy then, for the same heat flux, a lower fluid bulk temperature rise will be obtained when the mass flowrate is increased. This is also a consequence of the fluid property changes having minimal influence. The inner wall temperature shows a different inner wall temperature trend compared to parallel channel systems. The inner wall temperature rises until approximately 50% of the length then drops. The rising wall temperature is expected due to the increasing fluid temperature. The drop,
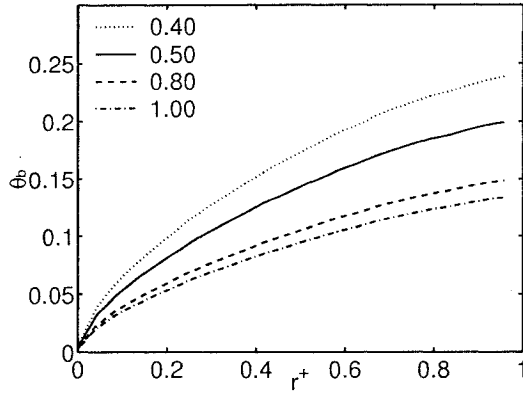
(a) Constant channel height, various inlet aspect ratios.
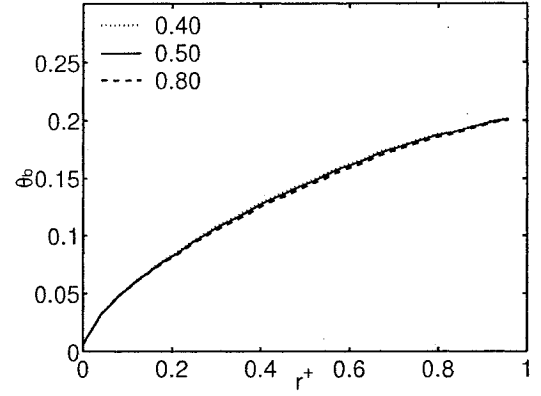
(b) Constant mass flowrate, various inlet aspect ratios.
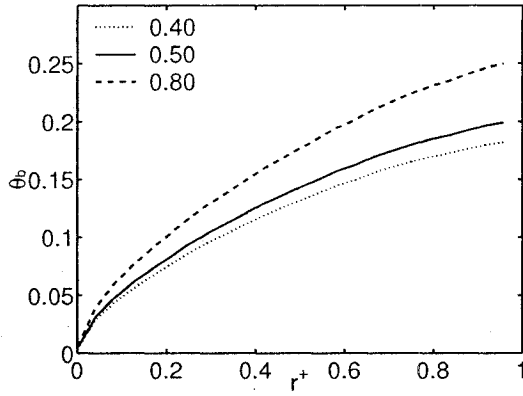
(c) Constant channel width, various inlet aspect ratios.
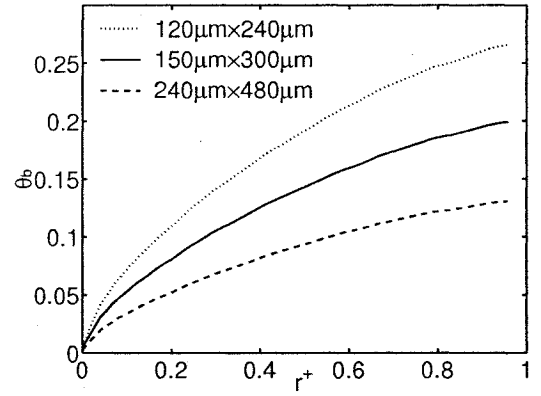
(d) $\alpha_{in} = 0.5$, various inlet areas.

Figure 7.9: Fluid bulk temperature.

however, arises from the thinning of the wall fins inherent in the radial configuration. In the case of a fixed mass flowrate (Fig 7.9 and 7.10 (b)), the fluid temperature rise is the same for all the cases. However, a lower inner wall temperature is obtained with inlet aspect ratio of 0.4. This results from a higher Nusselt number for the 0.4 aspect ratio channel, compared to the 0.8 aspect ratio channel under the same mass flow conditions.

Local Nusselt numbers for the various cases are presented in Figures 7.11 and 7.12 and are based on the local hydraulic diameters. In all cases, the local Nusselt values range from approximately 21 to 5. Additionally, they are still decreasing at the exit signifying that the flow is still thermally developing. For a 3-wall heated channel under fully developed conditions and for an aspect ratio of 0.5 with constant periphery wall temperature, the Nusselt number is 3.842 (Shah and London, 1978).

Considering varying channel inlet widths (fixed height, Fig. 7.11) at fixed heat fluxes, the Nusselt number changes only slightly between the cases. Additionally, the local Nusselt values rise slightly with increased channel width. Similarly in the case of varying channel inlet heights (fixed width, Fig. 7.12 (b)), the Nusselt number slightly rises with increased channel height. In general, an increase in the inlet area will produce a slightly higher Nusselt value for a fixed pressure drop.

Contours of the temperature resulting in a uniform channel and a converging channel of the same aspect ratio ($\alpha = 0.5$) are presented in Figures 7.13 and 7.14 respectively. Looking at the uniform channel case, Figure 7.13 (a) shows the surface temperature, with the channel located along the centre. The surface temperature
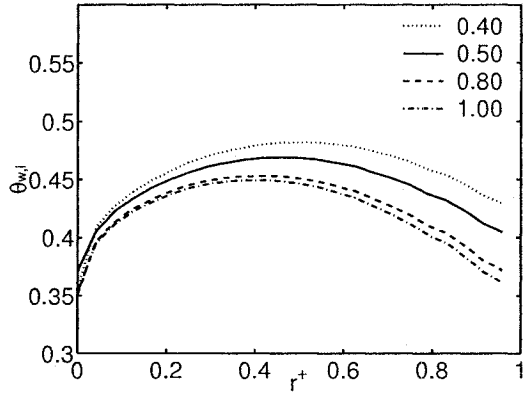
(a) Constant channel height, various inlet aspect ratios.
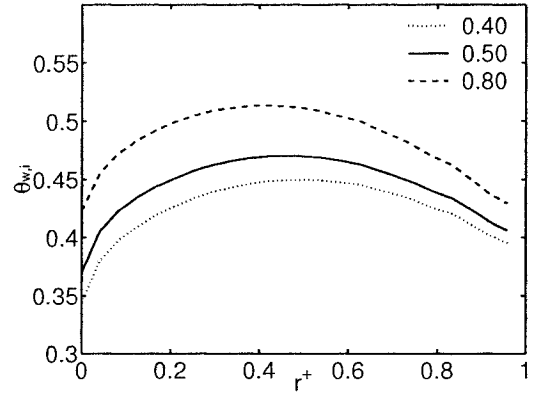
(b) Constant mass flowrate, various inlet aspect ratios.
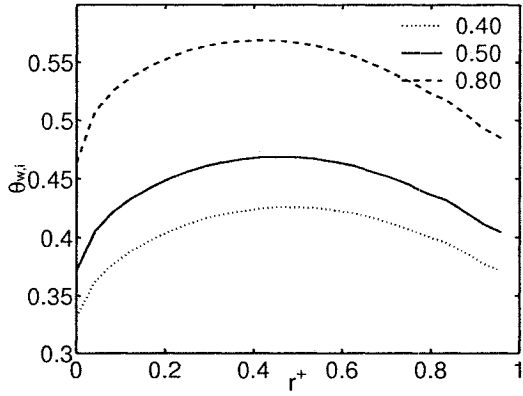
(c) Constant channel width, various inlet aspect ratios.
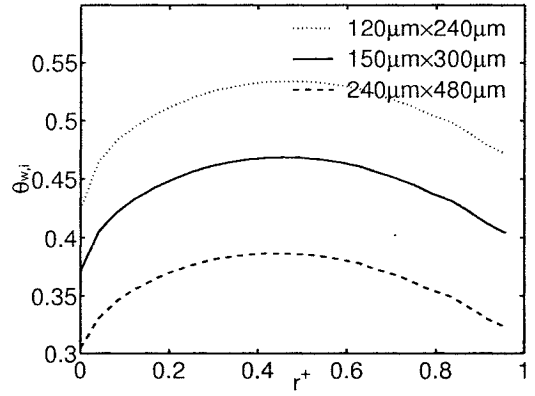
(d) $\alpha_{in} = 0.5$, various inlet areas.

Figure 7.10: 3-wall heated area average temperature.

(a) $q'' = 25.00$ W/cm^2.

(b) $q'' = 43.75$ W/cm^2.

(c) $q'' = 62.50$ W/cm^2.
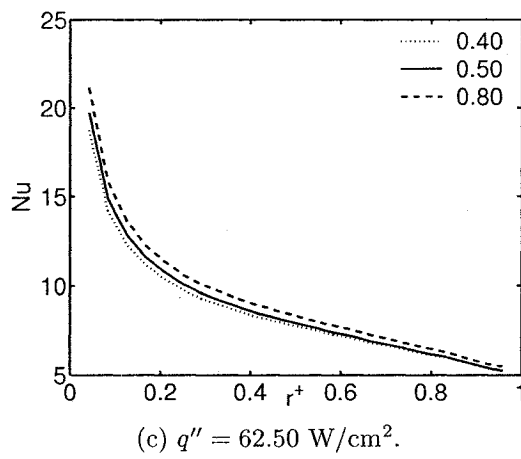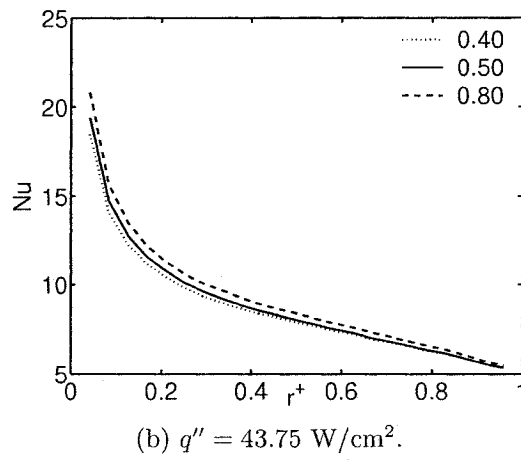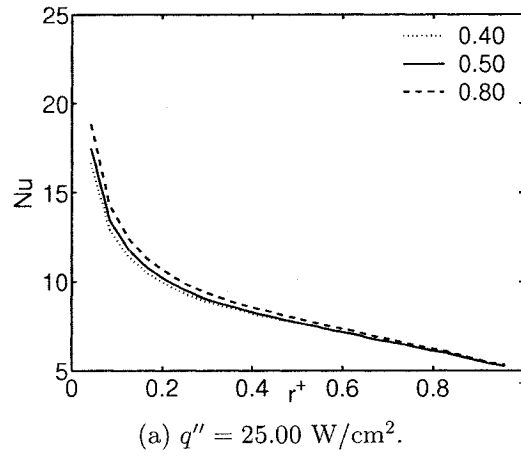
Figure 7.11: 3-wall heated area averaged Nusselt numbers for various heat flux and fixed channel height.
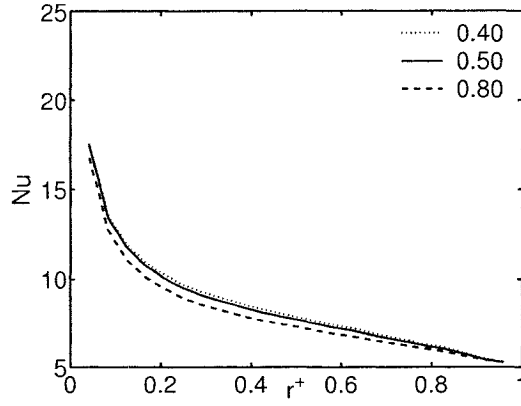
(a) Constant mass flowrate, various inlet aspect ratios.
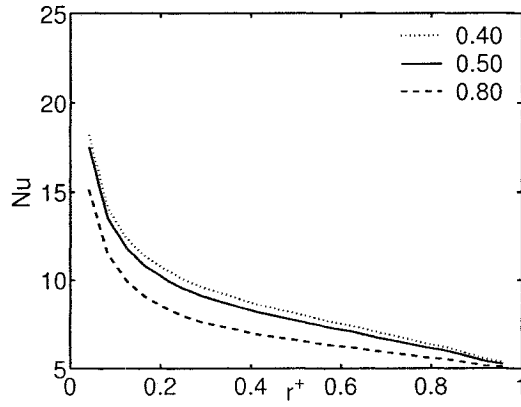
(b) Constant channel width, various inlet aspect ratios.
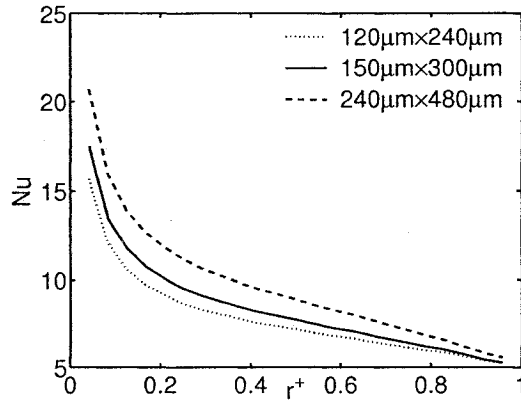
(c) $\alpha_{in} = 0.5$, various inlet areas.

Figure 7.12: 3-wall heated area average Nusselt numbers for various configurations.

218

shows the elevated temperature to lie in the mid-streamwise section, with the inlet and outlet temperatures both cooler. This is similarly related to the inner wall temperature rise and drop that was presented earlier (Fig. 7.10). Cross-sections of the silicon wafer temperature gradients normal to both inner wall surfaces, spread over a large distance at the inlet plane (Fig. 7.13 (b)). For subsequent planes, the reduction in area causes both a lower temperature gradient and spread. The inner wall temperature contours (Fig. 7.13 and 7.14 (c)) show that the temperature is somewhat constant around the periphery in the inlet and outlet regions. However, as the center of the channel is approached, the periphery temperature is increasingly more non-uniform. Comparing the uniform and converging channels, similar trends in the profiles are observed. The magnitudes, however, are significantly different as expected from the averaged plots presented earlier.

The velocity contours for the symmetry plane of a uniform channel ($\alpha = 0.5$) under varying heat flux, are presented in Figure 7.15. With an increase in heat flux, higher velocities are attained. This is expected as the fluid's viscosity decreases with increased temperature, providing a lower flow resistance. The velocity contours are also observed to be unsymmetrical with respect to the height, with higher velocity gradients obtained on the upper half of the channel. This is related once again to viscosity changes in the fluid, as the upper wall is heated and thus the fluid bulk temperature is hotter on the upper half.

Similarly, Figure 7.16 shows velocity contours for the symmetry plane for different geometrical configurations. Figure 7.16 (a) is for a channel with decreasing width, (b) is for a channel with decreasing height and in (c) both the width and the height are
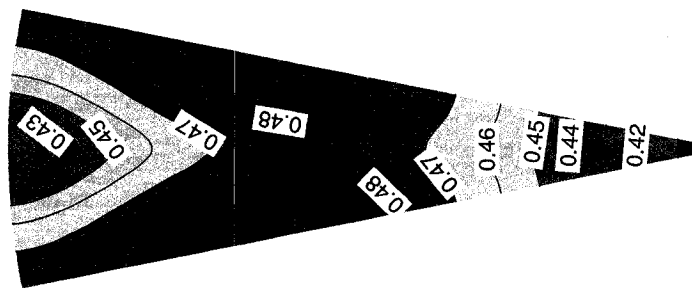
(a) Heated surface.
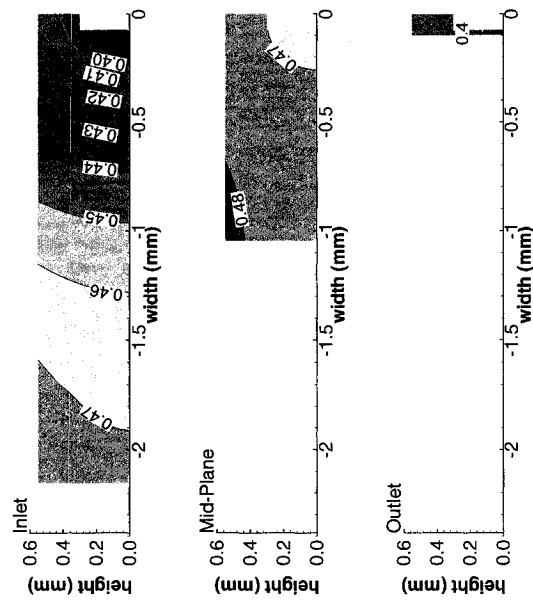
(b) Silicon cross-section.
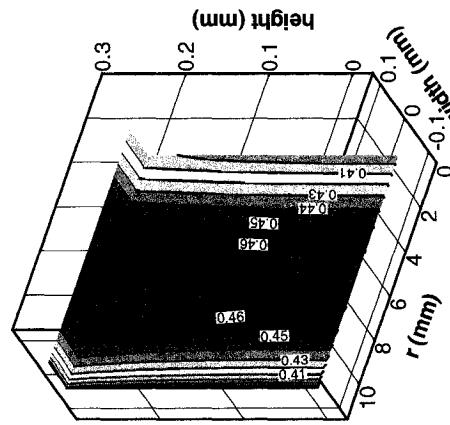
(c) Inner wall.

Figure 7.13: Non-dimensional temperature contours, uniform channel ($\alpha = 0.5$).
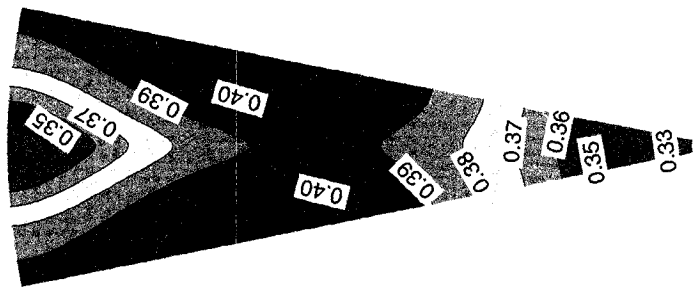
(a) Heated surface.
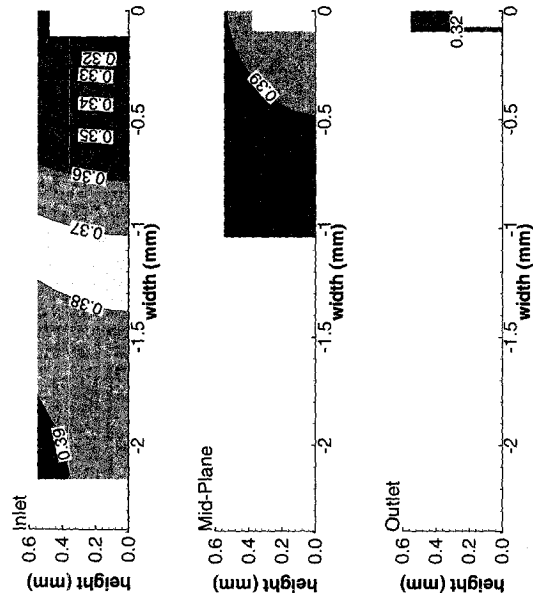
(b) Silicon cross-section.
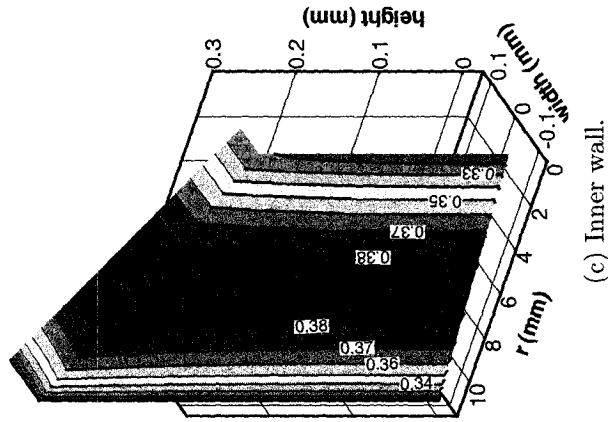
(c) Inner wall.

Figure 7.14: Non-dimensional temperature contours, converging channel with inlet area of $240 \mu m \times 480 \mu m$ ($\alpha_{in} = 0.5$).
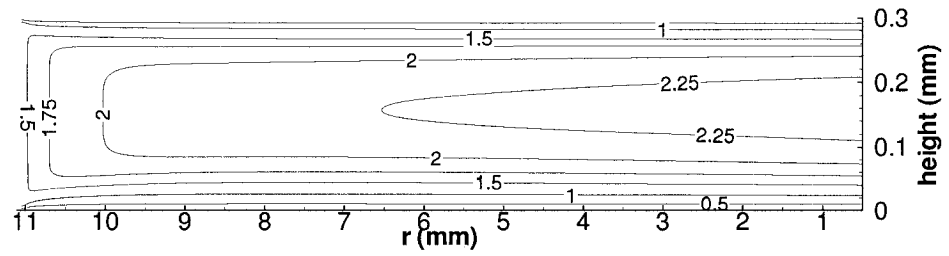
(a) $q'' = 25.00$ W/cm^2.
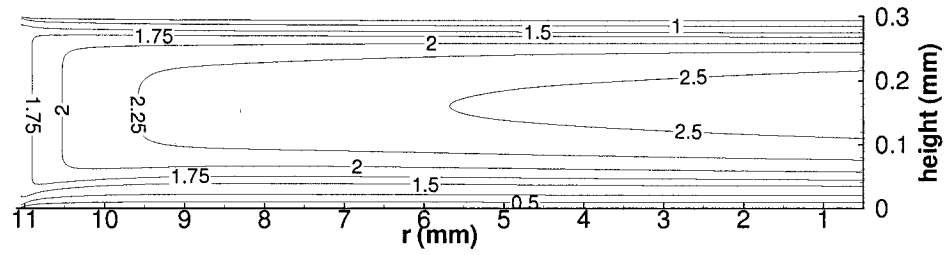
(b) $q'' = 43.75$ W/cm^2.
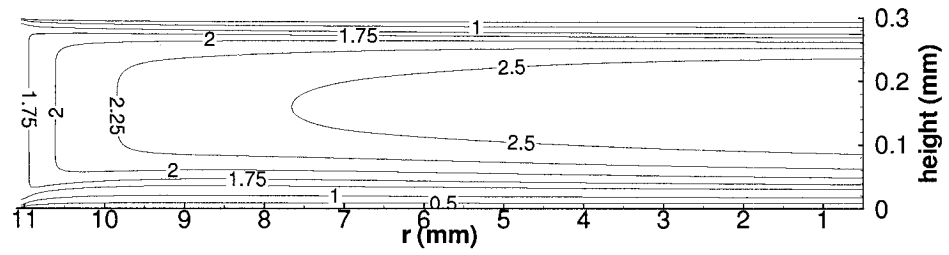
(c) $q'' = 62.50$ W/cm^2.

Figure 7.15: Influence of heat flux on center-plane velocity (m/s), uniform channel ($\alpha = 0.5$).
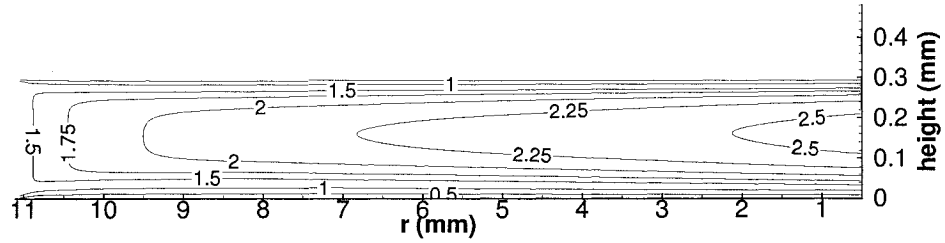
(a) Varying channel width (fixed height), $\alpha_{in} = 0.6$.
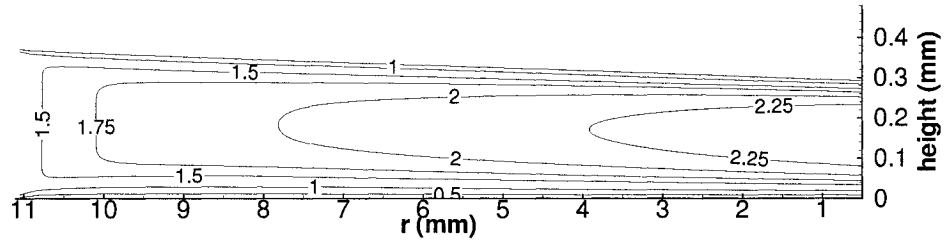
(b) Varying channel height (fixed width), $\alpha_{in} = 0.4$.
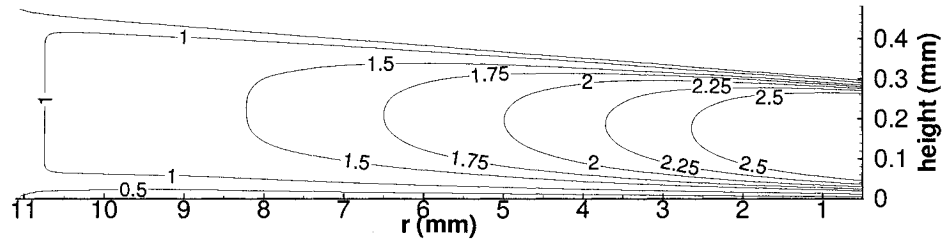
(c) Varying channel width and height (fixed aspect ratio), $\alpha_{in} = 0.5$.

Figure 7.16: Center-plane velocity (m/s) for various geometrical configurations.

decreasing. Increasing velocities are now obtained as a combination of a decreasing viscosity and a decreasing flow area. The case of simultaneously varying channel width and height has the highest velocity, and correspondingly the highest mass flowrate, and lowest maximum temperature.

7.4 Thermal Resistance Model Compared to Three-Dimensional Conjugate Analysis

The model developed by Bau (1998) and the present adaptations for the thermal resistance model, incorporating thermally developing flow and radially inward flow, have not been previously verified. These simplified models are advantageous for rapid geometry optimization, however, they contain a number of assumptions which may pose a limited applicability on their use. In this section, a comparison is made between these simplified models and a conjugate three-dimensional analysis, to explore the range of their applicability. The results for the conjugate three-dimensional analysis are derived from the previous section. In comparison to the simplified analysis, the three-dimensional model incorporates the fluid's temperature dependent properties, solid and fluid axial conduction, and flow development.

Figure 7.17 compares the one-dimensional thermal resistance model for parallel channels considering fully developed and thermally developing flows. The CFD analysis is from the benchmark case, which consisted of uniform channels with hydraulic diameters of approximately 318 μm and aspect ratios of approximately 0.22. Good
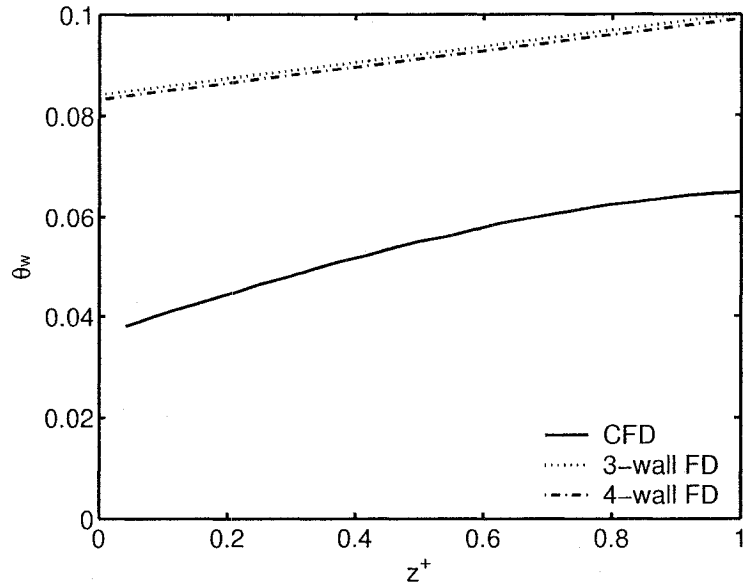
(a) 3-wall and 4-wall heated fully developed (FD) flow models.
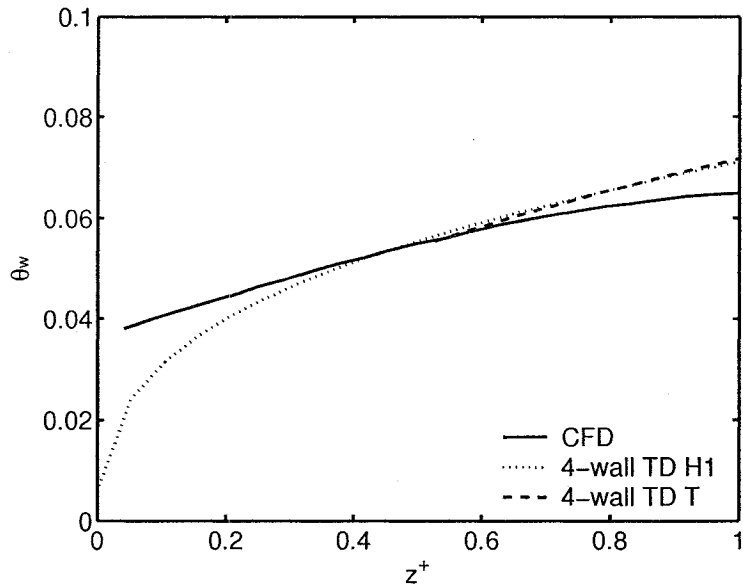
(b) 4-wall heated thermally developing (TD) flow models. Constant heat flux (H1) and constant temperature (T) boundary conditions.

Figure 7.17: Parallel uniform channel: One-dimensional thermal resistance model comparison with three-dimensional conjugate analysis.

agreement is obtained between the CFD analysis and the thermally developing flow cases with respect to the general trend and magnitude. The fully developed cases, however, largely over predict the wall temperature. This over prediction is in part due to the higher heat transfer coefficients available in the flow development region, which subsequently lowers the wall temperature. The thermally developing cases, however, do not predict the entrance or exit region wall temperatures well. For the entrance this is due to the thermal resistance model not accounting for axial conduction, as is discussed later. For the exit it is likely due to neglecting the fluids viscosity decrease with distance. The decreasing viscosity will produce a higher local Reynolds number, which increases the heat transfer coefficient while in the thermally developing regime.

The thermally developing cases are for the 4-wall heated cases, whereas the CFD analysis is a 3-wall heated case. This difference, however, produces negligible differences as is seen when comparing the 3-wall heated and 4-wall heated fully developed cases. Comparing the constant heat flux and constant wall temperature thermally developing cases, negligible differences are observed. The constant heat flux case, which has been utilized in the previous sections, however, is advantageous as it is available in a wider range of non-dimensional streamwise coordinates ($z^* = z/(RePrD_h)$), to better reproduce the inlet characteristics and for a wide range of aspect ratios. These results have demonstrated that for parallel channel systems, when optimizing for a channel with uniform cross-section, consideration of the thermal entrance region is imperative for accurate comparisons. This conclusion is also expected for parallel channels with varying cross-sectional areas.

Figure 7.18 compares the fully developed and thermally developing one-dimensional

226
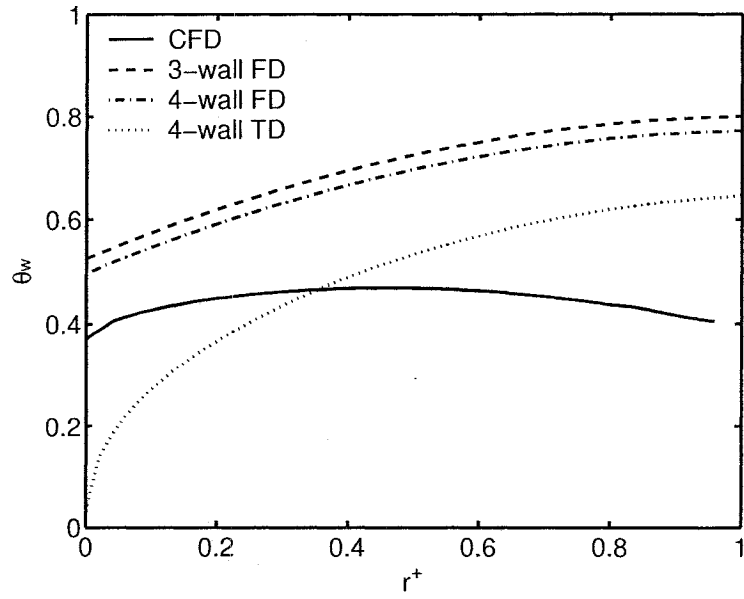
(a) Uniform channel, $\alpha = 0.5$.
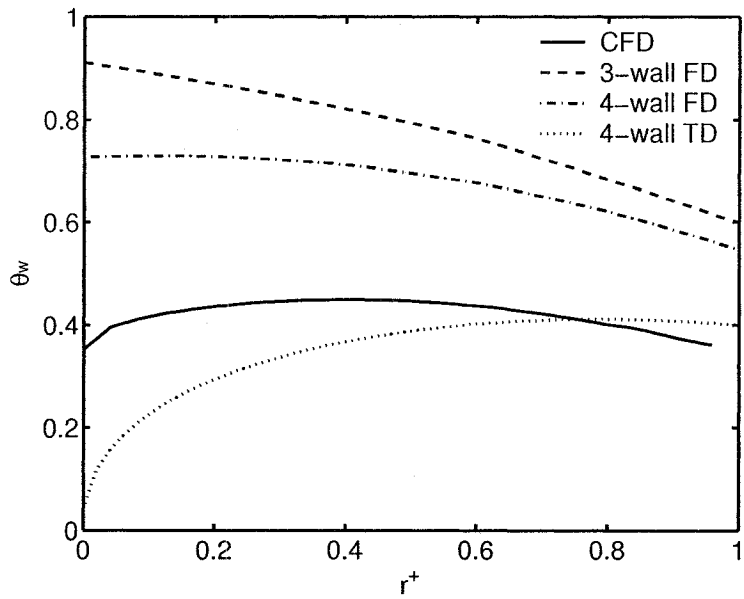
(b) Converging channel, $\alpha_{in} = 1.0$.

Figure 7.18: Radial channel: One-dimensional thermal resistance model comparison with three-dimensional conjugate analysis.

thermal resistance models with the three-dimensional conjugate analysis for radially inward flow configuration. Two cases are considered, a uniform channel ($\alpha = 0.5$) and a converging channel with unity inlet aspect ratio. Similar to the parallel channel cases, the trend and magnitudes are not well predicted by the fully developed flow cases when compared to the three-dimensional conjugate analysis. In addition, however, the thermally developing cases do not provide a good match with this analysis. To investigate this further, plots of the resulting heat flux in the conjugate analysis compared to a uniform heat flux distribution are presented in Figure 7.19. It is observed in this figure that in both the parallel and radial channel cases, the heat flux is non-uniform. However, in the case of the radial channel it is significantly greater. The mean deviation, defined as

$$MD = \frac{1}{L_{chn}} \int_0^{L_{chn}} \left(q''_{CFD} - q''_{1D,Uniform} \right) dz, \tag{7.18}$$

is calculated to be 25% for the radial channel compared to 2.9% for the parallel channel. This non-uniformity is due primarily to axial heat conduction within the solid travelling towards the channel entry. This can be expected particularly in the case of the radial channels, as a large part of the volume is solid and this region gets larger towards the inlet. In summary, the radial model which is an adaptation of the parallel channel model does not provide good predictability of the surface temperature, due to the assumption of negligible wall thickness. This negligible wall thickness translates into an assumption of a uniform heat flux distribution at the inner wall surface, which is a stark difference from the physical reality.
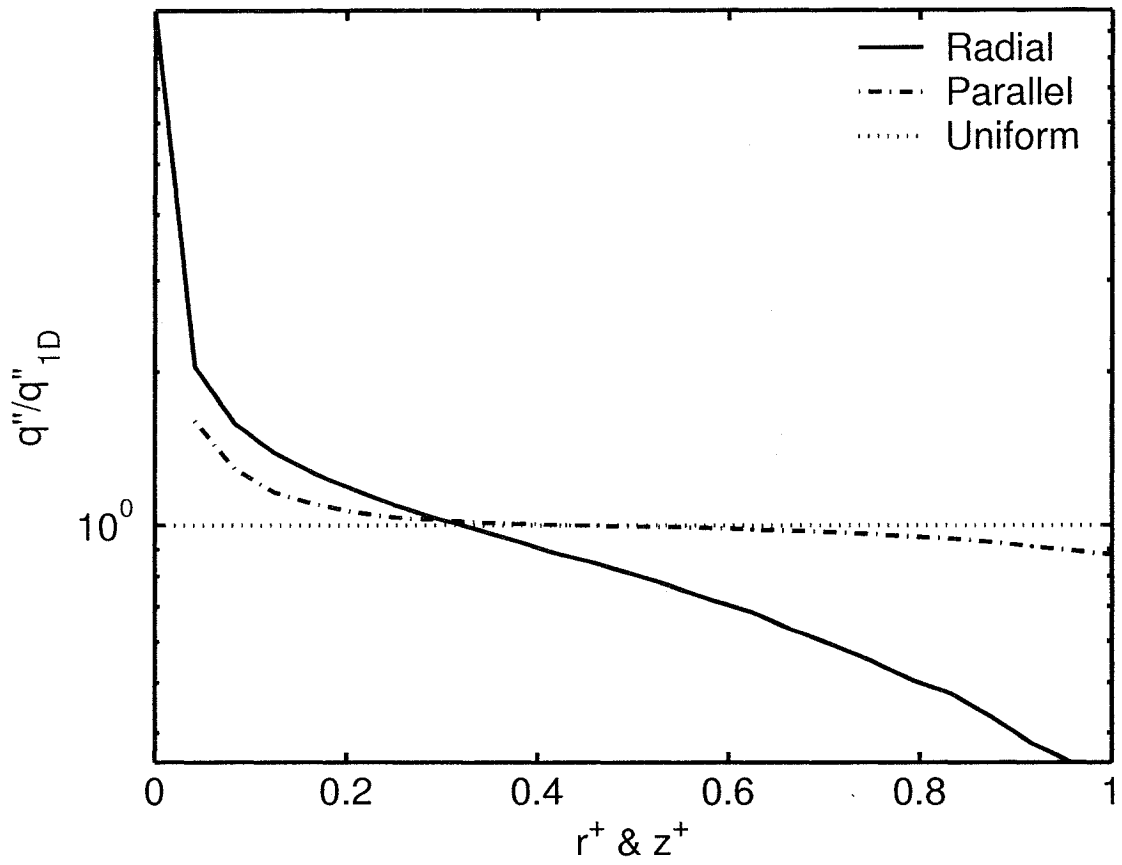
Figure 7.19: Resulting inner wall heat flux distribution from three-dimensional conjugate analysis compared to uniform one-dimensional heat flux distribution.

7.5 Summary

The design of a radial microchannel heat sink has been presented. Fabrication trials were performed but due to delamination of the various layers, experimental investigations were not pursued. The optimization of a radial inflowing microchannel heat exchanger has been investigated numerically. Unique to this optimization was consideration of channels with axially varying cross-sections. Three-dimensional conjugate analysis shows that when constrained by a fixed channel outlet area, increasing the channel inlet area will improve the thermal performance. This is due to increased mass flow providing for a decreased calorimetric resistance.

A one-dimensional thermal resistance model was explored for rapid optimization of channels with varying cross-section, for radially inflowing microchannel heat exchangers. This model is an adaptation of a previous model for parallel channel systems. In general, the analysis shows that linearly converging channels are superior to uniform channels. However, the model predictions do not fair well when compared to the three-dimensional conjugate analysis. This is mainly due to the assumption of a negligible wall thickness thermal resistance, which neglects the significant axial conduction possible in a radially inflowing configuration.

Chapter 8

Closing

8.1 Conclusions and Contributions

A state-of-the-art test facility has been developed for local heat transfer measurements in microchannel systems. The facility can accommodate a number of fluids including air, water and engineered fluids. Single phase and flow boiling measurements may be investigated with the facility.

The facility utilizes a unique Thermochromic Liquid Crystal technique for surface temperature measurement. High spatial resolution measurements, necessary for microgeometries, are enabled through use of the liquid crystal material in its un-encapsulated form. Test methods for using the un-encapsulated form of liquid crystal have been advanced through the development of a localized calibration procedure to account for inconsistencies in coating thickness and lighting, as well, through measurements on microtubes, down to 250 μm and microchannel heat sinks with 3.5 cm^2 footprint areas.

Single phase flow laminar heat transfer in microtubes down to 250 μm, is found to be well represented by conventional analytical treatment. The average turbulent heat transfer coefficient in microtubes down to 500 μm, is well represented using the correlation by Gnielinski (1976) and Adams et al. (1998).

The use of un-encapsulated TLC's has aided in partial flow visualization of flow boiling phenomena in a microtube. This includes a unique flow boiling onset of FC-72 in a 1 mm microtube while in a flow range of 770 kg/(m$^2 \cdot$s) to 1040 kg/(m$^2 \cdot$s). Wall temperatures during flow boiling of FC-72 in that range, were found to oscillate for a wide range of heat fluxes. The amplitude was on the order of 1 °C to 7 °C for low heat flux and the frequency around 10 Hz. The local heat transfer coefficient under flow boiling conditions for FC-72 in a 1 mm tube, has been presented for a quality up to 0.3. For the range of heat flux covered, the heat transfer coefficient is dependent on heat flux, but only mildly influenced by quality at a mass flux of 770 kg/(m$^2 \cdot$ s). At a mass flux of 1040 kg/(m$^2 \cdot$ s), the heat transfer coefficient is less dependent on the heat flux.

A cross-linked silicon microchannel heat sink was designed with 45, 250 μm wide channels and 3 cross-link paths with widths approximately equal to the channel width. Single phase flow in such a heat sink showed negligible differences to a standard heat sink of similar geometry, whereas, single phase heat transfer showed inflections in the wall temperature in the vicinity of the cross-links. Flow boiling in standard and cross-linked silicon parallel microchannel heat sinks has been identified as explosive, similar to other recent observations. This flow boiling phenomena is characterized by periodic oscillation in the fluid bulk parameters.

232

Flow boiling oscillations in a standard and a cross-linked silicon microchannel heat sink of related geometric configuration are similar. Both configurations show a decreasing oscillation frequency with increasing heat flux. Flow boiling oscillations for inlet temperature, outlet temperature and inlet pressure occur at the same frequency. For both configurations, the peak to peak oscillation amplitude increased with increasing heat flux. Flow boiling oscillation data for a standard silicon microchannel heat sink has been presented and correlated. The frequency of oscillation has been successfully correlated with the Boiling number, the Subcooling number, the Weber number and the number of channels. The inlet pressure amplitude has been successfully correlated with the Boiling number, the Subcooling number and the Weber number. The outlet temperature amplitude was successfully correlated with the Boiling number and the Subcooling number.

A radially inflowing microchannel heat exchanger was investigated through fabrication trials and a numerical study. A three-dimensional conjugate analysis of a radially inflowing microchannel heat exchanger was performed. Unique to this design was the incorporation of channels with linearly varying cross-sections. This analysis showed that when constrained by a fixed channel outlet area, increasing the channel inlet area will improve the thermal performance. The use of a one-dimensional thermal resistance model for optimization of radially inflowing microchannels with varying cross-section was explored. This model showed poor correspondence with the three-dimensional conjugate analysis and this was primarily attributed to its exclusion of axial conduction effects. These are found to be imperative for accurate modeling of radially inward flowing microchannel heat sinks.

8.2 Recommendations

8.2.1 TLC Methods

The biggest challenge in utilizing the un-encapsulated TLC material for thermal measurement is packaging it onto the surface of interest, while protecting it from environmental effects. Highly vibrant colour response and hence high signal to noise ratio, is possible when a transparent cover is placed in direct contact with the material. The use of transparent encapsulants compatible with TLC material should be investigated, as they offer the possibility for both an in-contact cover and protection from the environment. Packaging should be considered at the initial experimental design stages, when intending to use un-encapsulated TLC's. The glass slides used to seal the heat sinks, in Section 6.3.1, were effective for providing a highly vibrant color response. However, over time the coating would decay partially due to expansion on heating, which would cause it to seep out of the edges. Use of a tape around the edges provided sufficient compressive seal to prevent this. The sealed coating in this form was found to be highly vibrant and responsive for extensive periods, on the order of months. Based on this, not only is a cover in direct contact necessary, but also the coating should be prevented from escaping. Covering and sealing are increasingly difficult as the geometry reduces in size and offer unique challenges to the experimenter. For the microtubes, future investigators may consider using glass capillary tubes as covers. The capillary tubes diameter could be strategically selected to provide a directly contacting cover for the coated microtubes.

In applying the TLC coating, repeated trials were sometimes necessary, particularly with the microtubes, to obtain the necessary color response. This, however, is time consuming and can also be costly. Rather, a standard coating machine could be developed to provide consistently reproducible coatings. For planar surfaces an airbrush on a traversing mechanism could be developed.

8.2.2   Microtubes

The single phase measurements presented, investigated circular microtubes only. The methods used could similarly be applied to non-circular microtubes. The investigator would, however, need to address the two-dimensional conduction effects at the corners.

The flow boiling microtube experiments were advantageous in developing understanding of heat transfer mechanisms in microchannels, due to the use of a single channel. An expansion of the flow boiling investigations in sub-millimeter microtubes should be performed over a wider range of conditions. In addition to the above, alternative cross-sections could also be investigated. This will aid in understanding the unique flow boiling onset phenomenon of FC-72 in the microtube. Additionally, there was a lack of correspondence of the flow boiling heat transfer coefficient correlations, when compared with the 1 mm tube data flowing FC-72. Expanding the investigation with a variety of fluids would aid in developing versatile correlations.

8.2.3 Microchannel Heat Sinks

A limited experimental program of the cross-linked heat sinks was presented due to challenges with chip support packaging. A compliant adhesive is recommended for permanent chip bonding, however non-permanent bonding methods would be the most ideal.

Future works should investigate the single and two-phase heat transfer of the cross-linked scheme under a wider range of conditions and with varying gap widths. Visualization of flow boiling phenomena and two-phase flow patterns should also be investigated with the second packaging method. Through the use of two cameras, or appropriate optics, simultaneous flow visualization and thermal measurements could be performed. The added perspective of such an approach on the flow boiling physics would be of great value.

Challenges in fabrication produced a low yield of the radial heat sink. A modification to the design that may ease fabrication challenges, is to have the entry or exit at the outer radius, rather than re-diverting the flow towards the top of the heat sink. This would then only require a two-layer, rather than a three-layer stack. An experimental program of the radial heat sink under single phase and flow boiling conditions should be pursued for further characterization. Experiments need to consider both radially inward and outward flows.

An experimental program with MEMS based heat sinks can be an expensive endeavor and so the geometries of interest need to be selected strategically. One-dimensional thermal resistance models offer the possibility of rapid optimization to

identify geometries of interest. The one-dimensional thermal resistance model explored for the radial heat sink was limited. A simplified model accounting for axial conduction needs to be developed to aid in the rapid optimization of channels with varying cross-sections. Additionally, numerical correlations need to be developed for various wall heating conditions, for channels of various aspect ratios and possibly shapes, under thermally and simultaneously flow developing conditions. Other microsystems may be exposed to different wall heating conditions and readily available correlations would aid in their geometrical optimization.

Only linearly varying channels were considered in the present numerical program. Experimental measurements need to be performed in microchannels of varying cross-sections both for parallel and radially flowing systems. Finally, micro-PIV investigations should also be pursued for the cross-linked and radial heat sinks to provide validation data for numerical investigations.

References

3M. 3M Fluorinert electronic liquid FC-72, Product information. Technical report, 3M, 2000.

Adams, T., Abdel-Khalik, S., Jeter, S., and Qureshi, Z. An experimental investigation of single-phase forced convection in microchannels. *International Journal of Heat and Mass Transfer*, 41:851–857, 1998.

Alharbi, A., Pence, D., and Cullion, R. Thermal characteristics of microscale fractal-like branching channels. *Journal of Heat Transfer*, 126(5):744–752, 2004.

Aligoodarz, M., Yan, Y., and Kenning, D. Wall temperature and pressure variation during flow boiling in narrow channels. In *Proceedings of the 11th International Heat Transfer Confeference*, volume 2, pages 225–230, 1998.

Ammerman, C. *Experimental Investigation of Enhanced Convective Boiling in Small Channels*. PhD thesis, University of Texas at Arlington, U.S.A., 1997.

Anderson, M. *Thermochromic Liquid Crystal Thermography: Hysterisis, Illumination and Imaging System Effects, Image Processing and Applications*. PhD thesis, University of California Davis, Mechanical and Aeronautical Engineering Department,

U.S.A., 1999.

Azar, K., Benson, J., and Manno, V. Liquid crystal imaging for temperature measurement of electronic devices. In *Proceedings of the Seventh IEEE SEMI-THERM Symposium*, pages 23–33, 1991.

Bailey, D., Ameel, A., Warrington, R., and Savoie, T. Single phase forced convection heat transfer in microgeometries - A review. volume 2 of *Proceedings of the 30th Intersociety Energy Conversion Engineering Conference, IECEC*, pages 301–310. ASME, ASME, 1995.

Balasubramanian, P. and Kandlikar, S. Experimental study of flow patterns, pressure drop, and flow instabilities in parallel rectangular minichannels. *Heat Transfer Engineering*, 26:20–27, 2005.

Basu, N., Warrier, G., and Dhir, V. Onset of nucleate boiling and active nucleation site density during subcooled flow boiling. *Journal of Heat Transfer*, 124:717–728, 2002.

Bau, H. Optimization of conduits' shape in micro heat exchangers. *International Journal of Heat and Mass Transfer*, 41:2717–2723, 1998.

Bergles, A. *Two-Phase Flow and Heat Transfer in The Power and Process Industries*, chapter Instabilities in Two-Phase Systems, pages 383–423. Hemisphere Publishing Corporation, 1981.

Bowers, M. *High Heat Flux Dissipation Using Small Diameter Channels*. PhD thesis, Purdue University, U.S.A., 1994.

Brod, H. Invariance relations for laminar forced convection in ducts with slowly varying cross-section. *International Journal of Heat and Mass Transfer*, 44:977–987, 2001.

Cahill, D., Goodson, K., and Majumdar, A. Thermometry and thermal transport in micro/nanoscale solid-state devices and structures. *Journal of Heat Transfer*, 124: 223–241, 2002.

Chan, T., Ashforth-Frost, S., and Jambunathan, K. Calibrating for viewing angle effect during heat transfer measurements on a curved surface. *International Journal of Heat and Mass Transfer*, 44:2209–2223, 2001.

Chandrasekhar, S. *Liquid Crystals*. Cambridge University Press, 1977.

Chen, T. and Garimella, S. Effects of dissolved air on subcooled flow boiling of a dielectric coolant in a microchannel heat sink. In *Proceedings of the 3rd International Conference on Microchannels and Minichannels (ICMM2005)*, page 8, 2005.

Chen, Y. and Cheng, P. An experimental investigation on the thermal efficiency of fractal tree-like microchannel nets. *International Communications in Heat And Mass Transfer*, 32:931–938, 2005.

Chin, Y. *An Experimental Study on Flow Boiling in a Narrow Channel: From Convective to Nucleate Boiling*. PhD thesis, University of Houston, U.S.A., 1997.

Chin, Y., Lakshminarasimhan, M., Lu, Q., Hollingsworth, D., and Witte, L. Convective heat transfer in vertical asymmetrically heated narrow channels. *Journal of Heat Transfer*, 124:1019–1025, 2002.

Cho, E., Koo, J., Jiang, L., Prasher, R., Kim, M., Santiago, J., Kenny, T., and Goodson, K. Experimental study on two-phase heat transfer in microchannel heat sinks with hotspots. In *Annual IEEE Semiconductor Thermal Measurement and Management Symposium*, pages 242–246, 2003.

Clifford, R., Jones, T., and Dunne, S. Techniques for obtaining detailed heat transfer coefficient measurements within gas turbine blade and vane cooling passages. In *Gas Turbine Conference and Exhibit*, pages 1–6, 1983.

Colgan, E., Furman, B., Gaynes, M., Graham, W., Labianca, N., Magerlein, J., Polas-tre, R., Rothwell, M., Bezama, R., Choudhary, R., Marston, K., Toy, H., Wakil, J., Zitz, J., and Schmidt, R. A practical implementation of silicon microchannel coolers for high power chips. In *Annual IEEE Semiconductor Thermal Measurement and Management Symposium, 21st*, pages 1–7, 2005.

Collier, J. and Thome, J. *Convective Boiling and Condensation*. Oxford Science Publications, third edition, 1999.

Ding, Y., Kakac, S., and Chen, X. Dynamic instabilities of boiling two-phase flow in a single horizontal channel. *Experimental Thermal and Fluid Science*, 11:327–342, 1995.

Epstein, A. Millimeter-scale, MEMS gas turbine engines. In *Proceedings of the ASME Turbo Expo, Scholar Lecture*, pages 669–696, 2003.

Fergason, J. Liquid crystals in nondestructive testing. *Applied Optics*, 7(9):1729–1737, 1968.

Fujisawa, N., Aoyama, A., and Kosaka, S. Measurement of shear-stress distribution over a surface by liquid-crystal coating. *Measurement Science and Technology*, 39: 1655–1661, 2003.

Ghiaasiaan, S. and Chedester, R. Boiling incipience in microchannels. *International Journal of Heat and Mass Transfer*, 45:4599–4606, 2002.

Gnielinski, V. New equations for heat and mass transfer in turbulent pipe and channel flow. *International Chemical Engineering*, 16:359–368, 1976.

Goldstein, R., Chen, P., and Chiang, H. *Heat Transfer Handbook*, chapter Measurement of Temperature and Heat Transfer, pages 16.1–16.77. McGraw Hill, third edition, 1998.

Grohmann, S. Measurement and modeling of single-phase and flow-boiling heat transfer in microtubes. *International Journal of Heat and Mass Transfer*, 48:4073–4089, 2005.

Gu, Y., Ruan, X., Han, L., Zhu, D., and Sun, X. Imaging of thermal conductivity with sub-micrometer resolution using scanning thermal microscopy. *International Journal of Thermophysics*, 23:1115–1123, 2002.

Gungor, K. and Winterton, R. A general correlation for flow boiling in tubes and annuli. *International Journal of Heat and Mass Transfer*, 29:351–358, 1986.

Hallcrest. Hallcrest product information. Technical report, Hallcrest, 2000. DS-001 – DS-010.

Hapke, I., Boye, H., and Schmidt, J. Onset of nucleate boiling in minichannels. *International Journal of Thermal Sciences*, 39:505–513, 2000.

Harms, T., Kazmierczak, M., and Gerner, F. Developing convective heat transfer in deep rectangular microchannels. *International Journal of Heat and Fluid Flow*, 20: 149–157, 1999.

Hay, H. and Hollingsworth, D. A comparison of trichromic systems for use in the calibration of polymer-dispersed thermochromic liquid crystals. *Experimental Thermal and Fluid Science*, 12(1):1–12, 1996.

Hetsroni, G., Gurevich, M., Mosyak, A., and Rozenblit, R. Surface temperature measurement of a heated capillary tube by means of an infrared technique. *Measurement Science and Technology*, 14:807–814, 2003.

Hetsroni, G., Mosyak, A., Pogrebnyak, E., and Segal, Z. Explosive boiling of water in parallel micro-channels. *International Journal of Multiphase Flow*, 31:313–334, 2005a.

Hetsroni, G., Mosyak, A., Pogrebnyak, E., and Segal, Z. Fluid flow in micro-channels. *International Journal of Heat and Mass Transfer*, 48:1982–1998, 2005b.

Hetsroni, G., Mosyak, A., Pogrebnyak, E., and Segal, Z. Periodic boiling in parallel micro-channels at low vapor quality. *International Journal of Multiphase Flow*, 32: 1141–1159, 2006.

Höhmann, C. and Stephan, P. Microscale temperature measurement at an evaporating liquid meniscus. *Experimental Thermal and Fluid Science*, 26:157–162, 2002.

Holman, J. *Heat Transfer*. McGraw Hill, ninth edition, 2002.

Ireland, P. and Jones, T. Liquid crystal measurements of heat transfer and surface shear stress. *Measurement Science and Technology*, 11(7):969–986, 2000.

Jiang, L., Wong, M., and Zohar, Y. Forced convection boiling in a microchannel heat sink. *Journal of Microelectromechanical Systems*, 10:80–87, 2001.

Jiang, L., Koo, J., Wang, E., Bari, A., Cho, E., Ong, W., Prasher, R., Maveety, J., Kim, M., Santiago, J., and Goodson, K. Cross-linked microchannels for VLSI hotspot cooling. In *Proceedings ASME International Mechanical Engineering Congress and Exposition*, pages 13–17, 2002.

Jones, T. and Hippensteele, S. High-resolution heat-transfer coefficient maps applicable to compound-curve surfaces using liquid crystals in a transient wind tunnel. Technical report, NASA, 1987. Also ASME HTD vol. 71, pp.1-9, 1987.

Kakac, S. and Veziroglu, T. *NATO Advanced Research Workshop On The Advances in Two-Phase Flow and Heat Transfer, Fundamentals and Applications*, volume 2, chapter A Review of Two-Phase Instabilitiess, pages 383–411. Martinus Nijhoff Publishers, 1983.

Kandlikar, S. A general correlation for saturated two-phase flow boiling heat transfer inside horizontal and vertical tubes. *Journal Of Heat Transfer*, 112:219–228, 1990.

Kandlikar, S. Fundamental issues related to flow boiling in minichannels and microchannels. *Experimental Thermal and Fluid Science*, 26:389–407, 2002.

Kandlikar, S. and Balasubramanian, P. An extension of the flow boiling correlation to transition, laminar, and deep laminar flows in minichannels and microchannels. *Heat Transfer Engineering*, 25:86–93, 2004.

Kandlikar, S., Kuan, W., Willistein, D., and Borelli, J. Stabilization of flow boiling in microchannels using pressure drop elements and fabricated nucleation sites. *Journal of Heat Transfer*, 128:389–396, 2006.

Katto, Y. General features of CHF of forced convection boiling in uniformly heated rectangular channels. *International Journal of Heat and Mass Transfer*, 24:1413–1419, 1981.

Kays, W. and Crawford, M. *Convective Heat and Mass Transfer.* McGraw Hill, 1993.

Kays, W. and London, A. *Compact Heat Exchangers.* McGraw-Hill Book Company, 1964.

Kennedy, J., Dowling, G., Abdel-Khalik, M., Ghiasiaan, S., Jeeter, S., and Quershi, Z. The onset of flow instability in uniformly heated horizontal microchannels. *Journal Of Heat Transfer*, 122:118–125, 2000.

Kenning, D., Kono, T., and Wienecke, M. Investigation of boiling heat transfer by liquid crystal thermography. *Experimental Thermal and Fluid Science*, 25:219–229, 2001.

Kew, P. and Cornwell, K. Correlations for the prediction of boiling heat transfer in small-diameter channels. *Applied Thermal Engineering*, 17:705–715, 1997.

Kim, D., Kwon, L., and Lee, S. Micro-channel filling flow considering surface tension effect. *Journal of Micromechanics and Microengineering*, 12:236–246, 2002.

Klausner, J., Mei, R., and Chen, W. Liquid crystal thermography in boiling heat transfer. In *Proceedings of SPIE, - The International Society for Optical Engineering*, volume 2546, pages 152–159, 1995.

Kline, J. and McClintock, F. Describing uncertainties in single-sample experiments. *Mechanical Engineering*, 75:3–8, 1953.

Kosar, A. and Peles, Y. Thermal-hydraulic performance of a MEMS-based pin fin heat sink. *Journal of Heat Transfer*, 128:121–131, 2006a.

Kosar, A. and Peles, Y. Suppression of boiling flow oscillations in parallel microchannels by inlet restrictors. *Journal of Heat Transfer*, 128:251–260, 2006b.

Kosar, A. and Peles, Y. Reduced pressure boiling heat transfer in rectangular microchannels with interconnected reentrant cavities. *Journal of Heat Transfer*, 127: 1106–1114, 2005.

Kovacs, G. *Micromachined Transducers Sourcebook*. McGraw Hill, 1998.

Lee, H. and Lee, S. Heat transfer correlation for boiling flows in small rectangular horizontal channels with low aspect ratios. *International Journal of Multiphase Flow*, 27:2043–2062, 2001.

Lee, P. and Garimella, S. Investigation of heat transfer in rectangular microchannels. *International Journal of Heat and Mass Transfer*, 48:1688–1704, 2005.

Lee, P. and Garimella, S. Thermally developing flow and heat transfer in rectangular microchannels of different aspect ratios. *International Journal of Heat and Mass Transfer*, 49:3060–3067, 2006.

Lelea, D., Nishio, S., and Takano, K. The experimental research on microtube heat transfer and fluid flow of distilled water. *International Journal of Heat and Mass Transfer*, 47:2817–2830, 2004.

Li, S., Fozdar, D., Ali, M., Li, H., Shao, D., Vykoukal, D., Vykoukal, J., Floriano, P., Olsen, M., McDevitt, J., Gascoyne, R., and Chen, S. A continuous-flow polymerase chain reaction microchip with regional velocity control. *Journal of Microelectromechanical Systems*, 15:223–236, 2006.

Lin, S., Kew, P., and Cornwell, K. Flow boiling of refrigerant R141B in small tubes. *Transactions of IChemE*, 79:417–424, 2001.

Liu, C., Gau, C., and Dai, B. Design and fabrication development of a micro flow heat transfer process. *Biosensors and Bioelectronics*, 20:91–101, 2004.

Mantion, M. Low Reynolds number flow in slowly varying axisymmetric tubes. *Journal of Fluid Mechanics*, 49:451–459, 1971.

Mehendale, S., Jacobi, A., and Shah, R. Fluid flow and heat transfer in micro- and meso- scales with application to heat exchanger design. *ASME Applied Mechanics Reviews*, 53:175–194, 2000.

Moffat, R. Experimental heat transfer, Keynote paper. In *Proceedings of the 9th International Heat Transfer Conference*, pages 187–205, 1990. Keynote 11.

Morini, G. Single-phase convective heat transfer in microchannels: A review of experimental results. *International Journal of Thermal Sciences*, 43:631–651, 2004.

Mudawar, I. Assessment of high-heat-flux thermal management schemes. *IEEE Transactions on Components and Packaging Technologies*, 24:122–141, 2001.

Munson, B., Young, D., and Okiishi, T. *Fundamentals of Fluid Mechanics*. John Wiley And Sons, fourth edition, 2002.

OMEGA. *The Temperature Handbook*, volume 2. OMEGA Engineering, Canadian edition, 2006.

Owhaib, W. and Palm, B. Experimental investigation of single-phase convective heat transfer in circular microchannnels. *Experimental Thermal and Fluid Science*, 28: 105–110, 2004.

Paris, D., Birur, C., and Green, A. Development of MEMS microchannel heat sinks for micro/nano spacecraft thermal control. In *Proceedings of the International Mechanical Engineering Congress and Exposition (IMECE)*, volume 4, page 7, 2002.

Patil, V. and Narayanan, V. Spatially resolved temperature measurements in microchannels. *Microfluidics and Nanofluidics*, 2:291–300, 2006.

Pattekar, A. and Kothare, M. A radial microfluidic fuel processor. *Journal of Power Sources*, 147:116–127, 2005.

Peles, Y., Kosar, A., Mishra, C., Kuo, C., and Schneider, B. Forced convective heat transfer across a pin fin micro heat sink. *International Journal of Heat and Mass Transfer*, 48:3615–3627, 2005.

Pence, D. Reduced pumping power and wall temperature in microchannel heat sinks with fractal-like branching channel networks. *Microscale Thermophysical Engineering*, 6:319–330, 2002.

Piasecka, M. and Poniewski, M. Influence of selected parameters on boiling heat transfer in minichannels. In *Proceedings of the Second International Conference on Microchannels and Minichannels (ICMM2004*, pages 515–522. ASME, 2004.

Qu, W. and Mudawar, I. Prediction and measurement of incipient boiling heat flux in micro-channel heat sinks. *International Journal of Heat and Mass Transfer*, 45: 3933–3945, 2002.

Qu, W. and Mudawar, I. Flow boiling heat transfer in two-phase micro-channel heat sinks-i. experimental investigation and assessment of correlation methods. *International Journal of Heat and Mass Transfer*, 46:2755–2771, 2003.

Qu, W. and Mudawar, I. Measurement and correlation of critical heat flux in two-phase micro-channel heat sinks. *International Journal of Heat and Mass Transfer*, 47:2045–2059, 2004.

Reda, D., Muratore, J., and Heineck, J. Time and flow-direction responses of shear-stress-liquid crystal coatings. *AIAA Journal*, 39:693–699, 1994.

Rosenhow, W., Hartnett, J., and Cho, Y., editors. *Handbook of Heat Transfer*, chapter Forced Convection Internal Flow in Ducts, pages 16.1–16.77. McGraw Hill, third edition, 1998.

Saitoh, S., Daiguji, H., and Hihara, E. Effect of tube diameter on boiling heat transfer of R-134a in horizontal small-diameter tubes. *International Journal of Heat and Mass Transfer*, 48:4973–4984, 2005.

Shah, R. and London, A. *Laminar Flow Forced Convection in Ducts*. Academic Press, 1978.

Sharp, K. and Adrian, R. Transition from laminar to turbulent flow in liquid filled microtubes. *Experiments in Fluids*, 36:741–747, 2004.

Sobhan, C. and Garimella, S. A comparative analysis of studies on heat transfer and fluid flow in microchannels. In *Proceedings of International Conference on Heat Transfer and Transport Phenomena in Microscale*, volume 2, pages 80–92, 2000.

Steinke, M. and Kandlikar, S. An experimental investigation of flow boiling characteristics of water in parallel microchannels. *Journal of Heat Transfer*, 126:518–526, 2004a.

Steinke, M. and Kandlikar, S. Single-phase liquid heat transfer in microchannels. In *3rd International Conference on Microchannels and Minichannels*, page 12, 2005a.

Steinke, M. and Kandlikar, S. Single-phase liquid friction factors in microchannels. In *3rd International Conference on Microchannels and Minichannels*, page 10, 2005b.

Steinke, M. and Kandlikar, S. Control and effect of dissolved air in water during flow boiling in microchannels. *International Journal of Heat and Mass Transfer*, 47: 1925–1935, 2004b.

Streeter, V. *Handbook of Fluid Dynamics*. McGraw-Hill Book Company Inc, 1st edition, 1961.

Thome, J. Boiling in microchannels: A review of experiment and theory. *International Journal of Heat and Fluid Flow*, 25(2):128–139, 2004.

Tran, T., Wambsganss, M., and France, D. Small circular- and rectangular-channel boiling with two refrigerants. *International Journal of Multiphase Flow*, 22:485–498, 1996.

Tuckerman, D. *Heat-Transfer Microstructures for Integrated Circuits*. PhD thesis, Stanford University, Department Of Electrical Engineering U.S.A., 1984.

Tuckerman, D. and Pease, R. High-performance heat sinking for VLSI. *IEEE Electron Device Letters*, EDL-2(5):126–129, 1981.

Wagner, E., Sodtke, C., Schweizer, N., and Stephan, P. Experimental study of nucleate boiling heat transfer under low gravity conditions using tlc's for high resolution temperature measurements. *Heat and Mass Transfer*, 42:875–883, 2006.

Wang, X., Yap, C., and Mujumdar, A. Laminar heat transfer in constructal microchannel networks with loops. *Journal of Electronic Packaging*, 128:273–280, 2006.

Warrier, G., Dhir, V., and Momoda, L. Heat transfer and pressure drop in narrow rectangular channels. *Experimental Thermal and Fluid Science*, 26:53–64, 2002.

Wu, H. and Cheng, P. Boiling instability in parallel silicon microchannels at different heat flux. *International Journal of Heat and Mass Transfer*, 47:3631–3641, 2004.

Xu, J., Zhou, J., and Gan, Y. Static and dynamic flow instability of a parallel microchannel heat sink at high heat fluxes. *Energy Conversion And Management*, 46:313–334, 2005.

Yadigaroglu, G. and Bergles, A. Fundamental and higher-mode density-wave oscillations in two-phase flow. *Journal of Heat Transfer*, 94:189–195, 1972.

Yen, T., Kasagi, N., and Suzuki, Y. Forced convective boiling heat transfer in microtubes at low mass and heat fluxes. *International Journal of Multiphase Flow*, 29: 1771–1792, 2003.

Publications from Thesis Work

Journal

Muwanga, R., Hassan, I. and Macdonald, R., Characteristics of Flow Boiling Oscillations in Silicon Microchannel Heat Sinks, *Journal of Heat Transfer*, to appear in Oct. 2007 issue.

Muwanga, R. and Hassan, I., A Flow Boiling Heat Transfer Investigation of FC-72 in a Microtube using Liquid Crystal Thermography, *Journal of Heat Transfer*, to appear in Aug. 2007 issue.

Muwanga, R. and Hassan, I., Local Heat Transfer Measurements on a Curved Microsurface Using Liquid Crystal Thermography, *Journal of Thermophysics and Heat Transfer*, 20:884-894, 2006.

Muwanga, R. and Hassan, I., Local Heat Transfer Measurements in Microchannels Using Liquid Crystal Thermography: Methodology Development and Validation, *Journal of Heat Transfer*, 128:617-626, 2006.

Muwanga, R., Hassan, I. and Macdonald, R., Single Phase Flow and Heat Transfer in a Cross-Linked Silicon Microchannel Heat Sink. To be submitted.

Muwanga, R., Hassan, I. and Ghorab, M., A 3-D Numerical Heat Transfer Investigation of an Optimized Varying Cross-Section Microchannel Heat Sink. To be submitted.

Conference

Muwanga, R. and Hassan, I., Thermography and Heat Transfer In Microsystems Using Liquid Crystal Thermography, *Fifth Baltic Heat Transfer Conference (5th BHTC)*, 11 p, 19-21 September, 2007.

Muwanga, R. and Hassan, I., Thermo-Fluidic Characteristics in a Cross-Linked Silicon Microchannel Heat Sink, *ASME-JSME Thermal Engineering Summer Heat Transfer Conference (HT2007)*, 10 p, July 8-12, 2007.

Muwanga, R., Hassan, I., and Ghorab, M., Numerical Investigation of Heat Transfer in a Radially Flowing Microchannel Heat Exchanger With Varying Cross-Section Channels, *5th International Conference on Computational Heat and Mass Transfer (5ICCHMT07)*, 6 p, June 18-22.

Muwanga, R. and Hassan, I., Boiling Incipience and Heat Transfer in Microtubes: Experimental Measurements Using Liquid Crystal Thermography, *13th International Heat Transfer Conference (IHTC-13)*, August 13-18, 2006.

Muwanga, R. and Hassan, I., Flow Boiling Oscillations in Microchannel Heat Sinks, *9th AIAA/ASME Joint Thermophysics and Heat Transfer Conference*, June 5-8, 2006.

254

Muwanga, R. and Hassan, I., Local Heat Transfer Measurements in Microtubes Using Liquid Crystal Thermography, *The Second International Conference on Thermal Engineering Theory and Applications (ICTEA)*, January 3-6, 2006.

Muwanga, R. and Hassan, I., Novel Microchannel Heat Sinks For Micro/Nano Spacecraft Thermal Management, *The 5th Canadian Space Exploration Workshop (CSEW5)*, CSA, May 12-13, 2005.

Muwanga, R. and Hassan, I., Local Heat Transfer Measurements in Micro Geometries Using Liquid Crystal Thermography, *3rd International Conference on Microchannels and Minichannels (ICMM)*, ASME, June 13-15, 2005.

Appendix A

Experimental Data

A.1 Single Phase Flow and Heat Transfer in Microtubes

Table A.1: 1 mm, Water.

| | | Ambient Temperature, 24.6 °C $T_{in,avg} = 29.7°C$ | | |
| | | | | |
Re	f	Q_{vol} (ml/min)	Re	Nu_{avg}
1414	0.04310	29.2	778	5.26
1472	0.04624	40.2	1065	6.27
1578	0.04285	61.0	1614	7.97
1578	0.04283	80.2	2124	8.89
1749	0.03943	103.2	2765	13.89
1749	0.04007	121.2	3291	25.07
1845	0.03823	143.9	3935	30.70
1845	0.03867	158.0	4375	36.55
2192	0.03601			
2117	0.03886			
2390	0.03679			
2388	0.03669			
2606	0.03732			

Re	f	Q_{vol} (ml/min)	Re	Nu_{avg}
2612	0.03694			
2964	0.04154			
3006	0.04019			
3408	0.04163			
3400	0.04184			
3616	0.04160			
3616	0.04159			
4042	0.04162			
4040	0.04164			

Table A.2: 0.50 mm, Water.

Ambient Temperature, 22.2 °C			
$T_{in,avg} = 25.0°C$			
Q_{vol} (ml/min)	Re	f	Nu_{avg}
15.7	814	0.08970	3.63
19.9	1020	0.07421	4.35
25.4	1292	0.06316	5.32
29.8	1511	0.05771	5.43
35.5	1798	0.05222	6.95
41.4	2128	0.04727	7.29
44.8	2486	0.05598	15.87
51.5	2824	0.05576	19.67
60.3	3140	0.05475	27.76
71.3	3912	0.05514	33.42
77.0	4319	0.05189	31.09

Table A.3: 1 mm, FC-72.

Ambient Temperature, 22.6 °C $T_{in,avg} = 25.3°C$			
Q_{vol} (ml/min)	Re	f	Nu_{avg}
10.1	540	0.14243	7.00
16.0	849	0.09459	8.51
21.3	1129	0.07852	9.97
27.3	1445	0.05311	10.83
38.6	2041	0.04161	13.40
52.4	2804	0.03946	24.59
62.4	3369	0.04133	37.17
86.3	4657	0.04247	56.36
109.3	5941	0.04010	69.27
124.5	6862	0.04001	81.13
144.1	7966	0.03861	90.93
164.3	9112	0.03715	105.02
184.2	10257	0.03556	116.39
202.4	11193	0.03551	127.21

Table A.4: 0.5 mm, FC-72.

Ambient Temperature, 22.5 °C $T_{in,avg} = 25.1°C$			
Q_{vol} (ml/min)	Re	f	Nu_{avg}
10.1	1133	0.06684	8.08
14.8	1665	0.05241	10.03
19.0	2154	0.04787	14.67
22.8	2645	0.05237	24.71
28.8	3347	0.05271	34.34
37.6	4391	0.05097	48.26
46.8	5481	0.05457	65.86
57.2	6762	0.04995	80.50

Table A.5: 0.25 mm, FC-72.

Ambient Temperature, 25.5 $°C$			
$T_{in,avg} = 27.7°C$			
Q_{vol} (ml/min)	Re	f	Nu_{avg}
4.7	1085	0.07150	7.74
7.0	1603	0.05657	9.57
11.4	2622	0.03275	12.05
12.5	2884	0.03667	13.34
19.2	4454	0.02729	24.81
15.9	3696	0.02799	14.53

A.2 Flow Boiling in Microtubes

Table A.6: Local heat transfer coefficient, 770 kg/(m² · s).

43 kW/m²		54 kW/m²		74 kW/m²		83 kW/m²	
x	h $(\frac{kW}{m^2 \cdot {}^\circ C})$	x	h $(\frac{kW}{m^2 \cdot {}^\circ C})$	x	h $(\frac{kW}{m^2 \cdot {}^\circ C})$	x	h $(\frac{kW}{m^2 \cdot {}^\circ C})$
0.0389	3.6540	-0.0582	3.3711	-0.1038	0.0000	-0.0971	4.9333
0.0425	4.0944	-0.0544	3.5635	-0.1010	3.4808	-0.0910	4.6225
0.0460	3.2572	-0.0538	3.6740	-0.0977	3.5675	-0.0904	3.5836
0.0496	3.6141	-0.0500	3.7227	-0.0948	2.9857	-0.0844	3.6138
0.0532	3.2506	-0.0493	3.6928	-0.0916	3.2533	-0.0838	4.6260
0.0567	3.8628	-0.0456	3.6590	-0.0887	3.9669	-0.0778	4.4654
0.0620	3.5355	-0.0449	3.6041	-0.0855	3.1295	-0.0772	4.6176
0.0656	3.3710	-0.0412	3.4304	-0.0826	3.4480	-0.0711	4.0716
0.0691	3.2032	-0.0405	3.5251	-0.0793	3.1578	-0.0706	4.5933
0.0727	3.0653	-0.0368	3.7609	-0.0765	3.6737	-0.0645	4.0951
0.0762	3.1851	-0.0361	3.7343	-0.0732	2.9722	-0.0640	4.2386
0.0798	3.4211	-0.0324	3.9176	-0.0704	3.1567	-0.0579	3.8938
0.0818	3.3658	-0.0284	3.7594	-0.0671	3.0582	-0.0576	4.5281
0.0853	3.7260	-0.0240	4.4269	-0.0642	3.6827	-0.0510	4.1710
0.0889	3.5970	-0.0196	4.2798	-0.0611	3.5002	-0.0444	6.5386
0.0924	3.3119	-0.0152	4.7635	-0.0550	3.5896	-0.0379	6.9848
0.0960	3.6202	-0.0108	4.2650	-0.0489	4.2531	-0.0313	7.0332
0.0995	3.4112	-0.0064	4.8715	-0.0428	4.7842	-0.0247	6.6286
0.1031	3.4837	-0.0009	5.6245	-0.0367	4.6502	-0.0181	6.7482
0.1053	3.2652	0.0001	5.1523	-0.0306	5.2533	-0.0106	6.7555
0.1088	3.4652	0.0035	5.8273	-0.0206	6.7188	-0.0040	7.6653
0.1124	3.0497	0.0045	4.8811	-0.0145	7.7770	0.0026	8.0993
0.1159	3.7646	0.0079	5.2787	-0.0084	8.6685	0.0092	8.8925
0.1195	3.3048	0.0089	5.2080	-0.0023	9.8623	0.0158	8.3390
0.1230	3.6059	0.0123	5.9306	0.0038	7.8511	0.0224	7.8453
0.1252	0.0000	0.0133	5.2985	0.0099	9.7590	0.0295	6.4433
0.1288	3.2260	0.0167	5.3970	0.0123	6.2024	0.0361	9.3139
0.1323	3.2950	0.0177	5.3783	0.0184	5.6380	0.0427	7.8971
0.1359	3.7575	0.0211	6.3887	0.0245	7.0617	0.0493	8.2594
0.1394	3.1304	0.0221	4.7552	0.0305	5.9791	0.0559	9.1025
0.1430	3.3186	0.0255	4.7115	0.0366	6.0022	0.0625	8.6083
0.1465	3.0609	0.0325	5.3399	0.0427	6.2034	0.0696	10.1432
		0.0370	5.3708	0.0487	6.3429	0.0762	10.2951
		0.0414	5.1175	0.0525	7.7275	0.0828	9.9598
		0.0458	5.0451	0.0585	9.3993	0.0894	9.7453

43 kW/m²		54 kW/m²		74 kW/m²		83 kW/m²	
x	h $\left(\frac{kW}{m^2 \cdot °C}\right)$	x	h $\left(\frac{kW}{m^2 \cdot °C}\right)$	x	h $\left(\frac{kW}{m^2 \cdot °C}\right)$	x	h $\left(\frac{kW}{m^2 \cdot °C}\right)$
		0.0502	5.2275	0.0646	7.8375	0.0960	9.1529
		0.0546	4.9722	0.0706	8.6685	0.1026	8.9463
		0.0560	4.6751	0.0767	7.1597	0.1092	9.4826
		0.0594	5.1550	0.0827	8.3106	0.1119	10.5011
		0.0604	4.7088	0.0978	8.6033	0.1146	9.3619
		0.0638	4.8258	0.1039	8.3009	0.1169	10.6038
		0.0648	5.5836	0.1100	9.2293	0.1176	9.1665
		0.0682	5.0495	0.1161	9.3394	0.1185	11.5028
		0.0692	4.8889	0.1221	8.2705	0.1212	10.6173
		0.0726	4.9123	0.1282	8.2151	0.1235	9.1056
		0.0736	5.4193	0.1288	8.0020	0.1242	9.5300
		0.0770	4.9276	0.1344	8.0386	0.1251	8.3215
		0.0780	4.9728	0.1348	8.0396	0.1278	10.5182
		0.0813	4.9836	0.1404	7.3745	0.1301	11.0727
		0.0823	4.5532	0.1409	7.6861	0.1308	9.2776
		0.0842	4.9802	0.1465	7.8511	0.1317	11.2310
		0.0854	4.3913	0.1469	7.7356	0.1344	8.5051
		0.0886	5.1322	0.1526	7.1447	0.1367	8.2827
		0.0898	4.8926	0.1530	7.0988	0.1374	8.6847
		0.0930	4.4562	0.1587	7.1796	0.1383	10.4228
		0.0942	4.8579	0.1591	7.9636	0.1410	7.5211
		0.0974	4.2505	0.1647	8.1262	0.1433	6.5948
		0.0986	4.7040	0.1651	7.6336	0.1440	8.4195
		0.1018	4.4890	0.1662	6.9247	0.1449	11.2832
		0.1030	4.6777	0.1721	8.1960	0.1476	7.1201
		0.1062	4.5569	0.1723	6.9901	0.1499	5.6201
		0.1074	4.7780	0.1782	8.4910	0.1506	7.4860
		0.1115	4.3835	0.1783	7.2676	0.1515	8.8103
		0.1116	4.4747	0.1842	7.0393	0.1531	9.5990
		0.1159	4.7548	0.1844	8.0091	0.1538	8.6846
		0.1160	4.6499	0.1903	7.3229	0.1586	9.4874
		0.1203	4.6891	0.1904	6.5484	0.1597	9.9327
		0.1204	4.9921	0.1964	6.8813	0.1604	9.7596
		0.1247	4.4766	0.1965	6.7449	0.1651	8.5583
		0.1248	4.8382	0.2024	8.1594	0.1663	8.5724
		0.1291	4.7532	0.2025	7.0241	0.1670	8.6792
		0.1292	4.1566	0.2072	6.8999	0.1717	8.8877
		0.1335	4.4542	0.2133	7.6432	0.1729	8.8112
		0.1336	4.6006	0.2193	6.9797	0.1736	10.0720
		0.1379	4.5036	0.2254	7.4443	0.1783	8.7784
		0.1396	4.9456	0.2314	5.9030	0.1795	7.8054
		0.1440	4.4119	0.2375	6.9908	0.1802	9.2014

261

43 kW/m²		54 kW/m²		74 kW/m²		83 kW/m²	
x	h $\left(\frac{kW}{m^2\cdot{}^\circ C}\right)$	x	h $\left(\frac{kW}{m^2\cdot{}^\circ C}\right)$	x	h $\left(\frac{kW}{m^2\cdot{}^\circ C}\right)$	x	h $\left(\frac{kW}{m^2\cdot{}^\circ C}\right)$
		0.1484	4.5009	0.2456	6.6622	0.1849	7.9193
		0.1528	4.3603	0.2516	7.4430	0.1861	7.1359
		0.1572	4.2065	0.2576	6.9930	0.1868	6.7035
		0.1616	4.2555	0.2637	7.6958	0.1915	6.9635
		0.1661	4.4592	0.2697	6.3805	0.1927	6.7100
		0.1681	4.5190	0.2757	6.7860	0.1934	5.4732
		0.1725	4.3297				
		0.1769	4.1862				
		0.1813	3.9699				
		0.1857	4.2109				
		0.1901	3.9674				
		0.1945	3.9256				

Table A.7: Local heat transfer coefficient, 1040 kg/(m² · s).

48 kW/m²		57 kW/m²		70 kW/m²		83 kW/m²	
x	h $\left(\frac{kW}{m^2\cdot{}^\circ C}\right)$	x	h $\left(\frac{kW}{m^2\cdot{}^\circ C}\right)$	x	h $\left(\frac{kW}{m^2\cdot{}^\circ C}\right)$	x	h $\left(\frac{kW}{m^2\cdot{}^\circ C}\right)$
-0.0558	4.4396	-0.0500	4.3391	-0.0313	5.4091	-0.0263	8.5128
-0.0515	4.5164	-0.0482	4.5425	-0.0308	5.5877	-0.0229	6.5039
-0.0481	4.0424	-0.0471	3.4323	-0.0290	6.0112	-0.0196	7.5462
-0.0472	4.7431	-0.0450	3.9630	-0.0250	6.1876	-0.0163	7.9627
-0.0468	2.9730	-0.0432	4.4653	-0.0245	5.4732	-0.0130	8.3323
-0.0438	3.9567	-0.0421	3.3338	-0.0227	6.0663	-0.0097	6.9699
-0.0429	4.5918	-0.0399	3.9449	-0.0187	5.4275	-0.0064	7.3513
-0.0425	3.0482	-0.0381	4.1161	-0.0182	5.1545	-0.0030	7.8901
-0.0395	3.6595	-0.0370	3.4119	-0.0164	5.6629	0.0003	8.0789
-0.0382	2.8572	-0.0348	3.8332	-0.0124	5.8722	0.0036	7.7335
-0.0352	4.1499	-0.0335	4.3132	-0.0119	5.6604	0.0069	9.8272
-0.0341	4.7602	-0.0330	3.9814	-0.0101	6.2939	0.0103	8.3922
-0.0339	2.9069	-0.0319	3.3709	-0.0072	6.2890	0.0136	8.5544
-0.0326	3.6845	-0.0298	4.0824	-0.0058	6.5411	0.0169	7.7885
-0.0307	3.6050	-0.0284	4.0370	-0.0028	5.6820	0.0235	8.3081
-0.0298	5.6413	-0.0279	4.1080	-0.0009	6.1584	0.0269	8.0771
-0.0283	3.6312	-0.0270	4.0080	0.0005	5.7514	0.0302	8.3906
-0.0265	3.4019	-0.0238	4.3906	0.0035	7.2661	0.0335	7.5683
-0.0255	4.9751	-0.0233	4.6064	0.0054	7.4964	0.0368	7.4229

48 kW/m²		57 kW/m²		70 kW/m²		83 kW/m²	
x	h $\left(\frac{kW}{m^2 \cdot {}^\circ C}\right)$	x	h $\left(\frac{kW}{m^2 \cdot {}^\circ C}\right)$	x	h $\left(\frac{kW}{m^2 \cdot {}^\circ C}\right)$	x	h $\left(\frac{kW}{m^2 \cdot {}^\circ C}\right)$
-0.0240	4.2598	-0.0219	4.3048	0.0068	7.0008	0.0376	8.2693
-0.0222	4.1210	-0.0188	4.9554	0.0098	6.0320	0.0409	9.2980
-0.0212	5.3651	-0.0183	4.3883	0.0117	6.8370	0.0442	10.7111
-0.0197	3.8778	-0.0169	4.4510	0.0131	6.1802	0.0475	8.4552
-0.0179	3.9377	-0.0137	4.7541	0.0161	6.2427	0.0508	9.0072
-0.0165	7.4174	-0.0132	4.3022	0.0189	7.5897	0.0542	9.3686
-0.0163	4.9371	-0.0118	4.5102	0.0194	5.8604	0.0575	8.8536
-0.0154	3.9415	-0.0094	5.0797	0.0202	8.4095	0.0608	9.1490
-0.0122	7.1546	-0.0043	6.4121	0.0213	8.4970	0.0641	7.9959
-0.0120	6.1119	-0.0020	7.6651	0.0252	8.9105	0.0743	8.8446
-0.0098	6.7398	0.0008	5.8726	0.0265	9.6989	0.0776	8.1265
-0.0079	6.6189	0.0031	7.4519	0.0276	8.2898	0.0809	8.1539
-0.0077	5.0542	0.0058	6.0066	0.0315	7.3690	0.0843	8.0588
-0.0055	7.0813	0.0082	6.9682	0.0328	8.4356	0.0876	7.9429
-0.0036	5.7152	0.0133	6.1595	0.0340	7.9413	0.0909	7.6950
-0.0034	5.4882	0.0146	5.9312	0.0378	7.8166	0.0942	8.0930
-0.0012	6.5098	0.0183	6.9784	0.0391	8.0669	0.0976	7.3266
0.0009	5.1071	0.0197	5.5546	0.0403	7.5106	0.1009	7.0467
0.0031	6.0646	0.0217	7.2132	0.0441	7.1241	0.1026	7.9860
0.0059	6.3518	0.0234	6.3082	0.0470	8.5925	0.1059	7.1506
0.0069	7.2837	0.0247	5.5570	0.0472	8.8805	0.1092	6.8417
0.0089	6.7166	0.0267	6.8218	0.0487	8.1354	0.1125	7.7637
0.0102	7.0248	0.0285	6.8349	0.0533	8.7924	0.1158	6.6294
0.0112	7.2565	0.0298	5.8614	0.0535	7.8936	0.1192	7.5123
0.0132	6.1183	0.0318	6.8644	0.0550	7.8408	0.1225	6.3228
0.0145	6.2791	0.0336	6.7820	0.0596	7.9578	0.1258	6.5184
0.0155	6.6233	0.0356	7.3567	0.0598	8.0840	0.1291	6.5776
0.0171	8.2892	0.0361	6.6832	0.0613	7.5856	0.1324	6.3656
0.0175	6.2441	0.0369	5.8839	0.0659	8.0901	0.1350	7.3631
0.0188	6.0521	0.0400	7.2050	0.0661	8.2142	0.1383	7.7447
0.0198	6.4875	0.0407	7.7314	0.0676	7.0686	0.1417	7.5294
0.0214	8.9413	0.0412	7.6696	0.0711	8.5581	0.1450	7.2701
0.0218	5.3279	0.0451	6.5859	0.0746	8.4362	0.1483	7.7605
0.0232	6.6351	0.0458	7.9029	0.0759	8.0821	0.1516	6.6821
0.0237	5.6807	0.0463	7.7842	0.0774	8.9637	0.1549	7.2108
0.0257	9.1712	0.0502	6.3018	0.0809	8.4654	0.1583	7.0229
0.0274	7.8646	0.0509	7.2289	0.0822	7.8844	0.1616	6.4441
0.0280	6.5070	0.0514	7.3588	0.0838	8.6077	0.1649	6.5735
0.0300	7.9958	0.0534	7.5487	0.0873	7.9759	0.1713	7.1323
0.0317	7.8687	0.0545	8.2351	0.0886	7.9417	0.1746	7.0641
0.0323	6.3930	0.0552	6.2955	0.0901	8.0061	0.1779	7.5345
0.0360	7.0897	0.0559	6.1573	0.0936	7.9533	0.1812	7.1791

48 kW/m²		57 kW/m²		70 kW/m²		83 kW/m²	
x	h ($\frac{kW}{m^2 \cdot {}^\circ C}$)	x	h ($\frac{kW}{m^2 \cdot {}^\circ C}$)	x	h ($\frac{kW}{m^2 \cdot {}^\circ C}$)	x	h ($\frac{kW}{m^2 \cdot {}^\circ C}$)
0.0362	8.7079	0.0564	6.0341	0.0949	7.4512	0.1846	7.1489
0.0366	5.9341	0.0585	7.5569	0.0964	7.2152	0.1879	7.8571
0.0380	8.8835	0.0596	7.1297	0.0973	9.5203	0.1912	7.7080
0.0405	7.7207	0.0614	7.5106	0.1021	8.6858	0.1979	8.1570
0.0406	8.5222	0.0628	8.2298	0.1037	9.2876		
0.0409	5.1115	0.0629	7.6455	0.1060	7.2956		
0.0423	9.1355	0.0636	8.2922	0.1084	8.7175		
0.0436	6.2159	0.0647	8.0707	0.1100	8.1766		
0.0442	6.5840	0.0657	6.7384	0.1123	6.7316		
0.0448	8.5794	0.0665	8.2681	0.1147	8.1137		
0.0449	8.4651	0.0679	7.7147	0.1163	7.7657		
0.0466	8.5043	0.0680	8.1867	0.1186	5.5252		
0.0471	5.2771	0.0687	7.3268	0.1210	6.7280		
0.0479	6.3081	0.0697	7.4776	0.1226	6.5185		
0.0491	7.5372	0.0716	7.3767	0.1271	7.7263		
0.0492	8.1648	0.0730	8.2917	0.1283	7.7240		
0.0509	6.4480	0.0731	7.7631	0.1312	8.0321		
0.0514	4.7498	0.0758	6.9693	0.1334	7.7864		
0.0522	6.1257	0.0767	6.8043	0.1346	7.6080		
0.0528	7.1215	0.0781	5.9964	0.1375	7.9397		
0.0535	7.4645	0.0781	6.1675	0.1398	7.8918		
0.0557	4.5978			0.1409	7.8963		
0.0565	6.0108			0.1438	8.3415		
0.0571	5.7768			0.1461	8.7153		
0.0578	5.7379			0.1473	8.6523		
0.0600	4.4515			0.1501	7.7712		

A.3   Microchannel Heat Sink Heat Transfer and Boiling Oscillations

Table A.8: Single phase heat transfer with FC-72, INT02, $Re = 142$.

$Q_{vol} = 40$ ml/min
$Q = 11.0$ W
$T_{in} = 26.4°C$

z/D_h	z^*	$T_w(°C)$	Nu
9.0	5.380E-03	43.0	6.15
10.3	6.192E-03	44.1	5.82
11.7	7.004E-03	45.0	5.58
13.0	7.816E-03	45.8	5.40
14.4	8.628E-03	46.2	5.33
15.7	9.440E-03	46.5	5.30
17.1	1.025E-02	46.8	5.26
18.4	1.106E-02	47.3	5.18
19.8	1.188E-02	47.9	5.07
21.1	1.269E-02	48.5	4.97
22.5	1.350E-02	49.0	4.90
23.8	1.431E-02	49.2	4.89
25.2	1.512E-02	49.6	4.86
26.5	1.594E-02	49.8	4.85
27.9	1.675E-02	50.2	4.80
29.2	1.756E-02	50.3	4.82
30.6	1.837E-02	50.5	4.84
31.9	1.918E-02	50.6	4.85
33.3	2.000E-02	50.9	4.84
34.6	2.081E-02	50.9	4.88
36.0	2.162E-02	51.0	4.92
37.3	2.243E-02	51.0	4.98
38.7	2.324E-02	51.1	5.00
40.0	2.406E-02	51.1	5.06
41.4	2.487E-02	50.9	5.15
42.7	2.568E-02	50.9	5.23

Table A.9: Single phase heat transfer with FC-72, INT02, $Re = 210$.

$Q_{vol} = 60$ ml/min $Q = 13.3$ W $T_{in} = 26.4°C$			
z/D_h	z^*	$T_w(°C)$	**Nu**
9.0	3.643E-03	43.4	7.14
10.3	4.192E-03	44.6	6.69
11.7	4.742E-03	45.4	6.46
13.0	5.292E-03	45.9	6.33
14.4	5.842E-03	46.5	6.20
15.7	6.392E-03	47.1	6.05
17.1	6.942E-03	48.0	5.82
18.4	7.491E-03	48.9	5.62
19.8	8.041E-03	49.7	5.45
21.1	8.591E-03	50.3	5.33
22.5	9.141E-03	50.7	5.27
23.8	9.691E-03	51.1	5.22
25.2	1.024E-02	51.4	5.18
26.5	1.079E-02	51.8	5.13
27.9	1.134E-02	52.0	5.12
29.2	1.189E-02	52.3	5.11
30.6	1.244E-02	52.4	5.12
31.9	1.299E-02	52.5	5.12
33.3	1.354E-02	52.5	5.17
34.6	1.409E-02	52.5	5.20
36.0	1.464E-02	52.5	5.24
37.3	1.519E-02	52.6	5.27
38.7	1.574E-02	52.5	5.34
40.0	1.629E-02	52.4	5.42
41.4	1.684E-02	52.4	5.44
42.7	1.739E-02	52.3	5.51

Table A.10: Single phase heat transfer with FC-72, INT02, $Re = 307$.

$Q_{vol} = 85$ ml/min $Q = 13.7$ W $T_{in} = 28.0°C$			
z/D_h	z^*	$T_w(°C)$	Nu
9.0	2.535E-03	43.1	8.22
10.3	2.918E-03	44.3	7.65
11.7	3.300E-03	45.2	7.26
13.0	3.683E-03	45.9	7.01
14.4	4.066E-03	46.3	6.89
15.7	4.448E-03	46.9	6.73
17.1	4.831E-03	47.5	6.54
18.4	5.214E-03	48.3	6.31
19.8	5.596E-03	48.8	6.17
21.1	5.979E-03	49.3	6.04
22.5	6.362E-03	49.6	6.00
23.8	6.744E-03	49.8	5.97
25.2	7.127E-03	50.4	5.84
26.5	7.510E-03	50.8	5.74
27.9	7.892E-03	51.1	5.70
29.2	8.275E-03	51.4	5.65
30.6	8.658E-03	51.6	5.64
31.9	9.040E-03	51.7	5.65
33.3	9.423E-03	51.8	5.65
34.6	9.806E-03	51.8	5.67
36.0	1.019E-02	51.9	5.68
37.3	1.057E-02	51.9	5.73
38.7	1.095E-02	51.8	5.78
40.0	1.134E-02	51.7	5.86
41.4	1.172E-02	51.6	5.93
42.7	1.210E-02	51.5	5.99

Table A.11: Single phase heat transfer with FC-72, INT02, $Re = 559$.

$Q_{vol} = 150$ ml/min $Q = 15.5$ W $T_{in} = 30.2°C$			
z/D_h	z^*	$T_w(°C)$	Nu
9.0	1.427E-03	42.9	10.92
10.3	1.642E-03	43.6	10.46
11.7	1.858E-03	44.5	9.77
13.0	2.073E-03	45.5	9.19
14.4	2.289E-03	45.8	8.99
15.7	2.504E-03	46.2	8.84
17.1	2.719E-03	46.6	8.66
18.4	2.935E-03	47.3	8.32
19.8	3.150E-03	48.0	7.99
21.1	3.365E-03	48.8	7.67
22.5	3.581E-03	49.3	7.48
23.8	3.796E-03	49.7	7.36
25.2	4.012E-03	49.9	7.28
26.5	4.227E-03	50.4	7.14
27.9	4.442E-03	50.7	7.06
29.2	4.658E-03	51.0	6.95
30.6	4.873E-03	51.2	6.91
31.9	5.089E-03	51.4	6.87
33.3	5.304E-03	51.5	6.86
34.6	5.519E-03	51.6	6.85
36.0	5.735E-03	51.6	6.88
37.3	5.950E-03	51.6	6.92
38.7	6.166E-03	51.5	6.97
40.0	6.381E-03	51.4	7.04
41.4	6.596E-03	51.3	7.12
42.7	6.812E-03	51.1	7.23

Table A.12: Flow boiling oscillations, STR02, $T_{in} = 70°C$.

	q'' (W/cm²)	Bo	f_ω (Hz)	f^*	$P_{amp,in}$ (kPa)	P^*	$T_{amp,out}$ (K)	T^*
	4.3267	0.000211	0.260652	0.044	3.68611	0.427362	10.05	0.026935
	4.7829	0.000233	0.240602	0.0406	5.32379	0.617233	11.07	0.029659
$G = 91$ kg/(m²·s)	5.2837	0.000258	0.190476	0.0321	5.78191	0.670347	13.03	0.034929
$N_{sub} = 89.835$	5.7726	0.000281	0.160401	0.0271	6.24531	0.724073	13.78	0.036933
$We = 0.0405$	6.3603	0.000310	0.140351	0.0237	6.61392	0.766809	14.76	0.039558
	6.2915	0.000307	0.140351	0.0237	6.54546	0.758872	13.94	0.037353
	7.4679	0.000237	0.542714	0.0595	6.58233	0.322429	3.41	0.009144
	7.4538	0.000236	0.541353	0.0593	7.04046	0.344870	6.92	0.018558
	7.6971	0.000244	0.561404	0.0615	7.48279	0.366538	8.36	0.022391
$G = 140$ kg/(m²·s)	7.9223	0.000251	0.541353	0.0593	7.75661	0.379951	7.06	0.018915
$N_{sub} = 89.835$	8.1671	0.000259	0.541353	0.0593	8.02517	0.393106	9.31	0.024945
$We = 0.0958$	8.3654	0.000265	0.501253	0.0549	8.50963	0.416836	8.69	0.023290
	8.7557	0.000277	0.461153	0.0506	8.84665	0.433345	8.95	0.023976
	9.0177	0.000286	0.441103	0.0484	9.02569	0.442115	9.11	0.024404
	9.4798	0.000300	0.380952	0.0418	9.78924	0.479517	11.46	0.030708
	1.0533	0.000250	0.661654	0.0544	9.65232	0.265956	10.10	0.027056
	1.0532	0.000250	0.661654	0.0544	9.75765	0.268858	10.28	0.027553
$G = 186$ kg/(m²·s)	1.1012	0.000262	0.601504	0.0495	10.65284	0.293523	9.25	0.024801
$N_{sub} = 89.835$	1.1538	0.000274	0.561404	0.0462	10.92140	0.300923	9.21	0.024689
$We = 0.1703$	1.204	0.000286	0.521303	0.0429	11.36373	0.313111	10.60	0.028398
	1.2574	0.000299	0.421053	0.0346	12.20101	0.336181	13.59	0.036432
	1.2528	0.000298	0.461153	0.0379	12.11675	0.333859	13.87	0.037182

269

Table A.13: Flow boiling oscillations, STR02, $T_{in} = 80°C$.

	q'' (W/cm²)	Bo	f_ω (Hz)	f^*	$P_{amp,in}$ (kPa)	P^*	$T_{amp,out}$ (K)	T^*
$G = 140$ kg/(m²·s)	5.1237	0.000162	0.163636	0.0179	3.62291	0.177465	12.50	0.033492
$N_{sub} = 59.890$	5.1274	0.000162	0.141414	0.0155	3.42282	0.167663	12.70	0.034045
$We = 0.0958$	5.4576	0.000173	0.121212	0.0133	4.36540	0.213835	12.50	0.033491
	5.4559	0.000173	0.115152	0.0126	4.10210	0.200938	12.12	0.032483
	5.9143	0.000187	0.113131	0.0124	4.32854	0.212029	12.15	0.032551
$G = 185$ kg/(m²·s)	5.7016	0.000136	0.365829	0.0301	4.83406	0.133196	9.56	0.025616
$N_{sub} = 59.890$	5.9725	0.000142	0.225126	0.0185	4.36540	0.120282	11.37	0.030469
$We 0.1703$	6.4778	0.000154	0.205025	0.0169	4.70768	0.129713	11.09	0.029708
	6.922	0.000165	0.180905	0.0149	5.27640	0.145383	11.77	0.031546
$G = 228$ kg/(m²·s)	8.1815	0.0001587	0.393970	0.0264	4.79720	0.088083	12.30	0.032953
$N_{sub} = 59.890$	8.8191	0.000171	0.237186	0.0159	5.42910	0.099686	12.32	0.033005
$We = 0.2556$	9.7413	0.0001889	0.168844	0.0113	5.83984	0.107228	13.65	0.036580
	9.7384	0.0001889	0.172864	0.0116	5.83984	0.107228	14.70	0.039406

270

Table A.14: Flow boiling oscillation, INT01.

| $T_{in} = 70°C$ | | | | |
| $G = 140$ kg/(m$^2 \cdot$ s) | | | | |
q'' (W/cm^2)	f_ω (Hz)	$T_{amp,in}$ (K)	$T_{amp,out}$ (K)	$P_{amp,in}$ (kPa)
7.6334	0.3308	5.9	16.7	5.40730
7.8571	0.3008	8.5	17.7	6.16020
8.1260	0.2406	9.2	19.1	6.62880
8.4066	0.2206	9.7	19.3	6.83410
8.6896	0.1905	11.3	19.5	7.16580
8.9529	0.1805	11.9	20.3	7.33430
9.1153	0.1805	12.9	20.4	7.01840
9.5861	0.1604	14.9	20.4	7.40270

Appendix B

Example Code

```
1    %%%%%%%%%%%%%%%%%%%%%%%%%%%%%%%%%%%%%%%%%%%%%%%%%%%%%%%%%%%%%%%%%%%%%%%%%%
2    % TLC Rig
3    % Author: Roland S Muwanga
4    % Date: Jan 23/07
5    %        Based on Jun 30/06 and Sept 14/05
6    %
7    % Program: calibproc***
8    %
9    % Description: File to post-process TLC calibraton data
10   %
11   % Requires:
12   % 1. Calibration images and file location
13   % 2. image location rotation
14   %
15   % Promises:
16   % 1. calclulate ROI calibration curves and save them for multiple image
17   %    location
18   % 2. files saved with number equal to location number NxXNy polynomial
19   %    equations
20   % 3. filepolycoeff - Output file of polynomial coefficients
21   %
22   % Additional Notes:
23   % i. to be run from calibration data directory
24   % ii. to run type filename without '.m' at Matlab prompt
25   %%%%%%%%%%%%%%%%%%%%%%%%%%%%%%%%%%%%%%%%%%%%%%%%%%%%%%%%%%%%%%%%%%%%%%%%%%
26
27   close all;
28   warning off MATLAB:polyfit:RepeatedPointsOrRescale
29   clear all;
30
```

```
31
32   % INPUTS  %%%%%%%%%%%%%%%%%%%%%%%%%%%%%%%%%%%%%%%%%%%%%%%%%%%%%%%%%%%%
33   % Variable inputs
34   Nimg = 21; % number of images
35   Nloc = 1;  % number of image locations for measurement
36   NlocCalib = 1; % number of calibrated locations
37   krepresent = 0; % location which will be used for calibration
38                   % representation of uncalibrated locations
39   widthIMG = 640; heightIMG = 72; % TLC ROI of interest in pixels
40   dystart = 2; % number of pixels relative to y-coordinate
41   dx = 4; % interrogation ROI dimensions for calibration in pixels
42       % (needs to be divisible by respective widthIMG and heightIMG)
43   dy = 3;
44   Nx = widthIMG/dx; Ny =heightIMG/dy;
45
46   % Filename inputs
47   datafilename = 'calib.lvm'; % calibration data filename (*.lvm)
48                               % from LabVIEW - user input from LabVIEW
49   imagefilename = 'calib_0'; % Beginning of Hue image name (*.tif) to
50                              % before increments - user input from LabVIEW
51   imagefilenameRGB = 'calib_0_rgb'; % Beginning of RGB image name (*.TIFF)
52                                     % to before increments
53                                     % - user input from LabVIEW
54   calibhuefile = 'calibhue_4x3_0'; % ROI 4x3 lots of small region | one
55                                    % file per location - program created
56   filepolycoeff = 'polycoeff_'; % calibration polynomial coefficients |
57                                 % one file per location -
58                                 % program created (4x3)
59   coordinatesfile = 'coordcalib.txt'; % coordinates file - user creatd
60
61   % Process inputs
62   tempstyle = 'inlet_temps';
63   % choice between (1)average - 'average_temps'; (2)inlet temperature -
64   % inlet_temps; (3)exit  temperature - exit_temps;
65   % (4)interpolated - interp_temps
66   storedhuedata = 'yes';
67   savepolycoeffs = 'yes'; % save generated polynomial coefficients
68   SmoothZeros = 'yes'; % smooth zero polynomial coefficients
69   fitpolys = 'yes'; % generate polynomial coefficients
70   readpolys = 'no'; % read in poly coefficients for smoothing
71   xstart = 0;
72   rdist = 320;
73   Nsmooths = 10; % number of smoothings to do to get rid of
74               % zero polynomial coeeficients
75   fitorder = 5; % initial polynomial order of curve fit
76
77   % Additional corrections
```

```
78    % To obtain improved curve fit
79    ZeroTemp = 38; % TLC redstart
80    nzeros = fitorder - 3;
81    imgDisp = [1 2 3 4 5 6 7]; % location number RGB cropped image to be
82                                    % viewed
83    addforcedhue = 'true'; % Impose peak asymptotic temp for better fit
84    deltaforcehue = 25; % hue addition at which peak asymptotic hue will
85                            % be added
86    Tempforce = 53; % Imposed peak asymptotic temp for better curve fit
87    FindZeroLow = 0; % lower limit to search for peaks and troughs in
88                        % fitted curves
89    FindZeroHigh = 175; % upper limit to search for peaks and troughs in
90                            % fitted curves
91    Minus360HueUpper = 300; % upper limit for hue value at which negative
92                                % angle is used
93    dTtempcalibration = 1.5; % minimum increment in calibration images;
94                                % prevents extraneous points from being
95                                % included
96
97    % Optional
98    imgview = 'yes'; %'yes' or 'no'
99    imgview_kval = 1;
100
101   % REMINDERS
102   % i) change imglocArr appropriately
103   %%%%%%%%%%%%%%%%%%%%%%%%%%%%%%%%%%%%%%%%%%%%%%%%%%%%%%%%%%%%%%%%%%%%%%%%
104
105   % Calibration data file constants %%%%%%%%%%%%%%%%%%%%%%%%%%%%%%%%%%%%%%
106   nrows = 4;
107   headerlines = 23;
108   headercolumns = 0;
109   numblinesdatfile1 = 250; % because joining two files
110   imgMid = 10000; % number of images in 1st round / put to high number if
111                        % only one round
112   %%%%%%%%%%%%%%%%%%%%%%%%%%%%%%%%%%%%%%%%%%%%%%%%%%%%%%%%%%%%%%%%%%%%%%%%%
113
114   % Initialize coordinates %%%%%%%%%%%%%%%%%%%%%%%%%%%%%%%%%%%%%%%%%%%%%%%
115   [xindArr1 yindArr1] = textread(coordinatesfile...
116       ,'%f %f','delimiter','\t');
117   xleftArr = linspace(0,0,Nloc);
118   xrightArr = zeros(size(xleftArr));
119   yleftArr = zeros(size(xleftArr));
120   yrightArr = zeros(size(xleftArr));
121   rotArr = zeros(size(xleftArr));
122
123   rotArr1 = zeros(size(xleftArr));
124
```

```
125  % Read coordinates file into variables
126  j=1; % Nloc / 1, depends on which is first, for last location 1st use
127       % 'Nloc'
128  for i=1:2:2*Nloc
129      xleftArr(j) = xindArr1(i);
130      xrightArr(j) = xindArr1(i+1);
131      yleftArr(j) = yindArr1(i);
132      yrightArr(j) = yindArr1(i+1);
133      rotArr(j) = atan((yrightArr(j)-yleftArr(j))/(xrightArr(j)-...
134          xleftArr(j)))*180/pi;
135      theta = rotArr(j)*pi/180;
136      dyrot = rdist*sin(theta);
137      yposArr(j) = yrightArr(j) - floor(dyrot)+dystart;
138      j = j-1;
139      %+/- depends on which is first - for last location 1st use '-'
140  end
141
142  %%%%%%%%%%%%%%%%%%%%%%%%%%%%%%%%%%%%%%%%%%%%%%%%%%%%%%%%%%%%%%%%%%%%%%%%
143  % Array initializations
144  tempArr = zeros(1,Nloc);
145  polycoeff = zeros(Nx*Ny,fitorder+1,Nloc);
146
147  % Read calibration file
148  % skip first and last point as different size columns than the rest
149  Tamb = linspace(0,0,Nimg); leftknob = linspace(0,0,Nimg); rightknob =...
150      linspace(0,0,Nimg);
151  imgLocArr = linspace(0,0,Nimg);
152  counter2Img = linspace(1,1,Nloc); % re-initialize counter for image
153                                    % locations
154
155  [Xval TempIn TempOut Pout Pin Pdiff Voltage Current TubeTemp...
156  preheater1 preheater2 TankTemp PumpOutTemp PumpInTemp Tamb Tank2Temp...
157  PumpOutTemp2 flowmlminTestInSigma TestOutSigma PressOutSigma...
158  PressInSigma PressDiffSigma VoltSigma CurrentSigma Pbarometer...
159  leftknob rightknob casenumb Comment] = textread(datafilename,'%f %f...
160  %f %f %f %f %f %f %f %f %f %f %f %f %f %f %f %f %f %f %f %f %f %f...
161  %f %f %f %f %q','headerlines',headerlines,'delimiter','\t');
162
163  imgLocArr = leftknob-rightknob+1; %unique function to denote the number
164  % of locations, starting from 1 -> to create integer indexing
165
166  % Counter initializations
167  counterImg = linspace(0,0,Nloc);
168  for k=1:Nimg
169      counterImg(imgLocArr(k)) = counterImg(imgLocArr(k))+1;
170  end
171  %%%%%%%%%%%%%%%%%%%%%%%%%%%%%%%%%%%%%%%%%%%%%%%%%%%%%%%%%%%%%%%%%%%%%%%%
```

```matlab
172  %%%%%%%%%%%%%%%%%%%%%%%%%%%%%%%%%%%%%%%%%%%%%%%%%%%%%%%%%%%%%%%%%%%%%%%%%%%
173
174  Tamb = linspace(0,0,Nimg); leftknob = linspace(0,0,Nimg); rightknob =...
175      linspace(0,0,Nimg);
176  for k=1:Nimg
177      indexCount = imgLocArr(k);
178      switch tempstyle
179          case 'average_temps' % Recommended if temperature difference is
180                                % ~0.5C or less
181              calibdata = (TempIn(k)+ TempOut(k))/2;
182          case 'inlet_temps' % Recommended if concerned with inlet region
183                             % and larger temperature difference
184              calibdata = TempIn(k);
185          case 'exit_temps' % Recommended if concerned with exit region
186                            % and larger temperature difference
187              calibdata = TempOut(k);
188          case 'interp_temps' % treat as linear drop in temperature -
189                              % Recommended if concerned region and larger
190                              % temperature difference
191              calibdata = (TempIn(k) - TempOut(k))/(100)*(leftknob(k)+...
192                  rightknob(k))+TempIn(k);
193      end
194      indexCount = imgLocArr(k);
195      tempArr(counter2Img(indexCount),indexCount) = calibdata;
196      counter2Img(indexCount) = counter2Img(indexCount)+1;
197  end
198  %%%%%%%%%%%%%%%%%%%%%%%%%%%%%%%%%%%%%%%%%%%%%%%%%%%%%%%%%%%%%%%%%%%%%%%%%%%
199  NimgForLoc = max(counterImg);
200  disp('finished reading in temperature data');
201  %%%%%%%%%%%%%%%%%%%%%%%%%%%%%%%%%%%%%%%%%%%%%%%%%%%%%%%%%%%%%%%%%%%%%%%%%%%
202
203  %%%%%%%%%%%%%%%%%%%%%%%%%%%%%%%%%%%%%%%%%%%%%%%%%%%%%%%%%%%%%%%%%%%%%%%%%%%
204  counter2Img = linspace(1,1,Nloc); % re-initialize counter for image
205                                    % locations
206  counter = 1; % counter for ROI locations
207  hueImgArr = zeros(NimgForLoc,Nx*Ny,Nloc); % hue array [(No of images for
208                                            % locs)x(NxNy)x
209                                            % (No of image locs)]
210  xind = xstart;
211
212  % Parsing out and storing hue dat for each ROI %%%%%%%%%%%%%%%%%%%%%%%%%%%
213  kimg = 1;
214  if strcmp(storedhuedata,'yes')
215      for i=1:Nimg
216          kimg = i;
217          indexCount = imgLocArr(i);
218          yind = yposArr(imgLocArr(i));
```

```
219          Filename = [imagefilename int2str(kimg) '.tif'];
220          FilenameRGB = [imagefilenameRGB int2str(kimg) '.TIFF'];
221          imgA = imread(Filename,'tif');
222          imgA = imrotate(imgA,rotArr(indexCount),'crop');
223          if i == imgDisp(indexCount);
224              imgRGB = imread(FilenameRGB,'tif');
225              imgRGB = imrotate(imgRGB,rotArr(indexCount),'crop');
226              imgRGB = imcrop(imgRGB,[xind yind widthIMG heightIMG]);
227              imshow(imgRGB);
228          end
229          for j=1:Nx
230              for k=1:Ny
231                  imgCrop = imcrop(imgA,[xind yind dx dy]);
232                  imgDbl = double(imgCrop);
233                  sizeArr = size(imgDbl); rowsize = sizeArr(1); colsize...
234                      = sizeArr(2);
235                  hueDat = reshape(imgDbl,rowsize*colsize,1);
236                  roiMedian = median(hueDat)/255*360;
237                  hueImgArr(counter2Img(indexCount),counter,indexCount)...
238                      = roiMedian;
239                  yind = yind+dy;
240                  counter = counter+1;
241              end
242              xind = xind+dx;
243              yind = yposArr(indexCount);
244          end
245          counter2Img(indexCount) = counter2Img(indexCount)+1;
246          counter = 1;
247          xind = xstart;
248      end
249      % Writing
250      for k = 1:NlocCalib
251          Filename = [calibhuefile int2str(k) '.txt'];
252          dlmwrite(Filename,hueImgArr(:,:,k),'\t');
253      end
254      if NlocCalib < Nloc % if there are more measured than calibrated
255      % locations represent uncalibrated with location krepresent right
256      % now assumes representing location is last location
257          for k = 1:krepresent-1
258              Filename = [calibhuefile int2str(k) '.txt'];
259              hueImgArr(:,:,k) = hueImgArr(:,:,krepresent);
260              dlmwrite(Filename,hueImgArr(:,:,k),'\t');
261              counterImg(k) = counterImg(krepresent);
262              tempArr(:,k) = tempArr(:,krepresent);
263          end
264      end
265      disp('finished writing hue data...beginning poly curve fitting');
```

```
266   else
267       % Reading
268       for k = 1:Nloc
269           Filename = [calibhuefile int2str(k) '.txt'];
270           hueImgArr(:,:,k) = dlmread(Filename,'\t');
271       end
272       disp('finished reading in saved hue data....');
273   end
274   %%%%%%%%%%%%%%%%%%%%%%%%%%%%%%%%%%%%%%%%%%%%%%%%%%%%%%%%%%%%%%%%%%%%%%%
275
276
277   % Polynomial fitting %%%%%%%%%%%%%%%%%%%%%%%%%%%%%%%%%%%%%%%%%%%%%%%%%%%
278   donothing = 0;
279   if strcmp(fitpolys,'yes')
280       disp('beginning polynomial curve fitting.....');
281           counterzero = 0; counter3 = 0; counter5 = 0; counterback = 0;
282           hueX = linspace(0,260,30);
283           for k = 1:Nloc
284           for i = 1:Nx*Ny
285               %%% Initially assume 5th order fit %%%
286               huedat_orig = hueImgArr(1:counterImg(k),i,k);
287               tempdat_orig = tempArr(1:counterImg(k),k);
288               huedat_old = hueImgArr(1:counterImg(k),i,k);
289               tempdat_old = tempArr(1:counterImg(k),k);
290               sizearr = size(tempdat_old); sizearr = sizearr(1);
291               sizearrCount = sizearr;
292               for j = 1:sizearr
293                   if huedat_orig(j) > Minus360HueUpper;
294                       huedat_old(j) = 360 - huedat_old(j);
295                   end
296               end
297               hue_temp_arr = [huedat_old tempdat_old];
298               hue_temp_sorted = sortrows(hue_temp_arr,1);
299               % sorts data with respect to increasing hue values
300
301               huedat = hue_temp_sorted(1,1); tempdat =...
302                   hue_temp_sorted(1,2);
303               jprime = 2;
304               for j = 2:sizearr
305                   if hue_temp_sorted(j,2) > tempdat(jprime-1) &&...
306                           (hue_temp_sorted(j,2)-...
307                           tempdat(jprime-1))<dTtempcalibration
308                       % if the temperature increment is positive and less
309                       % than 1.5C the increment is a valid point
310                       huedat(jprime) = hue_temp_sorted(j,1);
311                       tempdat(jprime) = hue_temp_sorted(j,2);
312                       jprime = jprime+1;
```

```matlab
313             end
314         end
315         sizenew = size(huedat);
316
317         if strcmp(addforcedhue,'true');
318             huedat = [huedat huedat(sizenew(2))+deltaforcehue];
319             tempdat = [tempdat Tempforce];
320         end
321
322         polycoefftest = polyfit(huedat,tempdat,fitorder);
323         flag = '5th';
324         %%% Check to verify real numbers else set to zero %%%
325         isnanSum = sum(isnan(polycoefftest));
326         polycoefftest2 = 0;
327         if isnanSum > 0
328             polycoeffnew = 0;
329             counterzero = counterzero+1;
330         else
331             %%% If roots to derivative assume 3rd order fit %%%
332             polyderiv = polyder(polycoefftest);
333             isnanSum = sum(isnan(polyderiv));
334             if isnanSum == 0
335                 tempY = polyval(polycoefftest,hueX);
336                 dTempY = polyval(polyderiv,hueX);
337                 rootvals = roots(polyderiv);
338                 n=1;
339                 while n < fitorder
340                     if isreal(rootvals(n)) && rootvals(n) >...
341                             FindZeroLow &&....
342                             rootvals(n) < FindZeroHigh
343                             % if 5th has root stick
344                             % with 3rd, should be 25-175
345                         flag = '3rd';
346                         polycoefftest2 = [linspace(0,0,nzeros)...
347                                 polyfit(huedat,tempdat,3)];
348                         polyderiv = polyder(polycoefftest2);
349                         isnanSum = sum(isnan(polyderiv));
350
351                         if isnanSum == 0
352                             % if can fit 3rd order see if has roots
353                             n = n+1;
354                             tempY = polyval(polycoefftest2,hueX);
355                             dTempY = polyval(polyderiv,hueX);
356                             rootvals2 = roots(polyderiv);
357                             y = 1;
358                             while y <= 2
359                                 if isreal(rootvals2(y)) &&...
```

```
360              rootvals2(y) >...
361              FindZeroLow &&...
362              rootvals2(y) < FindZeroHigh
363          y = y+1;
364          % forcing the 0 hue to ZeroTemp
365          tempdatcheck =...
366              [ZeroTemp tempdat];
367          huedatcheck = [0 huedat];
368          polycoefftest3 =...
369              [linspace(0,0,nzeros) ...
370      polyfit(huedatcheck,tempdatcheck,3)];
371          polyderiv =...
372              polyder(polycoefftest3);
373          isnanSum = sum(isnan(polyderiv));
374          if isnanSum == 0
375              tempY =...
376                  polyval(polycoefftest3...
377                  ,hueX);
378              dTempY =...
379                  yval(polyderiv,hueX);
380              rootvals3 = roots(polyderiv);
381              z = 1;
382              while z <= 2
383                  % see if forcing the 0
384                  % hue to ZeroTemp solves
385                  % problem + new range
386                  if...
387                  isreal(rootvals3(z))...
388                  && rootvals3(z) >...
389          FindZeroLow && rootvals3(z) <...
390                      FindZeroHigh
391                      z = 3;
392                      y = 3;
393                      % third fails,
394                      % kick out of all
395                      n = fitorder;
396                      % third fails, kick
397                      % out of all
398                      flag = 'old';
399                  else
400                      flag = '3rdMOD';
401                      z = z+1;
402                  end
403              end
404          else
405              y = 3;
406              n = fitorder;
```

```
407                                         flag = 'old';
408                                     end
409                                 else
410                                     y = y+1;
411                                 end
412                             end
413                         else
414                             flag = 'old';
415                             n = fitorder;
416                             % 3rd no good forcing kick out
417                         end
418                     else
419                         n = n+1;
420                     end
421                 end
422             else
423                 polycoeffnew = 0;
424                 flag = 'old';
425             end
426             switch flag
427                 % -Sets the polynomial type to:
428                 % Modified 3rd order (3rdMOD), 3rd order,
429                 % or 5th order
430                 % -If dataset is junk (e.g. max hue < prescribed)
431                 % treats as a zero
432                 case '3rdMOD'
433                     if max(huedat) < 50;
434                         polycoeffnew = 0;
435                         %disp('zero');
436                         counterzero = counterzero+1;
437                     else
438                         polycoeffnew = polycoefftest3;
439                         %disp('3rd');
440                         counter3 = counter3+1;
441                     end
442                 case '3rd'
443                     if max(huedat) < 50;
444                         polycoeffnew = 0;
445                         %disp('zero');
446                         counterzero = counterzero+1;
447                     else
448                         polycoeffnew = polycoefftest2;
449                         %disp('3rd');
450                         counter3 = counter3+1;
451                     end
452                 case 'old'
453                     if max(huedat) < 50;
```

```
454                    polycoeffnew = 0;
455                    %disp('zero');
456                    counterzero = counterzero+1;
457               else
458                    polycoeffnew = 0;
459                    %disp('old');
460                    counterback = counterback+1;
461               end
462          case '5th'
463               if max(huedat) < 100;
464                    polycoeffnew = 0;
465                    %disp('zero');
466                    counterzero = counterzero+1;
467               else
468                    polycoeffnew = polycoefftest;
469                    %disp('5th');
470                    counter5 = counter5+1;
471               end
472          end
473
474          if strcmp(imgview,'yes') %&& k > imgview_kval
475               tempfinal = polyval(polycoeffnew,hueX);
476               temp3 = polyval(polycoefftest2,hueX);
477               temp5 = polyval(polycoefftest,hueX);
478               dispimgnumb = ['ROI no. ' num2str(i)...
479               ' location ' num2str(k)];
480          disp(dispimgnumb);
481               plot(huedat,tempdat,'bo',hueX,temp5,'r-',...
482          hueX,temp3,'y-',...
483          hueX,tempfinal,'g-',huedat_orig,tempdat_orig,...
484          'm*');
485          legend('corrected data','5th order','3rd order',...
486               'final curve','original data');
487               axis([0 360 35 55]);
488               pause;
489          end
490     end % 1st inan if statement
491     polycoeff(i,:,k) = polycoeffnew;
492     end
493     end
494
495     if strcmp(savepolycoeffs,'yes')
496     disp('finished poly coefficient determination....
497     writing out coefficients');
498     for k = 1:Nloc
499          Filename = [filepolycoeff int2str(k) '.txt'];
500          dlmwrite(Filename,polycoeff(:,:,k),'\t');
```

```
501          end
502          disp('finished gen & saving poly coeff...plotting & ending');
503          else
504          disp('finished generating...plotting and ending');
505          end
506
507          disp(['counter zero = ' num2str(counterzero)]);
508          disp(['counter backwards = ' num2str(counterback)]);
509          disp(['counter 3rd order = ' num2str(counter3)]);
510          disp(['counter 5th order = ' num2str(counter5)]);
511          countertotal = counterzero+counterback+counter3+counter5;
512          disp(['total number of locations is ' num2str(countertotal)]);
513  end
514
515  if strcmp(SmoothZeros,'yes')
516      disp('reading in polynomial coefficients for smoothing');
517      if strcmp(readpolys,'yes')
518              for k = 1:Nloc
519          Filename = [filepolycoeff int2str(k) '.txt'];
520          polycoeff(:,:,k) = dlmread(Filename,'\t');
521              end
522      end
523      counterzero2 = 0;
524      disp('finished reading poly coefficients for...
525      smoothing...beg smoothing');
526      for k=1:Nloc
527          for i = 1:Nx*Ny
528              if polycoeff(i,:,k) == 0
529                  counterzero2 = counterzero2+1;
530              end
531          end
532      end
533      disp(['number of zeros initially = ' num2str(counterzero2)]);
534          counterzero2 = 0;
535          for k=1:Nloc
536          for h = 1:Nsmooths
537              for i = 1:Nx*Ny
538                  if polycoeff(i,:,k) == 0
539                      rowi = ceil(i/Nx);
540                      coli = Nx + (i-Nx*rowi);
541                      if i == 1
542                          kappa = 2;
543                      elseif coli == 1
544                          kappa = i-Nx;
545                      else
546                          kappa = i-1;
547                      end
```

```
548                         polycoeff(i,:,k) = polycoeff(kappa,:,k);
549                     end
550                 end
551                 for i = 1:Nx*Ny
552                     if polycoeff(i,:,k) == 0
553                         rowi = ceil(i/Nx);
554                         coli = Nx + (i-Nx*rowi);
555                         if i == 1
556                             kappa = 2;
557                         elseif coli == Nx
558                             kappa = i-1;
559                         else
560                             kappa = i+1;
561                         end
562                         polycoeff(i,:,k) == polycoeff(kappa,:,k);
563                     end
564                 end
565             end
566         end
567     counterzero2 = 0;
568     for k=1:Nloc
569         for i = 1:Nx*Ny
570             if polycoeff(i,:,k) == 0
571                 counterzero2 = counterzero2+1;
572             end
573         end
574     end
575     disp(['counter zero second time = ' num2str(counterzero2)]);
576
577     disp('...writing out coefficients');
578     for k = 1:Nloc
579         Filename = [filepolycoeff int2str(k) '.txt'];
580         dlmwrite(Filename,polycoeff(:,:,k),'\t');
581     end
582 disp('finished generating smoothing and saving polynomial coefficients
583 ...plotting and ending');
584 end
585
586 disp('Good bye');
587 % END %%%%%%%%%%%%%%%%%%%%%%%%%%%%%%%%%%%%%%%%%%%%%%%%%%%%%%%%%%%%%%%%%%%%%
```

```matlab
%%%%%%%%%%%%%%%%%%%%%%%%%%%%%%%%%%%%%%%%%%%%%%%%%%%%%%%%%%%%%%%%%%%%%%%%%%%%%
% TLC Rig
% Author: Roland S Muwanga
% Date: July 05/06
% Based on Oct 05, 2005 and Sept 28/05
%
% Program - datprocboil***
%
% Description: Main program for post processing heat transfer data from
%                   a microtube flow boiling experiment
%
% Requires:
% 1. Calibration output file of polynomial coefficients from calibproc***
% 2. Outputed data file from LabVIEW - DAQMain_Boiling02.vi or similar
% 3. Nimg number of RGB and hue TLC images
% 4. Coordinates file identifying area of interest within images
%    - coordinates file contains 2 coordinates for each traversed location
% 5. nucalcboil_example.m or similar program for calculating the local
%    heat transfer coefficients is available
%
% Promises:
% 1. To calculate the local heat transer coefficient from a flow boiling
%    microtube experiment
% 2. Output - 'NussStrm' which is the averaged streamwise Nusselt number
%
%
% Additional Notes:
% i. to be run from measuremetn data directory
% ii. to run type filename without '.m' at Matlab prompt
%%%%%%%%%%%%%%%%%%%%%%%%%%%%%%%%%%%%%%%%%%%%%%%%%%%%%%%%%%%%%%%%%%%%%%%%%%%%%

close all;
regeneratedata = 'true'; % true/false - if data already loaded can set
                         % to false and continue with postcalculations
postcalculations = 'false'; % may include calculations for correlation
                            % comparison and plotting

if strcmp(regeneratedata,'true')
    close all;
    clear all;

    % Inputs %%%%%%%%%%%%%%%%%%%%%%%%%%%%%%%%%%%%%%%%%%%%%%%%%%%%%%%%%%%%
    inputfile = 'meas_mod.lvm'; % output data file from LabVIEW
    imgstart = 1; % image no. to start at
    coordfile = '..\Calibration\coordcalib.txt'; % coordinates file
    calibfile =
    '..\..\July0506_1.00BoilCalibRetrial\Calibration\polycoeff_mod_';
```

```
48      % output from calibration post processing
49
50      FiguresFilename = 'Figures\all_img'; % output filename for
51                                           % post-processed figure
52      fileOutput = 'SavedData\100FC72boilout.txt'; % miscellaneous
53                                                   % output data
54                                                   % filename
55      imgname = 'meas_0'; % beginning of image filename
56      writefigures ='true'; % true/false to write post-processed figures
57      postcalculations = 'true'; %true/false - see above
58
59      Nimg = 104; % number of images
60      Nloc = 7; % number of traversed locations
61      deltay = 72; % height of imaged location of interest (pixels)
62
63      Dh = 1.0668e-3; % hydraulic diameter (m)
64      Lhydraulic = 152.4/1000; % tube length (m)
65      heaterL = 0.106; % heated tube length (m)
66      powerratio = 0.95; % should be less than 1;
67                         % resistanceTube/resistanceTotal
68      umperpix = 15.528; % micrometers per pixel - resolution
69      pixperum = 1/umperpix; % pixles per micrometer
70
71      xinpix = 380; % based on (0,0) location at inlet
72      deltaxin = ((640-xinpix)*umperpix/1000)*(-1);
73      xlength = 640; % image length (pixels)
74      rdist = xlength/2; % distance from center of image rotation (pixels)
75      xorigin = 0;
76      xstart = 0; % number of pixels in length direction into the ROI to
77                  % to parse out ROI
78      dystart = 1; % number of pixels in height direction into the ROI to
79                   % to parse out ROI
80      streamX = xlength-xstart; % length of imaged region to present
81                                % (pixels)
82      streamY = deltay; % height of imaged region to present
83                        % (pixels)
84      dxCalib = 4; %calibration streamwise pixel difference (ROI)
85      dyCalib = 3; %calibration spanwise pixel difference (ROI)
86      %%%%%%%%%%%%%%%%%%%%%%%%%%%%%%%%%%%%%%%%%%%%%%%%%%%%%%%%%%%%%%%%%%%%%%%
87
88      % Read in LabVIEW data file
89      numheaderlines = 23; % header lines in LabVIEW data file
90      [Xval TempIn TempOut Pout Pin Pdiff Voltage Current TubeTemp...
91              preheater1 preheater2 TankTemp PumpOutTemp PumpInTemp...
92          AmbientTemp Tank2Temp PumpOutTemp2 flowmlmin TestInSigma...
93          TestOutSigma PressOutSigma PressInSigma PressDiffSigma...
94          VoltSigma CurrentSigma Pbarometer leftknob rightknob casenumb...
```

```
 95        Comment] = textread(inputfile,'%f %f %f %f %f %f %f %f %f %f...
 96        %f %f %f %f %f %f %f %f %f %f %f %f %f %f %f %f %f %f %f %q',...
 97        'headerlines',numheaderlines,'delimiter','\t');
 98
 99    % clear unused parameters
100    clear Xval Preheat1 Preheat2 Temp1 Temp2 TankTemp PumpInTemp...
101    PumpOutTemp Comment;
102
103    % Initialize coordinates %%%%%%%%%%%%%%%%%%%%%%%%%%%%%%%%%%%%%%
104    imgLocArr = round((leftknob+rightknob+5)/10)-3;
105    xin = (leftknob + rightknob + deltaxin)/1000 ;
106
107    % Read in coordinates data file %%%%%%%%%%%%%%%%%%%%%%%%%%%%%%%%%
108    [xindArr yindArr] = textread(coordfile,'%f %f','delimiter','\t');
109    xleftArr = linspace(0,0,Nloc);
110    xrightArr = zeros(size(xleftArr));
111    yleftArr = zeros(size(xleftArr));
112    yrightArr = zeros(size(xleftArr));
113    rotArr = zeros(size(xleftArr));
114
115    j=Nloc; % Nloc/1, depends on which is first, for last location 1st
116            % use 'Nloc'
117    for i=1:2:2*Nloc
118        xleftArr(j) = xindArr(i);
119        xrightArr(j) = xindArr(i+1);
120        yleftArr(j) = yindArr(i);
121        yrightArr(j) = yindArr(i+1);
122        rotArr(j) = atan((yrightArr(j)-yleftArr(j))/(xrightArr(j)-...
123            xleftArr(j)))*180/pi;
124        theta = rotArr(j)*pi/180;
125        dyrot = rdist*sin(theta);
126        yposArr(j) = yrightArr(j) - floor(dyrot);
127        j = j-1; % +/- depends on which is first - for last location
128                 % 1st use '-'
129    end
130    xind = xstart; %yind = yposArr(imgLocArr(1))+dystart;
131
132    QflArr = flowmlmin*(1e-6)/60; % convert flowrate to m3/s
133
134    % Initialize arrays of various parameter %%%%%%%%%%%%%%%%%%%%%%%%
135    xstar = zeros(Nimg,xlength); % x/RePrDh
136    xd = zeros(Nimg,xlength); % x/D for a given image
137    PrLocalArr = zeros(Nimg,xlength); % Prandtl number
138    xqualityArr = zeros(Nimg,xlength); % thermodynamic quality
139    rhoFLocalArr = zeros(Nimg,xlength); % liquid density
140    CpLocalArr = zeros(Nimg,xlength); % fluid specific heat
141    kcondLocalArr = zeros(Nimg,xlength); % liquid thermal conductivity
```

287

```
142     sigmaLocalArr = zeros(Nimg,xlength); % fluid surface tension
143     myuFLocalArr = zeros(Nimg,xlength); % liquid viscosity
144     rhoVLocalArr = zeros(Nimg,xlength); % vapor density
145     hfgLocalArr = zeros(Nimg,xlength); % fluid latent heat of vaporization
146
147     AvgNuThresh = linspace(0,0,Nimg); % Average Nu from AvghtcThresh
148     AvghtcThresh = linspace(0,0,Nimg); % Average htc from AvgTwThresh
149     AvgTwThresh = linspace(0,0,Nimg); % Average wall temperature
150                                        % thresholded between min and max
151                                        % temperature limits
152     ReynNum = linspace(0,0,Nimg); % Average Reynolds number
153     NuGnielArr = linspace(0,0,Nimg); % Nu from Gnielinski correlation
154     ImgHueAvg = linspace(0,0,Nimg); % Image average Hue value
155     TwStrm = zeros(size(xstar)); % Averaged streamwise wall temperature
156     TsatArr = zeros(size(xstar)); % Saturation temperature
157     TbArrAll = zeros(size(xstar)); % Fluid bulk temperature
158     TbArrtheo = zeros(size(xstar)); % Fluid bulk assuming no boiling
159     maxdelNuArr = zeros(size(ReynNum)); % Maximum Nu uncertainty
160     maxdelTwArr = zeros(size(ReynNum)); % Maximum Tw uncertainty
161     rhoIn = zeros(size(ReynNum)); % Inlet liquid density
162
163     frictfactArr = linspace(0,0,Nimg); %initialize friction factor array
164     Pdiff = (Pdiff+Pcorrection)*6894.75729317; %psi to Pascals
165     Pout = Pout*6894.75729317; %psi to Pascals
166     Pin = (Pin+Pcorrection)*6894.75729317; %psi to Pascals
167
168     Pbarometer = Pbarometer*6894.75729317; %psi to Pascals
169     PinCorr = Pout./Pout - 1; % zero array size of Pout
170     PinDelta = Pout./Pout - 1; % zero array size of Pout
171     PoutDelta = Pout./Pout - 1; % zero array size of Pout
172
173     % begin iterating through images
174     for i=imgstart:Nimg
175         % Read in hue image
176         indexCount = imgLocArr(i);
177         dispimagenumb = ['image no.' num2str(i)];
178         disp(dispimagenumb);
179         Filename = [imgname int2str(i) '.tif'];
180         imgA = imread(Filename,'tif');
181
182         % Rotate and crop hue image
183         imgA = imrotate(imgA,rotArr(indexCount),'crop');
184         imgCrop = imcrop(imgA,[xorigin yposArr(indexCount) streamX...
185                 streamY]);
186         imgInt = fliplr(imgCrop);
187         imgDbl = double(imgInt)*360/255; % convert to degrees scale
188
```

```matlab
189        % Read in RGB image
190        RGBname = [imgname '_rgb' int2str(i) '.TIFF'];
191        RGBimg = imread(RGBname,'tif');
192
193        % Rotate and crop RGB image
194        RGBrot = imrotate(RGBimg ,rotArr(indexCount),'crop');
195        RGBcrop = imcrop(RGBrot,[xorigin yposArr(indexCount) streamX...
196               streamY]);
197        for k = 1:3
198            RGBflip(:,:,k) = fliplr(RGBcrop(:,:,k));
199        end
200
201        imgSize = size(imgDbl);
202        xlengthI = imgSize(2);
203        xstar = xstar(:,1:xlengthI);
204        xd = xd(:,1:xlengthI);
205
206        % Read in polynomial coefficients
207        polycoeffFile = [calibfile int2str(indexCount) '.txt'];
208        polycoeff = dlmread(polycoeffFile,'\t'); % calibration
209                                                  % coefficients
210
211        % Calculate friction factor and correct for entry/exit losses
212        [frictfactArr(i) PinDelta(i) PoutDelta(i)] = frictionCalc...
213            (TempIn(i), TempOut(i), QflArr(i), Pdiff(i),Dh,...
214            Lhydraulic,'fc72');
215        % adjusting Pin/Pout for klosses at entrance/exit
216        PinCorr(i) = Pin(i)-PinDelta(i); PoutCorr(i) =...
217            Pout(i)+PoutDelta(i);
218
219        % Calculate Nusselt number
220        [xstar(i,:) xd(i,:) NussStrm(i,:) AvgNuThresh(i) ReynNum(i)...
221               TwArray PercIn(i) outofboundsI NuArray TwStrm(i,:)...
222               NuGnielArr(i) ImgHueAvg(i) maxdelNuArr(i)...
223               maxdelTwArr(i) UTwcArr TbArrExit(i) delValArr(i,:)...
224               BoilIndicate(i) QtoFluid(i) TsatOut(i) imgHue...
225               xdtoboil(i) TbArrAll(i,:) PrLocalArr(i,:) ...
226               xqualityArr(i,:) htcStrm(i,:) AvghtcThresh(i)...
227               AvgTwThresh(i) rhoFLocalArr(i,:) CpLocalArr(i,:)...
228               kcondLocalArr(i,:) sigmaLocalArr(i,:)...
229               myuFLocalArr(i,:) rhoVLocalArr(i,:) hfgLocalArr(i,:)...
230               ToutSing(i) TsatArr(i,:) TbArrtheo(i,:) rhoIn(i)] =...
231               nucalcboil_example(TempIn(i),TempOut(i), imgDbl...
232               Voltage(i),Current(i),QflArr(i), xin(i), polycoeff,...
233        fileOutput, dxCalib, dyCalib, umperpix, TestInSigma(i),...
234        TestOutSigma(i), AmbientTemp(i), powerratio, Pdiff(i),...
235        PoutCorr(i), PinCorr(i),Pbarometer(i),i);
```

```
236
237        xdtoboilArr(i,:) = [xdtoboil(i), xdtoboil(i), 0, 150];
238
239        QperA = QtoFluid/(pi*Dh*heaterL); % heat flux/unit area
240        Gflux = (rhoIn.').*QflArr/(pi*Dh^2/4); % mass flux
241
242        % Present processed figures if 'writefigures' is true
243        if strcmp(writefigures,'true')
244            % Hue image
245            titleSTR = ['Location ' num2str(i) ', Image No.'...
246                        num2str(i),', G~ ' num2str(Gflux(i),'%10.0f'),...
247                        'kg/(m^2\cdots), Q/A~ ', num2str(QperA(i)/1000,...
248                        '%10.0f') 'kW/m^2'];
249            SUBPLOT(5,1,1), imagesc(imgHue);
250            colormap(jet);
251            colorbar; axis equal;
252            caxis([0 360]);
253            ylabel('hue value');
254            title(titleSTR);
255
256            % Average Tw and Tb along streamwise direction
257            SUBPLOT(5,1,2), plot(xd(i,:),TwStrm(i,:),'bo',xd(i,:),...
258                TbArrAll(i,:),'r^');
259            AXIS([floor(xd(i,1)) ceil(xd(i,xlength)) 40 100]);
260            xlabel('x/D'); ylabel('T (^oC)');
261
262            % Average Nu along streamwise direction
263            plothigh = 1.5*AvgNuThresh(i);
264            if plothigh <= 0
265                plothigh = 10;
266            end
267            SUBPLOT(5,1,3), plot(xd(i,:),NussStrm(i,:),'bo');
268            AXIS([floor(xd(i,1))...
269                        ceil(xd(i,xlength)) 0 plothigh]);
270            xlabel('x/D'); ylabel('Nu');
271
272            % Average htc along streamwise direction
273            plothigh = 1.5*AvghtcThresh(i);
274            if plothigh <= 0
275                plothigh = 1000;
276            end
277            SUBPLOT(5,1,4), plot(xd(i,:),htcStrm(i,:),'bo');
278            AXIS([floor(xd(i,1))...
279                        ceil(xd(i,xlength)) 0 plothigh]);
280            xlabel('x/D'); ylabel('h (W/(m^2^.^oC)');
281
282            % Average RGB intensity
```

```matlab
283              SUBPLOT(5,1,5), imshow(RGBflip);
284              ylabel('raw image');
285
286              % Write out plot to file
287              X=getframe(gcf);
288              plotfiletitle = [FiguresFilename num2str(i) '.jpg'];
289              imwrite(X.cdata, plotfiletitle,'jpg');
290          end
291      end
292  end
293
294
295  if strcmp(postcalculations,'true')
296      %%%%%%%%%%%%% Misc Post calculations %%%%%%%%%%%%%%%%%%%%%%%%%%%
297      % Miscellaneous plotting and file saving commands may be included as
298      % necessary
299  end
300  % END  %%%%%%%%%%%%%%%%%%%%%%%%%%%%%%%%%%%%%%%%%%%%%%%%%%%%%%%%%%%%%%%%
```

```matlab
1    %%%%%%%%%%%%%%%%%%%%%%%%%%%%%%%%%%%%%%%%%%%%%%%%%%%%%%%%%%%%%%%%%%%%%%%
2    % TLC Rig
3    % Author: Roland S Muwanga
4    % Date: July 05, 2006
5    % Modified: Oct 21, 2005
6    % - added calculation for Tw mean and htc mean
7    % - modified htc to 28 from 25
8    % - outputting htc average and stream
9    % Based on Sept 28/05 and Oct0105
10   %
11   % function [xstar, xd, AvgNuStrm, AvgNuThresh, Reyn, TwFilter, PercIn,.
12   %           outofbounds, NuArrFilter, AvgTwStrm, NuGniel, ImgHueAvg,...
13   %           maxdelNu, maxdelTw, UTwc, TbArrExit,delVals, BoilIndicate,...
14   %           QtoFluid, TsatOut, imgHue, xdtoboil,TbArr, PrLocal, xquality,
15   %           AvghtcStrm, AvghtcThresh, AvgTwThresh,rhoLocal, CpLocal,...
16   %           kcondLocal, sigmaLocal, myuLocal, rhoVLocal, hfgLocal,...
17   %           ToutSing, Tsat, TbArrtheo, rhoIn] = NuCalcTubeJun3006(Tin,...
18   %           Tout, imgHue, Vvolt, Iamp, Qfl, xin, polycoeff,fileOutput,...
19   %           dxCalib,dyCalib,umperpix, TinStdev, ToutStdev,xlength,deltay,
20   %           Tamb,powerratio,Pdiff,Pout,Pin,Pbaro,imgNumber)
21   %
22   %
23   % Requires:
24   % 1. Hue image 'imgHue' of only of area to be converted to Tw based on
25   %    polynomial coefficients in file 'polycoeff'
26   % 2. 'polycoeff' formated in output based on calibproc*** or similar
27   % 3. Vvolt, and Iam are power applied to tube
28   % 4. Qfl is flowrate in m3/s
29   % 5. Pin, Pout, Pbar, Pdiff are inlet, outlet, barometric and
30   %    differential pressure in Pascals
31   % 6. Tin,Tout are inlet and outlet temperatures of tube
32   % 7. dxCalib and dyCalib the x and y ROI sizes from calibration
33   %
34   %
35   % Promises: Nusselt number calculations for a microtube
36   %           boiling experiment with FC-72
37   %
38   %
39   %%%%%%%%%%%%%%%%%%%%%%%%%%%%%%%%%%%%%%%%%%%%%%%%%%%%%%%%%%%%%%%%%%%%%%%
40   function [xstar, xd, AvgNuStrm, AvgNuThresh, Reyn, TwFilter, PercIn,...
41            outofbounds, NuArrFilter, AvgTwStrm, NuGniel, ImgHueAvg,...
42            maxdelNu, maxdelTw, UTwc, TbArrExit,delVals, BoilIndicate,...
43            QtoFluid, TsatOut, imgHue, xdtoboil,TbArr, PrLocal, xquality,...
44            AvghtcStrm, AvghtcThresh, AvgTwThresh,rhoLocal, CpLocal,...
45            kcondLocal, sigmaLocal, myuLocal, rhoVLocal, hfgLocal,...
46            ToutSing, Tsat, TbArrtheo, rhoIn] = NuCalcTubeJun3006(Tin,...
47            Tout, imgHue, Vvolt, Iamp, Qfl, xin, polycoeff,fileOutput,...
```

```matlab
48                dxCalib,dyCalib,umperpix, TinStdev, ToutStdev,...
49                Tamb,powerratio,Pdiff,Pout,Pin,Pbaro,imgNumber)
50
51     % SOLUTION & OUTPUTS %%%%%%%%%%%%%%%%%%%%%%%%%%%%%%%%%%%%%%%%%%%%%%
52     maxdelNu = 0; maxdelTw = 0; UTwc = 0;
53
54     heaterL = 0.106; % heated length
55     ChannelLength = heaterL; % flow length
56     Dh = 1.0668e-3; % hydraulic diameter
57     Dhouter = 1.27e-3; % tube outer diameter
58     houter = 28; %(W/m2C) - identified from pretesting
59     kcondSS = 16.2; %(W/mC) Type304 ANSI SS - Matweb
60     Acs = pi*Dh^2/4; % inner cross-sectional area
61
62     % Area of interest size
63     imgSize = size(imgHue);
64     xlength = imgSize(2);
65     ylength = imgSize(1);
66
67     %%%% FC-72 Properties %%%%%%%%%%%%%%%%%%%%%%%%%%%%%%%%%%%%%%%%%%%%%%%
68     [rhoIn, CpIn, kcondIn, sigmaIn, myuIn, PrIn, rhoVIn, hfgIn] =...
69         fc72properties(Tin); % Inlet fluid properties, ref 1.
70     hfgIn = hfgIn*1000;
71     [rhoOut, CpOut, kcondOut, sigmaOut, myuOut, PrOut, rhoVOut, hfgOut] =...
72         fc72properties(Tout); % Outlet fluid properties, ref 1.
73     hfgOut = hfgOut*1000;
74     %%%% Average fluid Properties  %%%%%%%%%%%%%%%%%%%%%%%%%%%%%%%%%%%%%%
75     TbAvg = (Tin+Tout)/2;
76     [rho, Cp, kcond, sigma, myu, Pr, rhoV, hfg] = fc72properties(TbAvg);
77     % ref 1.
78     hfg = hfg*1000;
79
80     %%%% Fluid Properties interpolation %%%%%%%%%%%%%%%%%%%%%%%%%%%%%%%%%
81     % Local fluid properties along tube assuming all liquid flow
82     kcondLocal = linspace(kcondIn,kcondOut,xlength);
83     PrLocal = linspace(PrIn,PrOut,xlength);
84     myuLocal = linspace(myuIn,myuOut,xlength);
85     rhoLocal = linspace(rhoIn,rhoOut,xlength);
86     CpLocal = linspace(CpIn,CpOut,xlength);
87
88     %%%%%%%%%%%%%%%%%%%%%%%%%%%%%%%%%%%%%%%%%%%%%%%%%%%%%%%%%%%%%%%%%%%%%%
89
90     Reyn = rho*(Qfl/Acs)*Dh/myu; % Average Reynolds number
91     mdot = Qfl*rhoIn; % mass flowrate
92     ReynLocal = rhoLocal*(Qfl/Acs)*Dh./myu; % Local Reynolds number
93
94     imgMax = 210; imgMin = 0; % max and min values for filtering identified
```

```
95                                     % from calibration
96     ImgHueAvg = mean(mean(imgHue));
97
98     % Initialization of parameter for conversion of hue to temperature
99     x0 = 1; x1 = dxCalib; y0 = 1; y1 = dyCalib;
100    xind = 0; yind = 0;
101    Nx = xlength/dxCalib; Ny = ylength/dyCalib;
102    counterY = 1;
103
104    % Calculate Tw Outer %%%%%%%%%%%%%%%%%%%%%%%%%%%%%%%%%%%%%%%%%%%%%%%%
105    imgHue = fliplr(imgHue);
106    UTwc = zeros(size(imgHue)); % initialize temperature-hue uncertainty
107                                     % array
108    for k = 1:Nx*Ny
109        Dpolycoeff = polyder(polycoeff(k,:)); % derivatives of coefficients
110        TwArr(y0:y1,x0:x1) = polyval(polycoeff(k,:),imgHue(y0:y1,x0:x1));
111        % TwArr - wall temperature
112        UTwc(y0:y1,x0:x1) = polyval(Dpolycoeff,imgHue(y0:y1,x0:x1));
113        % UTWc - wall temperature gradient for uncertainty calc
114        counterY = counterY+1;
115        if counterY < Ny+1
116            y0 = y1;
117            y1 = y1+dyCalib;
118        else
119            counterY = 1;
120            y0 = 1;
121            y1 = dyCalib;
122            x0 = x1;
123            x1 = x1+dxCalib;
124        end
125    end
126    TwArr = fliplr(TwArr);
127    TwMedian = reshape(TwArr,xlength*ylength,1);
128    TwAvg = median(TwMedian);
129    %%%%%%%%%%%%%%%%%%%%%%%%%%%%%%%%%%%%%%%%%%%%%%%%%%%%%%%%%%%%%%%%%%%%%%%
130
131    % Q to fluid %%%%%%%%%%%%%%%%%%%%%%%%%%%%%%%%%%%%%%%%%%%%%%%%%%%%%%%%%%
132    delHfl_fluid = mdot*(CpOut*Tout-CpIn*Tin); % single phase energy balance
133    Qgen = Vvolt*Iamp*powerratio; % generated power times correction ratio
134    % accounting for losses to environment
135    QtoFluid = Qgen - houter*(pi*Dhouter*heaterL)*(TwAvg - Tamb);
136    PercIn = delHfl_fluid/(mean(QtoFluid))*100;
137    QperA = QtoFluid/(pi*Dh*heaterL); mean(QperA); % power per unit area
138    %%%%%%%%%%%%%%%%%%%%%%%%%%%%%%%%%%%%%%%%%%%%%%%%%%%%%%%%%%%%%%%%%%%%%%%
139
140    % Account for radial heat conduction %%%%%%%%%%%%%%%%%%%%%%%%%%%%%%%%%%
141    ThetaTLC = TwArr - Tamb; mean(mean(ThetaTLC));
```

```matlab
142    QgenperA = (Qgen)/(pi*(Dhouter^2-Dh^2)*heaterL);
143    Ro = Dhouter/2; Ri = Dh/2;
144    C1 = (-2*houter*ThetaTLC + Ro*QgenperA)*Ro/(2*kcondSS);
145    C2 = ThetaTLC + (Ro^2/4)*(QgenperA/kcondSS) - C1*log(Ro);
146    ThetaHTC = -(Ri^2/4)*(QgenperA/kcondSS) + C1*log(Ri) + C2;
147    TwInner = ThetaHTC + Tamb; mean(mean(TwInner));
148    %%%%%%%%%%%%%%%%%%%%%%%%%%%%%%%%%%%%%%%%%%%%%%%%%%%%%%%%%%%%%%%%%%%
149
150    % Calculate HTC %%%%%%%%%%%%%%%%%%%%%%%%%%%%%%%%%%%%%%%%%%%%%%%%%%%%
151    imgHue = fliplr(imgHue);
152    TbArr = zeros(1,xlength);
153    TbArrtheo = zeros(1,xlength);
154    Lch = ChannelLength;
155    x = zeros(1,xlength);
156
157    %%%%%%%%%%%%%%% Tbulk / Tsat Calcs %%%%%%%%%%%%%%%%%%%%%%%%%%%%%%%%
158    % Assumes boiling occurs when Tbulk = Tsat
159    % Flow is initialized to Tbulk based on Tin and Tout linear interp
160    % Local Tsat is calculated based Pin/Pout interpolation
161    % @ location where Tbulk=Tsat, all location after are set to local Tsat
162    TsatIn = 1562/(9.729-LOG10(Pin+Pbaro))-273.15; % inlet Tsat, ref 1.
163    TsatOut = 1562/(9.729-LOG10(Pout+Pbaro))-273.15; % outlet Tsat, ref 1.
164    [rhoSat, CpSat, kcondSat, sigmaSat, myuSat, PrSat, rhoVSat, hfgSat]...
165        = fc72properties(TsatOut); % calculate FC-72 properties at outlet
166    hfgSat = hfgSat*1000;
167    TimgSatIn = TsatIn - ((TsatIn-TsatOut)/heaterL)*xin; % Sat temp at inlet
168                                                        % of image
169    TimgSatOut = TsatIn - ((TsatIn-TsatOut)/heaterL)*...
170        (xin+(xlength*umperpix/1e6)); % Sat temp
171    % at outlet of image
172    Tsat = linspace(TimgSatIn,TimgSatOut,xlength); % local Sat temp
173                                                    % accross image
174
175    xd(j) = (xin+((j-1)*umperpix/1000000))/(Dh);
176    Tsatflag = 0; % when zero boiling location not found, when 1 boiling
177                  % location found
178    for i=1:xlength
179        x(i) = xin + (i-1)*umperpix/1e6;
180        TbArr(i) = Tin + pi*Dh*x(i)*QperA/(mdot*CpLocal(i));
181        TbArrtheo(i) = TbArr(i);
182        if Tsat(i) < TbArr(i) % simple correction for saturation
183                              % temperature assuming linear drop
184            TbArr(i) = Tsat(i);
185        end
186        [rhoLocal(i), CpLocal(i), kcondLocal(i), sigmaLocal(i),...
187                myuLocal(i), PrLocal(i),rhoVLocal(i), hfgLocal(i)] =...
188            fc72properties(TbArr(i)); % update properties w/ Tbulk improved
```

295

```
189                                             % and in case boiling
190     end
191     hfgLocal = hfgLocal*1000;
192     TbArrExit = TbArr(xlength);
193     ToutSing = Tin + pi*Dh*heaterL*QperA/(mdot*Cp);
194     Psat = Pin + Pbaro + (Pdiff)/Lch*x;
195     %%%%%%%%%%%%%%%%%%%%%%%%%%%%%%%%%%%%%%%%%%%%%%%%%%%%%%%%%%%%%%%%%%
196
197     %%%%%%% Length to boil%%%%%%%%%%%%%%%%%%%%%%%%%%%%%%%%%%%%%%%%%%%%%
198     % Calculated from equating:
199     % (Tb,out-Tb,in)/heaterL = (Tsat,boiling-Tb,in)/lengthtoboil
200     % & (Tsat,out-Tsat,in)/heaterL = (Tsat,boiling-Tsat,in)/lengthtoboil
201     BoilIndicate = mdot*(CpOut*Tout-CpIn*Tin);%- QtoFluid;
202     TsatSlope = (TsatOut - TsatIn) / heaterL;
203     TbulkOutTheo = Tin + pi*Dh*heaterL*QperA/(mdot*Cp); % calculated with
204                                             % average prop's
205     TbulkSlope = (TbulkOutTheo - Tin) / heaterL; %
206     lengthtoboil = (TsatIn - Tin) / (TbulkSlope - TsatSlope);
207
208     xdtoboil = lengthtoboil/Dh;
209     xquality = (QperA*pi*Dh*(x-lengthtoboil))./(mdot*hfg);
210     %%%%%%%%%%%%%%%%%%%%%%%%%%%%%%%%%%%%%%%%%%%%%%%%%%%%%%%%%%%%%%%%%%%
211     % Heat Transfer Coefficient Calculation
212     hArr = zeros(size(TwInner));
213     for i=1:xlength
214         hArr(:,i) = QperA*((TwInner(:,i)-TbArr(i)).^(-1));
215     end
216     %%%%%%%%%%%%%%%%%%%%%%%%%%%%%%%%%%%%%%%%%%%%%%%%%%%%%%%%%%%%%%%%%%%
217
218     % Filter Results %%%%%%%%%%%%%%%%%%%%%%%%%%%%%%%%%%%%%%%%%%%%%%%%%%
219     % Filters based on max and min Tw expected
220     % - usually based from calibration
221     NuArr = zeros(size(TwInner));
222     NuArr = hArr*Dh/kcond;
223     inu = 1; jnu = 1;
224
225     NuArrFilter = NuArr;
226     hArrFilter = hArr;
227     TwInnerFilter = TwInner;
228     TwFilter = TwArr;
229     imgHueFilter = imgHue;
230     maxNu = max(max(NuArrFilter));
231     outofbounds = 1;
232     Tmax = 97; Tmin = 68;
233     for j=1:xlength
234         for i=1:ylength
235             if ((TwInner(i,j) > Tmax) || (TwInner(i,j) < Tmin))
```

```
236                outofbounds = outofbounds + 1;
237            end
238            if ((imgHue(i,j) > imgMax) || (imgHue(i,j) < imgMin))
239                NuArrFilter(i,j) = 0;
240                hArrFilter(i,j) = 0;
241                TwInnerFilter(i,j) = 0;
242                imgHueFilter(i,j) = 0;
243                TwFilter(i,j) = 0;
244            end
245        end
246    end
247    %%%%%%%%%%%%%%%%%%%%%%%%%%%%%%%%%%%%%%%%%%%%%%%%%%%%%%%%%%%%%%%%%%%%%%%
248
249    % Uncertainty Calc %%%%%%%%%%%%%%%%%%%%%%%%%%%%%%%%%%%%%%%%%%%%%%%%%%%
250    delNu = ones(size(NuArr));
251    delh = ones(size(NuArr));
252    delTw = ones(size(NuArr));
253
254    [delNu delh delf delTw delRe delxd delxstar delQfl delTb] =...
255        uncertainty2phasetube(Dh, heaterL, Cp, myu,Pr, kcond, Qfl, rho,...
256        x, xlength, umperpix, Reyn, Lch, Pdiff, Iamp, Vvolt, UTwc,...
257        hArrFilter, Lch,Dhouter, houter, TwFilter, Tamb, TbArr, kcondSS,...
258        QtoFluid, TinStdev, ToutStdev, '1.00mm', 'powerinput',Tsat,...
259        TbArrtheo, Pin, Pout, Pbaro, Psat);
260
261
262    % Calculate averages and output to file %%%%%%%%%%%%%%%%%%%%%%%%%%%
263    AvgTwall = mean(mean(TwInner));
264    AvgNu = mean(mean(NuArr));
265
266    counter = 0;
267    counterStrm = 0;
268    AvgNuSum = 0;
269    AvghtcSum = 0;
270    AvgTwSum = 0;
271
272    AvgNuStrm = zeros(1,xlength);
273    maxdelNu = 0;
274    maxdelTw = 0;
275    AvgdelTw = 0;
276    AvgdelNu = 0;
277    Avgdelh = 0;
278    for j=1:xlength %Column-wise
279        AvgNuColSum = 0; % Reset the column sum to zero
280        AvghtcColSum = 0; % Reset the column sum to zero
281        AvgTwColSum = 0;
282        xstar(j) = (xin+((j-1)*umperpix/1000000))/(ReynLocal(j)*...
```

```
283    PrLocal(j)*Dh);
284        xd(j) = (xin+((j-1)*umperpix/1000000))/(Dh);
285        for i=1:ylength %Row-wise
286            if ((imgHue(i,j) < imgMax) && (imgHue(i,j) > imgMin))
287                % Check if original image values within calibration range
288                if ((TwInner(i,j) < Tmax) && (TwInner(i,j) > Tmin))
289                    AvgNuSum = AvgNuSum + NuArr(i,j);
290                    AvgNuColSum = AvgNuColSum + NuArr(i,j);
291                    AvghtcSum = AvghtcSum + hArr(i,j);
292                    AvghtcColSum = AvghtcColSum + hArr(i,j);
293                    AvgTwSum = AvgTwSum + TwInner(i,j);
294                    AvgTwColSum = AvgTwColSum + TwInner(i,j);
295                    counter = counter+1;
296                    counterStrm = counterStrm+1;
297                    AvgdelNu = AvgdelNu + delNu(i,j);
298                    Avgdelh = Avgdelh + delh(i,j);
299                    AvgdelTw = AvgdelTw + delTw(i,j);
300                    if (delNu(i,j) > maxdelNu)
301                        maxdelNu = delNu(i,j);
302                        inu = i; jnu  = j;
303                    end
304                    if (delTw(i,j) > maxdelTw)
305                        maxdelTw = delTw(i,j);
306                        iTw = i; jTw = j;
307                    end
308                end
309            end
310        end
311
312        if counterStrm > 0
313            AvgNuStrm(j) = AvgNuColSum/counterStrm;
314            AvghtcStrm(j) = AvghtcColSum/counterStrm;
315            AvgTwStrm(j) = AvgTwColSum/counterStrm;
316        else
317            AvgNuStrm(j) = 0;
318            AvghtcStrm(j) = 0;
319            AvgTwStrm(j) = 0;
320        end
321        counterStrm = 0;
322    end
323    AvgNuThresh = AvgNuSum/counter;
324    AvghtcThresh = AvghtcSum/counter;
325    AvgTwThresh = AvgTwSum/counter;
326    AvgdelNu = AvgdelNu/counter;
327    AvgdelTw = AvgdelTw/counter;
328    AvgdelNuPerc = AvgdelNu/AvgNuThresh*100;
329    MaxdelNuPerc = delNu(inu,jnu)/NuArr(inu,jnu)*100;
```

```
330   MaxdelhPerc = delh(inu,jnu)/hArr(inu,jnu)*100;
331   sizeImg = size(delNu); sizeNew = sizeImg(1)*sizeImg(2);
332   histArr1 = reshape(delNu,sizeNew,1);
333   histArr2 = reshape(NuArr,sizeNew,1);
334   typicaldelNu = median(histArr1);
335   typicaldelNuPerc = typicaldelNu/median(histArr2)*100;
336   histArr1 = reshape(delh,sizeNew,1);
337   histArr2 = reshape(hArr,sizeNew,1);
338   typicaldelh = median(histArr1);
339   typicaldelhPerc = typicaldelh/median(histArr2)*100;
340   histArr1 = reshape(delTw,sizeNew,1);
341   histArr2 = reshape(TwFilter,sizeNew,1);
342   typicaldelTwTLC = median(histArr1);
343   typicaldelTwTLCPerc = typicaldelTwTLC/median(histArr2)*100;
344   histArr1 = reshape(delTb,xlength,1);
345   histArr2 = reshape(delTb,xlength,1);
346   typicaldelTb = median(histArr1);
347   typicaldelTbPerc = typicaldelTb/median(histArr2)*100;
348
349   AvgHue = mean(mean(imgHue));
350   Avgh = mean(mean(hArr));
351   AvgNuStrmSize = size(AvgNuStrm);
352
353   % Screen outputs %%%%%%%%%%%%%%%%%%%%%%%%%%%%%%%%%%%%%%%%%%%%%%%%%%%%%%
354   disp('%%%%%%%%%%%%%%%%%%%%%%%%%%%%%%%%%%%%%%%%%%%%%%%%%%%%%%%%%%%%%%%%');
355   disptext0 = ['Image no.' num2str(imgNumber)];
356   disptext1 = ['max Nusselt uncertainty = ' num2str(maxdelNu)];
357   disp(disptext1);
358   maxdelTw = max(max(delTw));
359   disptext2 = ['max Temp1b uncertainty = ' num2str(maxdelTw)];
360   disp(disptext2);
361   disptext3 =...
362      ['Supposed percentage energy to fluid = ' num2str(PercIn) '%'];
363   disp(disptext3);
364   disptext4 = ['average filtered Nusselt no. = ' num2str(AvgNuThresh)];
365   disp(disptext4);
366   disptext5 =...
367      ['Average wall temperature uncertainty = ' num2str(AvgdelTw)];
368   disp(disptext5);
369   disptext6 = ['Average Nusselt number uncertainty = ' num2str(AvgdelNu)];
370   disp(disptext6);
371   disptext7 = ['Average Nusselt unceratinty (percentage)= '...
372          num2str(AvgdelNuPerc) '%'];
373   disp(disptext7);
374   disp(['Nusselt: (' num2str(inu) ',' num2str(jnu) ') Temp: ('...
375          num2str(iTw) ',' num2str(jTw) ')' ]);
376   disptext8 = ['Max nusselt unceratinty = ' num2str(MaxdelNuPerc) '%'];
```

```
377    disp(disptext8);
378    disp(['Nusselt: (' num2str(inu) ',' num2str(jnu) ') Temp: ('...
379            num2str(iTw) ',' num2str(jTw) ')' ]);
380    disptext9 = ['Max htc unceratinty = ' num2str(MaxdelhPerc) '%'];
381    disp(disptext9);
382    disptext10 =...
383        ['Typical Nusselt unceratinty = ' num2str(typicaldelNuPerc) '%'];
384    disp(disptext10);
385    disptext11 =...
386        ['Typical htc unceratinty = ' num2str(typicaldelhPerc) '%'];
387    disp(disptext11);
388    disptext12 =...
389        ['Reynolds no. uncertainty = ' num2str(delRe/Reyn*100) '%'];
390    disp(disptext12);
391    disptext13 =...
392        ['Typical x/d uncertainty = ' num2str(delxd(100)/xd(100)*100) '%'];
393    disp(disptext13);
394    disptext14 = ['Typical xstar uncertainty = '...
395            num2str(delxstar(100)/xstar(100)*100) '%'];
396    disp(disptext14);
397    disptext15 = ['Flow rate uncertainty = ' num2str(delQfl/Qfl*100) '%'];
398    disp(disptext15);
399    disptext16 = ['average filtered Tw = ' num2str(AvgTwThresh)];
400    disp(disptext16);
401    disptext17 = ['average filtered htc = ' num2str(AvghtcThresh)];
402    disp(disptext17);
403    disptext18 =...
404        ['Typical Tw uncertainty = ' num2str(typicaldelTwTLC) '\circC'];
405    disp(disptext18);
406    disptext19 =...
407        ['Typical Tbulk/sat uncertainty = ' num2str(typicaldelTb) '\circC'];
408    disp(disptext19);
409
410    % File outputs %%%%%%%%%%%%%%%%%%%%%%%%%%%%%%%%%%%%%%%%%%%%%%%%%%%%%%%%%%
411    disp('%%%%%%%%%%%%%%%%%%%%%%%%%%%%%%%%%%%%%%%%%%%%%%%%%%%%%%%%%%%%%%');
412    disp00 = ['%%%%%%%%%%%%%%%%%%%%%%%%%%%%%%%%%%%%%%%%%%%%%%%%%%%%%%%%%%%%%%'];
413    fid = fopen(fileOutput,'a');
414    fprintf(fid,'%s\n',disp00);
415    fprintf(fid,'%s\n',disptext0);
416    fprintf(fid,'%s\n',disptext16);
417    fprintf(fid,'%s\n',disptext17);
418    fprintf(fid,'%s\n',disptext4);
419    fprintf(fid,'%s\n',disptext1);
420    fprintf(fid,'%s\n',disptext2);
421    fprintf(fid,'%s\n',disptext3);
422    fprintf(fid,'%s\n',disptext5);
423    fprintf(fid,'%s\n',disptext6);
```

```
424    fprintf(fid,'%s\n',disptext7);
425    fprintf(fid,'%s\n',disptext8);
426    fprintf(fid,'%s\n',disptext9);
427    fprintf(fid,'%s\n',disptext10);
428    fprintf(fid,'%s\n',disptext11);
429    fprintf(fid,'%s\n',disptext18);
430    fprintf(fid,'%s\n',disptext19);
431    fprintf(fid,'%s\n',disp00);
432    fprintf(fid,'\n');
433    fclose(fid);
434
435    delReynPerc = (delRe/Reyn*100);
436    delxdperc = delxd(100)/xd(100)*100;
437    delxstarperc = delxstar(100)/xstar(100)*100;
438    delQflperc = delQfl/Qfl*100;
439
440    delVals = [typicaldelNuPerc typicaldelhPerc delf typicaldelTwTLC...
441            delReynPerc delxdperc delxstarperc delQflperc];
442    %%%%%%%%%%%%%%%%%%%%%%%%%%%%%%%%%%%%%%%%%%%%%%%%%%%%%%%%%%%%%%%%
443
444    % END %%%%%%%%%%%%%%%%%%%%%%%%%%%%%%%%%%%%%%%%%%%%%%%%%%%%%%%%%%%
445
446    % References:
447    % 1. 3M Fluorinert Electronic Liquid FC-72, Product Information, 2000.
```

```matlab
1    %%%%%%%%%%%%%%%%%%%%%%%%%%%%%%%%%%%%%%%%%%%%%%%%%%%%%%%%%%%%%%%%%%%%%%%%%%%%
2    % TLC Rig
3    % Author: Roland S Muwanga
4    % Date: Apr 03/06
5    %
6    % Program: function manualfilter(imgdir,imgdirFilt,rgbbeg,imgi)
7    %
8    %
9    %
10   % Promises: Manually filter an image and return a binary mask
11   %               identifying the filtered region
12   %
13   %
14   %%%%%%%%%%%%%%%%%%%%%%%%%%%%%%%%%%%%%%%%%%%%%%%%%%%%%%%%%%%%%%%%%%%%%%%%%%%%
15
16   function manualfilter(imgdir,imgdirFilt,rgbbeg,imgi)
17
18   sizeimgi = size(imgi); sizeimgi = sizeimgi(2);
19
20   for i = 1:sizeimgi
21       j = imgi(i);
22       dispimagenumb = ['image no.' num2str(j)]; disp(dispimagenumb);
23       FilenameIn = [imgdir rgbbeg int2str(j) '.TIFF'];
24
25       RGBimg = imread(FilenameIn,'tif');
26       HSVimg = rgb2hsv(RGBimg);
27       Vimg = HSVimg(:,:,3);
28
29       VimgBW = roipoly(Vimg);
30
31       HSVimg(:,:,1) = HSVimg(:,:,1).*VimgBW;
32       HSVimg(:,:,2) = HSVimg(:,:,2).*VimgBW;
33       HSVimg(:,:,3) = HSVimg(:,:,3).*VimgBW;
34       RGBimg = hsv2rgb(HSVimg);
35       imshow(RGBimg); pause;
36
37       FilenameOut = [imgdirFilt rgbbeg '_filter' int2str(j) '.TIFF'];
38       imwrite(VimgBW,FilenameOut,'tif');
39   end
40   % END %%%%%%%%%%%%%%%%%%%%%%%%%%%%%%%%%%%%%%%%%%%%%%%%%%%%%%%%%%%%%%%%%%%%%%
```

```
1  %%%%%%%%%%%%%%%%%%%%%%%%%%%%%%%%%%%%%%%%%%%%%%%%%%%%%%%%%%%%%%%%%%%%%%%%%%%%
2  % TLC Rig
3  % Author: Roland S Muwanga
4  % Date: Apr 03/06
5  %
6  % Program: function [HimgNew] = hueBrightDarkfilter(Filename)
7  %
8  %
9  %
10 % Promises: Automated filtering to remove black paint regions
11 %            and bright spots from hue image
12 %
13 %
14 %%%%%%%%%%%%%%%%%%%%%%%%%%%%%%%%%%%%%%%%%%%%%%%%%%%%%%%%%%%%%%%%%%%%%%%%%%%%
15
16 function [HimgNew] = hueBrightDarkfilter(RGBimg)
17
18 threshVal = 300/360;
19 VAL1 = 0.5; VAL2 = 0.9;
20 HUE1 = 0.1; HUE2 = 0.9;
21 SAT1 = 0.1;
22
23 HSVimg = rgb2hsv(RGBimg);
24 Himg = HSVimg(:,:,1);
25 Vimg = HSVimg(:,:,3);
26 Simg = HSVimg(:,:,2);
27
28 % modify red color showing high hue to appropriately show low hue
29 Mult1 = ceil(threshVal - Himg); % less than threshval to 1
30 Mult2 = ceil(Himg - threshVal); % greater than threshval to 1
31
32 Himg = (Himg.*Mult1 + (1-Himg).*Mult2);
33
34 % black has low value and may have high hue -> MODIFIED APPROACH
35 ValSplit  = ceil(Vimg - VAL1); % lose dark val ->  val < VAL1 to 1
36                                 % rest to 1
37 HueSplit = ceil(HUE2 - Himg); % lose high hue
38 HueBlack1 = HueSplit.*ValSplit ; %
39 HueBlack1 = im2bw(HueBlack1,0.5); % keep image with with val > VAL1 and
40                                    % hue < HUE1
41 HueBlack2 = 1;
42
43 % white has dark saturation and bright value
44 ValSplit  = ceil(VAL2 - Vimg); % lose bright val -> bright val to 0
45                                 % rest to 1
46 SatSplit = ceil(Simg - SAT1); % lose dark  sat -> dark sat to 0 rest to
47                                 % 1
```

```
48    HueWhite = ValSplit + SatSplit;
49    HueWhite = im2bw(HueWhite,0.5); % keep image with sat > SAT1 combined
50                                    % with val < VAL2
51
52    HueMult = 1;%HueBlack1 .* HueBlack2 .* HueWhite;
53    % bright and dark filter % temporarily ignore filtering
54
55    HimgNew = Himg.*HueMult;
56
57    close all
58    % END %%%%%%%%%%%%%%%%%%%%%%%%%%%%%%%%%%%%%%%%%%%%%%%%%%%%%%%%%%%%%%
```

```
1   %%%%%%%%%%%%%%%%%%%%%%%%%%%%%%%%%%%%%%%%%%%%%%%%%%%%%%%%%%%%%%%%%%%%%%%%%%%
2   % TLC Rig
3   % Author: Roland S Muwanga
4   % Date: Apr 03/06
5   % - added htc to output
6   %
7   % Program: function [iend, ImgJoin] = joinImage(SubCase,subcaseIter,i,..
8   %       totLengthPix,xPixSize,yPixSize,imgname,imgdirFilt,rgbbeg,...
9   %       indexMM,ypixpos,Nimg,plane,filterimg);
10  %
11  % Requires:
12  % SubCase - vector size of Nimg and containing the subcase to which image
13  % belongs, i.e.
14  % subcaseIter - counter for number of images in particular subcase
15  % i - image counter based on Nimg
16  % totLengthPix - total height of joined image in pixel
17  % xPixSize and yPixSize - width and height of individual images in pixes
18  % imgname - beginning name for image -> for saving
19  % imgdirFilt - directory of binary filters
20  % rgbbeg - additional file location information for filter
21  % indexMM - image location integer
22  % ypixpos - absolute reference frames for image locations in pixels
23  %          - column 1 contains bottom location
24  %          - column 2 contains top location
25  % Nimg - number of images
26  % plane - either 'single' or 'triple' plane denoting type of image
27  % filterimg - 'true'/'false'whether to apply binary filter to images
28  %            - usually 'true'
29  %            - setup only for 'triple' plane option
30  %
31  %
32  % Promises:
33  % - Join images in a given SubCase
34  % - Will join a single plane or triple plane image based on 'plane'
35  %
36  %%%%%%%%%%%%%%%%%%%%%%%%%%%%%%%%%%%%%%%%%%%%%%%%%%%%%%%%%%%%%%%%%%%%%%%%%%%
37
38  function [iend, ImgJoin] = joinImage(SubCase,subcaseIter,i,...
39      totLengthPix,xPixSize,yPixSize,imgname,imgdirFilt,rgbbeg,...
40      indexMM,ypixpos,Nimg,plane,filterimg);
41
42  switch plane
43      case 'single' % single plane image (hue)
44          ImgOnes = ones(yPixSize,xPixSize);
45          ImgJoin = zeros(totLengthPix,xPixSize);
46          ImgDev = zeros(totLengthPix,xPixSize); % counter for number of
47                                                 % active elements
```

```
48
49          while SubCase(i) < subcaseIter
50              dispimagenumb = ['image no.' num2str(i)];
51              disp(dispimagenumb);
52              FilenameIn = [imgname int2str(i) '.tif'];
53
54              imgInt = imread(FilenameIn,'tif');
55              imgDbl = double(imgInt) + 1; %imagesc(imgDbl);
56
57              ImgJoin((ypixpos(indexMM(i),1)):
58              (ypixpos(indexMM(i),2)),:) = ...
59                  ImgJoin((ypixpos(indexMM(i),1)):...
60                  (ypixpos(indexMM(i),2)),:) + imgDbl;
61              ImgDev((ypixpos(indexMM(i),1)):...
62                  (ypixpos(indexMM(i),2)),:) =...
63                  ImgDev((ypixpos(indexMM(i),1)):...
64                  (ypixpos(indexMM(i),2)),:) + ImgOnes;
65              i = i+1;
66
67              if i > Nimg, break, end
68          end
69
70          ImgDev = ceil(abs(ImgDev - 0.1));
71          ImgJoin = (ImgJoin./ImgDev);
72          iend = i;
73
74      case 'triple' % triple plane image (RGB/HSV)
75          ImgOnes = ones(yPixSize,xPixSize);
76          ImgJoinHue = zeros(totLengthPix,xPixSize);
77          ImgDevHue = zeros(totLengthPix,xPixSize); % counter for number
78                                                    % of active elements
79          ImgJoinSat = zeros(totLengthPix,xPixSize);
80          ImgDevSat = zeros(totLengthPix,xPixSize);
81          ImgJoinVal = zeros(totLengthPix,xPixSize);
82          ImgDevVal = zeros(totLengthPix,xPixSize);
83          HSVJoin = zeros(totLengthPix,xPixSize,3);
84
85          while SubCase(i) < subcaseIter
86              dispimagenumb = ['image no.' num2str(i)];
87              disp(dispimagenumb);
88              FilenameIn = [imgname int2str(i) '.TIFF'];
89
90              RGBimg = imread(FilenameIn,'tif');
91              HSVimg = rgb2hsv(RGBimg);
92
93              Himg = HSVimg(:,:,1);
94              Simg = HSVimg(:,:,2);
```

```
 95                   Vimg = HSVimg(:,:,3);
 96
 97                   if strcmp(filterimg,'true')
 98                       FilenameFilter = [imgdirFilt rgbbeg '_filter'...
 99                               int2str(i) '.TIFF'];
100                       Filterimg = imread(FilenameFilter,'tif');
101                       Himg = Himg.*Filterimg;
102                       Imgadj = im2bw(Himg,0.8333); % to take negative hue of
103                                                    % angles >300
104                       Imgmult = ~(Imgadj);
105                       Himg = Imgmult.*Himg + (ImgOnes-Himg).*Imgadj;
106                       Simg = Simg.*Filterimg;
107                       Vimg = Vimg.*Filterimg;
108                   end
109
110                   ImgJoinHue((ypixpos(indexMM(i),1)):...
111                       (ypixpos(indexMM(i),2)),:) = ...
112                       ImgJoinHue((ypixpos(indexMM(i),1)):...
113                       (ypixpos(indexMM(i),2)),:) + Himg;
114                   ImgDevHue((ypixpos(indexMM(i),1)):...
115                       (ypixpos(indexMM(i),2)),:) = ...
116                       ImgDevHue((ypixpos(indexMM(i),1)):...
117                       (ypixpos(indexMM(i),2)),:) + ImgOnes;
118
119                   ImgJoinSat((ypixpos(indexMM(i),1)):...
120                       (ypixpos(indexMM(i),2)),:) = ...
121                       ImgJoinSat((ypixpos(indexMM(i),1)):...
122                       (ypixpos(indexMM(i),2)),:) + Simg;
123                   ImgDevSat((ypixpos(indexMM(i),1)):...
124                       (ypixpos(indexMM(i),2)),:) = ...
125                       ImgDevSat((ypixpos(indexMM(i),1)):...
126                       (ypixpos(indexMM(i),2)),:) + ImgOnes;
127
128                   ImgJoinVal((ypixpos(indexMM(i),1)):...
129                       (ypixpos(indexMM(i),2)),:) = ...
130                       ImgJoinVal((ypixpos(indexMM(i),1)):...
131                       (ypixpos(indexMM(i),2)),:) + Vimg;
132                   ImgDevVal((ypixpos(indexMM(i),1)):...
133                       (ypixpos(indexMM(i),2)),:) = ...
134                       ImgDevVal((ypixpos(indexMM(i),1)):...
135                       (ypixpos(indexMM(i),2)),:) + ImgOnes;
136               i = i+1;
137
138               if i > Nimg, break, end
139           end
140
141       ImgDevHue = ceil(abs(ImgDevHue - 0.1)); % sets zero terms to 1
```

```
142                                                    %so don't divide by zero
143            ImgJoinHue = (ImgJoinHue./ImgDevHue);
144            ImgDevSat = ceil(abs(ImgDevSat - 0.1)); % sets zero terms to 1
145                                                    %so don't divide by zero
146            ImgJoinSat = (ImgJoinSat./ImgDevSat);
147            ImgDevVal = ceil(abs(ImgDevVal - 0.1));% sets zero terms to 1
148                                                    % so don't divide by zero
149            ImgJoinVal = (ImgJoinVal./ImgDevVal);
150
151            HSVJoin(:,:,1) = ImgJoinHue;
152            HSVJoin(:,:,2) = ImgJoinSat;
153            HSVJoin(:,:,3) = ImgJoinVal;
154            ImgJoin = hsv2rgb(HSVJoin);
155
156            iend = i;
157
158     end
159     % END %%%%%%%%%%%%%%%%%%%%%%%%%%%%%%%%%%%%%%%%%%%%%%%%%%%%%%%%%%%%%%
```

Appendix C

Simplified Analysis

C.1   Derivations

C.1.1   Parallel Channel Derivations
General Definitions:

$$Nu = \frac{hD_h}{k};$$

$$\alpha\left(z\right) = \frac{W_{chn}(z)}{H_{chn}};$$

$$A_{cs} = W_{chn}H_{chn} = \alpha H_{chn}^2;$$

$$A_3 = \left(W_{chn} + 2H_{chn}\right)L_{chn} = \left(\alpha + 2\right)H_{chn} \cdot L_{chn};$$

$$A_4 = 2\left(W_{chn} + H_{chn}\right)L_{chn} = \left(\alpha + 2\right)H_{chn} \cdot L_{chn};$$

$$A_{plan,cell} = W_{cell}L;$$

$$D_h = \frac{4A_{cs}}{Per_{cs}} = \frac{2\alpha H_{chn}}{(1+\alpha)};$$

$$Per_{cs} = \frac{4A_{cs}}{D_h} = 2\left(W_{chn} + H_{chn}\right) = 2H_{chn}\left(1 + \alpha\right);$$

$$\dot{m}_0 = \frac{H_{chn}^4 \Delta P}{\nu L_{chn}};$$

Average Shear Stress:

$$\Delta P = f \frac{L_{chn}}{D_h} \frac{\rho V_{chn}^2}{2}$$

The average shear stress in a constant cross-sectional area channel may be obtained as,

$$\tau_w = \Delta P \cdot {A_{cs}}/{L_{chn} Per} = f \frac{L_{chn}}{D_h} \frac{\rho V_{chn}^2}{2} \cdot {A_{cs}}/{L_{chn} Per}$$

Given,

$$\mathrm{Re} = \frac{\rho V D_h}{\mu} \text{ or } \rho V = \frac{\mathrm{Re}\mu}{D_h}$$

then,

$$\tau_w = f \frac{L_{chn}}{D_h} \frac{\mathrm{Re}\mu}{D_h} \frac{V_{chn}}{2} \cdot \frac{D_h A_{cs}}{L_{chn} 4 A_{cs}} = f \frac{\mathrm{Re}\mu}{D_h} \frac{V_{chn}}{8}$$

and

$$Po\left(\alpha\right) = f\mathrm{Re} = 96 \left[1 - 1.3553\alpha + 1.94673\alpha^2 - 1.7012\alpha^3 + 0.9564\alpha^4 - 0.2537\alpha^5\right]$$

we have,

$$\tau_w = \frac{Po\mu}{D_h} \frac{V_{chn}}{8}.$$

For a channel with varying cross-section then,

$$\tau_w\left(\alpha\right) = \frac{Po\left(\alpha\right)\mu}{D_h} \frac{V_{chn}}{8}.$$

Mass Flow Rate:

$$\Delta P \cdot A_{cs} = \int_{0}^{L_{chn}} \tau_w \cdot Per \cdot dx$$

$$\Delta P \cdot A_{cs} = \int_{0}^{L_{chn}} \frac{1}{8} \frac{\mu V_{chn}}{D_h} Po \cdot Per \cdot dz \text{ and given } \dot{m} = \rho V_{chn} A_{cs} \text{ and } Per = \frac{4A_{cs}}{D_h}, \text{ we have}$$

$$\Delta P \cdot A_{cs} = \int_{0}^{L_{chn}} \frac{1}{8} \frac{\mu \dot{m}}{\rho D_h A_{cs}} Po \cdot \frac{4A_{cs}}{D_h} \cdot dz \text{ or } \Delta P \cdot A_{cs} = \int_{0}^{L_{chn}} \frac{1}{2} \frac{\dot{m}}{D_h} Po \cdot \frac{\nu}{D_h} \cdot dz.$$

Finally,

$$\dot{m} = \frac{\Delta P \cdot A_{cs}}{\int_{0}^{L_{chn}} \frac{1}{2} \frac{\nu}{D_h^2} Po\left(\alpha\right) \cdot dz} \text{ or } \dot{m} = \frac{\Delta P \cdot W_{chn} \times H_{chn}}{\int_{0}^{L_{chn}} \frac{1}{2} \frac{\nu}{\left(4\alpha^2 H_{chn}^2 / (1+\alpha)^2\right)} Po\left(\alpha\right) \cdot dz}$$

$$\dot{m} = \frac{\Delta P \cdot \alpha H_{chn}^2}{\int_{0}^{L_{chn}} \frac{1}{2} \frac{\nu}{\left(4\alpha^2 H_{chn}^2 / (1+\alpha)^2\right)} Po\left(\alpha\right) \cdot dz}$$

Non-dimensionalizing with $\dot{m}$,

$$\frac{\dot{m}_0}{\dot{m}} = \int_{0}^{L_{chn}} \frac{1}{8} Po\left(\alpha\right) \frac{(1+\alpha)}{\alpha^3} \left(\frac{dz}{L_{chn}}\right) = \int_{0}^{1} \frac{1}{8} Po\left(\alpha\right) \frac{(1+\alpha)}{\alpha^3} dz^+ = \frac{1}{\dot{m}^+}$$

Convective Resistance:

$$q'' A_{plan,cell} = h A_3 \left(T_w\left(z\right) - T_b\left(z\right)\right)$$

$$q'' W_{cell} L_{chn} = h \left(\left(W_{chn} + 2H_{chn}\right) L_{chn}\right) \left(T_w\left(z\right) - T_b\left(z\right)\right)$$

311

we define,

$$\theta_s\left(z\right) = \frac{T_w\left(z\right) - T_b\left(0\right)}{\left(\frac{q''H_{chn}}{k}\right)} \text{ and } \theta_b\left(z\right) = \frac{T_b\left(z\right) - T_b\left(0\right)}{\left(\frac{q''H_{chn}}{k}\right)}$$

substituting the above plus general definitions we have,

$$q''W_{cell}L_{chn} = \frac{Nu \cdot k(1+\alpha)}{2\alpha H_{chn}}\left(H_{chn}\left(\alpha+2\right)L_{chn}\right)$$

$$\times\left[\frac{\theta_w(z)q''H_{chn}}{k} + T_b\left(0\right) - \frac{\theta_b(z)q''H_{chn}}{k} - T_b\left(0\right)\right]$$

simplifying,

$$W_{cell} = \frac{Nu\left(1+\alpha\right)}{2\alpha}\left(\alpha+2\right)H_{chn}\left[\theta_w\left(z\right) - \theta_b\left(z\right)\right]$$

and rearranging,

$$\theta_s\left(z\right) - \theta_b\left(z\right) = \frac{2\alpha}{Nu\left(1+\alpha\right)\left(2+\alpha\right)}\frac{W_{cell}}{H_{chn}} = R_{conv}$$

Defining,

$$\alpha_{\max} = \max\left(\frac{W_{chn}\left(z\right)}{H_{chn}}\right) = \max\left(\alpha\left(z\right)\right); W_{w,\min}^+ = \min\left(\frac{W_w\left(z\right)}{H_{chn}}\right)$$

we have,

$$R_{conv,3} = \frac{2\alpha}{Nu\left(1+\alpha\right)\left(2+\alpha\right)}\left(\alpha_{\max} + W_{w,\min}^+\right).$$

Similarly following the above except using the 4-wall heated area A_4 we have,

$$R_{conv,4} = \frac{\alpha}{Nu\left(1+\alpha\right)^2}\left(\alpha_{\max} + W_{w,\min}^+\right).$$

312

Calorimetric Resistance:

$$q'' W_{cell} z = \dot{m} Cp \left(T_b \left(z \right) - T_b \left(0 \right) \right)$$

Substituting previous definitions of θ_b and $\dot{m}$ we have,

$$q'' W_{cell} z = \dot{m}_0 \dot{m}^+ Cp \theta_b \left(z \right) {}^{q'' H_{chn}}\!/\!_{k_f}$$

therefore,

$$\theta_b \left(z \right) = \frac{k_f W \left(z^+ L_{chn} \right)}{Cp H_{chn} \left(\dot{m}_0 \dot{m}^+ \right)} = R_{cal}$$

and finally substituting χ,

$$R_{cal} = \chi \frac{\left(\alpha_{max} + W_w^+ \right)}{\dot{m}^+} z^+ .$$

Total Resistance: For 3-wall heated,

$$R_{Total,3} = R_{conv} + R_{cal} = \left(\alpha_{max} + W_{w,min}^+ \right) \left\{ \frac{2\alpha}{Nu \left(1 + \alpha \right) \left(2 + \alpha \right)} + \frac{\chi}{\dot{m}^+} z^+ \right\}$$

and for 4-wall heated,

$$R_{Total,4} = R_{conv} + R_{cal} = \left(\alpha_{max} + W_{w,min}^+ \right) \left\{ \frac{\alpha}{Nu \left(1 + \alpha \right)^2} + \frac{\chi}{\dot{m}^+} z^+ \right\} .$$

C.1.2 Radial Channel Derivations

General Definitions: Aspect ratio as a function of radius:

$$\alpha\left(r\right) = \frac{W_{chn}\left(r\right)}{H_{chn}} = \frac{r\beta_2}{H_{chn}};$$

$\alpha_i = \frac{r_{in}\beta_2}{H_{chn}}$; and $\alpha_o = \frac{r_{out}\beta_2}{H_{chn}}$

Wall surface areas:

$$A_{hor} = \int_{r_{in}}^{r_{out}} \left(r\beta_2\right) dr = \left.\frac{r^2\beta_2}{2}\right|_{r_{in}}^{r_{out}} = \frac{\left(r_{out}^2 - r_{in}^2\right)\beta_2}{2} = \frac{\left(r_{out} - r_{in}\right)\left(r_{out} + r_{in}\right)\beta_2}{2}$$

$$= \frac{\left(r_{out} - r_{in}\right)\left(\alpha_o + \alpha_i\right)H_{chn}}{2} = \frac{L_{chn}\left(\alpha_o + \alpha_i\right)H_{chn}}{2}$$

$$A_{ver} = \left(r_{out} - r_{in}\right)H_{chn} = L_{chn}H_{chn}$$

$$A_3 = A_{hor} + 2A_{ver} = \frac{L_{chn}\left(\alpha_o + \alpha_i\right)H_{chn}}{2} + 2L_{chn}H_{chn}$$

$$A_3 = L_{chn}H_{chn}\left(\frac{\left(\alpha_o + \alpha_i\right)}{2} + 2\right)$$

$$A_4 = 2A_{hor} + 2A_{ver} = L_{chn}\left(\alpha_o + \alpha_i\right)H_{chn} + 2L_{chn}H_{chn}$$

$$A_4 = L_{chn}H_{chn}\left[\left(\alpha_o + \alpha_i\right) + 2\right]$$

Cross-sectional area, perimeter and hydraulic diameter definitions remain the same as for the parallel channel definitions.

Convective Resistance:

$$\frac{q''\pi\left(r_{out}^2 - r_{in}^2\right)}{N_{chn}} = hA_{3/4}\left(T_w\left(r\right) - T_b\left(r\right)\right)$$

Substituting the previously defined non-dimensional temperatures ($\theta_{W/B}$), the Nusselt number (Nu) and the appropriate areas ($A_{3/4}$) we have,

$$\theta_w(r) - \theta_b(r) = \frac{2\alpha\pi\left(r_{out}^2 - r_{in}^2\right)}{Nu(1+\alpha)\left(L_{chn}H_{chn}\left(\frac{(\alpha_o+\alpha_i)}{2}+2\right)\right)N_{chn}} = R_{cs} \text{ for 3-wall heating case and}$$

$$\theta_w(r) - \theta_b(r) = \frac{2\alpha\pi\left(r_{out}^2 - r_{in}^2\right)}{Nu(1+\alpha)\left(2L_{chn}H_{chn}\left(\frac{(\alpha_o+\alpha_i)}{2}+1\right)\right)N_{chn}} = R_{cs} \text{ for 4-wall heating case.}$$

Calorimetric Resistance:

$$\Delta P \cdot A_{cs} = \int_{r_{out}}^{r_{out}} \tau_w \cdot P_{cs} \cdot dr$$

Following similar steps as for the parallel channel case we arrive at,

$$\dot{m} = -\frac{\Delta P \cdot A_{cs}}{\int_{r_{out}}^{r_{in}} \frac{1}{2}\frac{\nu}{D_h^2}Po(\alpha) \cdot dr}$$

Note, the negative is due to a negative velocity due to radially inward flow. Substituting for D_h and A_{cs},

$$\dot{m} = -\frac{\Delta P \cdot \alpha H_{chn}^2}{\int_{r_{out}}^{r_{in}} \frac{1}{2}\frac{\nu}{\left(2\alpha H_{chn}/(1+\alpha)\right)^2}Po(\alpha) \cdot dr} = -\frac{\Delta P \cdot \alpha^3 H_{chn}^4}{\int_{r_{out}}^{r_{in}} \frac{1}{8}\nu(1+\alpha)Po(\alpha) \cdot dr}$$

Dividing by the characteristic mass flow to get the non-dimensional mass flow $\dot{m}_0 = \frac{H_{chn}^4 \Delta P}{\nu L_{chn}}$,

$$\dot{m}^+ = \frac{\dot{m}}{m_0} = -\frac{\Delta P \cdot \alpha^3 H_{chn}^4}{\int_{r_{out}}^{r_{in}} \frac{1}{8}\nu(1+\alpha)Po(\alpha) \cdot dr} \times \frac{\nu L_{chn}}{H_{chn}^4 \Delta P} = -\frac{\alpha^3 L_{chn}}{\int_{r_{out}}^{r_{in}} \frac{1}{8}(1+\alpha)Po(\alpha) \cdot dr}$$

Defining $r^+ = \frac{r_{out} - r}{r_{out} - r_{in}}$ which will then span 0 to 1 from outer to inner radius.

Then,

$$dr^+ = \frac{-dr}{r_{out} - r_{in}}$$

Substituting it into the non-dimensional mass flow,

$$\dot{m}^+ = \frac{\alpha^3 L_{chn}}{\int_0^1 \frac{1}{8}\left(1 + \alpha\right) Po\left(\alpha\right)\left(r_{out} - r_{in}\right) dr^+} = \frac{\alpha^3}{\int_0^1 \frac{1}{8}\left(1 + \alpha\right) Po\left(\alpha\right) dr^+}$$

Which is the same form as for parallel channels except integrated with respect to r.

For the thermal resistance term:

$$\frac{q'' \pi \left(r_{out}^2 - r^2\right)}{N_{chn}} = \dot{m} Cp \left(T_b\left(r\right) - T_b\left(r_{out}\right)\right)$$

Substituting the previously defined non-dimensional temperatures (B), and mass flowrate parameters,

$$\theta_b = \frac{\pi \left\{r_{out}^2 - \left(r_{out} - r^+\left(r_{out} - r_{in}\right)\right)^2\right\}}{N_{chn}} \left(\frac{k_f}{Cp}\right) \left(\frac{1}{\dot{m}^+ \cdot \dot{m}_o H_{chn}}\right)$$

Where,

$$r^+ = \frac{r_{out} - r}{r_{out} - r_{in}}$$

C.1.3 Parallel Channel Code Validation

The equations presented have been coded into MATLAB to determine optimal channel configurations. To verify the code, comparisons were made with the test case

316

presented by Bau (1998). For this case the working fluid was water, flowing in a 1500 μm deep channel, 1 cm long and with a 20 kPa pressure supply. Fluid properties were noted to be calculated at room temperature for which the present has assumed to be at 20 °C. Bau (1998) considered the objective function given by,

$$J\left(K_1, K_2\right) = \min_{0 \leq z \leq 1} \left\{ K_1 \max_{0 \leq z \leq 1} \left(\theta_w\left(z\right)\right) + K_2 \int_0^1 \left(\frac{d\theta\left(z\right)}{dz}\right)^2 dz \right\}.$$

The case $(K_1 = 1, K_2 = 0)$ will determine the minimum peak temperature and $(K_1 = 0, K_2 = 1)$ the minimum gradient. Depending on the problems objective, $(K_1 = 1$ and $K_2 = 0)$ may be adjust appropriately. In the analysis for minimizing the maximum temperature gradient the coefficients were set to $(K_2/K_1 = 5 \times 10^3)$. This has also been incorporated in the following for comparison. The polynomial form for the wall contours has been set to second order.

Figure C.1 shows the results from the analysis compared with the results from Bau (1998). The figure presents the wall temperature profiles and the corresponding wall contours. Reasonable agreement is observed both for minimizing the peak temperature and the temperature gradient. Differences are attributed to differences in the numerical minimization routines utilized. These results validate the developed code for evaluation of optimum channel configurations.
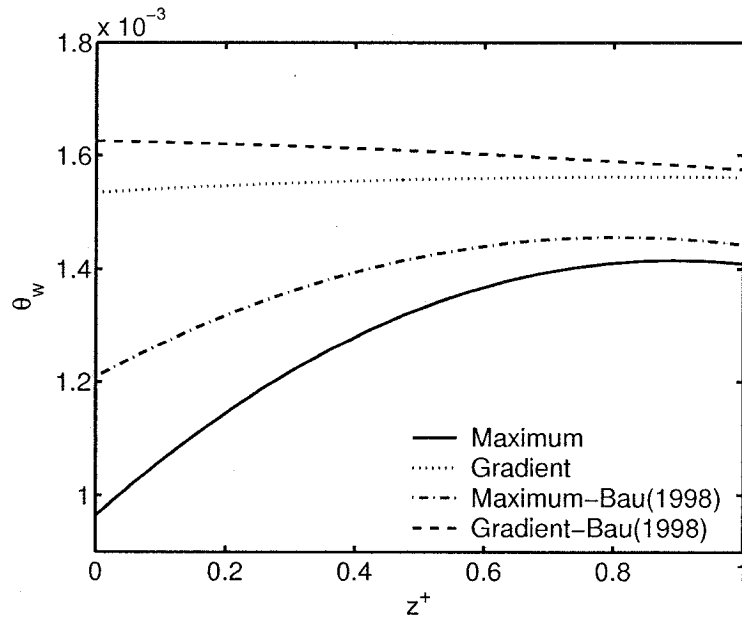
(a) Non-dimensional wall temperature, 3-wall fully developed.
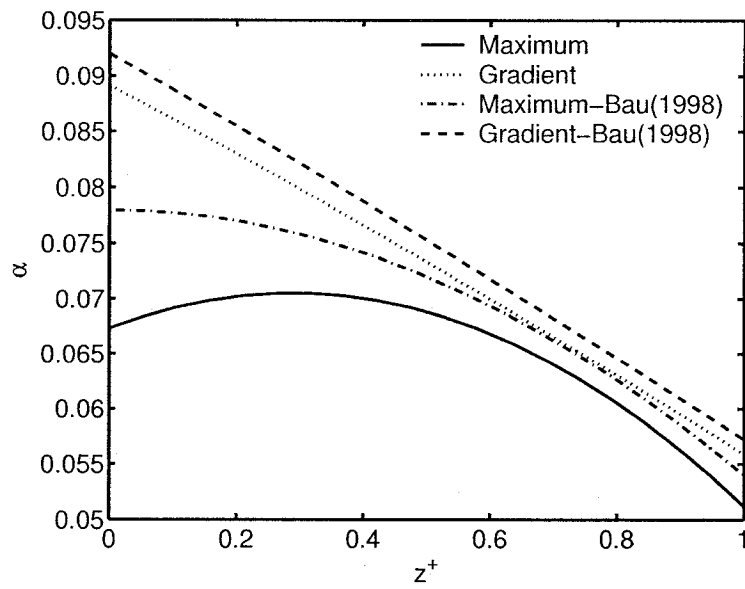
(b) Aspect ratio, 3-wall fully developed.

Figure C.1: Comparison of developed code results with Bau (1998).

C.2 Results for Parallel Channel System

C.2.1 Parallel Channels: Influence of Boundary Condition

Figure C.2 presents the optimized wall temperature and aspect ratios for channels with linearly varying cross-sections and for different thermal boundary conditions. These results are for the case of minimizing the peak wall temperature and the results are compared with an optimized uniform channel. The analysis was performed for χ values of $2.60e^{-3}$, $2.60e^{-4}$, $2.60e^{-5}$ and $5.21e^{-6}$, corresponding to pressure drops of 0.1 psi, 1 psi, 10 psi and 50 psi. In the case of fully developed flow (C.2 a & c), the wall temperature linearly rises, whereas a non-linear rise is observed for thermally developing flow. Comparing the uniform channel to varying cross-sectional area channels, negligible differences are observed in the thermal profile and consequently the aspect ratio. Observed in the results in general is a trend towards optimized channels with smaller cross-sections for increased pressure drop availability. This is not surprising as with increasing pressure drop availability, narrower channels can be accommodated and are advantageous due to the increased heat transfer coefficients.

Figure C.3 presents the results for minimizing the wall temperature gradient, comparing uniform channels with linearly varying cross-sectional area channels. For the 3-wall heated case at higher pressures, a slightly converging channel produces both a lower peak temperature and lower temperature gradient. With higher pressures in all the cases however, the temperature rise is small and hence the motivation for minimizing the gradient is low. For the 4-wall heated cases however, negligible benefit is obtained from using a channel with varying cross-section. Additionally the optimal
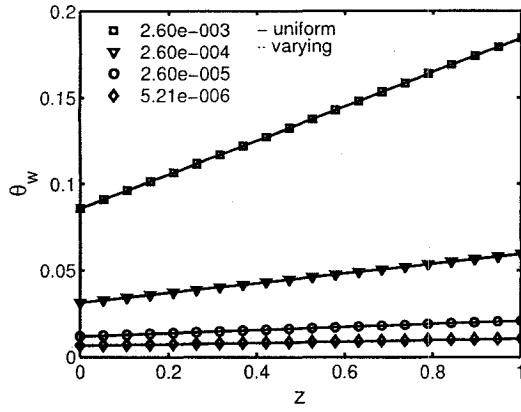
(a) 3-wall, fully developed
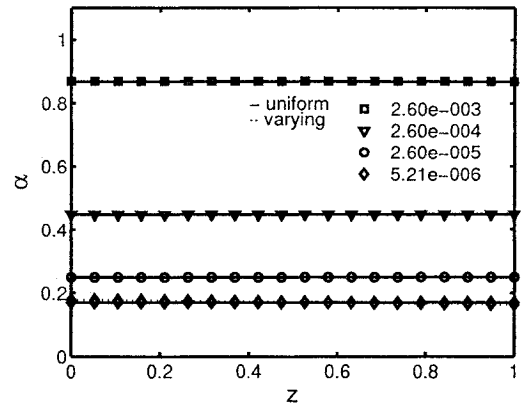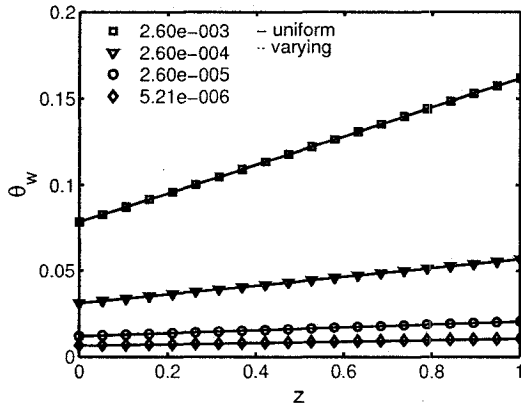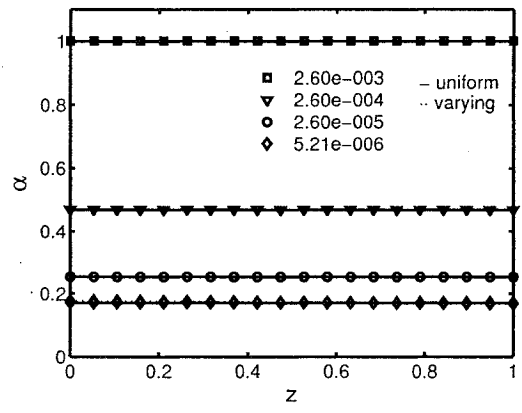
(b) 3-wall, fully developed

(c) 4-wall, fully developed

(d) 4-wall, fully developed
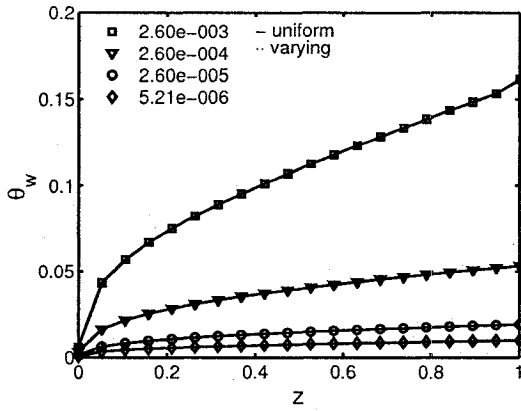
(e) 4-wall, thermally developing
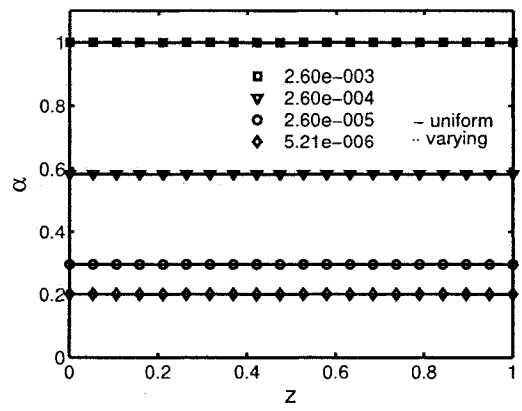
(f) 4-wall, thermally developing

Figure C.2: Minimizing peak temperature: Linear profile.
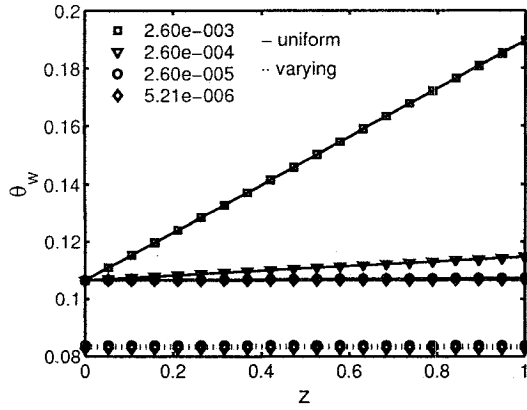
(a) 3-wall, fully developed
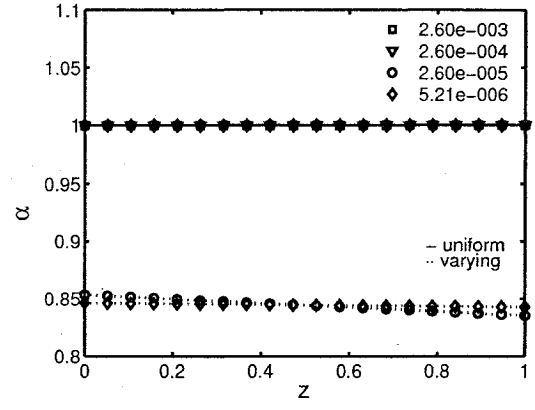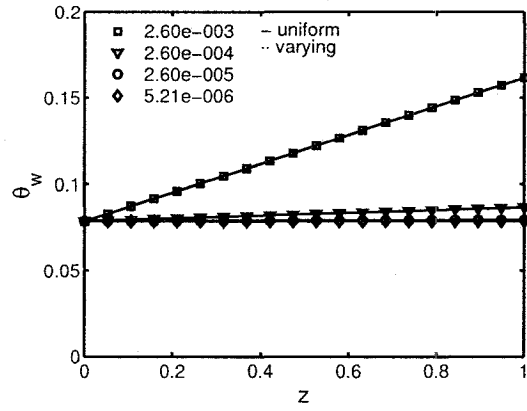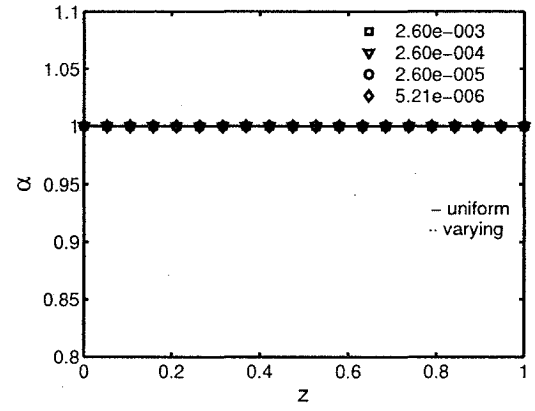
(b) 3-wall, fully developed

(c) 4-wall, fully developed

(d) 4-wall, fully developed
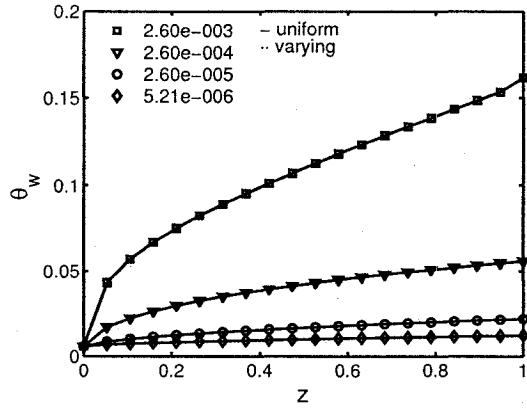
(e) 4-wall, thermally developing
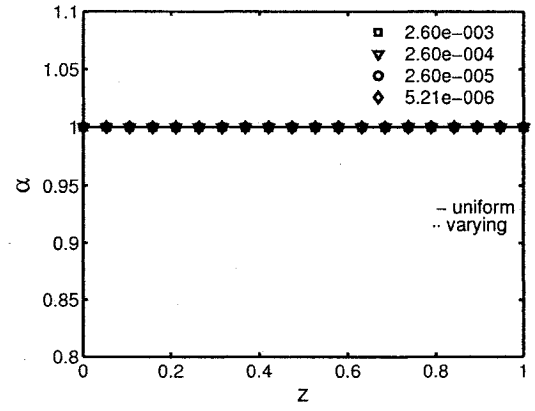
(f) 4-wall, thermally developing

Figure C.3: Minimizing temperature gradient: Linear profile.

321

aspect ratio for 4-wall heated channels is 1. Comparing Figures C.2 and C.3, a lower temperature gradient may indeed be obtained, however this in all cases occurs at the cost of an increased maximum wall temperature.

C.2.2 Parallel Channels: Influence of Wall Contour Polynomial

The previous section considered the case of channels with linearly varying cross-sections only. This section presents results for channels with quadratic and cubic contoured channels. In particular the 4-wall heated case with thermally developing flow is presented as it is a more realistic scenario due to the flows thermal development. Figure C.4 presents the wall temperature and contour profiles for the case of minimizing the peak wall temperature. With exception of the low pressure case, the contoured channels all tend toward a significantly converging channel at the exit. The wall temperature profiles show negligible differences however when compared to the uniform channel profiles. In the case of minimizing the wall temperature gradient uniform channels with aspect ratio of 1 are found to be optimal over a quartic or cubic wall profile (Figure C.5).
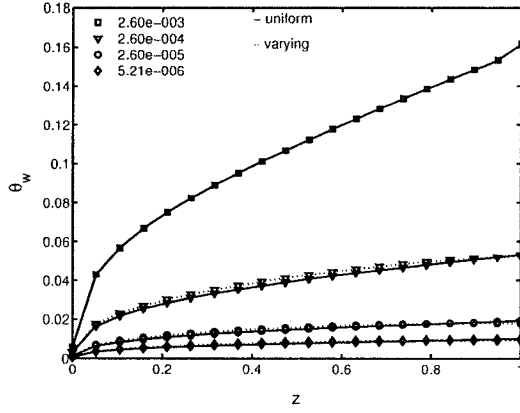
(a) Quadratic profile
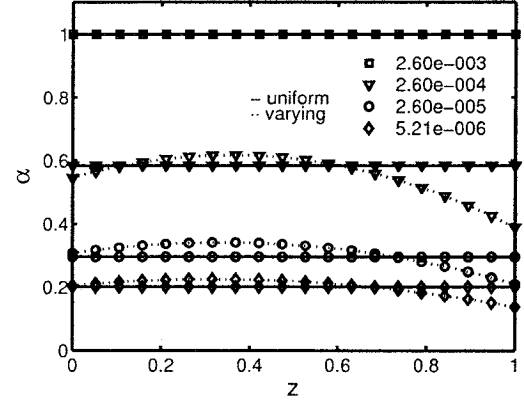
(b) Quadratic profile
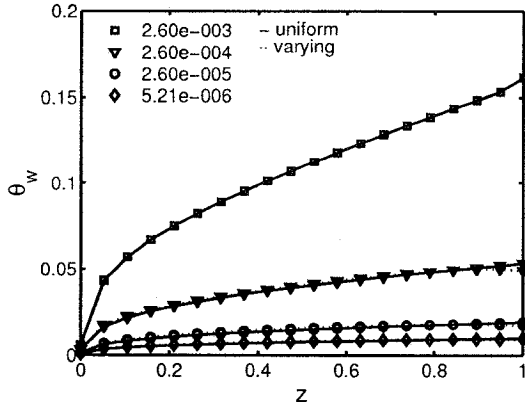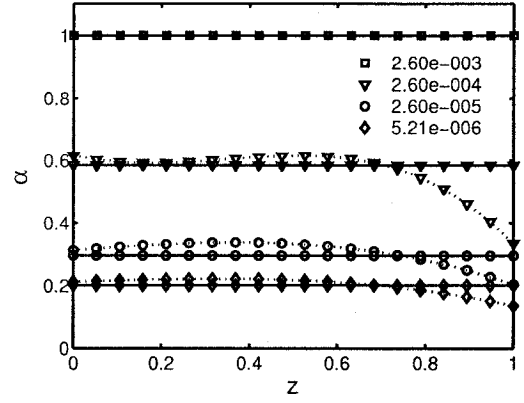
(c) Cubic profile

(d) Cubic profile

Figure C.4: Minimizing peak temperature: 4-wall heated, thermally developing.
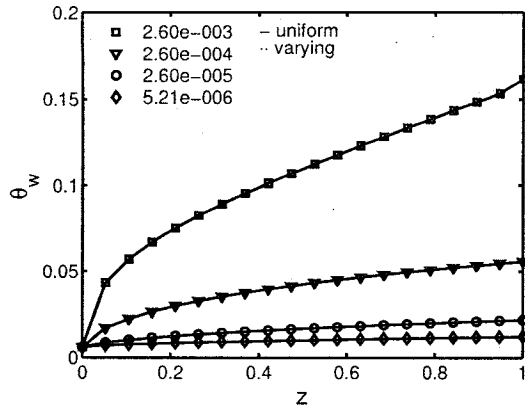
(a) Quadratic profile
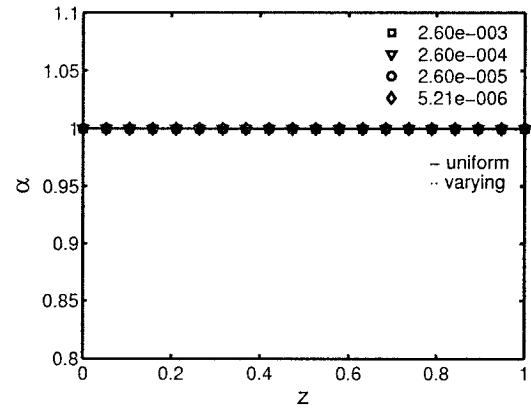
(b) Quadratic profile
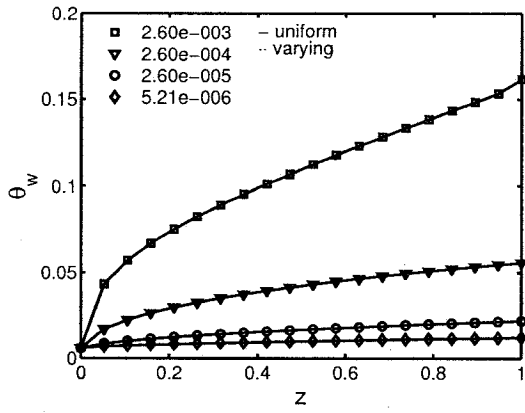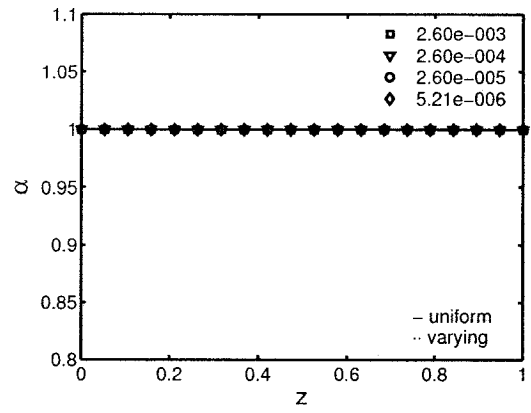
(c) Cubic profile

(d) Cubic profile

Figure C.5: Minimizing temperature gradient: 4-wall heated and thermally developing.

Appendix D

Part Drawings

D.1 Microtube Drawings

0.26

0.26

0.12

1.30

0.12

1.30

1.30

0.12

2.25

1.50

0.25

0.50

0.50

Ø 0.25 X 0.30 DEEP
1/16 NPT Tap
TYPICAL

0.25

0.75

0.75

Ø 0.125 THROUGH.
TYPICAL

Microtube
Inlet/Outlet
Chamber

Tube Test Module
Material: Polycarbonate
All dimensions in inches
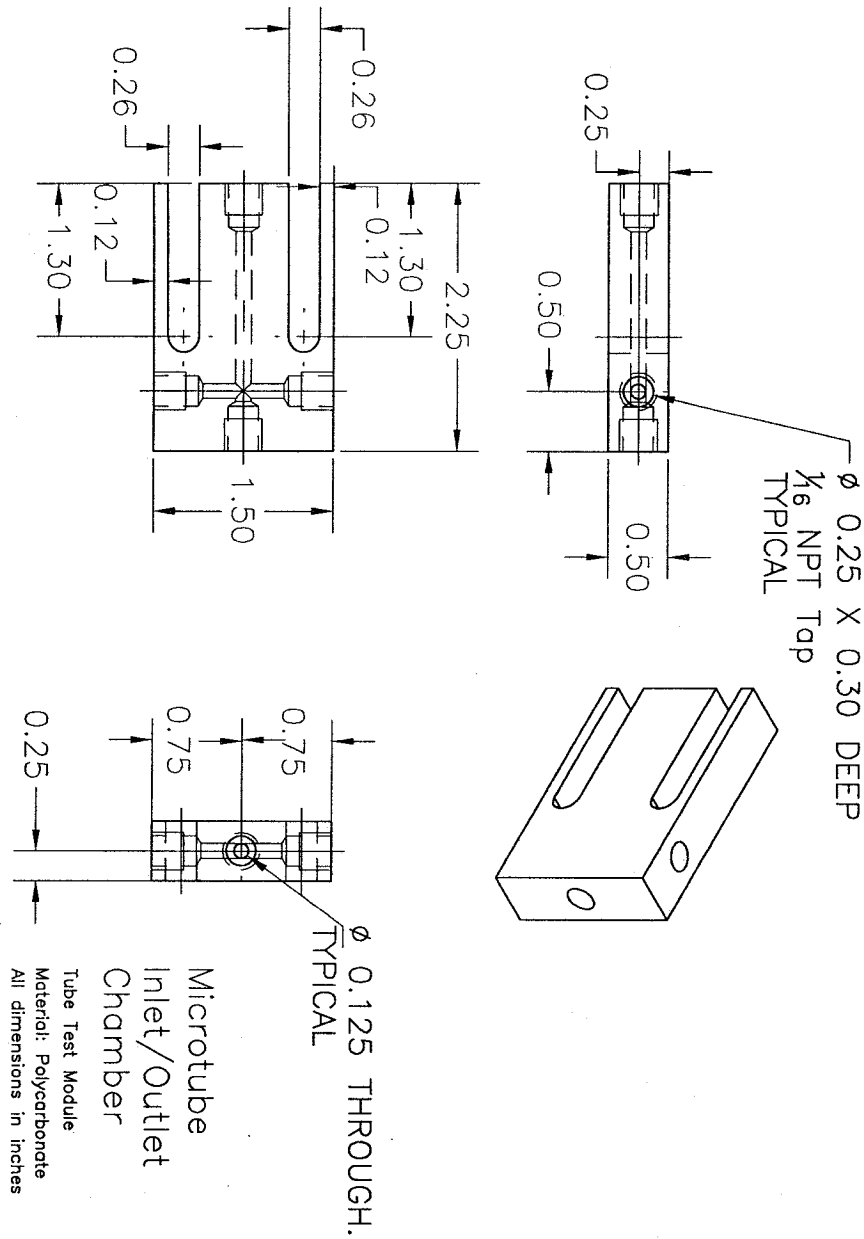
D.2 Cross-linked Heat Sink Drawings
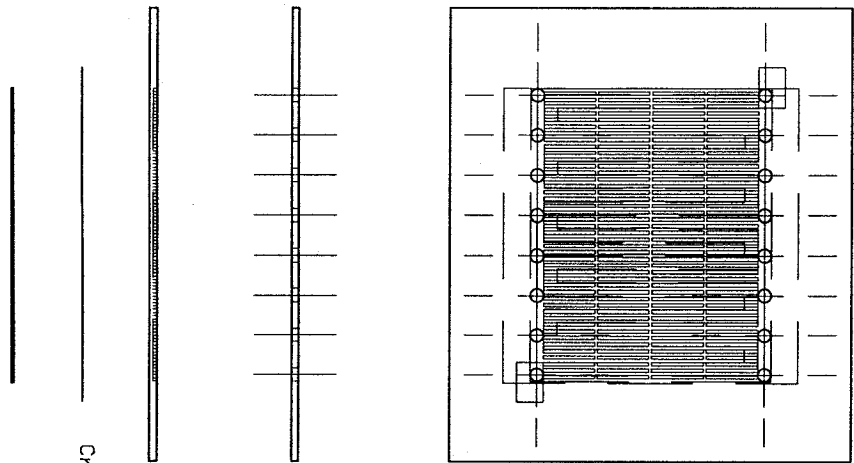
Cross-Linked Assembly
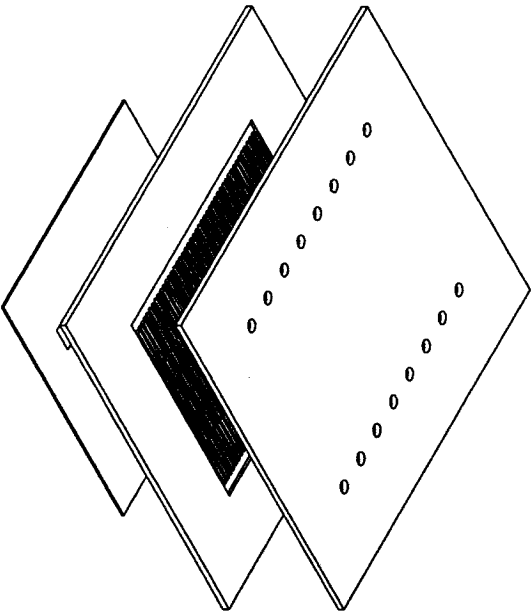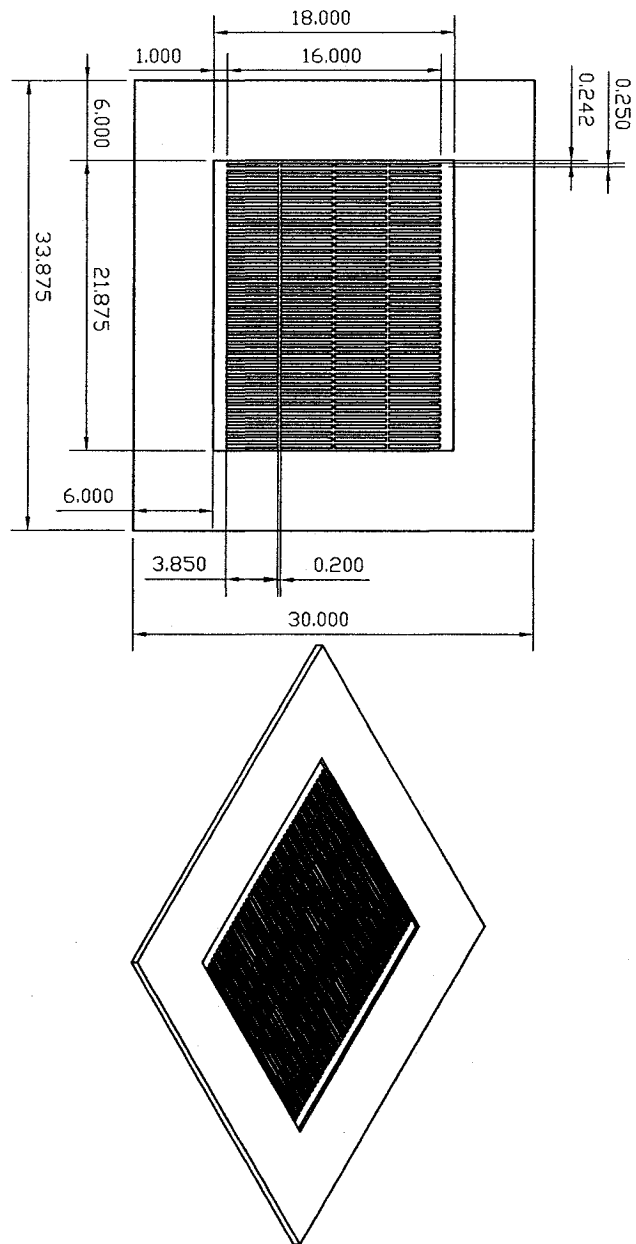
Silicon Base
Cross-Linked Design
All Dimensions in millimeters (mm)

0.300

0.550

100nm SiO2 layer

18.000
1.000
16.000
0.250
0.242
6.000
33.875
21.875
6.000
3.850
0.200
30.000

VIEW A

0.200

0.242

0.250

1.000

16.000

21.875

33.875

30.000
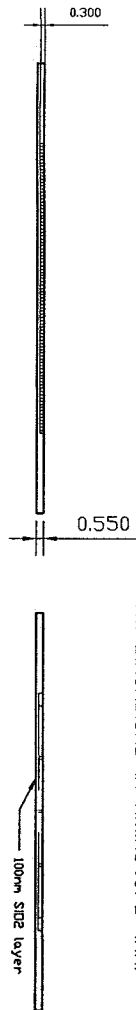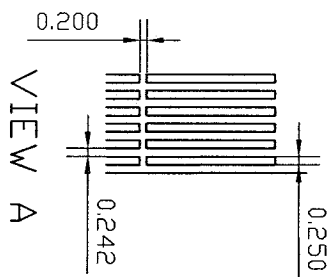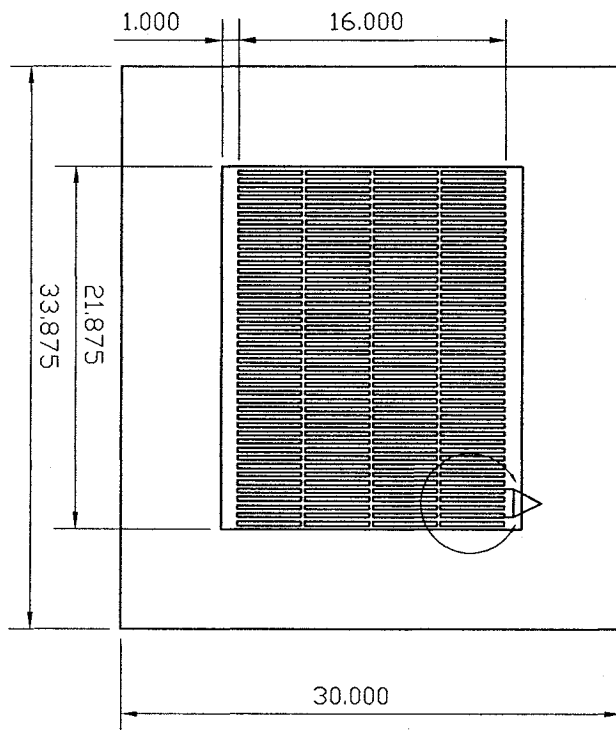
Silicon Base – Detail
View
Cross-Linked Design

All dimensions in millimeters (mm)

329
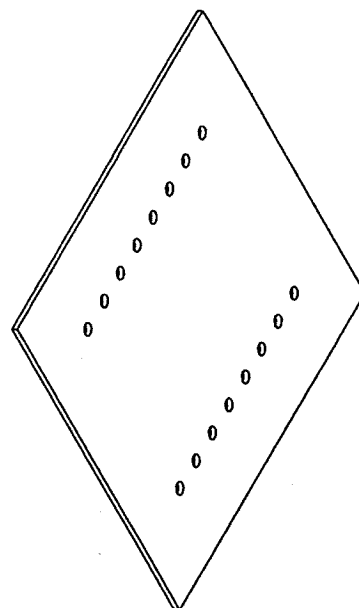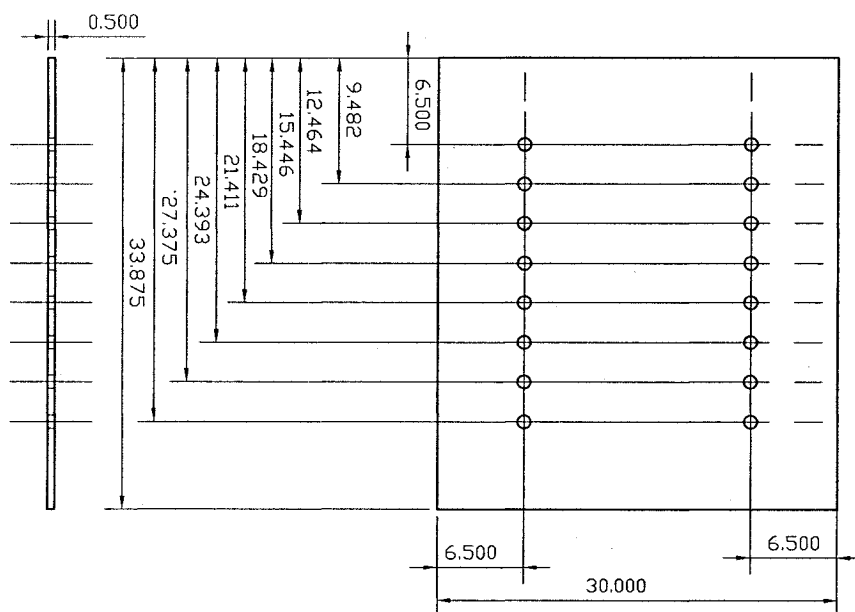
Pyrex Cover
Cross-Linked Design

All Dimensions in millimeters (mm)

0.500

9.482
12.464
15.446
18.429
21.411
24.393
27.375
33.875

6.500

6.500

6.500

30.000

330

Film Heater Pattern
All dimensions in millimeters (mm)
Deposition Thickness
Platinum - 0.2um
(0.0002mm)

18.000

16.000

15.000

14.000

2.000

1.000

3.000

1.000

1.000

3.000

2.000

1.000
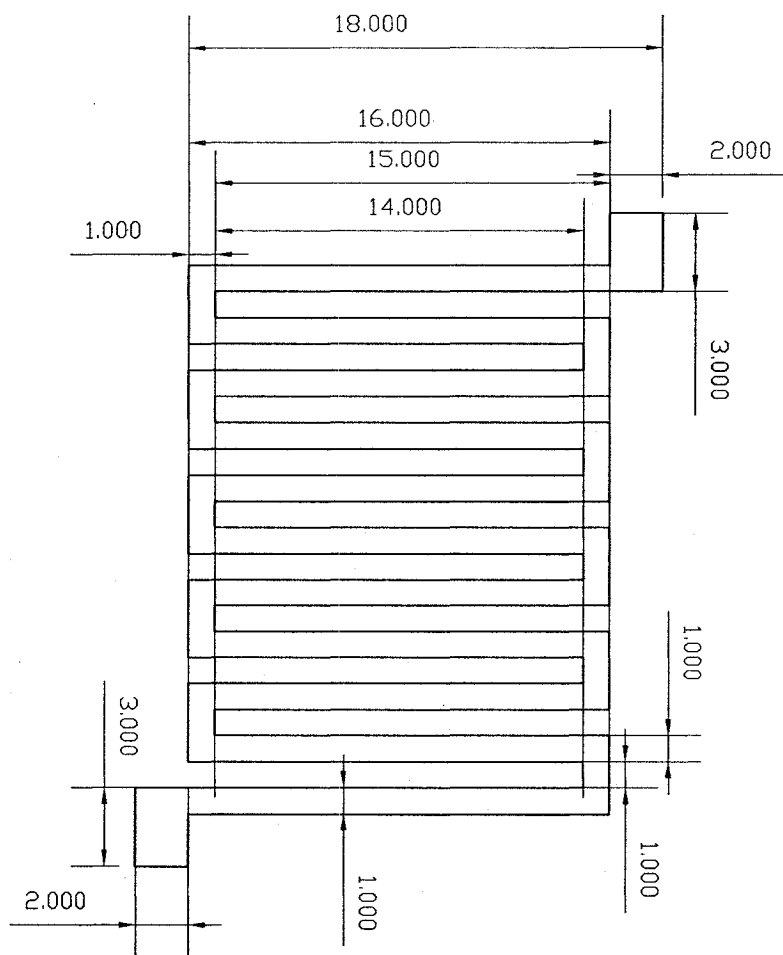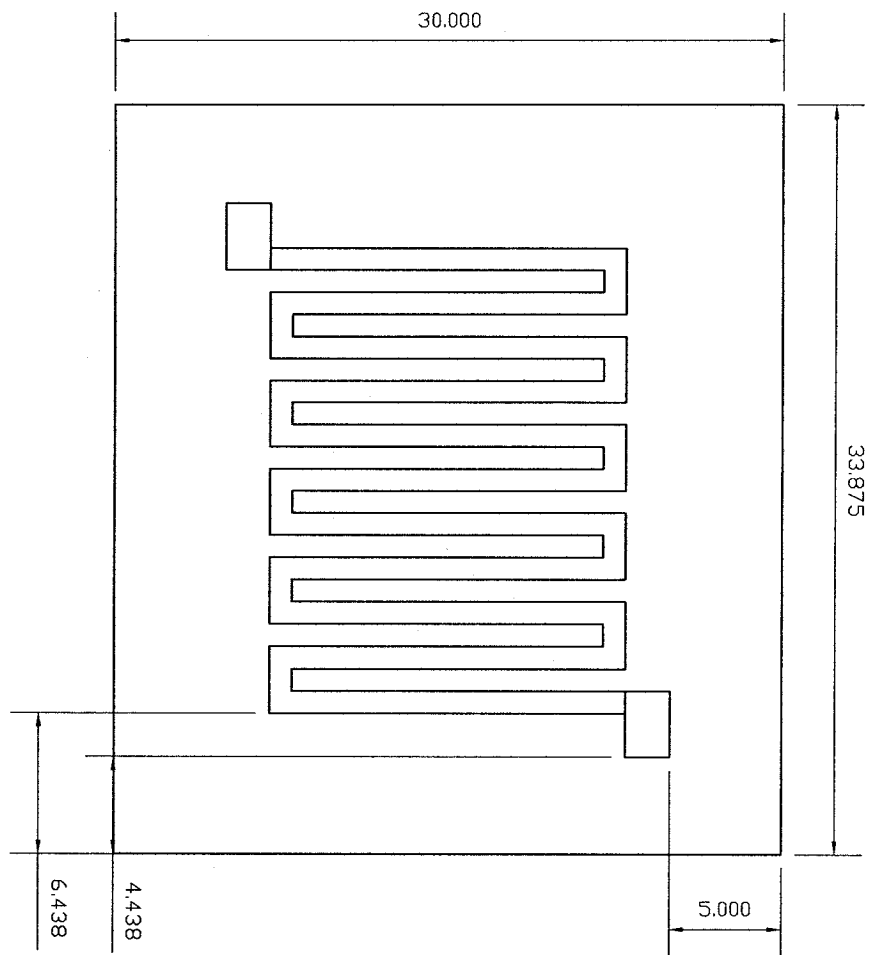
Parallel Heat Sink Heater Pattern Location
All dimensions in millimeters (mm)

30.000

33.875

6.438

4.438

5.000

D.3 Radial Heat Exchanger Drawings

Assembly
Radial Design

0.55

Ø1.056
Ø23.110
Ø21.110

0.115

15.498

4.806

10.280

31.110

15.555

15.555

31.110

0.300

Silicon Base
Radial Design
All Dimensions in millimeters (mm)

100nm SiO2 layer

10.280

A

0.115

Ø23.110

Ø21.110

31.110

15.555

15.498

Ø1.056

15.555

4.806

31.110

VIEW A

0.115

Silicon Base — Detail
Radial Design

All Dimensions in millimeters (mm)

31.110

15.555

31.110

15.555

0.500

⌀21.110

⌀23.110

⌀1.056
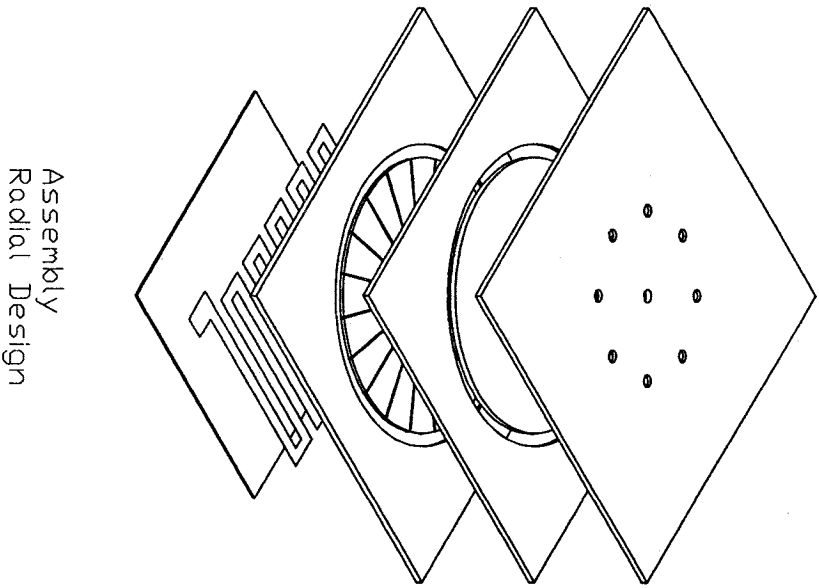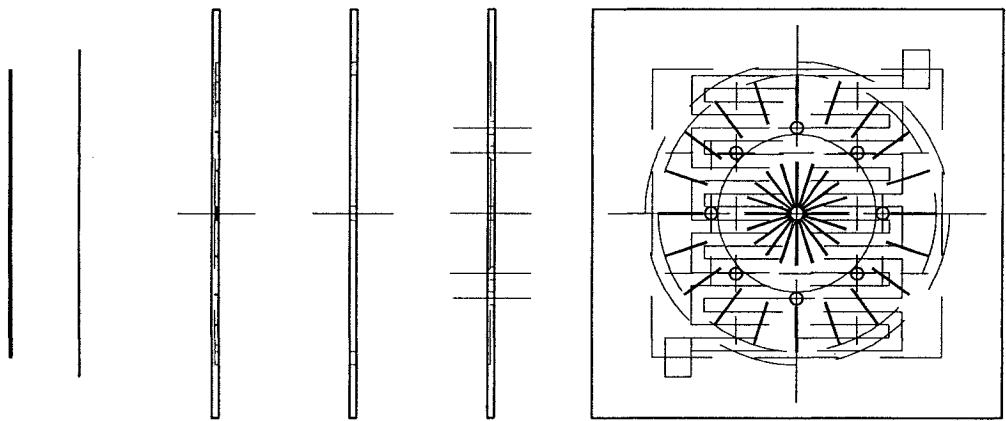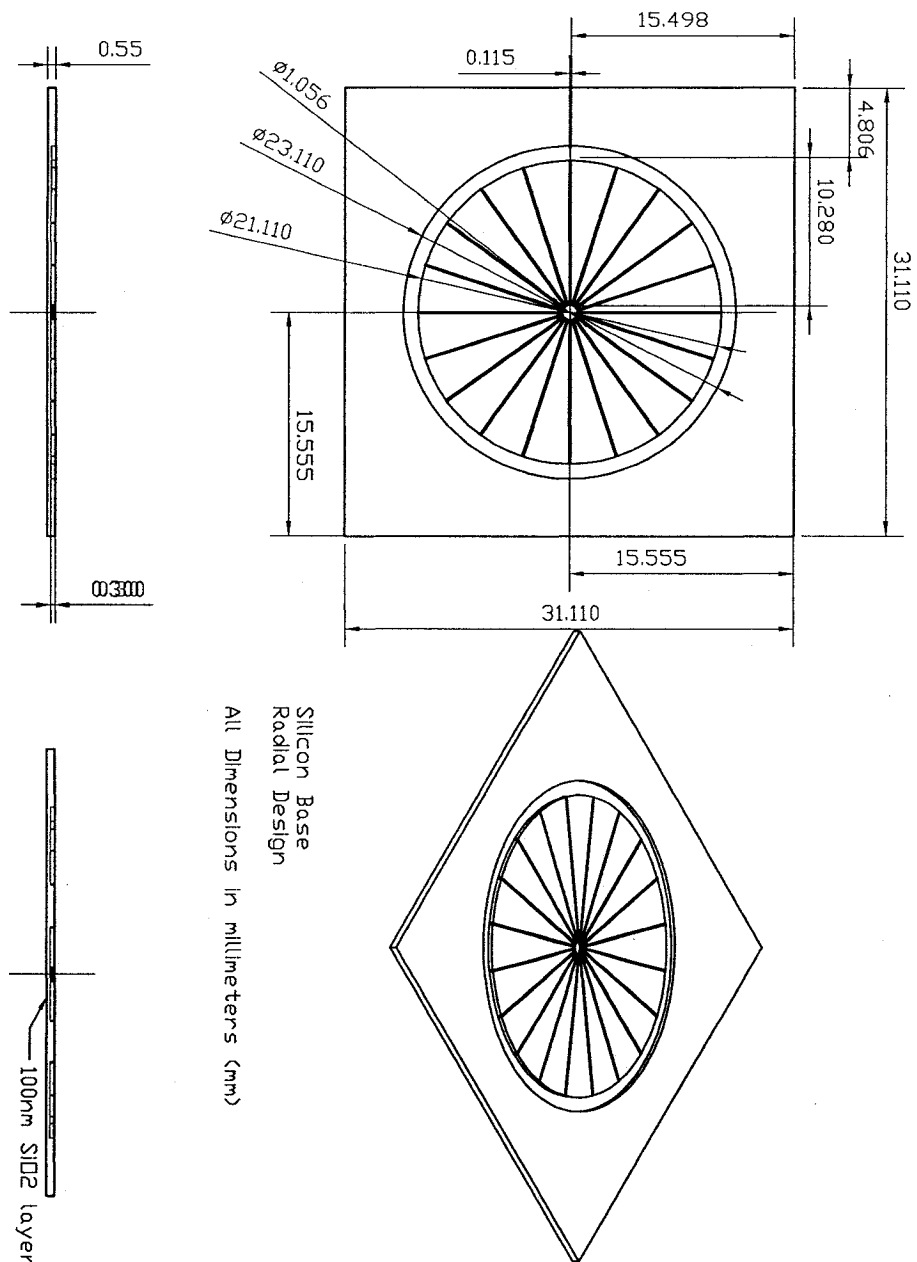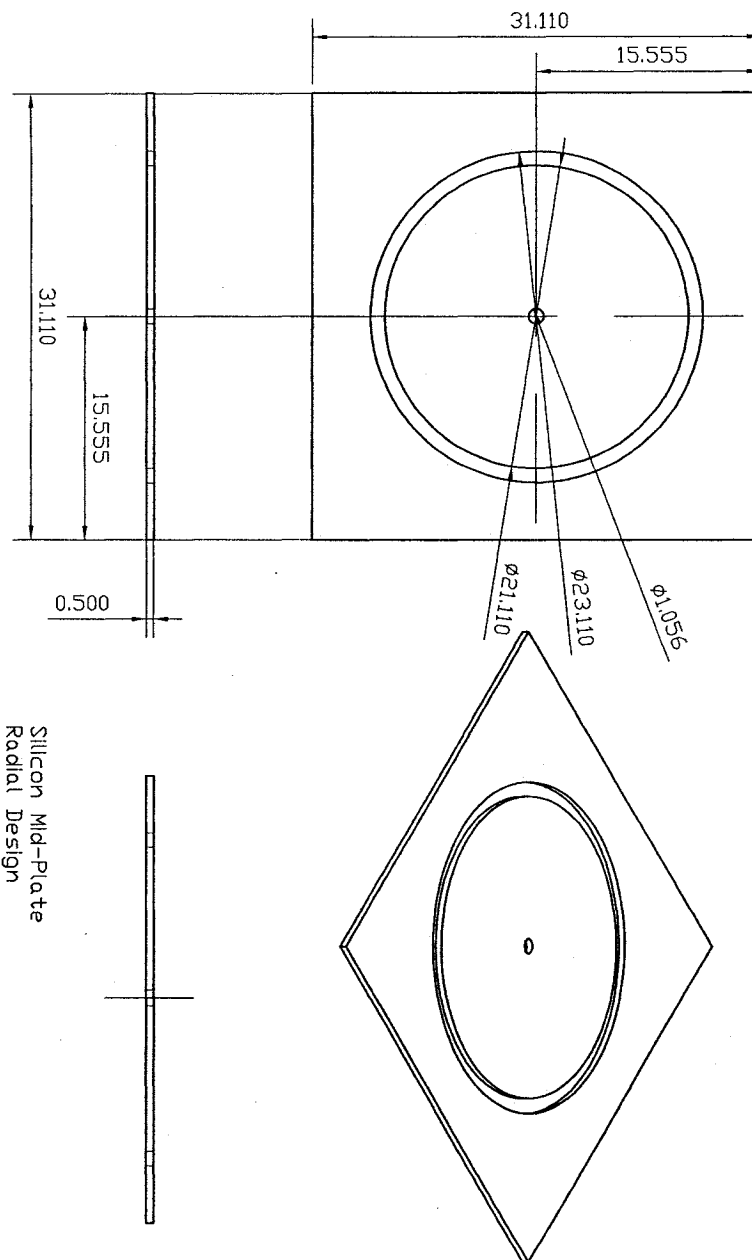
Silicon Mid-Plate
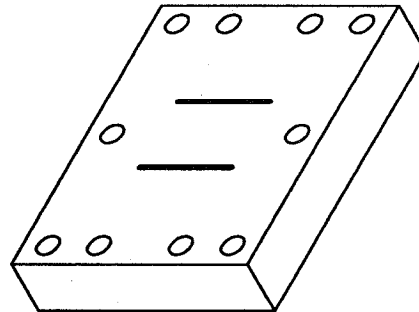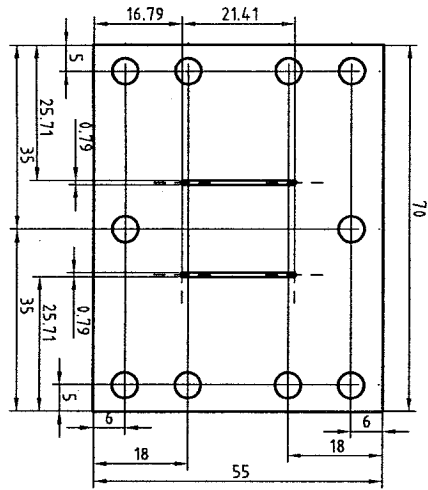Radial Design

All Dimensions in millimeters (mm)

31.110
15.555 15.555
10.960 10.960
9.055   9.055
0.500
10.960
9.055
15.555
31.110
15.555
10.960
9.055
0.200
Ø23.110
Ø12.000
Ø1.056

Pyrex Cover
Radial Design

All Dimensions in millimeters (mm)

31.111

31.110

5.555

3.055

5.055

Heater pattern location
Radial Design

All dimensions in millimeters
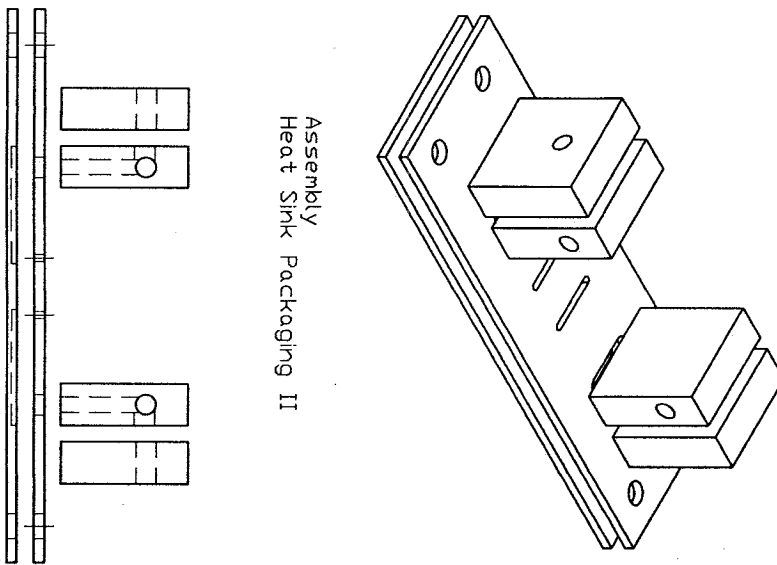(mm)

338
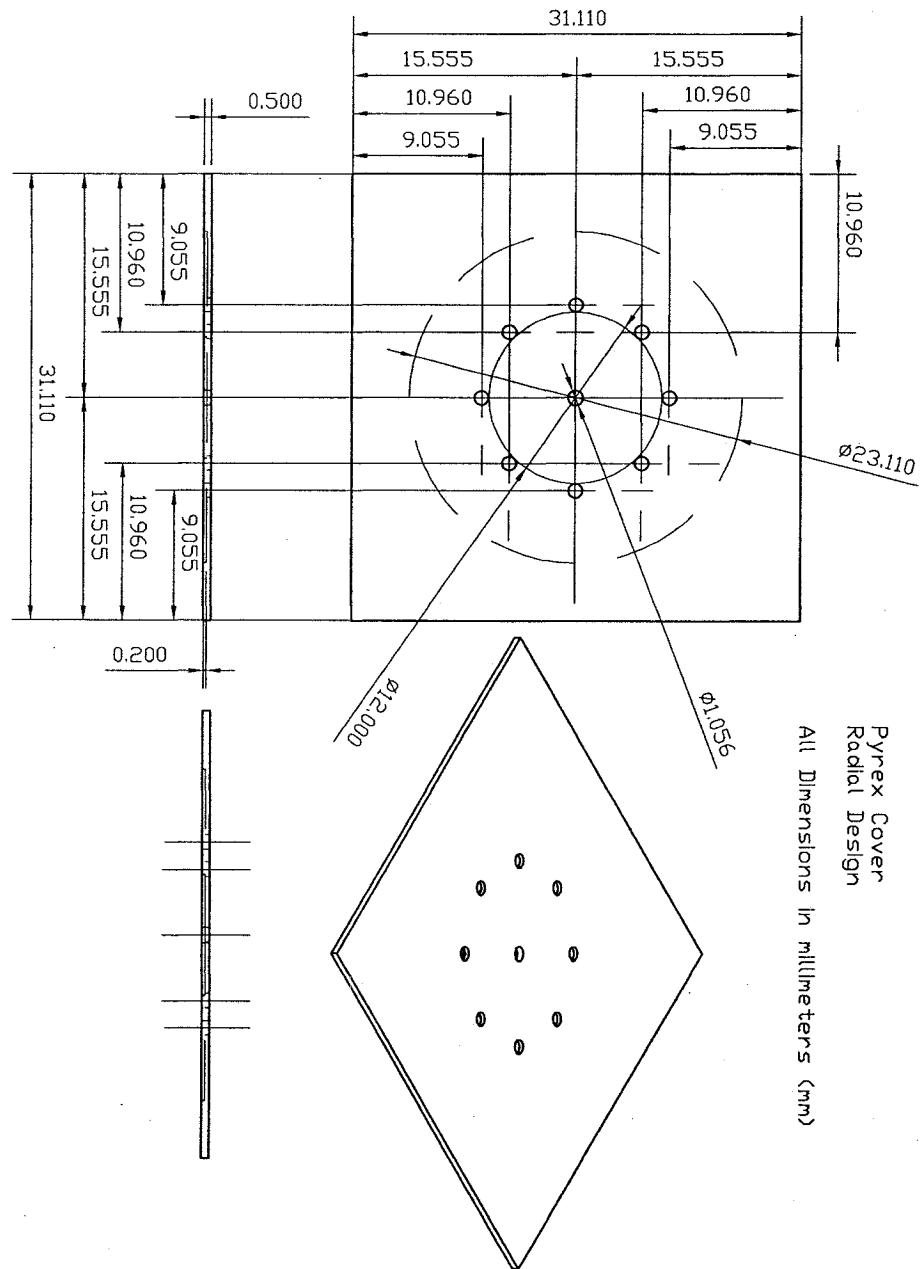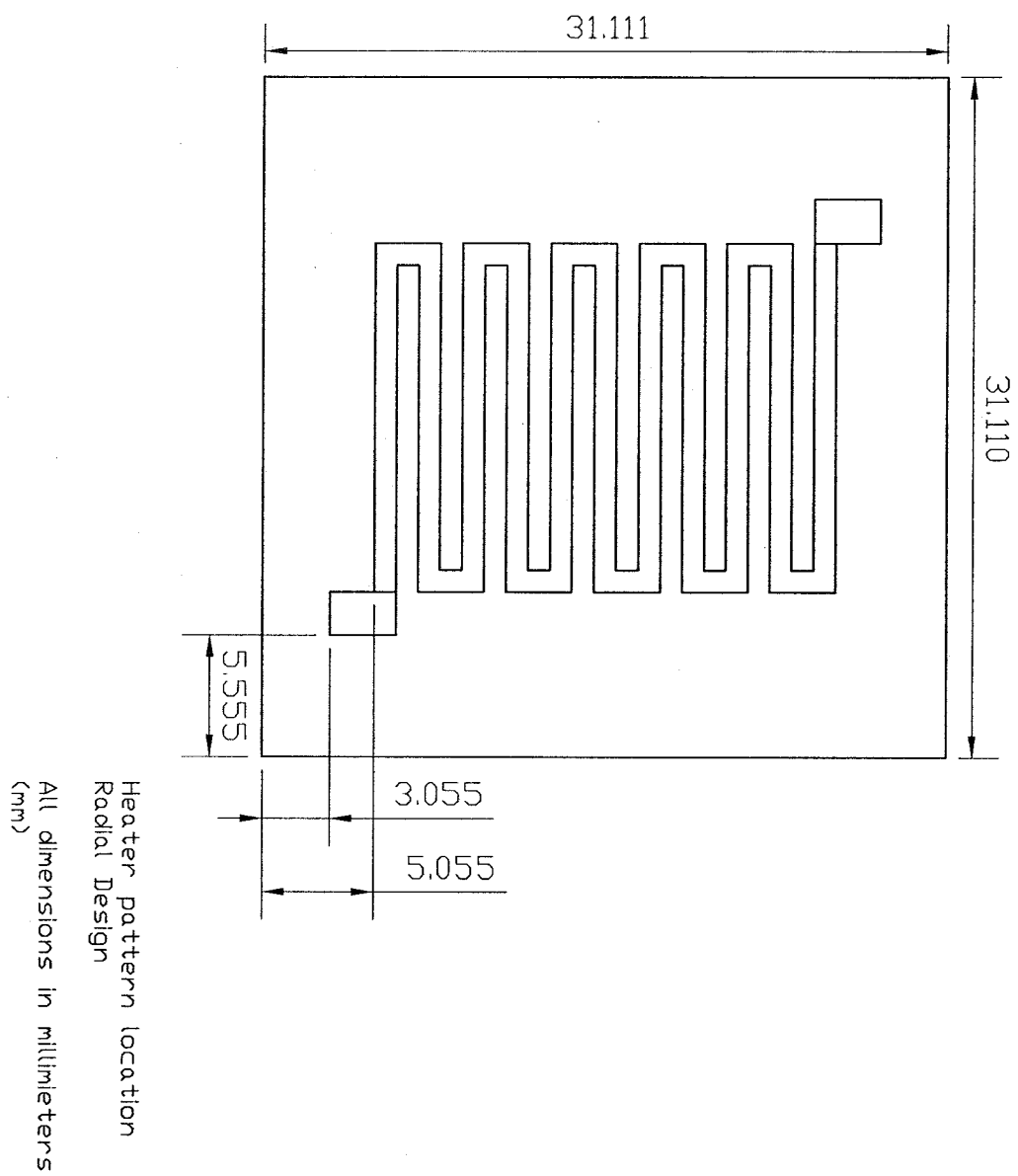
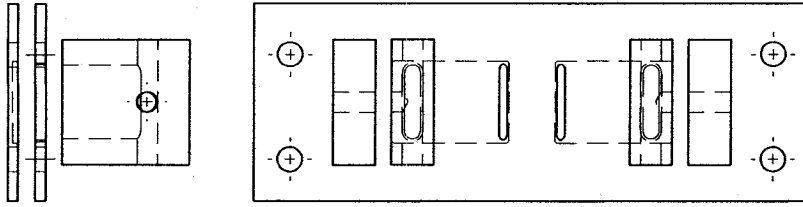# D.4   Parallel Channel Packing System I
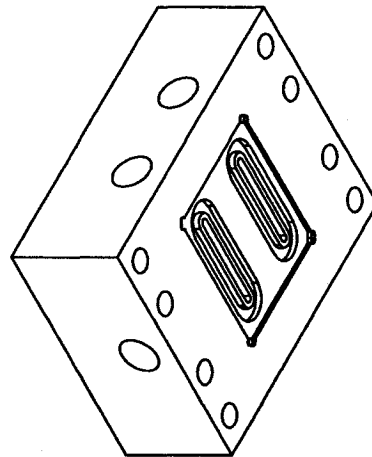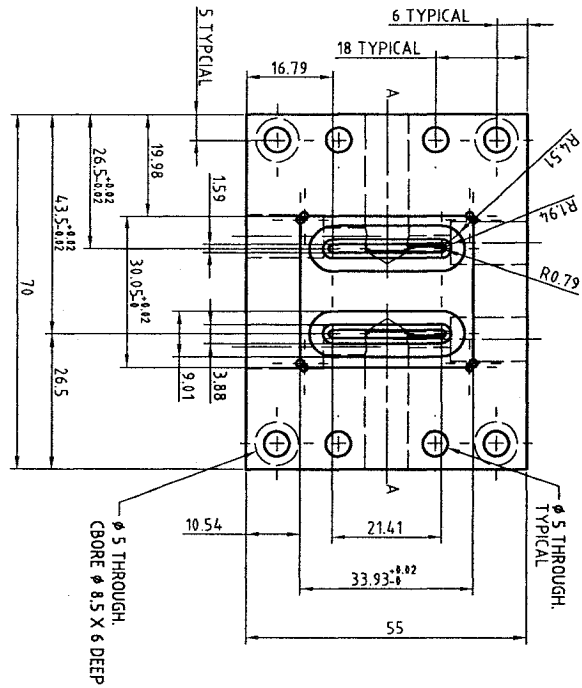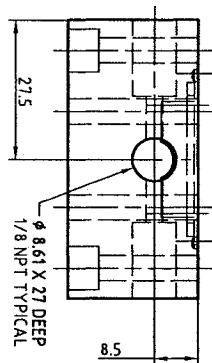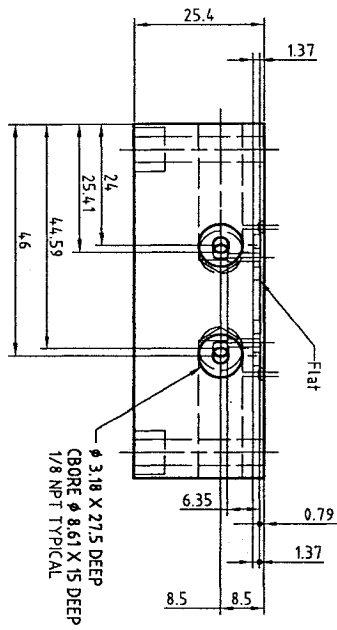
Standard / Cross–Linked Support I
All dimensions in millimenters
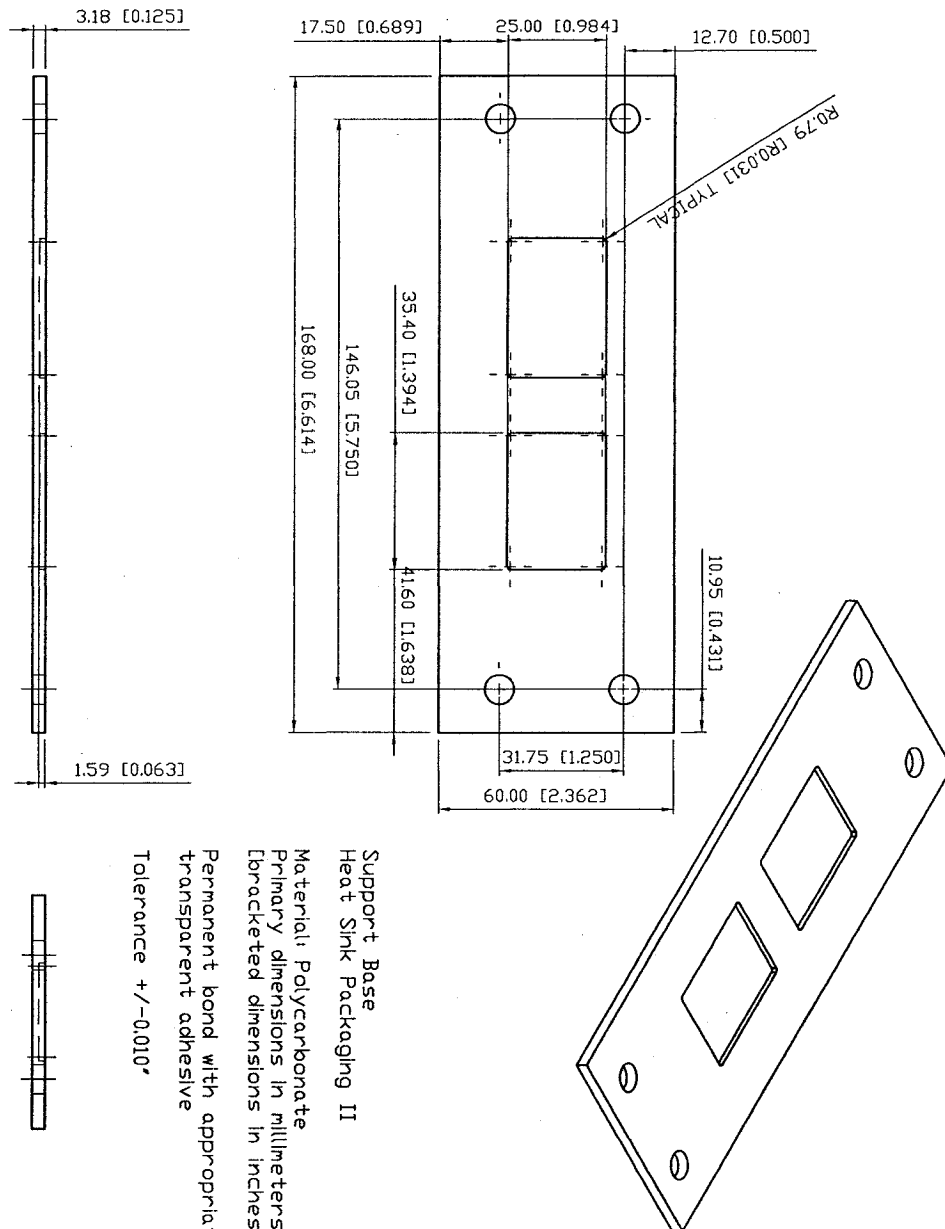Material: Teflon
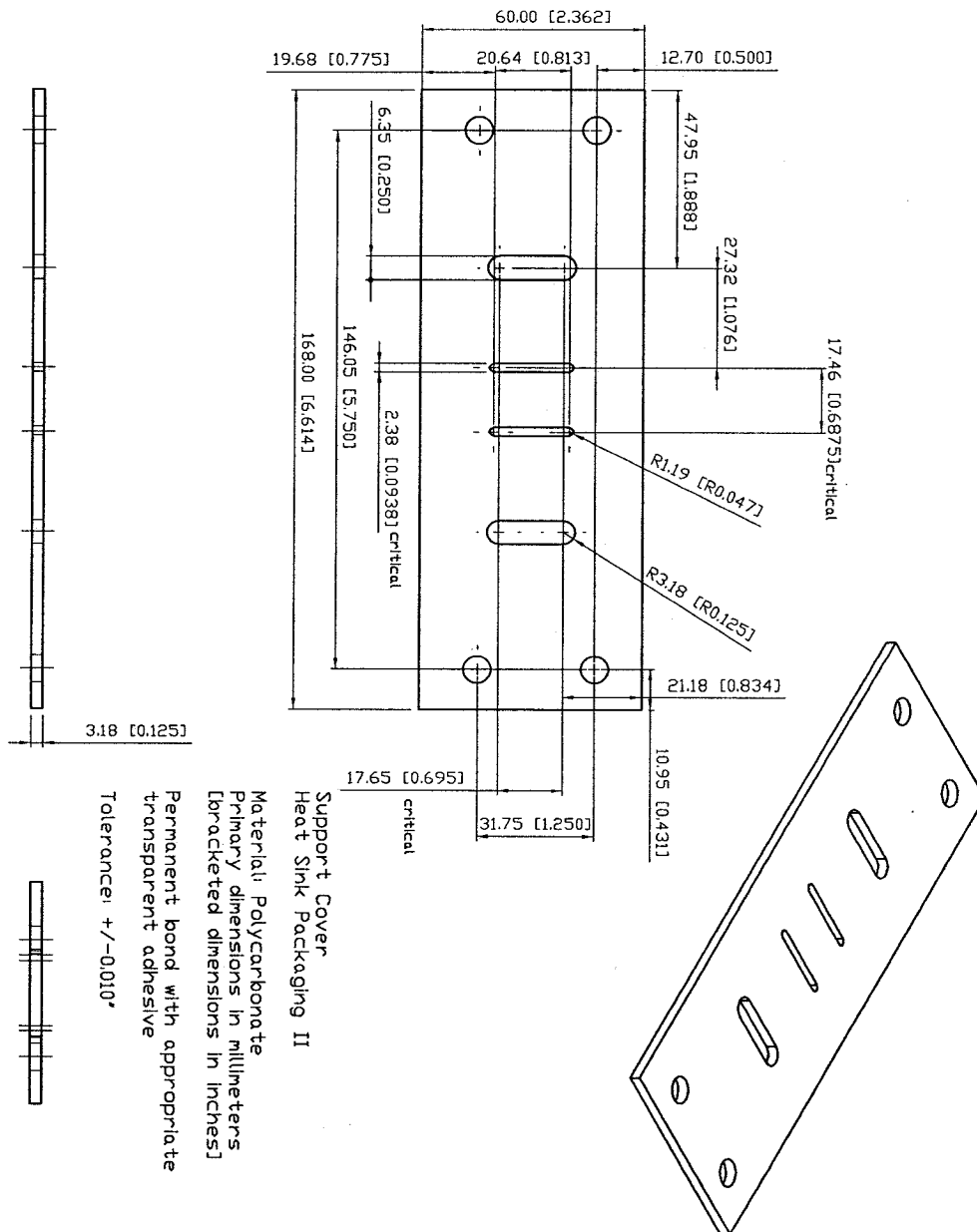Tolerance: 0.1 mm unless otherwise noted

Straight / Cross-Linked Support Mid-Plate
All dimensions in millimeters (mm)
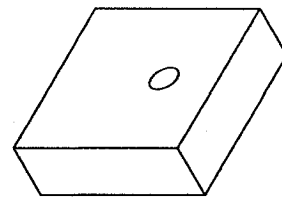Material: Teflon
Tolerance: 0.1 mm unless otherwise noted
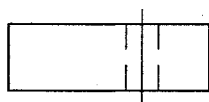
340

D.5 Parallel Channel Packaging System II

Assembly
Heat Sink Packaging II

3.18 [0.125]

17.50 [0.689]   25.00 [0.984]   12.70 [0.500]

R0.79 [R0.03] TYPICAL

35.40 [1.394]

146.05 [5.750]

168.00 [6.614]

10.95 [0.431]

41.60 [1.638]

31.75 [1.250]

60.00 [2.362]

1.59 [0.063]

Support Base
Heat Sink Packaging II

Material: Polycarbonate
Primary dimensions in millimeters
[bracketed dimensions in inches]

Permanent bond with appropriate
transparent adhesive

Tolerance +/-0.010"

60.00 [2.362]

19.68 [0.775]   20.64 [0.813]   12.70 [0.500]

6.35 [0.250]

47.95 [1.888]

27.32 [1.076]

17.46 [0.6875]critical

168.00 [6.614]

146.05 [5.750]

2.38 [0.0938] critical

R1.19 [R0.047]

R3.18 [R0.125]

21.18 [0.834]

3.18 [0.125]

17.65 [0.695]
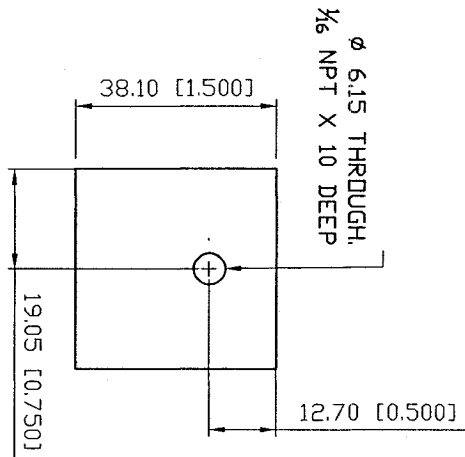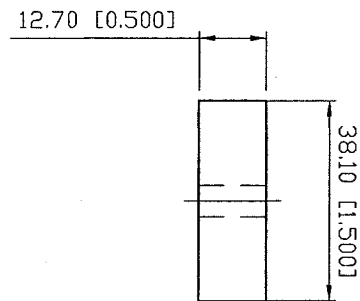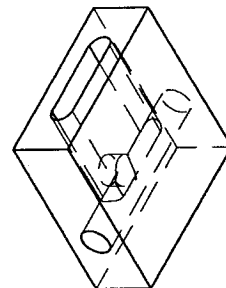critical

31.75 [1.250]

10.95 [0.431]

Support Cover
Heat Sink Packaging II

Material: Polycarbonate
Primary dimensions in millimeters
[bracketed dimensions in inches]

Permanent bond with appropriate
transparent adhesive

Tolerance: +/-0.010"

343

38.10 [1.500]

19.05 [0.750]

12.70 [0.500]

⌀ 6.15 THROUGH.
⅛₆ NPT X 10 DEEP
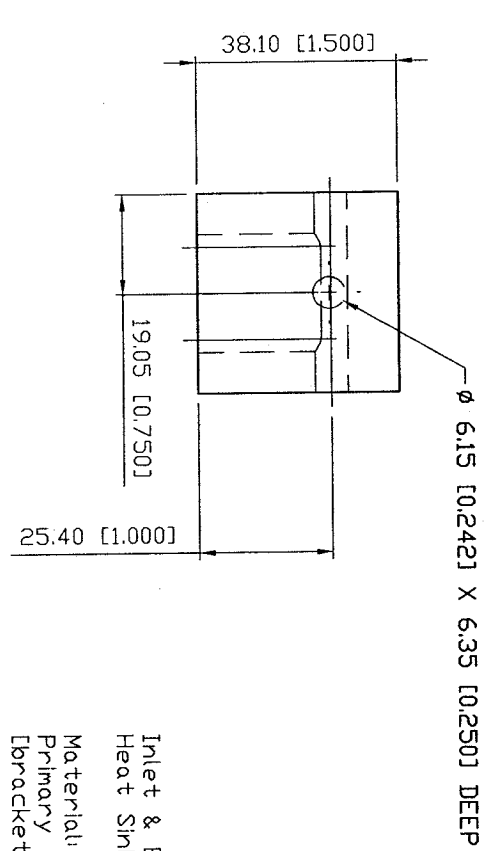
12.70 [0.500]

38.10 [1.500]

Heat Sink Packaging II

Material: Polycarbonate
Primary dimensions in millimeters
[bracketed dimensions in inches]

Permanent bond with appropriate
transparent adhesive

Tolerance +/-0.010'

344

4.76 [0.188]

10.23 [0.403]

38.10 [1.500]

17.65 [0.695]

6.35 [0.250]

12.70 [0.500]

38.10 [1.500]

19.05 [0.750]

25.40 [1.000]

ø 6.15 [0.242] X 6.35 [0.250] DEEP

ø 6.15 THROUGH.
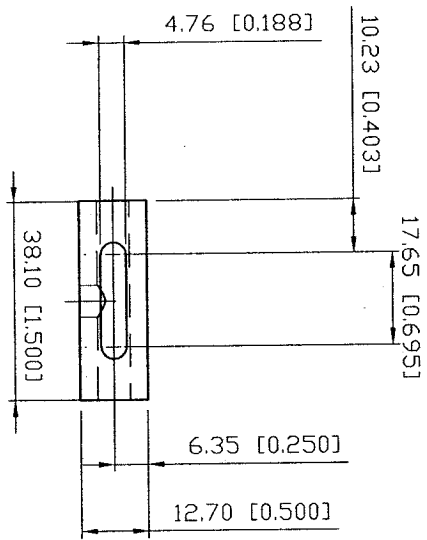1/16 NPT x 10 DEEP - BOTH SIDES

25.40 [1.000]

6.35 [0.250]

Inlet & Exit Ports
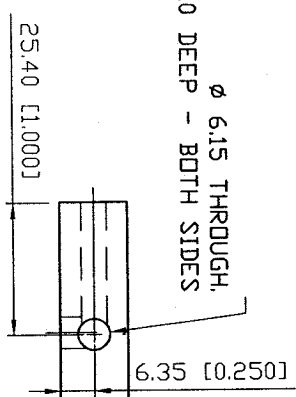Heat Sink Packaging II

Material: Polycarbonate
Primary dimensions in millimeters
[bracketed dimensions in inches]

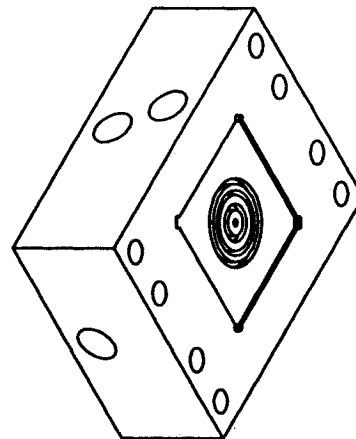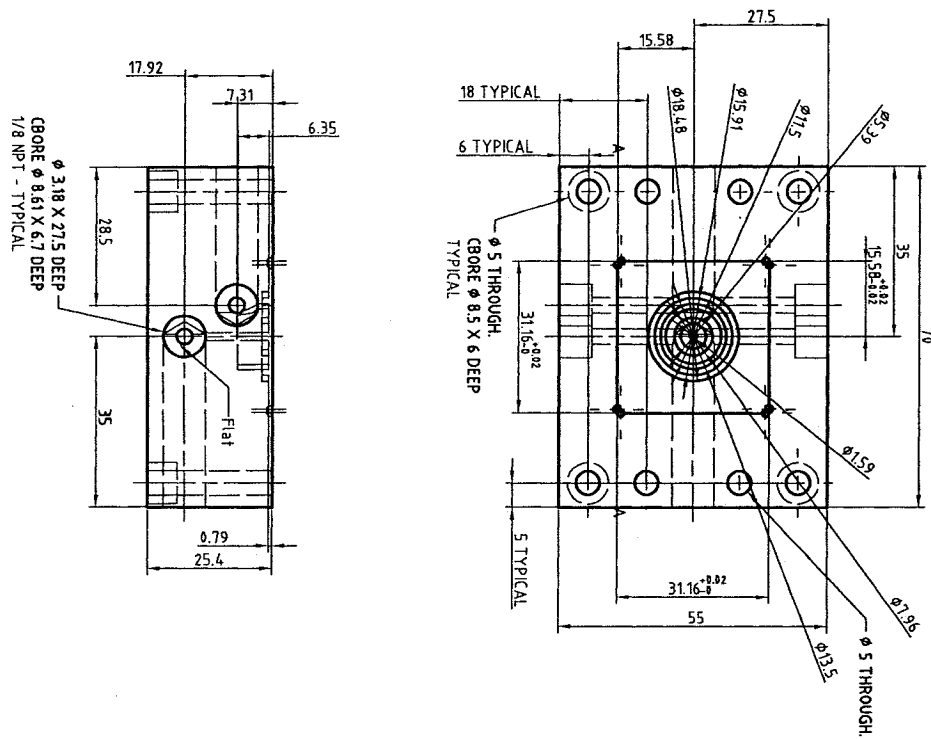Permanent bond with appropriate
transparent adhesive

Tolerance +/-0.010"

D.6 Radial Channel Packaging System

17.92

7.31

6.35

CBORE ∅ 8.61 X 6.7 DEEP
∅ 3.18 X 27.5 DEEP
1/8 NPT - TYPICAL

28.5

35

Flat

0.79
25.4

27.5

15.58

18 TYPICAL

6 TYPICAL

∅ 5 THROUGH.
CBORE ∅ 8.5 X 6 DEEP
TYPICAL

∅18.48

∅15.91

∅15

∅5.3

35

15.58$^{+0.02}_{+0.02}$

70

31.16$^{+0.02}_{-0}$

5 TYPICAL

∅15.9

31.16$^{+0.02}_{-0}$

55

∅13.5

∅7.96

∅ 5 THROUGH.

7.31

27.5

∅ 8.61 X 35.5 DEEP
1/8 NPT - TYPICAL

17.92

Radial Support
Heat Sink Packaging I

All dimensions in millimeters
Material: Teflon
Tolerance: 0.1mm unless otherwise specified

346